Atomic Layer Deposition Reflective Coatings for future Astronomical Space Telescopes and the Solar Corona viewed through the MinXSS (*Miniature X-ray Solar Spectrometer*) CubeSats

by

Christopher Samuel Moore

M.S., Astrophysical and Planetary Science, University of

Colorado-Boulder, 2014

B.S., Physics, University of Iowa, 2010

B.S., Astronomy, University of Iowa, 2010

A thesis submitted to the

Faculty of the Graduate School of the

University of Colorado in partial fulfillment

of the requirements for the degree of

Doctor of Philosophy

Department of Astrophysical and Planetary Science

2017

ProQuest Number: 10680697

ProQuest 10680697

This thesis entitled:
Atomic Layer Deposition Reflective Coatings for future Astronomical Space Telescopes and
the Solar Corona viewed through the MinXSS (*Miniature X-ray Solar Spectrometer*)
CubeSats
written by Christopher Samuel Moore
has been approved for the Department of Astrophysical and Planetary Science

_____

Prof. Kevin C. France

_____

Dr.. Thomas N. Woods

_____

Dr.. Amir Caspi

_____

Prof. Steve R. Cranmer

_____

Prof. James C. Green

Date _____

The final copy of this thesis has been examined by the signatories, and we find that both
the content and the form meet acceptable presentation standards of scholarly work in the
above mentioned discipline.

Moore, Christopher Samuel (Ph.D., Astrophysical and Planetary Science)

Atomic Layer Deposition Reflective Coatings for future Astronomical Space Telescopes and

the Solar Corona viewed through the MinXSS (*Miniature X-ray Solar Spectrometer*)

CubeSats

Dissertation directed by Prof. Kevin C. Franceand Dr.. Thomas N. Woods

Advances in technology and instrumentation open new windows for observing astrophysical objects. The first half of my dissertation involves the development of atomic layer deposition (ALD) coatings to create high reflectivity UV mirrors for future satellite astronomical telescopes. Aluminum (Al) has intrinsic reflectance greater than 80% from $90 - 2,000$ nm, but develops a native aluminum oxide (Al_2O_3) layer upon exposure to air that readily absorbs light below 250 nm. Thus, Al based UV mirrors must be protected by a transmissive overcoat. Traditionally, metal-fluoride overcoats such as MgF_2 and LiF are used to mitigate oxidation but with caveats. We utilize a new metal fluoride (AlF_3) to protect Al mirrors deposited by ALD. ALD allows for precise thickness control, conformal and near stoichiometric thin films. We prove that depositing ultra-thin ($\sim$3 nm) ALD ALF_3 to protect Al mirrors after removing the native oxide layer via atomic layer etching (ALE) enhances the reflectance near 90 nm from $\sim$5% to $\sim$30%.

X-ray detector technology with high readout rates are necessary for the relatively bright Sun, particularly during large flares. The hot plasma in the solar corona generates X-rays, which yield information on the physical conditions of the plasma. The second half of my dissertation includes detector testing, characterization and solar science with the *Miniature X-ray Solar Spectrometer* (MinXSS) CubeSats. The MinXSS CubeSats employ Silicon Drift Diode (SDD) detectors called X123, which generate full sun spectrally resolved ($\sim$0.15 FWHM at 5.9 keV) measurements from the sparsely measured, $0.5 - 12$ keV range. The absolute radiometric calibration of the MinXSS instrument suite was performed at the National

Institute for Standards and Technology (NIST) Synchrotron Ultraviolet Radiation Facility (SURF) and spectral resolution determined from radioactive sources. I used MinXSS along with data from the *Geostationary Operational Environmental Satellites* (GOES), *Reuven Ramaty High Energy Solar Spectroscopic Imager* (RHESSI), *Hinode X-ray Telescope* (XRT), *Hinode Extreme Ultraviolet Imaging Spectrometer* (EIS) and *Solar Dynamics Observatory* (SDO) *Atmospheric Imaging Assembly* (AIA) to study the solar corona. This resulted in new insights on the coronal temperature distribution and elemental abundance variations for quiescence, active regions and during solar flares.

Dedication

This dissertation is dedicated to all those kids out there that dare to DREAM BIG and never be deterred. To those that eventually reach their dreams. I dedicate this dissertation to those that helped me along on this journey. To those that helped a kid keep his dream alive. Your compassion, assistance and time has not been in vain. This is dedicated to my friends that have supported me over the years. This is dedicated to Adrienne Vesey. Hopefully it can inspire her to follow her dreams.

This dissertation is dedicated to my family. Especially my mother and father, who sacrificed some of their dreams to make mine a reality. The dream of a better life when my father left the Jim Crow segregated Alabama in the second wave of the African American 'Great Migration'. The dream of a better life when my mother when she left the public housing in Chicago for a home in the suburbs. The dream of a better life of my paternal grandparents had as they worked in Alabama. The dream of a better life when my maternal grandfather and grandmother left the Jim Crow southern states of Louisiana and Georgia to move to Chicago, Illinois in the first wave of the African American 'Great Migration'. Although my ancestors history has been somewhat lost, I am sure many of them dreamed of a better life while in shackles. The dreams of a better life while slaves in the southern United States. The dreams of "life, liberty and the pursuit of happiness", the so-called 'American Dream'. While many of then never realized those dreams, their sacrifice has not been in vain. Because this descendant has realized his dream!

Acknowledgements

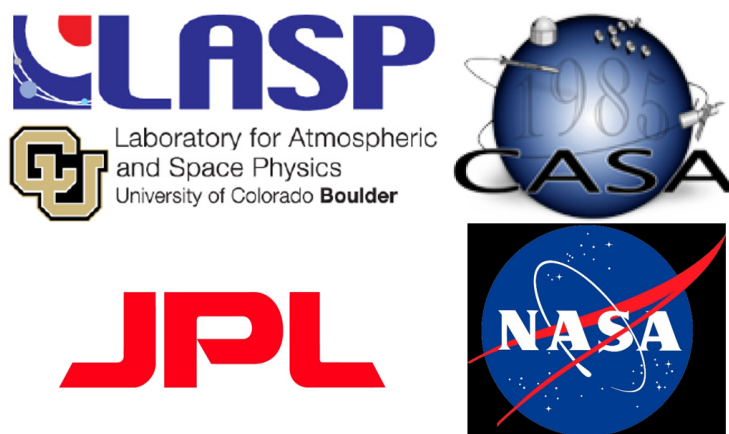Figure 1: Special thanks for the opportunity to pursue the research in this Dissertation goes out to the University of Colorado - Boulder, Center for Astrophysics and Space Astronomy (CASA), Laboratory for Atmospheric and Space Physics (LASP), National Aeronautics and Space Administration (NASA) and the Caltech Jet Propulsion Laboratory (JPL).

Contents

Chapter

Tables

Table

Figures

Figure

Chapter 1

Introduction

1.1   Technology Development and Instrumentation for Astrophysics

Humans have always wondered about our place in the heavens. Observing shining objects in the night sky has raised interest about their origin, and their relation to us on planet Earth. To investigate these sparkling objects we use our natural light detectors, our eyes. Eyes are the quintessential instrument for detecting light and diagnosing the properties of our surrounding environment. The advent of optical aids to detect objects in the night sky such as the telescope (first documented by Euro-centric history in 1608, by Hans Lippershey and popularized by Galileo Galilei) has augmented our understanding of celestial bodies. Because many astrophysical objects are far away, the majority of the information that we attain on their properties is derived from the light that we can collect from them.

There are exceptions. In situ measurements of particles, electric and magnetic fields in interplanetary space, fluorescent measurements of rocks by robots on Mars, samples collected from the Moon are only a few examples of direct measurements in our Solar System. Aside from the recent detection of gravitational waves [1], and cosmic rays, for all objects residing outside of the heliosphere (the Sun's local region of influence) electromagnetic radiation is our only source of information. Thus, developing understanding of phenomena that can create and modify light, and creating devices to measure and analyze light are pivotal for astrophysics. Astrophysics and astronomy are highly dependent upon observations. There have been many phenomena that were not fathomed until a new observations revealed them.

This brings us to the theme of this PhD dissertation, summarized in Figure 1.1. New technology leads to improved instrumentation, enabling better observations and data to assess theoretical models and numerical simulations.
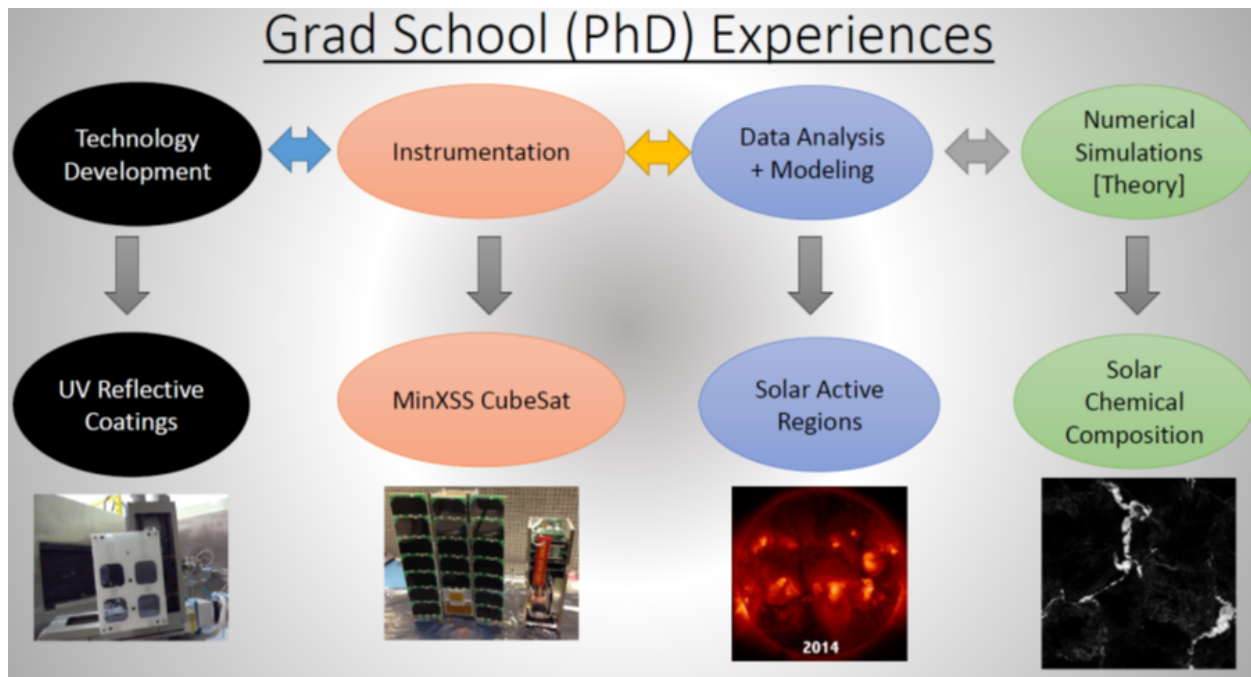
Figure 1.1: Diagram of a few main aspects of astrophysics: Technology Development, Instrumentation, Observations plus Data Analysis, and Numerical Simulations. The bottom rows illustrate the research included in this dissertation.

Now in reality, the flow chart does not always begin with technology and end with theory. The reverse can be true in that current theory may not be capable of describing an observed phenomena. This puts a need for higher quality observations, which in turn drives the need for improved or different instrumentation that may not be capable until new advances in technology. This dissertation is a journey in technology development with an ultraviolet (UV) coatings project, instrumentation involving the X-ray detectors of the Miniature X-ray Solar Spectrometer (MinXSS) CubeSat, observations and data analysis (science) on the solar corona.

I would like to acknowledge and thank the funding sources that helped make this research possible. The National Aeronautics and Space Administration (NASA) Space Tech-

nology Research Fellowship (NSTRF), the University of Colorado - Boulder Astrophysical and Planetary Sciences (APS) Department, the Center for Astrophysics and Space Astronomy (CASA), the Laboratory for Atmospheric and Space Astronomy (LASP) and the Caltech Jet Propulsion Laboratory (JPL), see Figure 1.

This PhD dissertation is heavily focused on technology development to enable new discoveries in astrophysics in the ultraviolet (UV) and instrumentation in X-rays for solar physics. Thus this dissertation is divided into three sections. The first is the NSTRF project to develop new UV mirror coatings for the next generation of astronomical space telescopes. This is the focus of Chapter 3, Chapter 4 and Chapter 5. The second portion of this dissertation involves the testing and performance of the X-ray instruments on-board the Miniature X-ray Solar Spectrometer CubeSat in Chapter 7, Chapter 8, Chapter 9. The third aspect of this dissertation is focused on solar science using the MinXSS-1 CubeSat and other solar observatories of the corona in Chapter 9, Chapter 10, Chapter 11, and Chapter 12.

To set the tone and supply background information on these three segments are Chapter 2 with introductory material on basic atomic and radiative properties, and basic implications of UV coating technology on astrophysics science. Chapter 6 is an introduction on the solar corona. Essentially Chapters 2 - 5 are UV coatings based and Chapters 6 - 12 are MinXSS CubeSat based.

Chapter 2

Atomic Processes and Science with UV Coatings

A wealth of information on the physical processes occurring in on object resides in the light emitted by that object. Astronomy and astrophysics takes advantage of this fact to explore our universe and better comprehend the cosmos. Employing analysis utilizing fundamental physical principles allows scientist to extract the relevant information on an object. The electromagnetic (EM) spectrum (as we currently understand it) spans many orders of magnitude in photon energy (E_{ph}), which is related to the frequency of a photon, ν by the relation $E_{ph} = h\nu$. h is the Planck constant where h = 6.26 x 10^{-34} joules s in meter-kilogram-second (mks) units. The Planck constant is a great example that astronomy deals with very small and very large numbers. The wavelength of a photon, λ is connected to the energy by $E_{ph} = \frac{hc}{\lambda}$, where c is the speed of light in vacuum and c = 3.0 x 10^8 m s^{-1} in mks units.

Figure 2.1 demonstrate the extreme variation of the wavelengths and frequencies in the electromagnetic spectrum The continuum of 'long' wavelength (low energy) emission have been labeled radio, microwave and sub-millimeter. The 'middle' range includes infrared and visible wavelengths. The shortest wavelength (highest energy) photons are in the ultraviolet, X-ray and gamma-ray regime. The UV and X-ray spectral emission is the emphasis of this dissertation and we shall focus on the atomic processes that generate these type of emissions.
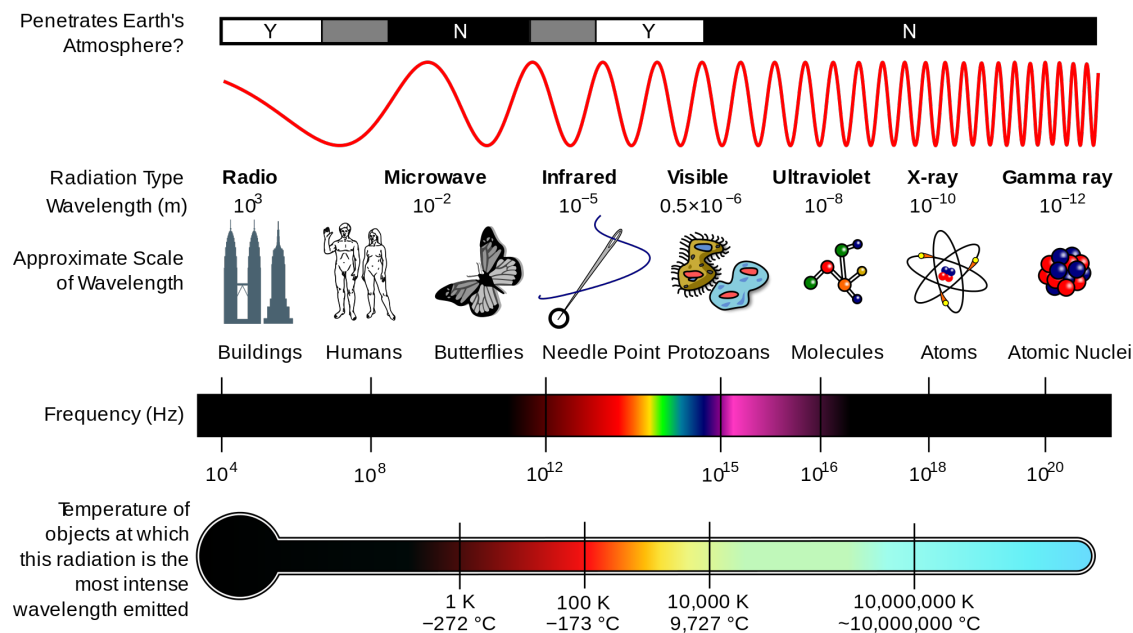
Figure 2.1: The electromagnetic spectrum is vast, spanning over 15 orders of magnitude in wavelength, frequency and energy space. Source: https://commons.wikimedia.org/wiki/File:EM_Spectrum_Properties_edit.svg under the Creative Commons Attribution-Share Alike 3.0 Unported Liscence (https://creativecommons.org/licenses/by-sa/3.0/deed.en).

2.1 UV and X-ray Radiation and their Diagnostic Capabilities

In general the UV wavelengths span from 399 nm to 10 nm. This includes the Near Ultraviolet (NUV), nominally from 300 - 399 nm, the Mid Ultraviolet (MUV) from 200 - 299 nm, the Far Ultraviolet (FUV) from 121 - 199 nm, the Lyman Ultraviolet from 90 - 121 nm, the Extreme Ultraviolet (EUV) from 10 - 89 nm. These partitions are simply names of the regions and are not strictly defined. Different groups maintain different definitions. The properties of light at a range of wavelengths and its interaction with matter (solids, liquids, gases and plasma) dictate the separation of the EM spectrum. The conversion between the wavelength of light in nanometers to energy units in keV is given by Equation 2.1, for ease

of interpretation for the rest of this thesis.

$$E_{keV} = \frac{hc}{\lambda} \approx \frac{1.24}{\lambda_{nm}} \qquad (2.1)$$

Where c = 299,792,458 m s^{-1} is the speed of light in vacuum. The X-ray regime is normally described in terms of the photon energy versus its wavelength, due to the interactions between the photons and particles, become more 'particle-particle' like. X-rays are generally broken up as soft X-rays spanning ∼0.124 - 12.4 nm (10 - 0.1 keV) and the hard X-rays for photon wavelengths less (greater) than 0.124 nm (10 keV) to about 0.0124 nm (100 keV). The main aspects of this dissertation involves the LUV, FUV, EUV and soft X-rays. Bound electronic transitions in atoms and interactions between atoms and free electrons (in general the free electrons' velocity is much greater than the free protons' velocity for the same energy, so we will assume electrons dominate the interactions). Figure 2.2 demonstrates the different ionic states:

- An atom with the same number of protons (quantized charge $^+$e) as electrons (quantized charge $^-$e) is electrically neutral.

- An atom with more protons than electrons is a positive ion.

- An atom with less protons than electrons is a negative ion.

A collection of ions is generally referred to as a plasma and at many pressures commonly observed in a vapor type state. Particles with temperatures greater than a few hundred Kelvin could possibly contain some ions based off the thermal energy content.

Figure 2.3 displays a non-exhaustive list of atomic processes. The processes discussed here are the most relevant for the analysis in this dissertation. The processes can be partitioned into bound-bound, free-bound (or bound-free) and free-free. The next sections go into detail on the basics of each class of interaction.
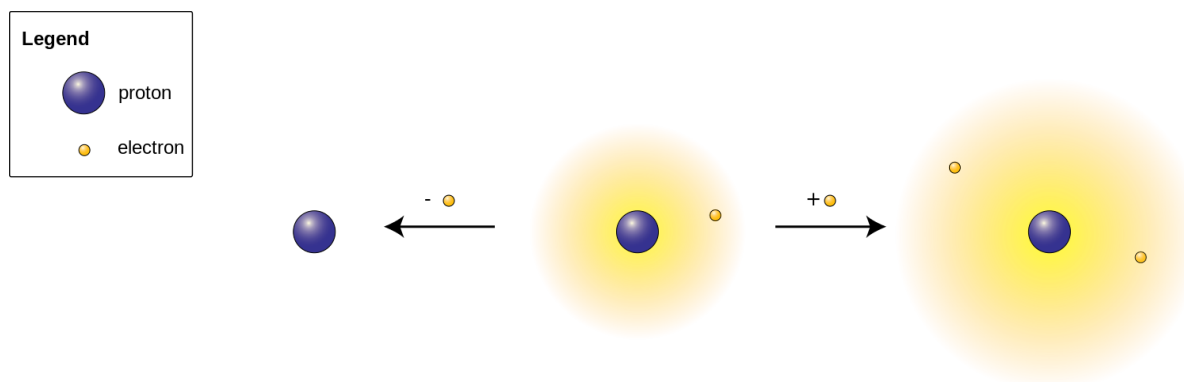
No. of protons	1	1	1
No. of electrons	0	1	2
Charge	+1	0	-1
Notation	H$^+$	H	H$^-$
Classification	cation	neutral (not an ion)	anion

Figure 2.2: Diagram describing charge balance in ions, using hydrogen (H) as an example. If the number of protons and electrons are equal, then the atom is electrically neutral. Positive ions have more protons than electrons. Negative ions have less protons than electrons. Source: https://commons.wikimedia.org/wiki/File:Ions.svg under the Creative Commons Attribution-Share Alike 3.0 Unported Liscence (https://creativecommons.org/licenses/by-sa/3.0/deed.en).

2.1.1   Bound-Bound

Bound-Bound transitions include all processes that start with an electron electrically bound to the native atomic nucleus in an energy state 1 and ending with the same electron bound to the same atomic nucleus but in a different energy state, 2 (the relation of the energy states are arbitrary at this point). These include induced absorption, collisional excitation, spontaneous emission, collisional de-excitation plus more. The energy of the photon emitted or absorbed (or atom for transitions that do not involve a photon) is determined by the energy difference between the lower energy state, i, and the upper energy state, j ($E_{ph} = |E_j - E_i$—). Thus, the term bound-bound. This results in spectral line absorption and emission for the photon processes.
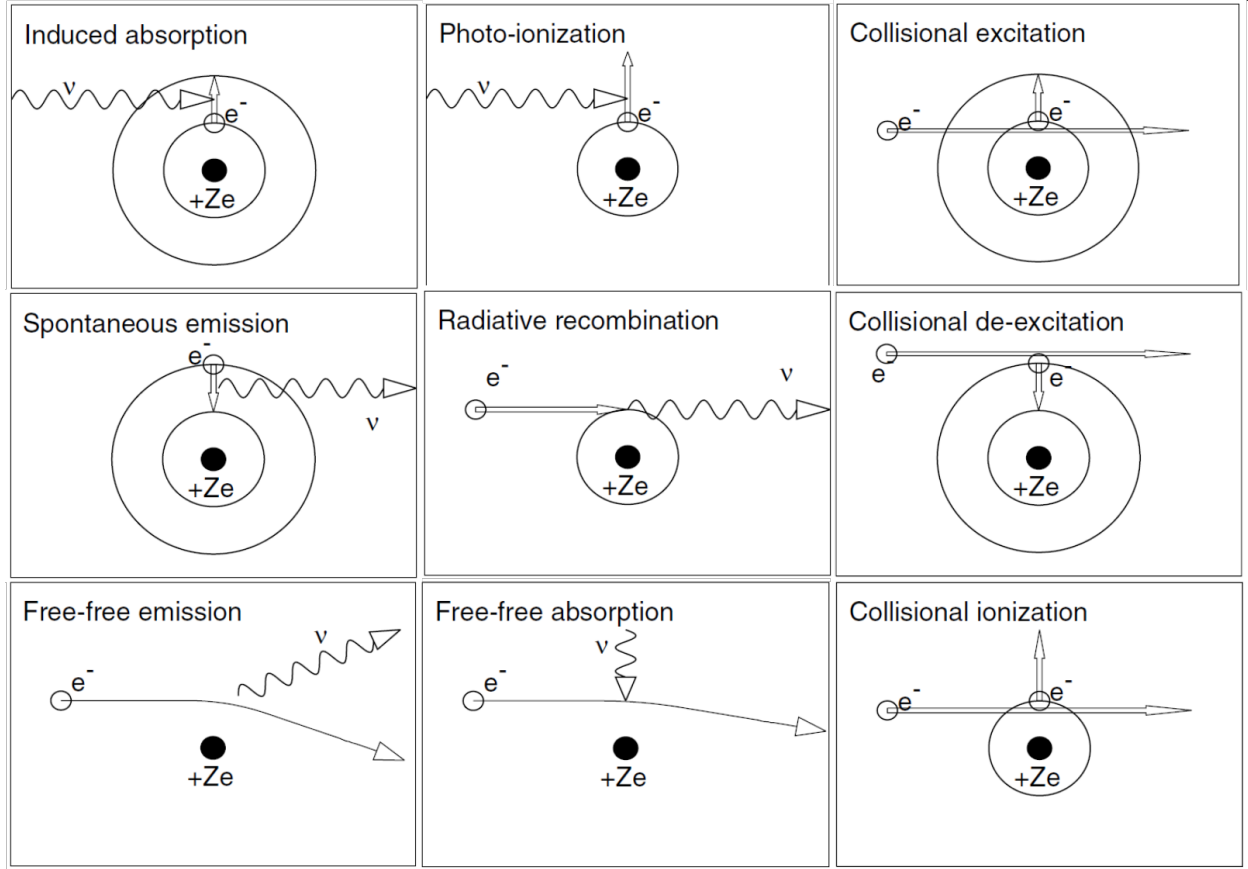
Figure 2.3: A subset of atomic processes relevant for the study in this dissertation. Adopted from Aschwanden 2005 [6].

2.1.2   Free-Bound

When the electron starts (ends) in a state not electrically bound to an atom/ion, called a 'free' electron, and ends (starts) in a state bound to an atom/ion then this is called a free-bound (bound-free) transition. These include but are not limited too, radiative recombination and photo-ionization. The energy of the photon in these interactions is determined by the kinetic energy of the free electron and the difference between the energy state of the electron in the atom/ion and the ionization potential, I, of that atom/ion via the relation $E_{ph} = |\frac{1}{2}m_e v^2 - I|$. For the interactions that involve photons, the free-bound interactions result in photon creations and the bound-free transition, the absorption of a photon, which is an important contributor to opacity. Generally, the free-bound (bound-free) interactions

lead to 'edges' in the optical properties of chemical elements and is commonly used to identify elements in unknown sources (as are bound-bound transitions).

2.1.3   Free-Free

A dominant process in the spectral profile in soft X-rays is the free-free interaction. As the name states, the electron starts free and ends free, with the aid of a photon either being absorbed or emitted during this interaction. The photon absorption is a strong contributer to plasma opacity and a source of heating the plasma. This emission is a dominant cooling process for fully ionized plasmas (generally with $T \geq 10^7$ K). The kinetic energy loss (gain) of the electron during emission (absorption) goes into the photon involved in the interaction and is related by $E_{ph} = h\nu = \frac{1}{2}m_e|v_{initial}^2 - v_{final}^2|$. Where m_e is the mass of an electron, and v is the magnitude of the velocity of the electron before and after the interaction.

There are many classes of free-free emission. Thermal bremsstrahlung (German for radiation breaking) is the free-free interaction where the velocity of the electron arises from thermal agitation. The details of the thermal bremsstrahlung spectral radiation profile is described in Section 2.1.4. Conversely, non-thermal bremsstrahlung involves electrons with a non-thermal velocity distribution. The non-thermal electron velocity distributions could be attained from a variation of acceleration processes that are poorly described by a Maxwell-Boltzmann velocity distribution . A class of non-thermal free-free emission, where the electrons are accelerated by magnetic fields is called synchrotron emission and discussed in Section 2.1.5.

$$f(v)dv = \left(\frac{2}{\pi}\right)^{1/2}\left(\frac{m_e}{k_BT}\right)^{3/2}v^2e^{-\frac{m_ev^2}{2k_BT}} \tag{2.2}$$

2.1.4   Thermal Bremsstrahlung

The photon spectrum arising from a Maxwell-Boltzmann thermal electron velocity distribution (see Equation 2.2) dominates the soft X-ray flux detected in the Solar mea-

surements discussed in Chapter 6 - Chapter 12, thus there is a brief section is dedicated here. Equation 2.3 describes the functional form of the photon spectrum and its dependence on the plasma temperature, T. The power-law portion $(T^{-1/2})$ dominates when for photon energies less than or comparable to the plasma thermal energy (steadily increasing photon flux vs. photon energy). At the higher photon energies, the exponential term dominates and theres is an exponential 'fall-off' of the photon flux. As the plasma temperature increases, this 'roll-off' value in photon energy increases. Thus, hotter plasma, generates more higher energy photons. This is a vital point that will be explored later in this dissertation.

$$F(\epsilon) \approx 8.1 \times 10^{-39} \int_V n_e n_p e^{-\frac{\epsilon}{k_B T}} T^{-1/2} dV \ [\text{keV s}^{-1} \ \text{cm}^{-2} \ \text{keV}^{-1}] \tag{2.3}$$

2.1.5 Synchrotron Radiation

Synchrotron radiation is one of the few manifestations of light generation that has a closed form solution (has an analytic expression) for the spectral and spatial distribution. This has resulted in synchrotron emission being used as an absolute radiation standard. This unique characteristic is vital for the UV coating testing and X-ray detector characterization in this dissertation, so we expound upon the basics here. A full treatment and description of the detailed physics are in [79, 84], I will simply summarize the main properties in this thesis.

An accelerating charge radiates and in general, the radiation will most likely propagate perpendicular to the direction of motion. When the charge has a velocity close to the speed of light, v ∼ c, then the radiation is beamed toward the direction of motion, and spans a cone angle dependent upon the velocity (see Figure 2.4). The synchrotron basic principle revolves around accelerating charges (in this case electrons) by magnetic fields into a loop path (circle or ring). These electrons are already moving near the speed of light, thus the radiation is beamed in the forward direction through apertures for use by experiments.

The photon spectral flux as a function of wavelength and angle distribution is given
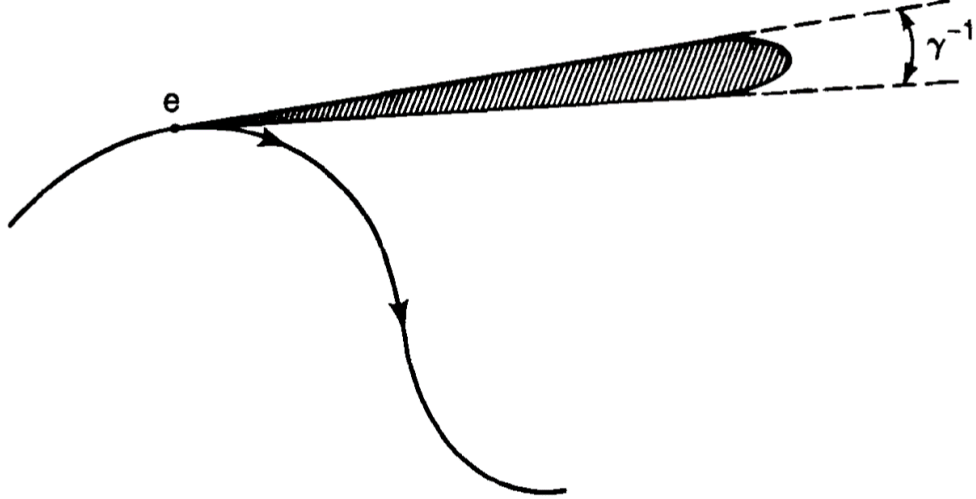
Figure 2.4: Diagram adopted from Kim 1989 [84] displaying the beamed radiation pattern of the accelerated electron, with velocity near the speed of light, traveling a curved path.

by the Schwinger equation [79, 145], $\frac{d^2\Phi_{\lambda,SR}}{d\lambda d\Omega}$. Equation 2.4 demonstrates a few important qualities of synchrotron radiation from a collection of electrons of mean energy E_e.

$$\frac{d^2\Phi_{\lambda,SR}}{d\lambda d\Omega} = \frac{27e^2}{32\pi^3\rho^2}\left(\frac{\lambda_c}{\lambda}\right)^4\gamma^8(1+\gamma^2\psi^2)^2\left[K_{2/3}^2(z) + \frac{\gamma^2\psi^2}{1+\gamma^2\psi^2}K_{1/3}^2(z)\right] \qquad (2.4)$$

ψ is the angle above and below the observer plane (in the situation for this dissertation the horizontal electron beam ring). ρ is the electron orbit radius of curvature, λ is the photon wavelength and $z = \frac{\lambda_c}{2\lambda}(1+\gamma^2\psi^2)^{3/2}$. $K_{1/3}$ and $K_{2/3}$ are modified Bessel functions of the first and second kind respectively. They dictate the angular dependence of the radiation in the vertical and horizontal planes. When $\psi = 0$, the beam is completely linearly polarized and elliptically polarized in all other cases. Polarization will be discussed in more depth in Appendix A. The critical wavelength is defined as, $\lambda_c = \frac{4\pi\rho}{3\gamma^3}$, and is the wavelength at which 50% of the energy is radiated above and below. γ relates the electron kinetic energy to the rest energy, $\gamma = \frac{E_e}{m_ec^2}$. An important detail is the dependence of the ratio of the critical wavelength to the photon wavelength in Equation 2.4. This ratio in the parenthesis is taken to the fourth power, exhibiting the strong spectral dependence to the energy of the electrons (because λ_c is a function of E_e). Increasing the electron energy yields more photon flux at

all wavelengths and shifts the critical wavelength to lower wavelengths.
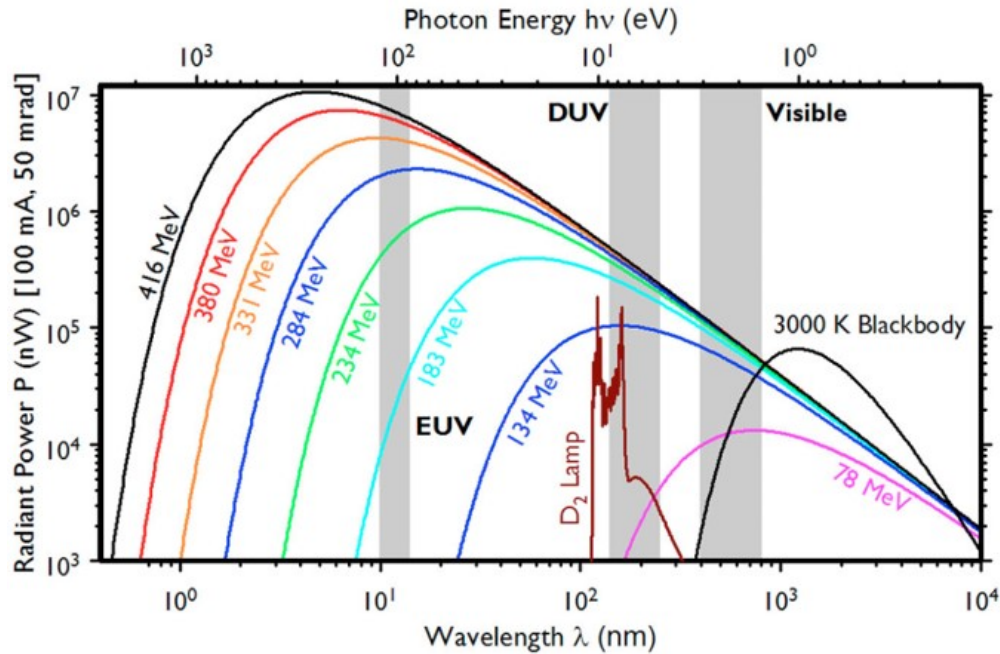
Figure 2.5: Example spectral flux as a function of the mean electron energy (E_e). The greater the electron energy the greater the photon flux at all photon wavelengths (energies). Synchrotron radiation spans large portions of the electromagnetic spectrum. Adapted from Arp et al. 2011 [5]

Figure 2.5 is an example of the synchrotron spectral distribution from the National Institute for Standards and Technology (NIST) Synchrotron Ultraviolet Radiation Facility (SURF). There is a clear dependence on the mean electron energy on the spectral flux, which again, can be calculated analytically. The synchrotron source can be much greater than deuterium and incandescent (blackbody) light sources. Synchrotron radiation is a great broadband (many wavelength) light source and has tremendous utility for instrument characterization, such as used for the MinXSS Instrument calibrations.

2.2   Future Science Enabled by UV Coatings

The UV bandpass contains the richest suite of spectral diagnostics for understanding physical processes (see Figure 2.6). Thus, UV astrophysics benefits from numerous atomic

and molecular spectral transitions that can be used to probe material of different phases in a multitude of systems. The hydrogen (H) Lyman series extends down to 91.2 nm and the characteristic energy gaps near 10 eV for carbon (C), oxygen (O), nitrogen (N), carbon monoxide (CO), molecular hydrogen (H_2) and water (H_2O) lead to increases in electronic transitions in the 100 nm range. For example, a set of important diagnostic transitions are the lithium-like ion (ions with only three electrons) doublet transitions of O VI (103.2 and 103.8 nm), N V (123.8 and 124.0 nm) and C IV (154.8 and 155.0 nm). The O VI doublet, C III transition at 97.7 nm and H short wavelength Lyman series transitions can be measured with numerous other longer wavelength transitions for future observations if a mirror system with sufficient throughput for $\lambda > 90$ nm can be flown in space. Observations from a space observatory from 90 2,000 nm with advanced instrumentation can unveil more information on densities, temperatures, pressures and chemical compositions of nearby astrophysical systems such as stars in the Milky Way Galaxy, more distant galaxies and the intervening gas between and prevailing inside of galaxies [42, 16, 152, 29, 60].

Below I expound upon some of the astrophysical phenomena that would benefit from improved UV mirror throughput, and go into detail where necessary. This is relevant for the first project in this dissertation, UV mirror coatings for future astronomy missions. Later in Chapter 6 I will elaborate more on stars because it is more relevant to the Miniature X-ray Solar Spectrometer CubeSat project.

2.2.1   Stellar Winds

Stars with massess greater than $8M_\odot$, burn carbon in their cores, have a strong photon flux across the EM spectrum, have strong winds which significantly impact their mass loss rate and their circumstellar environment. These massive stars dominate the local dynamics during their relatively short stellar lives (~ 50 million years). Massive stars are the main creators of heavy elements (elements other than H and He). Studying massive star formation, evolution and death is critical for modeling galaxy evolution [42, 27].
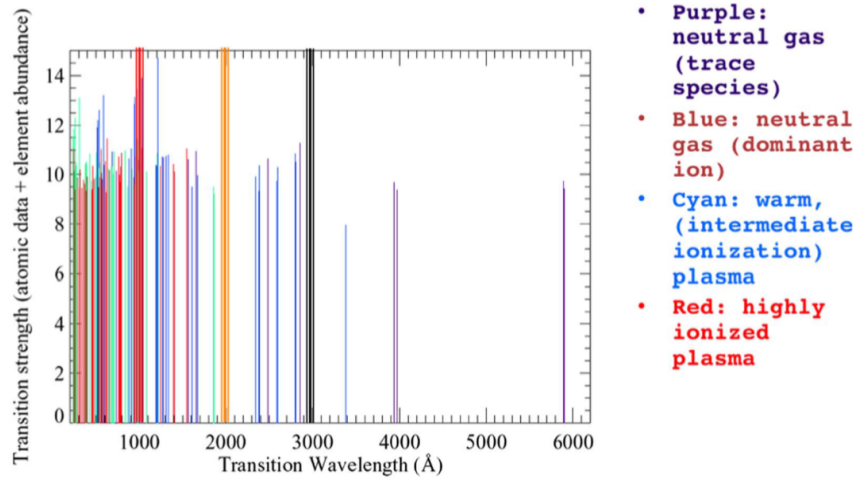
Figure 2.6: The number of relevant resonance lines for astrophysical investigations in general increases into the FUV and LUV. Below 1,000 $\mathring{A}$ is the highest density. Adapted from [141]

There are numerous transitions in the 90 - 180 nm range that can study the winds from these massive stars and other phenomena. If high resolution spectroscopy is implemented (R = 10,000) resonance lines of many 'metals' (O IV, O V, O VI, C III, C IV, N IV, N V, plus more) can be used to constrain the stellar wind mass-loss, composition and dynamics in the wind [141]. These stars also enrich the circumstellar environment at the end of thier lives when the undergo core collapse supernovae

2.2.2   Supernovae

The very massive stars are relatively short lived ($\sim 10^6$ - 10^8 years) and end their lives in huge explosions called supernovae, which enrich the interstellar medium with elements including carbon, oxygen, helium, silicon and iron. The resulting remnants (emission nebulae) and the explosion dynamics can be studied using the C III 97.7 nm line, which is most probable at temperatures around 10^4 K [16, 17]. The remaining material is used to form the

next generation of stars and planets, with a modified chemical abundance.

The outflowing material from the supernovae can have a range of speeds. Material at the front can collide with the interstellar medium (ISM), a shock can form, and the material will heat up. Additionally, material behind the initial ejected material moving at a faster velocity can interact with the slower moving material and also create shocks. The velocity of these shocks can be inferred from spectral line shifts and the temperature of the plasma inferred from ionic emission lines. For example, the O VI doublet (103.2 and 103.8 nm) is expected to be formed near (3×10^5 K assuming collisional ionization equilibrium models), but shocked gas is not necessarily in equilibrium and care must be taken in its inference. This doublet emission is not expected until the velocity of the ejected material reaches near 160 km s^{-1} [17].

2.2.3 Exoplanets

The less massive stars that 'live' relatively long lives ($\sim 10^9$ - 10^{10} years) are believed to be the most viable option for hosting exoplanets capable for harboring life. UV radiation emitted by the host star can be modified when passing through an exoplanet atmosphere. This modified UV light can be used to investigate exoplanetary atmospheric chemistry and thermodynamic conditions. Lower mass stars have high UV variability that can be better understood with sufficient modeling. For example, exoplanetary atmospheric absorption of hydrogen Lyman series (91.2 121.6 nm) on the emission lines from the host star can give information on the dynamics and properties of the exoplanetary atmosphere [152].

Understanding the time variability and the spectrum of the host star is vital for any type of exoplanet atmospheric extraction. Since the stars are mostly low mass, they have fairly explosive (flares, coronal mass ejections, more on this in Chapter 6) outer atmospheres. The temperature ranges of these atmospheres vary between 10^3 - 10^6 K. The EUV and LUV have an abundance of spectral diagnostics already mentioned spanning these formation temperatures. N III transitions at 99.1 and 175 nm respectively, C III line at 117.5 nm, C

II at 133.5 nm, O IV at 140.7 nm, plus many others [92]. Furthermore, the shape of the host star spectrum between 100 - 175 nm effect the stability of H_2O, CH_4, and CO_2 in an Earth size planet in the habitual zone. The spectral shape between 175 - 320 nm influence the reactions of oxygen [141].

2.2.4   Warm Hot Intergalactic Medium (WHIM)

The amount of baryonic mass (protons, neutrons, etc.) that has been readily measured in our local universe does not seem to add up to mass estimates from earlier times (high redshift). Thus, the term 'missing' baryons. There is belief that some of this gas is yet to be effectively measured. A significant amount of material between the early galaxies is warm, highly ionized (T $\sim 10^5$ - 10^7 K) and thus called the Warm-Hot Intergalactic Medium (WHIM). Some of the 'missing' baryons could be in the low redshift intergalactic medium (IGM). One set of prominent lines that can be used to infer the mass and metalicity content of plasma with temperatures near temperatures of 3 x 10^5 K is the O VI 103.2 and 103.8 doublet. Using quasars as a background light source, probing for the O VI doublet in absorption as a function of redshift can be critical in increasing the baryonic mass content that has been detected in stars, HII regions, molecular clouds, plus more [29].

Understanding the metalicity content of the IGM is an evolving investigation. Detection of redshifted Ne VIII, Si VII and/or Mg X UV lines would unambiguously indicate the presence of hot halo gas around 10^6 - 10^7 K [122]. This gas can interact with the matter surrounding galaxies, the Circumgalactic Medium (CGM), where gas condenses into the galaxies and provide material for stellar formation [16, 152, 29, 60]. The UV spectral region hosts numerous diagnostics for analyzing the evolution of the universe on both the large and small size scales.

Chapter 3

UV Mirror Coatings History

The Lyman-ultraviolet (LUV; 90 - 121 nm) and Far-ultraviolet (FUV; 121 - 200 nm) harbor some of the highest line densities per unit wavelength in the electromagnetic spectrum and contain numerous spectral diagnostics of molecular, neutral, and ionized astrophysical gas [141]. With the Hubble Space Telescope aging, there is desire among the astrophysics community for a future astronomical space telescope with sensitivity from 90 - 2,500 nm, to exploit this. The Large Ultraviolet/Optical/Infrared (LUVOIR) Surveyor and HabEx mission concepts currently under study [144]. Due to the lack of bulk materials with sufficient transmissive properties from the UV to the IR, mirrors must be employed for high throughput. Mirrors with reflectivity higher than $\sim$50% from 90 – $\sim$120 nm and greater than 80% from 120 – $\sim$2,500 nm are desired. The latest Cosmic Origins Program Annual Technology Report (https://ntrs.nasa.gov/search.jsp?R=20160011973) [120] has explicitly called out high reflective coatings.

The 'NASA 2010 Astronomy and Astrophysics Decadal Survey', and the science objectives of the LUVOIR Surveyor satellite in the 'NASA Astrophysics in the Next Three Decades Roadmap' emphasize the importance of the science goals mentioned in the previous paragraph and mirror coating capabilities from 90 – 2,000 nm. Additionally, the recently proposed UV telescope concept of High-Definition Space Telescope (HDST) by the Association of Universities for Research in Astronomy (AURA; http://www.hdstvision.org/) reiterates the aforementioned science objectives and calls for mirror coatings with high performance from

100 – 2,000 nm. Our goal is to develop the technology to enable these capabilities on a future mission. Now, I will review the historical options for high reflective optics in the UV and the motivation for this work. A brief review of optical constants and the procedure to calculate all the theoretical reflectance values are in AppendixA A.

3.1   Optical Constants

Optical constants (η = n - ik) provide a framework for modeling light interaction with matter [73]. Assuming that the light propagating is a plane wave, the material is homogeneous and isotropic, and that the interface between different media is sharp, optical constants provide a very practical approximation to material properties. The real component, n, the refractive index, is related to the phase velocity of a monochromatic light wave propagation in the media, v, to the velocity of light in vacuum, c, by the definition, n = $\frac{c}{v}$ = $\sqrt{\frac{\epsilon\mu}{\epsilon_0\mu_0}}$. ϵ_0 (ϵ) is the permittivity of free space (in the medium), the ability to *resist* electric fields in the medium. μ_0 (μ) is the permeability of free space (in the medium), the ability to support a magnetic field in the medium.

The imaginary component of the optical constants, k, is called the extinction coefficient. The extinction coefficient is a function of the radial frequency of the light, ω, the effective conductivity of the material, σ, and encompassess the absorptive properties of the material. The induced electric field in the medium generates near surface currents which can be dissipated via collisions (resistance). Let's consider a light wave with radial frequency ω , wave number κ, propagating, in the $\hat{z}$ direction into a medium with optical constants n and k to a depth, z. The electric field vector, $\overrightarrow{E(z)}$, at the depth z, with amplitude $\mathbf{E_0}$ is given by Equation 3.1

$$\overrightarrow{E(z)} = \hat{z}\mathbf{E_0}e^{i(\omega t - \frac{2\pi(n-ik)z}{\lambda})}$$
$$= \hat{z}\mathbf{E_0}e^{i(\omega t - \frac{2\pi nz}{\lambda})}e^{-\frac{2\pi kz}{\lambda}}$$

(3.1)

The sign in the exponential, just changes the direction of the wave propagation. λ is the wavelength of the light in vacuum. The first two products are just the light wave, but the exponential with the extinction coefficient is REAL. Thus, when we compute the intensity in the medium at a depth z, $I(z)$, (see Equation 3.2) this component survives.

$$
\begin{aligned}
I(z) &= \overrightarrow{E(z)}\overrightarrow{E(z)^*} \\
&= \mathbf{E_0^2}e^{-\frac{4\pi k z}{\lambda}}
\end{aligned}
\tag{3.2}
$$

Equation 3.2 is an important expression. The exponential term with the extinction coefficient survives, because it is real and attenuates the intensity as a function of depth into the medium. This is commonly referred to as Beer's Law. The relation between n and k as a function of wavelength are pivotal in metal, thin films and other materials in terms of the electrical and optical properties.

3.2   Silicon Carbide (SiC)

Silicon carbide (SiC) has been used as a reflective layer for UV mirrors on sounding rocket missions [22, 49], the short-wavelength channels of the *Far-Ultraviolet Spectroscopic Explorer* [116, 133], and the solar physics based *Solar Heliospheric Observatory* (SOHO) *Solar Ultraviolet Measurement of Emitted Radiation* (SUMER) instrument. SiC can provide reflectance (R) greater than 40% from 90 - 120 nm, but has R < 40% for λ > 300 nm (see Figure 3.1 plot A) [82, 85]. Because of these long wavelength limitations it will not be discussed further.
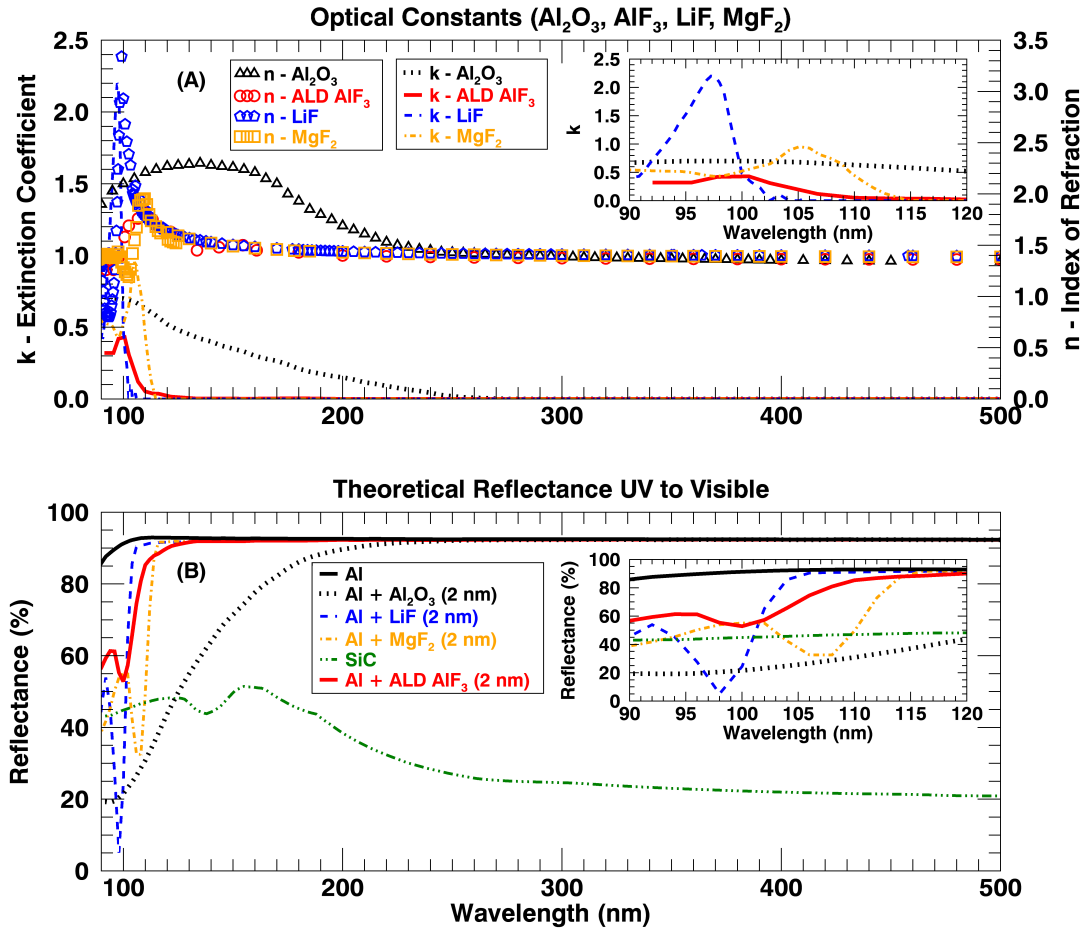
Figure 3.1: (A) Optical Constants from 90 - 500 nm for Al_2O_3, AlF_3, LiF and MgF_2. The insert is only the extinction coefficient from 90 - 120 nm. Al_2O_3 has substantial absorption below 250 nm, AlF_3 has moderate absorption below 107 nm, LiF has strong absorption below 102 nm and MgF_2 is absorbing below 115 nm. (B) Reflectance calculations from 90 - 500 nm based on optical constants for Al + Al_2O_3, Al + AlF_3, Al + LiF, Al + MgF_2 (all 2 nm thick) and SiC. The insert is from 90 - 120 nm and demonstrates that ALD AlF_3 has the highest *average* reflectance in this wavelength range. The inverse relation between the extinction coefficient, k, and reflectance is apparent

3.3   Aluminum (Al)

Metals in general are good broadband reflectors. This is primarily due to the free electrons that oscillate out of phase with the incident electric field of the incident photon. This electron 'reaction' creates a shallow skin depth, the characteristic length that an electromagnetic wave can propagate into a material until it is attenuated by a factor e^{-1}, [79, 65, 73].

The fact that metals have a non-zero k, means that the light wave do not propagate deep into the metal. Many metals have wavelengths with n <, thus the light wave is 'bounced' out of the metal (reflected). The non-zero k, means that metals will always absorb some light. Thus metals are not loss-less.

Aluminum (Al) has an intrinsic reflectance greater than 80% from 90 - 2,500 nm and is commonly employed as a broadband reflector. Below 90 nm Al begins to become transmissive (below the plasma frequency $\sim$85 nm) [71, 43]. Silver (Ag) could also be a viable candidate but its reflectivity is much less than Al for wavelengths less than 300 nm [125]. The intrinsic Al reflective properties are rarely realized because Al readily develops an a few-nanometer thick layer of aluminum oxide (Al_2O_3) upon exposure to oxygen, which strongly absorbs light below 250 nm (see Figure 3.1). This oxidation has evenly been observed in the vacuum chamber directly after deposition at low pressures [105, 72]. Al must be deposited quickly and in low vacuum conditions [82, 19, 105] in order to reduce the Al_2O_3 composition *inside* Al mirror and the optical degradation. This oxide severely compromises UV mirror performance.

To further mitigate the effects of Al oxidation on reflectance, protective transmissive overcoats can be used. The characteristic that makes metals like Al efficient reflectors is the exact same physical property that we want to avoid for a highly transmissive protective coating, namely that we desire a coating with a very low extinction coefficient, k. The highly transmissive coating allows light to penetrate to the Al layer, reflect off the Al and propagate out of the coating to create a highly reflective material combination with minimal light loss (see Figure 3.2). We desire a coating material, thickness and deposition mechanism to preserve the broadband reflective qualities of Al.
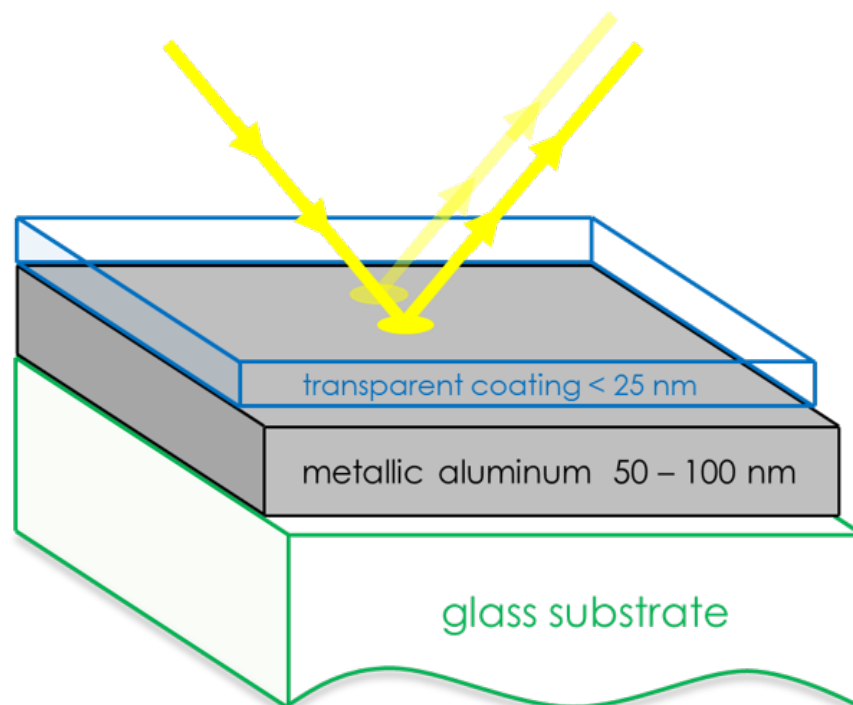
Figure 3.2: Diagram depicting the general mirror architecture implemented in this dissertation. The substrate is either glass or silicon. The transparent coatings discussed include magnesium fluoride (MgF$_2$), lithium fluoride (LiF) and the main focus of this dissertation, aluminum fluoride (AlF$_3$).

3.4   Metal Fluorides

Metal-fluoride overcoats of have traditionally been deposited in-situ after the aluminum deposition. In general, metal fluorides possess high optical transmission from the UV to the IR. One of the reasons for this is the high bond strength between the fluorine and metal atoms. Fluorine has the largest electronegativity (ability of an atom to attract an electron) in both the Allred-Rochow and Pauling scales [102], and one of the largest in the revised electronegativity scale calculated by Ghosh et al. 2009 [56] (see Figure 3.3). The strong bond of fluorine with metals on the lower end of the electronegativity scale shifts absorption bands to higher energy (shorter wavelength) and leads to higher UV transmittance.

Thus the transmissive films in the UV and visible generally have an optical constant real component (n; index of refraction) near unity and an imaginary component near zero.

Theoretical reflectance calculations displayed in Figure 3.1 exhibit how the intrinsic film absorption is directly related to the magnitude of k for Al_2O_3 which has strong absorption contribution below 250 nm.

Figure 3.3: Adopted from https://byjus.com/chemistry/electronegativity/. The Pauling scale for electronegativity. Fluorine (F) has the highest electronegativity, thus it readily attracts electrons to its outer orbital. Li, Mg and Al have lower values of electronegativity and will give up their electrons more readily. The bonding of molecules with atoms on opposite ends of the electronegativity scale is one reason why metal fluorides have high transmittance in the UV.

3.4.1   Magnesium Fluoride (MgF_2) and Lithium Fluoride (LiF)

Two of the most utilized transmissive metal fluorides are magnesium fluoride (MgF_2; highly transmissive for $\lambda > 110$ nm) and lithium fluoride (LiF; transmissive for $\lambda > 102$ nm) deposited immediately after Al deposition to protect the sensitive reflective coating. Both MgF_2 and LiF have environmental stability concerns, but MgF_2 to a lesser degree [82]. These protective fluorides are typically tens of nanometers thick (14-25 nm) in order to overcome deposition non-uniformities that result in pinhole formation and low film density that would allow oxygen to penetrate and react with the Al layer below.

MgF_2 has been pursued as an overcoat for many years. MgF_2 coatings have been used for the primary mirrors for the Hubble Space Telescope (HST) [108] and Galaxy Evolution Explorer (GALEX) [106], but MgF_2 has intrinsic absorption bands near 115 nm [96] (see Figure 3.4). Thus, the utility of MgF_2 is limited below 115 nm, even though it has proven to be one of the most environmentally stable overcoats. LiF has been used on the long-wavelength channels of FUSE [121, 66] and a series of sounding rocket flights [50].

LiF overcoats possess a lower resonance absorption wavelength near 102 nm [25]. The hygroscopic nature of LiF necessitates strict environmental storage control which may drive mission integration procedures. Even though LiF has the lowest energy cutoff of the known metal fluorides, the theoretical reflectance of LiF has been extremely difficult to attain. Probably due to impurities in the parent crucibles used to deposit LiF, previous exposure to moisture, or not being able to obtain an optically optimal crystalline structure after deposition. Annealing of a thin film give the deposited atoms in the lattice enough kinetic energy to rearrange themselves and 'migrate' to new locations in the lattice. This process commonly results in the atoms moving to a lower more stable energy state. Annealing post deposition has dramatically improved the optical performance of LiF and these hot LiF depositions by Quijada et al. 2014 [128] yield highest reflectivity from 105 - 120 nm to date (see Figure 3.4).

3.4.2 AlF_3

Because of the limitations of MgF_2 and LiF we have pursued the development of a newer, less studied metal fluoride. Aluminum fluoride (AlF_3) has recently emerged as a prospect for a protective Al mirror overcoat [19, 80]. Use of AlF_3 as a protective overcoat is not as common and literature on its optical properties is sparse. Thus we investigate the viability of AlF_3 as another protective overcoat for future astronomical UV-Vis-IR space observatories. For wavelengths with non-zero k, absorption in thin film overcoats will always occur. Thus, we attempt to minimize this natural absorption by making the protective film
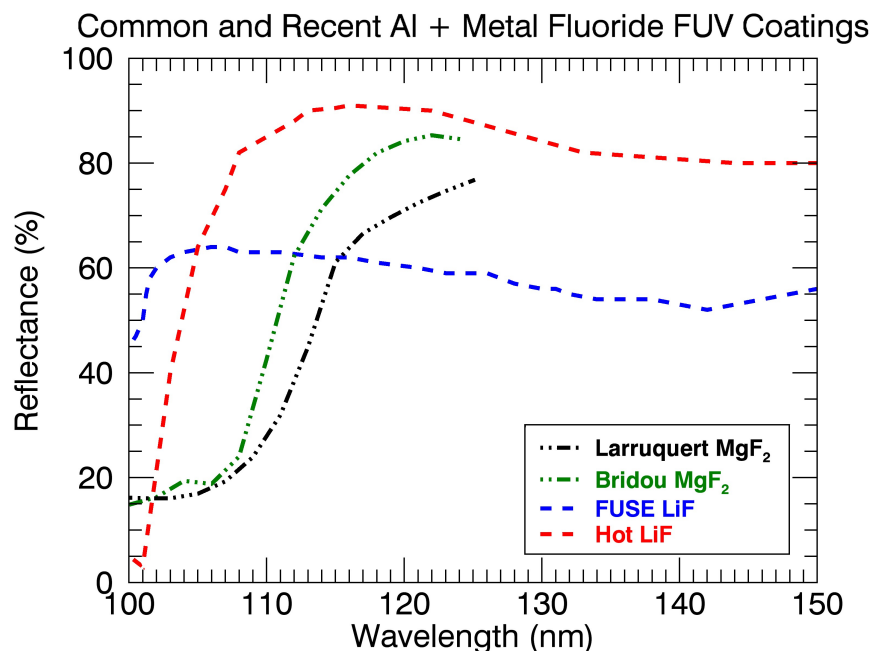
Figure 3.4: A non-exhaustive example of the current optical coatings of MgF_2 and (LiF) on Al. Adopted from Moore et al. 2016 [113].

as thin as possible, but thick enough to resist oxidation and other environmental effects. Theoretical reflectance calculations of very thin (2 nm) layers of MgF_2, LiF, and AlF_3 on Al are displayed in Figure 3.1. Optical constants of Al, SiC, MgF_2 and LiF are from Palik 1998 [123], while the Al_2O_3 and AlF_3 optical constants have been extracted from atomic layer deposited films prepared for this and previous work [80]. These theoretical calculations predict that AlF_3 will have the highest average reflectance from 90 - 110 nm as compared to MgF_2 and LiF for the same physical thickness.

UV mirror over-coats have been traditionally deposited by physical vapor deposition (PVD). These techniques include thermal evaporation, ion beam, magnetron or plasma assisted sputtering [82, 96, 132]. These techniques are normally limited by line of sight effects between the crucible and the substrate surface features (see Figure 4.1). An additional limitation is the fact that all coating constituents are in the chamber for the entire deposition process. Finally, PVD often requires very low vacuum for efficient deposition [96]. Chemical

Vapor Deposition (CVD) can also be used but is less common for UV mirror applications. All aforementioned techniques are generally limited in the aspect ratios that they can coat and may not have strict thickness control.

To obtain precise thickness control, we turn to an older deposition technique that has been revitalized in the coating industry. Atomic Layer Deposition (ALD) holds the promise of thin film growth via one atomic layer at a time. Our first step is the exploration of atomic layer deposited aluminum fluoride (AlF_3) properties and suitability as an UV mirror coating. Chapter 4 discussed the details of ALD and related techniques. Chapter 5 reports on the current progress in this investigation. Presented are assesssments of atomic layer deposition (ALD) grown AlF_3 surface roughness, and optical properties on silicon wafers. These include reflectance measurements from 90 - 1,000 nm, polarization sensitivity from 200 - 800 nm via ellipsometric parameters and environmental stability on reflectance.

Chapter 4

Atomic Layer Modification (ALM)

In order to mitigate loss in the protective coating we use Atomic Layer Deposition (ALD) to prepare ultra-thin (< 5 nm) films on Al mirrors. These films must be thin enough that absorption from 90 - 120 nm is minimized, while still providing protection from environmental oxidation to the underlying Al. This can be difficult, as thin films can develop pinholes which could allow oxidation to occur. Figure 4.1 depicts how PVD and CVD can suffer from non-uniform film thickness and poor conformality from source line-of-sight effects, and film contaminants (contaminants in the in the crucible for PVD). ALD allows for precise thickness control, conformal and near stoichiometric thin films by the cyclic alternating exposure of chemical reactants [54]. ALD also offers great uniformity, minimal degradation to surface roughness, and a relatively clean coating process. Energetically favorable reactions result in layer-by-layer adsorption of surface species to create the desired film constituents. Additionally, ALD should be scalable to meter sized optics which will be employed on the next large UV/vis/IR mission (e.g. LUVOIR). We desire pinhole free, high purity, and environmentally durable, thin films of metal fluorides deposited on Al mirrors.

Atomic layer deposition is utilizes exothermic reactions (release energy to the surroundings) to initiate film deposition. These chemical reactions will proceed spontaneously if they have a negative Gibbs Free energy ($\Delta G < 0$) [99]. Thus, the goal is to use precursor gases containing the desired constituents of the final film that have chemistries that satisfy the above criteria. The first precursor gas is introduced into the chamber in either shower head
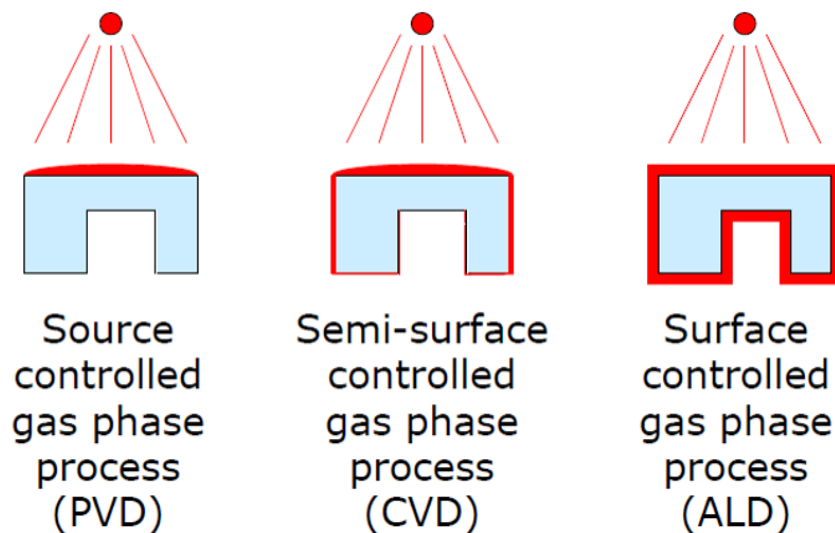
Figure 4.1: Atomic layer processes sequentially introduces gas phase precursors to grow films via chemical reactions at the substrate surface. With sufficient precursor gas flow, atomic layer processes like atomic layer deposition (ALD) and atomic layer etch (ALE) the reactions are uniform over the substrate. Physical vapor deposition (PVD) and chemical vapor deposition (CVD) can suffer from line of sight effects, resulting in non-uniform film deposition. Adopted from Pinna and Knez [127].

or cross-flow style to initial either thermal or plasma enhanced chemical reactions at the surface substrate. These reactions proceed until a terminal layer is reached (self-limiting). This terminal layer is nominally a 'few' atoms thick and has been dubbed a 'mono-layer'. The chamber is purged of the reactant gas by inert gases like Ar or N_2. This is the first half-cycle. The second reactant gas flows into the chamber and ligand (group of molecules) exchange occurs (see Figure 4.2). One collection of molecules adsorbs to the surface, while the second group desorbs. The volatile group (leaving group) is purged from the chamber with Ar or N_2. Ideally, this reaction is also self-limiting, and thus results in the final desired stoichiometry with a specified thickness. The self-limiting nature of both phases of the reaction result in mono-layer growth. The cycle is repeated until the desired film thickness is obtained.
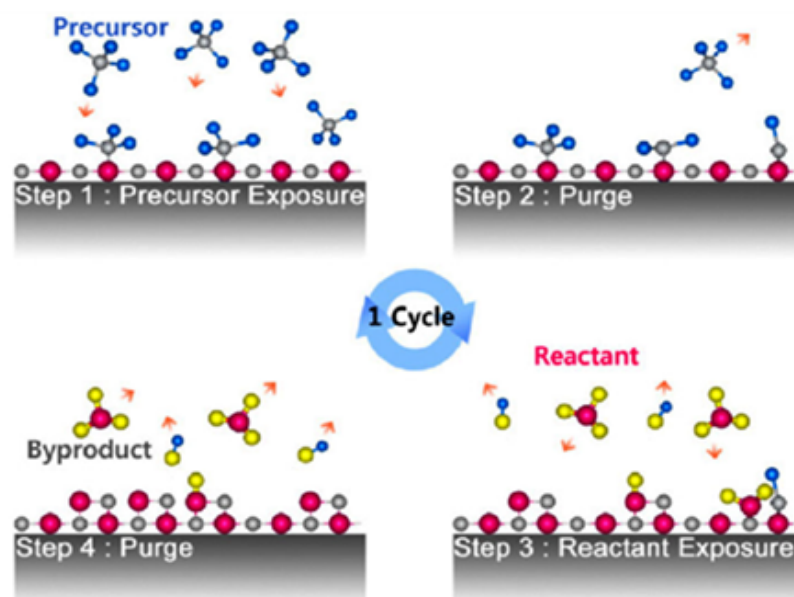
Figure 4.2: Atomic layer deposition steps. Step1: Precursor gas is introduced and adheres to the substrate. Step 2: Residual gas is purged from the chamber. Step 3: The second reactant gas is introduced. Step 4: Ligand exchange occurs and the byproduct is purged from the chamber. This is one cycle creating a mono-layer of film. Adopted from Kim et al. 2009 [83].

4.1 Atomic Layer Deposition (ALD) of Aluminum Fluoride (AlF$_3$)

ALD of MgF$_2$, LiF and AlF$_3$ has been successfully performed at JPL [75, 114, 113, 31] and by others [97]. This dissertation is restricted to the ALD processes of AlF$_3$. The ALD process grows the AlF$_3$ film via surface fluorination by a hydrogen fluoride (HF) exposure, ligand exchange in the TMA (Al[CH$_3$]$_3$) exposure which results in mostly AlF[CH$_3$]$_2$ on the surface and another HF exposure to convert the surface monolayer to AlF$_3$, with mostly methane (CH$_4$) as the leaving group (see Figure 4.3). Each of these precursor gas exposures are separated by a chamber purge of the reactant gas, with an inert gas like Ar or N$_2$. The AlF$_3$ thickness-change-per-cycle (tcpc) for the HF - TMA precursors varies as a function of substrate temperature (thermal ALD) and is positive for T$_{sub}$ < 205°C (see Figure 4.4). The deposition rate is also dependent the flow rates (sccm) and exposure times (resident times) if not operating in the saturation regime.
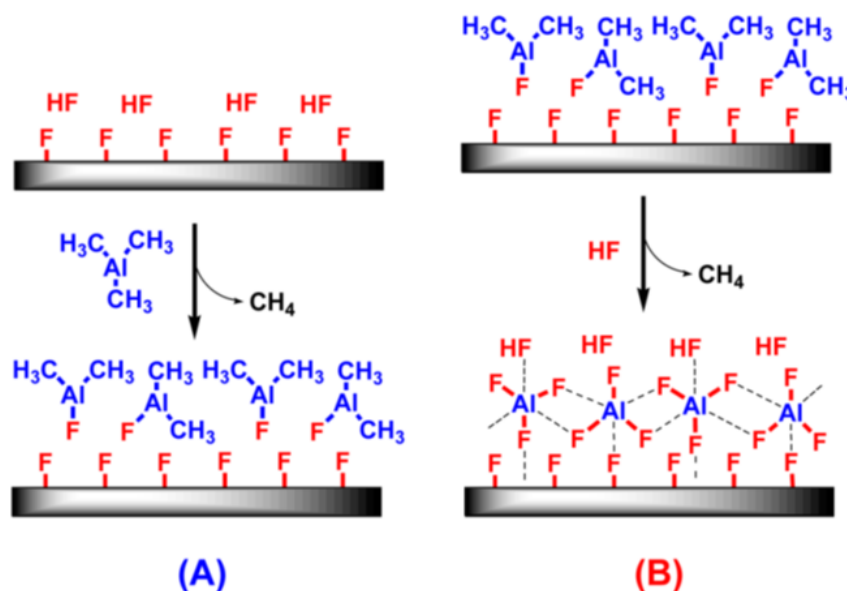
Figure 4.3: ALD of AlF$_3$ using hydrogen fluoride (HF) and trimethylaluminum (TMA) for the F and Al containing precursor gases respectively. Subsequent exposure of the precursor gases can lead to self-limiting, near stoichiometric mono-layer growth, providing a precise thickness-change-per-cycle for ideal conditions. Cyclic exposure of the precursors leads to steady conformal film growth. Figure adapted from Lee et al. 2015 [97].

This thermal ALD process with TMA and HF has resulted in films with residual oxygen content less than 2% from X-ray photoelectron spectroscopy (XPS) [75], less than 15% increase in substrate surface roughness from atomic force microscopy (AFM; see Figure 4.5) [114], with good optical properties in the UV (see Chapter 5). Future environmental storage tests will be pursued to investigate the stability of the ALD AlF$_3$ coating to controlled environments. Additionally, spaceflight tests on a NASA sounding rocket can be pursued to raise the Technology Readiness Level (TRL) for future satellite mirrors.

The next step would be to deposit ALD AlF$_3$ on ALD Al in the same vacuum (without a break to atmospheric pressures), but there is currently no known repeatable ALD Al process. Al has a high surface energy, thus it prefers to adhere (bond, stick) to elements other than itself. This makes the pure and efficient extraction of Al from its ligands difficult. Al will generally stay bonded to other elements and lead to a low quality film. Furthermore, thermal atomic layer deposition does not appear to generate enough energy to ignite the dissociation

Thickness Change per Cycle

ALD (AlF$_3$ growth)
$\Delta\tau_{ALD} = -0.0066 T_{sub} + 1.82$

ALE (Al$_2$O$_3$ etch)
$\Delta\tau_{ALE} = -0.0068 T_{sub} + 0.79$
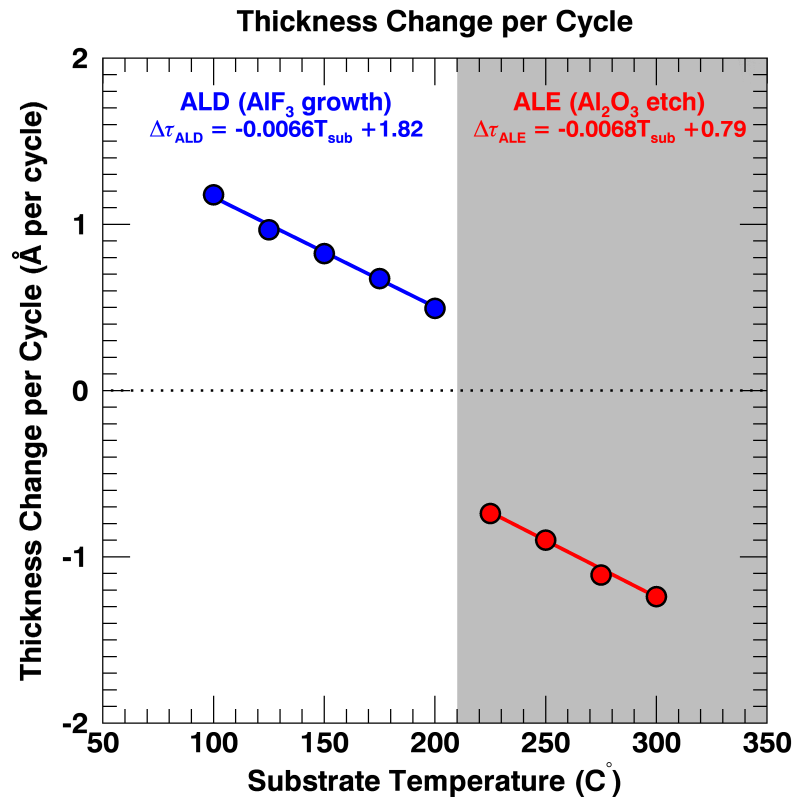
Figure 4.4: Thickness change per cycle in angstroms $\mathring{A}$, as a function of substrate temperature. The ALE of Al$_2$O$_3$ (red) and the ALD of AlF$_3$ (blue) temperature regime data are the symbols and the linear fits are the lines. The offset difference is primarily due to the LiF pre-conditioning in the ALE process, but the tcpc are very similar. ALD data is from Hennessy et al. 2016A [75] and ALE data is from Hennessy et al. 2017 [76].

and subsequent ligand exchange of the Al precursor gas. Plasma-ALD is an alternative. The RF plasma source can provide the additional energy needed to commence the chemical reactions for Al ALD while not raising the substrate temperature to high. The difficulty arises in the particulars of the plasma process. When and where in the ALD chamber to 'spark' the plasma, what are the optimal frequencies, etc. Any current Al will be evaporated and transferred into the ALD chamber for processing with a native oxide layer. A method must be devised to remove the Al$_2$O$_3$ layer. Fortunately, a new technique for Al$_2$O$_3$ removal was recently uncovered.
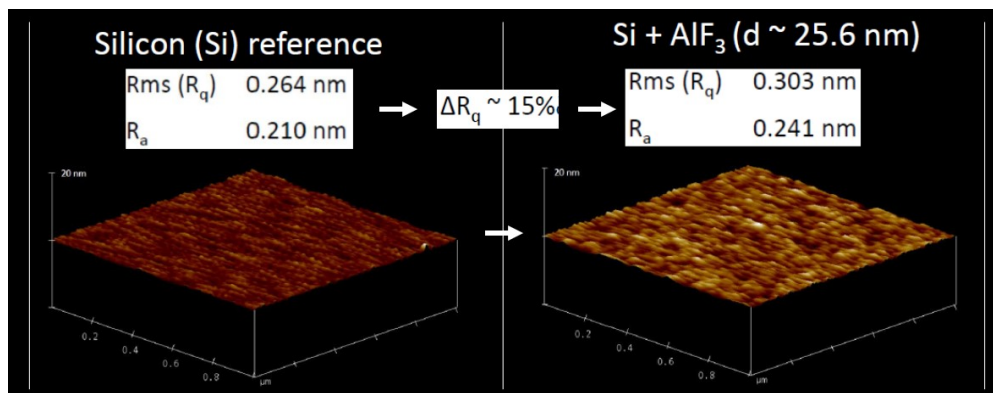
Figure 4.5: Atomic force microscopy (AFM) profile of surface roughness comparing a bare Si wafer and ALD of AlF$_3$ of ~25.6 nm. The ALD AlF$_3$ only increases the wafer surface roughness by ~15% at an absolute thickness value of 0.303 nm root-mean-square (RMS). RMS = R$_q$ = $\sqrt{\frac{1}{n}(\sum_{i=1}^{n} z_i^2)}$ and the arithmetic average roughness, R$_a$ = $\sqrt{\frac{1}{n}(\sum_{i=1}^{n} |z_i|)}$. Which is much smaller than the lowest wavelengths (90 nm) of the designed usage. Figure adapted from Moore et al. 2015 [114].

4.2   Atomic Layer Etching (ALE) of Aluminum Oxide (Al$_2$O$_3$)

In general, atomic layer processes are a competition between film adsorption and desorption rates, which depends on the surface species volatility. If the film adsorption rate is greater (less) than the desorption rate, then the resultant surface group will increase (decrease) in thickness and ALD (atomic layer etch; ALE) occurs. This depends on the energy of the surface group (thermal or plasma enhanced), pressure in the chamber and exposure durations.

Low temperature, thermal ALE of Al$_2$O$_3$ was recently discovered [99, 98] and our group has developed an 'enhanced' ALE technique that uses a LiF chamber conditioning process [76]. The same precursor gases of TMA and anhydrous HF for ALD of AlF$_3$ can be introduced sequentially into the reactor chamber, results in removal of Al$_2$O$_3$ for substrate temperatures greater than ~215 °C. So T$_{sub}$ > 215°C results in Al$_2$O$_3$ etch and T$_{sub}$ < 205°C results in AlF$_3$ deposition (see Figure 4.4). In our ALE process, surface fluorination via ligand exchange between Al$_2$O$_3$ and HF (with the LiF pre-conditioning) result in AlF$_3$, which at

the higher temperatures will desorb (etch away) with transmetalation with the subsequent TMA exposure (see Figure 4.6).
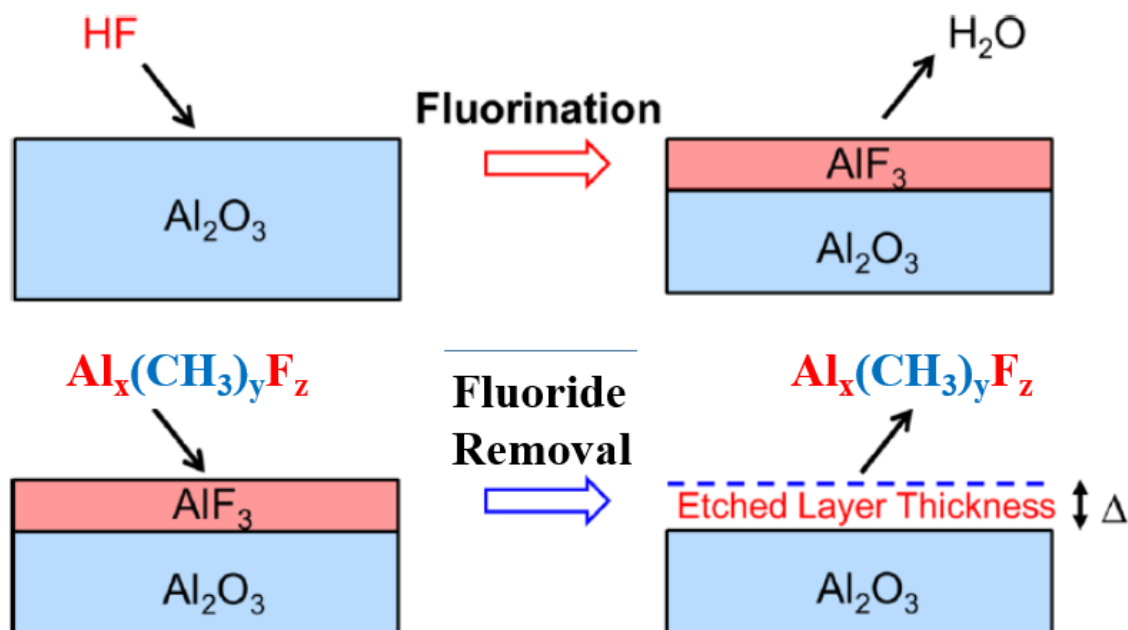
Figure 4.6: ALE of Al_2O_3 with sequential exposure to hydrogen fluoride (HF) and trimethylaluminum (TMA). HF exposure to Al_2O_3 at temperatures greater than $\sim 250°$ leads to ligand exchange. H_2O is a by product and a monolayer of mostly AlF_3 is left on the surface. TMA exposure promotes another ligand exchange to a hypothesized $Al_x(CH_3)_yF_Z$ group, which is volitle and leaves. This is the etching of a monolayer of Al_2O_3. The thickness-change-per-cycle is consistent per temperature with LiF preconditioning. Figure modified from George and Lee 2016 [55].

Similarly as with the ALD of AlF_3, the ALE of Al_2O_3 has proven to contain minimal oxygen content. The XPS data displayed in Figure 4.7 confirms the reduction in the oxygen content. The strength of the Al_2O_3 binding energy peak for an oxidized Al sample is reduced in comparison to a sample with Al, that has undergone the ALE process and capped with an ALD AlF_3 coating (to prevent re-oxidation). Optically inferred, the light absorption due to interracial oxide is greatly suppressed (see Figure 5.13).

The surface roughness of the ALE Al_2O_3 sample that has been capped with ALD of AlF_3 is reduced with respect to a sample with Al and ALD of AlF_3, but has not undergone the etching procedure (see Figure 4.8). The surface roughness can be important for short
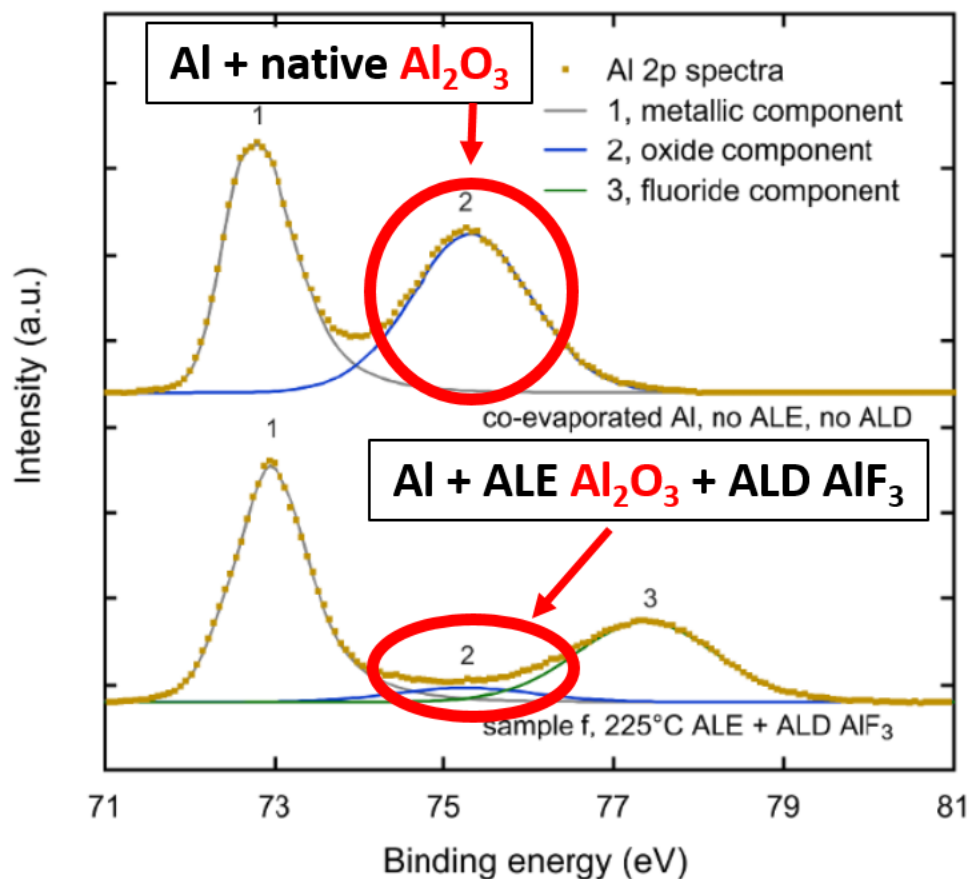
Figure 4.7: X-ray photoelectron spectroscopy (XPS) of Al + native Al_2O_3 compared to the Al + ALE Al_2O_3 + ALD AlF_3. The photoelectron spectrum is variable depending upon the element atomic and molecular bonds. In the top section, XPS signal is strong at the characteristic native Al_2O_3 electron binding energy (2). The bottom section, XPS signal for the ALE Al_2O_3 sample at the characteristic Al_2O_3 electron binding energy (2) is much lower in comparison to the Al signal (1). The ALD AlF_3 XPS signal (3) is apparent in the lower section. Adapted from Hennessy et al. 2017 [76].

wavelength reflectance. Diffuse reflection results in scattered light. Diffuse reflection can be induced by surface roughness when the magnitude of the RMS surface deviations are on the order of the wavelength of light being reflected ($\sigma_{RMS} \sim \lambda$). The decrease in surface roughness of the etched sample (close to the bare aluminum value) is a promising feature for the applicability of ALE to optical surfaces. This ALE procedure was pursued in the theme of generating high reflectance UV mirrors. Thus a combined ALE-ALD approach can be used to recover some the high LUV reflectance properties of the Al base reflector.
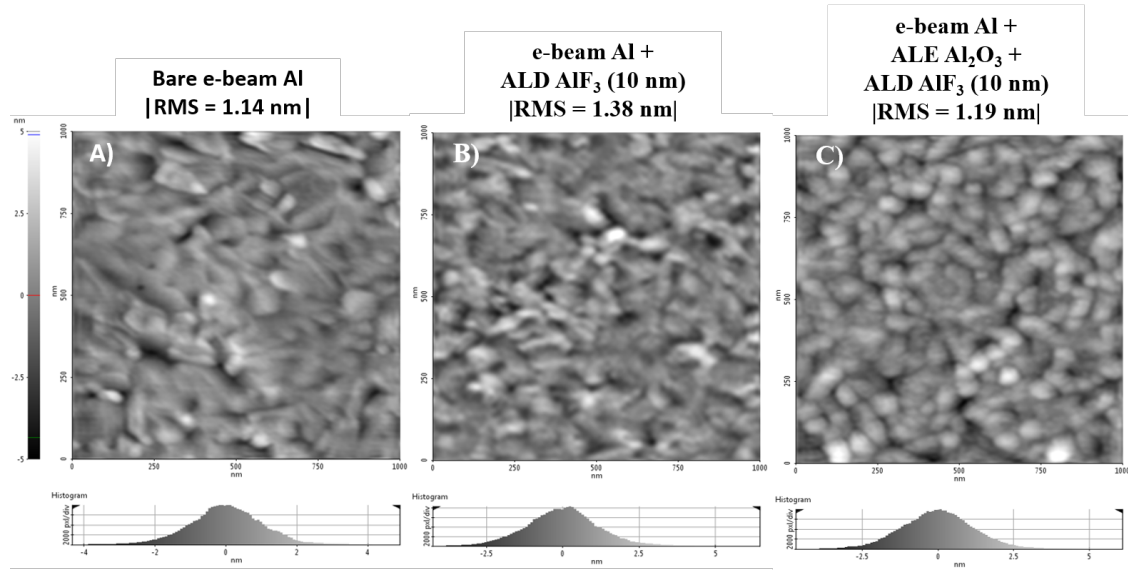
Figure 4.8: Atomic force microscopy (AFM) profile of surface roughness. The ALD of AlF$_3$ increases the surface roughness (as expected). The ALE of Al$_2$O$_3$ maintains a smooth surface which is beneficial for UV reflectance.

4.3   Subsequent ALE of Al$_2$O$_3$ then ALD of AlF$_3$ UV Mirrors

We set out to prove that the ALE-ALD etch technique can improve reflectance below 200 nm (especially between 90 - 120 nm over the unetched sample) and maintain reflectance comparable to unprocessed Al above 200 nm. These results are an extension of the initial findings in Hennessy et al. 2017 [76] to the LUV and the full ALE and ALD process details can be found there.

To generate an Al base reflector layer we electron-beam (e-beam) evaporate (AJA International Systems) 60 nm of Al on silicon wafers in the Microdevices Laboratory (MDL) facility at the Jet Propulsion Laboratory (JPL). We then transport the samples ex situ to the ALD system (vs. a load-lock transfer that maintains the same vacuum). The air exposure further oxidizes the Al. We estimate the terminal thickness of the native oxide layer to be between 2 - 3 nm based on previous studies [80], but the quality of the e-beam Al can be variable and influence the optically inferred oxide layer thickness. Additionally, we employ a reference set of Al and Al$_2$O$_3$ optical constants in our modeling that can lead to uncertainties

in the best fit oxide thickness. What is important for our study is the decrease in Al_2O_3 thickness for the Al_2O_3 removal process we discussed in this dissertation. Next we utilize an ALE of Al_2O_3 to remove the native oxide before the ALD protective overcoat growth.

We use the same precursors for ALD of AlF_3 to etch Al_2O_3 at a substrate temperature of 225 °C and then subsequently 'ramp' the temperature down to 150 °C for steady film growth. Our current process of gradually changing the substrate temperature results in an uncertainty in our exact Al_2O_3 final etch thickness and our resultant AlF_3 film thickness. Furthermore, the surface quality is dependent upon under- or over-etching of Al_2O_3. Etching past the amount of native Al_2O_3 can lead to pitting of the underlying Al surface and degrade optical performance. Under-etching will lead to residual Al_2O_3 in the final film system. To avoid over-etching and deteriorating the Al optical properties we intentionally under-etched Al_2O_3 in this study and determine the inter-facial oxide thickness from reflectance measurements. We determine Al_2O_3 and AlF_3 thicknesses via optical models fit to the measured reflectance plotted in Figure 5.13 and are listed in Table 4.1.

Table 4.1: **Coating sample in this study. Set A was measured at CU-LASP and JPL, while Set B was measured at NIST-SURF.**

	Set A (Sample ID)			Set B (Sample ID)		
	A	B	C	D	E	F
Process	None	ALD	ALE/ALD	None	ALD	ALE
Al_2O_3 thickness (nm)	2.1	1.8	0.8	2.7	1.7	1.1
AlF_3 thickness (nm)	0.0	2.4	2.1	0.0	4.4	0.9

Two sets of samples were generated to assess the improvement in LUV reflectance (and the sustained broadband reflectance) of the ALE-ALD process, Samples C and F only have Al plus ALD growth of AlF_3 (without the ALE Al_2O_3 removal). Samples B and E have undergone the full ALE-ALD process. Samples A and D are the reference oxidized Al samples. Reflectance measurements and analysis of this ALE-ALD project are discussed in Section 5.1.5. Details on the measurement systems and other subsidiary studies rom this UV coating project are elaborated upon in Chapter 5

Chapter 5

Optical Measurements of Prototype ALD Protected Mirrors for Future Astronomical Space Missions

Let's take a coordinate system, such that plane electromagnetic waves are propagating in a medium with a component of propagation in the $\hat{z}$ direction. There is an interface between the two media is oriented orthogonal to the $\hat{z}$ direction (lies in the $\hat{x}$-$\hat{y}$ plane). The reflectance of light from an interface between the two media is defined as the ratio of the light incident upon that interface, I_0, to the amount of light returned, I_R (now with a -$\hat{z}$ propagation component). This ratio calculation ($R = \frac{I_R}{I_0}$) is straight-forward. For example, just take the ratio of the signal measured reflected off of the mirror to the magnitude of input light. This is true, but in practice there are many effects that can complicate the accurate and precise determination of I_0 and I_R. Scattered light in a measurement apparatus, detector, response variability (spatially on the active area, temporally, vs. temperature, vs. light intensity, vs. bias voltage, etc.), light source fluctuations (current, gas flow, gas content, temperature, etc.), electronics and many other things can necessitate extreme caution in this reflectance measurement.

To determine the spectral reflectance, in many systems the light must be spatially dispersed which can further complicate the measurement. The UV is an unique realm in the electromagnetic spectrum. Light below ~320 nm is attenuated by Earth's atmosphere and below ~190 nm is severely absorbed. Thus measurements below 190 nm *must* be taken in vacuum. Commonly pressures below 10^{-3} torr (atmospheric pressure at sea level is near

760 torr and 1.0×10^5 pa). Secondly, there are not many transmissive materials below 200 nm that are vacuum compatible (low out-gassing, chemically stable, etc.) and safe for humans. Windowed light sources and detectors nominally operate down to $\sim$110 nm (MgF_2 window). So what are the best methods to measure light in the LUV (90 - 120 nm)? It has to be windowless detectors like microchannel plate detectors and Si-photodiodes. Light sources have to be windowless and operate under vacuum. Discharge gas light sources, are a specific class of hallow cathode lamps (HCL) that flow gas of a specified chemical purity. High voltage is applied, the induced electric field promoted collisions between the molecules, atoms and eventually ions, which disassociate molecules, ionize atoms and collisionally excite molecules, atoms and ions which de-excite radiatively. This creates the HCL light at a given pressure, temperature, bias voltage and current.

5.1   Optical Measurements

Using this knowledge and set of tools, UV/optical/IR reflectance of ALD AlF_3 coated samples only will be discussed in this dissertation. Measurements of glass, Al, LiF and MgF_2 coated optics were also conducted during this PhD project but are omitted for this dissertation text. Measurements of reflectance were conducted at CASA, LASP, NIST and JPL. Spectroscopic ellipsometric measurements occurred at JPL. I will focus only on initial silicon (Si) wafer coated with ALD AlF_3 measurements, Si + Al only, Si + Al + ALD AlF_3 and Si + Al + ALE Al_2O_3 + ALD AlF_3 samples in this dissertation.

5.1.1   Center for Astrophysics and Space Astronomy (CASA)

The University of Colorado Boulder (CU) Center for Astrophysics and Space Astronomy (CASA) has had a long cherished history in UV astronomy. Two of the most notable contributions are involvement with the Fuse Ultraviolet Spectroscopic Explorer (FUSE) [116] and being the P.I. institution for the Cosmic Origins Spectrograph (COS) [61]. These missions helped establish UV science at CASA and a substantial equipment, capable of mea-

suring UV light under vacuum. The Square Tank is heritage equipment designed to test large optics that has been modified for reflectance measurements. The is a central optics mount that can rotated 360° and translate the optics horizontally and vertically on linear translation stages. There is a 'swing-arm' that translates the detector along an arc of about 200° (see Figure 5.1).

The detectors used in this investigation are bare (no photocathode) z-stack microchannel plates (MCP) for wavelengths between 80 - 130 nm (see Figure 5.2) and a photomultiplier tube (PMT) with a MgF_2 window for wavelengths between 110 - 340 nm. The ACTON VM502 monochromator contains a holographically ruled 1,200 grooves per mm concave grating coated with Al + MgF_2 with a parabolic off-axis gold coated mirror and is a Seya-Namioka design on a Rowland Circle. The light sources used in this dissertation are HCL with H/Ar (35%/65% mix), Ne, and pure Ar gases and a sealed platinum-neon lamps. To remove second order light that can dominate the spectrum above 220 nm (due to PMT MgF_2 window) when using the PMT for measurements greater than 220 nm, a potassium bromide (KBr) window is inserted into the optical path. KBr has strong absorption below 200 nm, moderate transmittance from 200 – ∼235 nm and transmittance greater than 80% for wavelengths greater than ∼235 nm. Figure 5.3) demonstrates the suppression of 2nd order light, allowing measurements above 210 nm to be conducted in the CASA Square Tank.

Figure 5.2 displays a spectral scan of HCL H/Ar gas with the MCP. The input and output slit widths were adjusted to give a nominal spectral resolution near 0.6 nm ($\Delta\Lambda \approx$ 0.6). Spectral features from various spectral line groups are clearly observed. A few spectral lines are identified using data from the NIST Atomic Spectral Database https://physics.nist.gov/PhysRefData/ASD/lines_form.html. There are contributions from molecular hydrogen (H_2), atomic hydrogen (Lyman α, β and γ), atomic argon (Ar) and ionized Ar. The hydrogen Lyman lines are an ideal target for future astronomical space missions.

The Square Tank performance capability was characterized and numerous reflectance
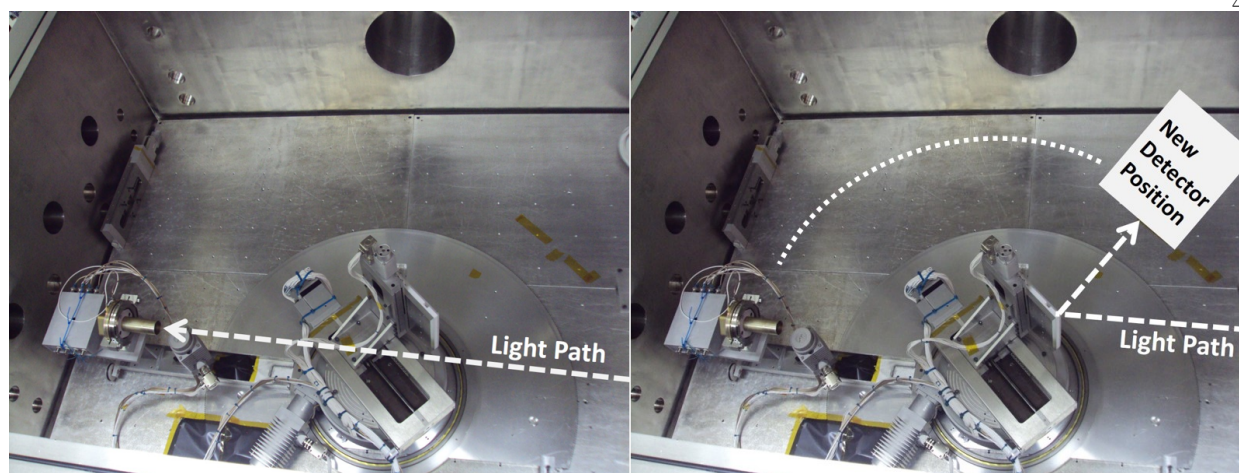
Figure 5.1: Inside the CASA Square Tank chamber. A microchannel plate detector is used from 90 - 130 nm and a photomultiplier tube with a MgF_2 window for wavelengths between $120 - \sim 300$ nm. The left picture shows the detector position for the input light measurement (I_0) and the right plot the position for reflected light measurement (I_r).

measurements of samples created at JPL were conducted. However, I will only discuss one series of measurements. In the initial phases of this project we only deposited ALD AlF_3 on Si wafers. Si has well known optical chemical, thermal and mechanical properties. Thin film Al has variable optical properties which can depend on the deposition rate, crucible type, chamber cleanliness and oxygen exposure. So to isolate the optical characteristics of ALD AlF_3, we perform initial tests on Si + ALD AlF_3. The only test in this series that will be discussed in this dissertation is a quasi-environmental storage test to assess the change in UV reflectance measured by the CASA Square Tank. Thus we are only concerned with the relative change, not the absolute reflectance value.

5.1.1.1 Environmental Storage Sensitivity

About 30 nm of ALD AlF_3 was prepared on two Si wafers for a environmental storage test. Figure 5.4 shows the UV reflectance results comparing the two samples. One sample was prepared in the Jet Propulsion Laboratory Microdevices lab (JPL MDL) and measured within 1 week at CU CASA. The second sample was measured after storage in the JPL MDL
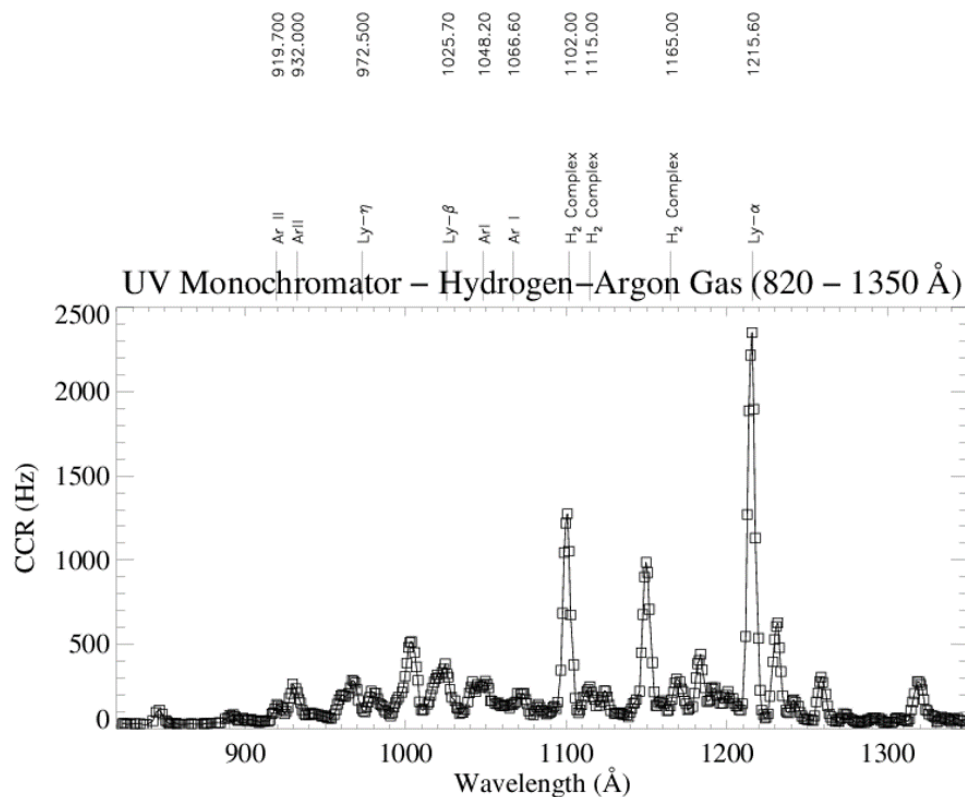
Figure 5.2: CASA Square Tank UV Monochromator spectral scan of hallow-cathode H/Ar (35%/65% mix) measured with a microchannel plate (MCP) detector from 820 - 1350 Å. Prominent spectral lines are labeled from the NIST Atomic Spectral Database https://physics.nist.gov/PhysRefData/ASD/lines_form.html.

glove box for 2 months. The glove box is maintained at 40 °C and 1% relative humidity. This initial environmental storage test provides a good baseline for detecting sample sensitivity to humidity and temperature, before more exhaustive tests are performed.

UV reflectance data in Figure 5.4 demonstrate the ALD AlF$_3$ coating samples robustness to the glove box environment. Minimal reflectance differences are expected from the slight thickness differences and our coupled wavelength-intensity uncertainties between measurement periods can account for the differences in reflectance observed at the strong absorption band (reflectance change) near 108 nm. Our measurements at that time, indicate that ALD AlF$_3$ maintains its optical performance in the 90 − 300 nm range. Coatings with strong environment sensitivity typically degrade in quality and exhibit decreases in UV
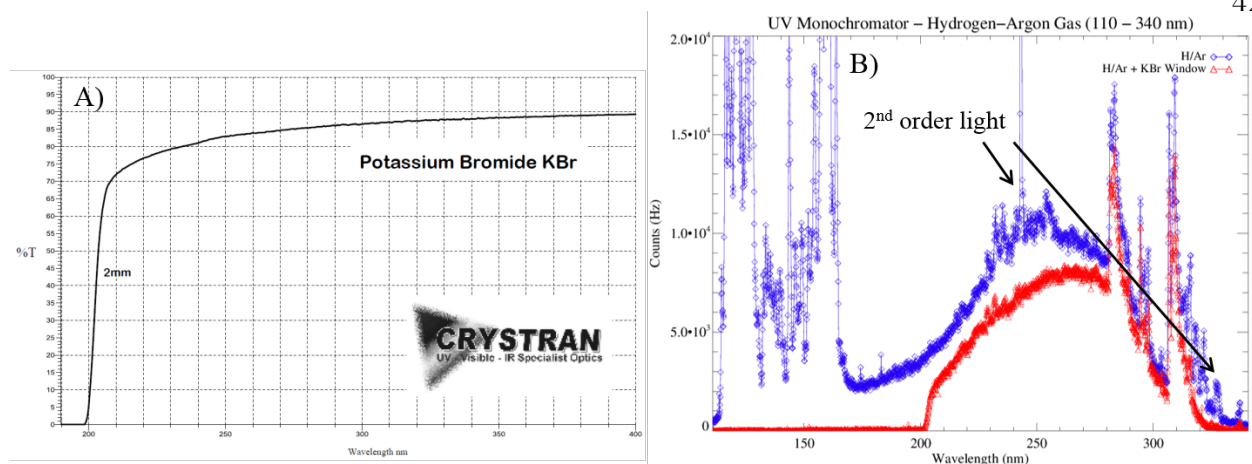
Figure 1. A) Transmission curve for a KBr window. B) Background subtracted intensity from our Hydrogen-Argon (H/Ar - 35%/65% mix) discharge gas with second order diffracted light for λ > 220 nm, in blue diamonds. Overploted is the resultant intensity of the H/Ar with the KBr window, the red triangles. The second order light for λ > 220 nm has been attenuated and light for λ < 200 nm has been completely removed.

Figure 5.3: A) Transmission curve for a KBr window. B) CASA Square Tank UV monochromator background subtracted intensity from our Hydrogen-Argon (H/Ar - 35%/65% mix) discharge gas with second order diffracted light for $\lambda > 220$ nm, in blue diamonds. Overplotted is the resultant intensity of the H/Ar with the KBr window, the red triangles. The second order light for $\lambda > 220$ nm has been attenuated and light for $\lambda < 200$ nm has been completely removed.

reflectance when compromised. These optical effects can be modeled macroscopically as an increase in the extinction coefficient k and generally manifest as a gradual increase in film absorption as Λ decreases [105]. This optical effect occurs, on the microscopic level, because of gradual oxide growth infused throughout the film (from pinholes), poor initial deposition quality or both. Thus a new composite material with a modified index of refraction (effective medium) can be calculated to account for the change [18]. Our ALD AlF$_3$ films with d > 20 nm have not exhibited such degradation and are resilient to the glove box storage conditions.

5.1.2   Jet Propulsion Laboratory (JPL)

The Jet Propulsion Laboratory (JPL) Microdevices Lab deposited all the ALD thin films discussed in this research. JPL is a research facility of the California Institute for Technology (Caltech) and managed partly by NASA. Their relationship is complicated. The
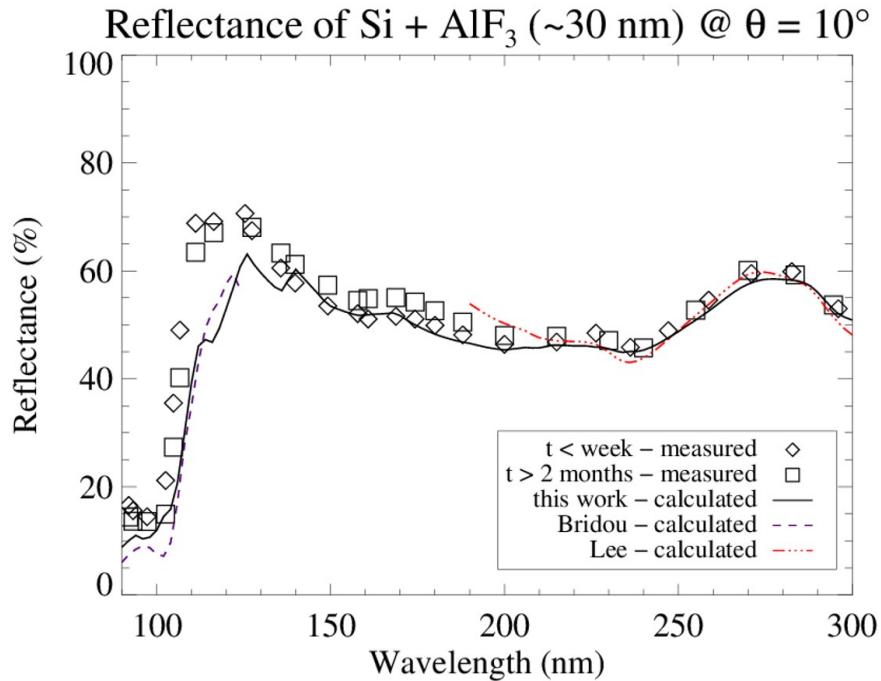
Figure 5.4: UV (90 − 300 nm) near-normal ($\theta = 10°$) absolute reflectance measurements for ∼30 nm of AlF$_3$ on Si for two samples, one deposited and measured within 1 week (diamonds) and the other measured after storage in the JPL MDL glove box for 2 months (squares). Performance differences are within measurement uncertainties ($\sim +/- 5\%$) indicating that the optical performance is not strongly modified by MDL glove box storage. Measurements follow the general spectral shape from calculated values of this work (black solid line), Bridou (blue dashed line; thermal evaporation) and Lee (red dash-dotted line; magnetron sputtered).

JPL MDL also has a few mechanisms for measuring sample reflectance. The newer Filmetrics system measures the normal incidence ($\theta = 0°$) reflectance from 190 − 1,000 nm in air. The systems consist of a CCD detector with deuterium (D$_2$) and blackbody light sources, and a fiber-optic system. The reflectance results of this system are in Figure 5.13.

JPL also has a system capable of conducting near normal incidence ($\theta \sim 10°$) from 120 - 200 nm. The ACTON VM 502 FUV system can attain a vacuum of $\sim 10^{-5}$ torr. The light source is a MgF$_2$ windowed deuterium (D$_2$) lamp and the detector is a MgF$_2$ windowed photomultiplier tube. The system can take one sample at a time and perform quick initial measurements of freshly deposited ALD AlF$_3$ samples. While the wavelength does not extend down to 90 nm (because of the MgF$_2$ window), measurements in the FUV

are vital for diagnosing the severity of any film optical degradation for Si + ALD ALF$_3$ and the level of oxidation for Al samples. If the samples do not perform well in the 120 - 200 nm range as measured by this system, then it is not worth shipping to CU or NIST for measurements down to 90 nm. The ALE-ALD sample set discussed in Section 4.3 were measured using this system. The reflectance results are plotted in Figure 5.13 and discussed in depth in Section 4.3.

The MDL also has a spectroscopic ellipsometer (SE). SE is useful for measuring the polarization sensitivity of optics, and extraction either thin film thickness if the optical constants as a function of wavelength are known, or the optical constants is the film thickness is known from an external source, but not both simultaneously. The SE system at JPL also can measure the oblique ($\theta > 40°$) incidence reflectance in p and s or unpolarized ($I_{unpolarized}$ = 0.5(I_p + I_s)).

5.1.2.1 Spectroscopic Ellipsometry

Polarization effects occur when the induced response of a photon's incident electric field I_S different in orthogonal directions within a medium. This typically occurs at angles of incidence larger than $10°$ (at an interface between two media) for media with a homogeneous and isotropic index of refraction. Birefringent materials can alter the polarization state of transmitted light at normal incidence, due to the directional dependence on the index of refraction. We consider AlF$_3$ as non-birefringent when not highly stressed (all materials exhibit polarization effects when highly stressed) for this study. Polarization differences can be a desirable effect in some optical systems depending on the application, but in many systems, it can be an undesirable reality that needs to be accounted for. An example includes Lyot chronographs that can be implemented for exoplanet investigations. Common performance requirements demand host star light attenuation of $\sim 10^{-10}$ so that the exoplanet signal can be cleanly discerned. Phase differences in polarization states ($\Delta = \Phi_p - \Phi_p$) can contribute to incomplete destructive interference of the host star light in the final image

plane, leading to 'polarization leakage' and a contaminated or noisier exoplanet signal. In some instances, the existence of a phase shift alone I_S not the issue, rather the dispersion or spectral variation of the phase shift across the instrumental bandpass I_S problematic. Optical coatings can be used to accommodate an undesirable phase dispersion present in an optical system. Thus for many systems, knowledge of the polarization effects induced by an optical coating I_S valuable.

We monitor the polarization properties of our ALD AlF_3 films during development through spectroscopic ellipsometric measurements. We used the JPL MDL HORIBA UVISEL2 Polarization/Phase Modulation (PM) Spectroscopic Ellipsometer to obtain the ellipsometric angles of psi (Ψ) and delta (Δ) extracted from measurements of I_S and I_C Ψ I_S related to the ratio of the modulus of the Fresnel coefficients for p and s states ($\tan\Psi = |r_p|/|r_s|$) and I_S indicative of the polarized reflection amplitudes. For more details on the SE, see the Appendix B. The SE measures the polarization state induced upon light reflected off the sample. SEs are commonly used for in-situ film deposition monitoring of film thickness, ellipsometric angles and optical constant extraction [95].

Figure 5.5 and Figure 5.6 demonstrate the agreement between measured Δ and Ψ ($\tan\Psi$) I_S plotted for ease of physical interpretation) at $\theta = 45°$, $55°$ and $65°$ from 200 – 800 nm for 34 nm and 24 nm of AlF_3 deposited at 100 °C on Si (represented by symbols) and optical constant calculations (lines) from 'this work', and Lee. These results bolster confidence in the optical quality and the ability to model the optical properties of our ALD AlF_3 films. Due to differing conventions of phase shift, a +/- Π may be needed for consistency between references. Bare Si wafer measurements are over-plotted to serve as a reference to the change in $\tan(\Psi)$ and Δ with respect to the substrate. The total phase shift and ratio of polarization reflection amplitudes are substrate dependent and will be different on an Al reflector base layer film (our final objective), but it I_S good to observe the change to the substrate imparted by the AlF_3 coating. Thus we monitor it here on Si.

Many optical systems utilize a 'fold mirror' or a mirror positioned 45° to the optic
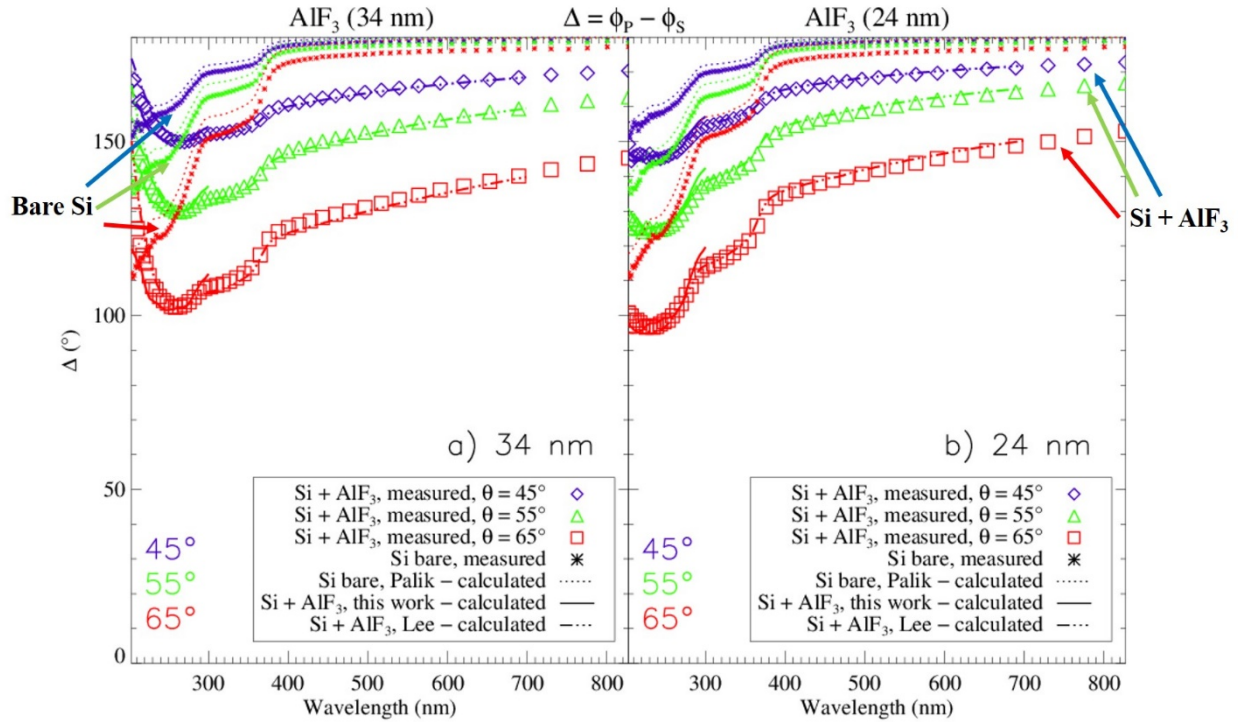
Figure 5.5: Measurements of Δ, the phase shift between p and s polarization states induced by 34 nm (Panel a) and 24 nm (Panel b) of AlF$_3$ on Si wafers at $\theta = 45°$, 55° and 65° (blue, green and red symbols respectively). Measurements agree with optical constant calculations from both this work (solid line, ALD) and Lee (dash-dotted line, magnetron - sputtered). For reference, bare Si substrate (with probable native oxide) measurements are over-plotted with small symbols (asterisks) and calculations from the Palik archive optical constants (dotted line). Measurement and model synergy indicate the predictive power. Δ combined with Ψ describe polarization state changes (between linear, circular and/or elliptical) upon reflection from our Si + AlF$_3$ combination.

axis to bend the light 90°. Thus, this angle of incidence I$_S$ probably the most commonly implored oblique angle used within measurement capabilities of the SE (it can measure $\theta >$ 40°) and I$_S$ important to monitor. The dispersion in the phase shift increases for the AlF$_3$ films with respect to the bare Si substrate for both thickness and all three angles of incidence, but I$_S$ expected to change minimally for very thin films that we desire to grow in the future (few nm). Figure 5.6 displays the reflection amplitude depolarization ($\tan \Psi = |r_p|/|r_s|$ shift towards unity) effect of the AlF$_3$ coating on the Si substrate. While the magnitude of this shift I$_S$ small for $\theta >$ 400 nm, it I$_S$ substantial between $200 - 250$ nm with indication from

the measurements, 'this work' and Lee calculations that it resides near unity for $\theta < 200$ nm. This could be a very instrumental property for fold mirrors used in UV optical systems, if a silicon reflective surface was ever used. Additionally, Δ approaches 180° (minimal change or 'flipping' of phase shifts depending on the convention used) near 200 nm. This strengthens the argument for AlF_3 capabilities to alter the polarization properties of a substrate. The powerful trait of thin film coatings.
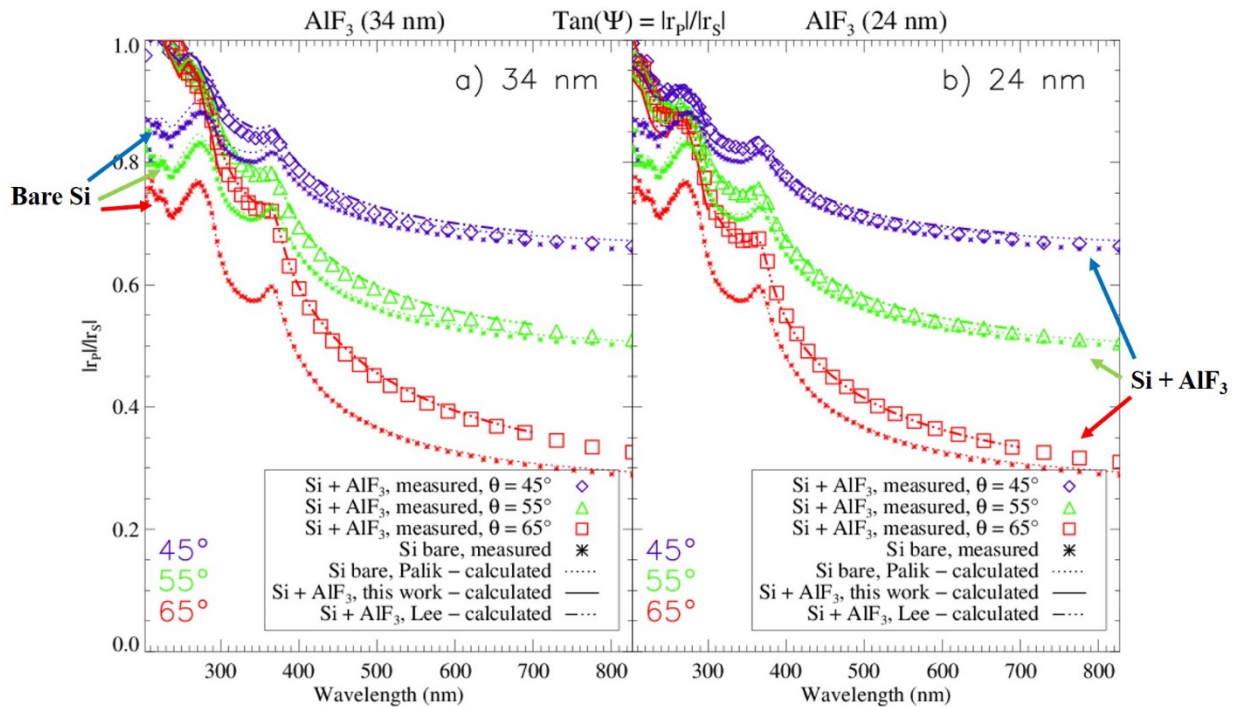
Figure 5.6: Measurements of tan Ψ, the ratio of the modulus of the p to s polarization state Fresnel coefficients for 34 nm (Panel a) and 24 nm (Panel b) of AlF_3 on Si wafers at $\theta = 45°$, 55° and 65° (blue, green and red symbols respectively). Values near unity indicate even amounts of reflected light for both polarization states. Deviations from unity mean different amounts of each state are reflected. For reference, bare Si substrate (with probable native oxide) measurements are over-plotted with small symbols (asterisks) and calculations from the Palik archive optical constants (dotted line). Measurements agree in general with optical constant calculations from 'this work' (solid line, ALD) and well with Lee (dash-dotted line, magnetron - sputtered). Δ combined with Ψ describe polarization state changes (between linear, circular and/or elliptical) upon reflection from our Si + AlF_3 combination.

Ψ and Δ together fully determine the polarization properties of a system (e.g. linear, circular and elliptical states). For example, light with Ψ = any angle in the domain ($0° \leq$

$\Psi \leq 45°$), and $\Delta = 0°$ or $180°$ for a particular wavelength describe linearly polarized light, for $\Psi = 45°$ (or $|r_p|/|r_s| = 1$) and $\Delta = 90°$ or $270°$ describe circularly polarized light and any other combination of Ψ and Δ describe the most common state of polarized light, elliptical.36 The 34 nm of AlF$_3$ sample measurements at an angle of incidence of $45°$ can be interpreted near wavelengths of 200 nm, to nearly efficiently impart a change in elliptical light to linear and vice versa. A similar characteristic could be designed for a coating thickness thinner than 24 nm at longer wavelengths for a $45°$ angle of incidence. ALD AlF$_3$ can address a range of light manipulation needs for future UV optical systems.

5.1.3   National Institute for Standards and Technology (NIST) Synchrotron Ultraviolet Radiation Facility (SURF)

The National Institute for Standards and Technology (NIST) is know for just what there name states, a standard or a benchmark in precision and accurate measurements. The Synchrotron Ultraviolet Radiation Facility (SURF) is one of a few synchrotron light sources in the world capable of precision measurements. Readers can be reminded of the basic principles stated in Section 2.1.5 and more detail is in the references stated there. The NIST SURF reflectometer system consists of a Si-photodiode detector, the synchrotron light source a series of grazing incidence gratings and a set of filters to isolate spectral ranges for the mitigation of higher order light contamination.

The spectral bandapass filters include Indium (In) for 76 – 108 nm, LiF for 108-210 nm, sapphire (Al$_2$O$_3$) for 160-320 nm, and a glass filter for 300-600nm. Measurements were performed on a semi-autonomous system in both P and S polarizations. The final measurements were averaged/corrected to generate unpolarized values. The NIST SURF reflectometer was recently set up and thus needed to be characterized. The low wavelength range is dictated by the project interest and the 500 nm long wavelength limit by the performance of the Si-photodiode. There is still sensitivity out to $\sim$ 600 nm but the goal of the reflectance measurements at NIST are to assess the ALD AlF$_3$ coating performance and cross-check

with our JPL and LASP systems. Figure 5.7 is a picture of the inside of the NIST SURF reflectometer chamber. The author of this dissertation is visible in the reflected image off of the optic.
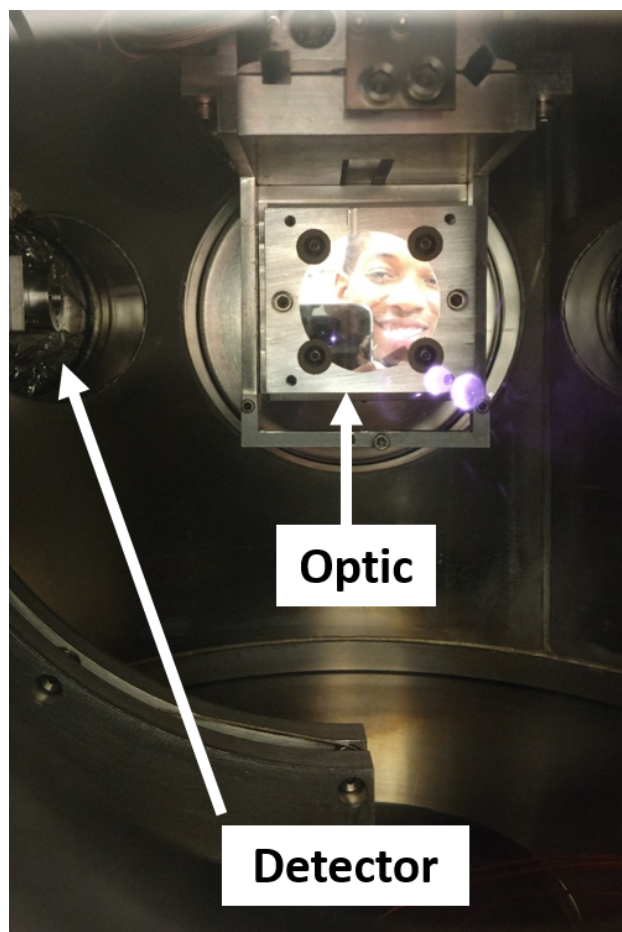
Figure 5.7: The optics section of the NIST SURF reflectometer. The detector is a Si-photodiode. The mirror sample was very shiny (in visible light) and smooth. So smooth, that we can see the author of this dissertation in the mirror.

We were the initial testing run of this system and commenced by measuring a gold sample from 76 - 500 nm. Gold is known to have stable UV properties and be resilient to oxidation. Thus, the performance of gold in the UV is a suitable reference standard to assess the capabilities of the NIST SURF reflectometer. The JPL MDL electron beam deposited roughly 100 nm of gold onto a Si wafer. Figure 5.8 displays the agreement between the NIST SURF, JPL ACTON system (JPL-Bala), and CU-LASP measurements of the same

deposition process at JPL. There is excellent agreement among the three systems. The theoretical reflectance calculation based on optical constants from Palik diverge because those optical constants are extracted from bulk gold. Thin film deposition processes can lead to various film structures (crystalline, polycrystalline, amorphous) depending on the deposition technique. Thus bulk thin film optical constants are not necessarily a firm representation of what can be expected from thin film growth, but merely serve as a qualitative guide.

There is better agreement between the three sytsm measurements and the thin film Au measurements plotted from Canfield et al. 1964 [24]. The consistency between all the NIST SURF reflectometer spectral ranges proves that the system can perform quality measurements (when all system variations and systematics are taken into account and adjusted for). An accomplishment of this dissertation is helping commission the NIST SURF UV reflectometer. Measurements using this system were also conducted on the Al only, Al + ALD AlF_3, and Al + ALE Al_2O_3 + ALD AlF_3. The results of those measurements are in Figure 5.13 and discussed in depth in Section 5.1.5 and Section 5.2.

5.1.4   Laboratory for Atmospheric and Space Physics (LASP)

The Laboratory for Atmospheric and Space Physics touts an impressive resumé as it has had an instrument go to every planet in the Solar System. LASP has participated in many missions that employ various aspects of the EM spectrum, particle detectors, electric field and magnetic fields. Thus, there is numerous spare spaceflight qualified equipment available from past missions. The Si-diode flight spares from the recent GOES-R (GOES-16) mission were used for the measured stability and sensitivity to UV light to augment our reflectance measurements in the LUV and FUV. Calibration Chamber #3 (CTE3) at LASP was refurbished and modified to conduct reflectance measurements from 90 - 160 nm. A picture of the interior of the chamber is in Figure 5.9. To avoid moving detectors, which can induce noise and deteriorate the nano, fempto amps signals, we employ two stationary detectors. The left-most detector in Figure 5.9 is the reflected detector and the right-most
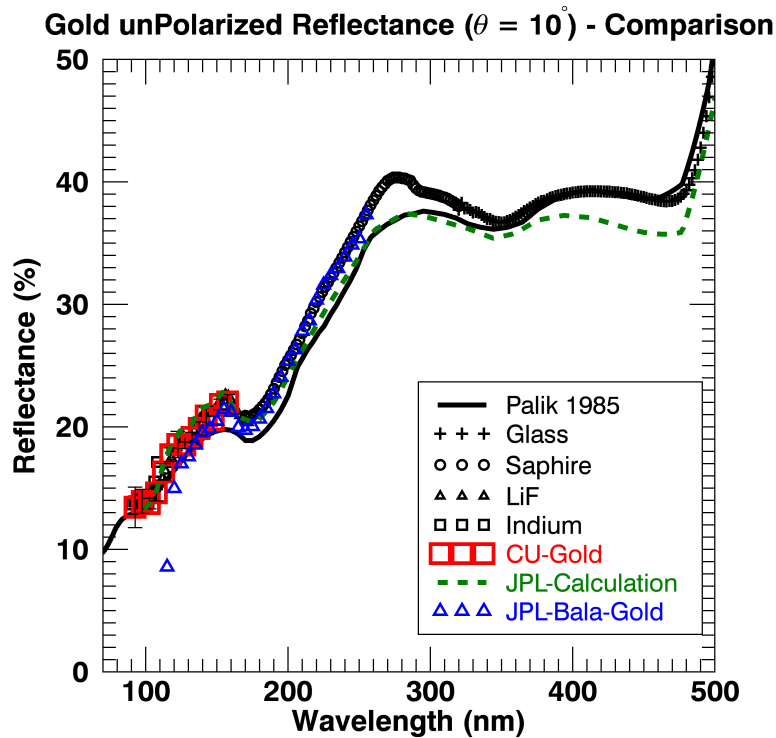
Figure 5.8: NIST SURF reflectance measurements of reference gold (Au) sample. The yellow and black lines are calculations based upon optical constants. The symbols are the NIST SURF measurements for each segment. The red squares are measurements from CU-LASP-CTE3. The black line are optical constant calculations from Palik 1985 and Palik 1998 [123]. The green dashed line are the results from Canfield et al. 1964 [24]. The blue triangles are measurements from the JPL ACTON VM 502 FUV system.

detector, the input light detector. The optics reside on vertical and linear translational stages. Labview software was written for autonomous data accumulation, which greatly expedited the measurement process.

To calculate a precise reflectance spectrum, the temporal stability of the light source and detector must be assesssed and improved if needed. Fortunately, the flight-spare Si-photodiodes exhibited little time variation over a 5-hour test. Figure 5.10 shows the input and reflected detector simultaneous dark signals over 5-hours. The dark current oscillates between positive and negative values (due to drifts in the silicon and preamp noise), with
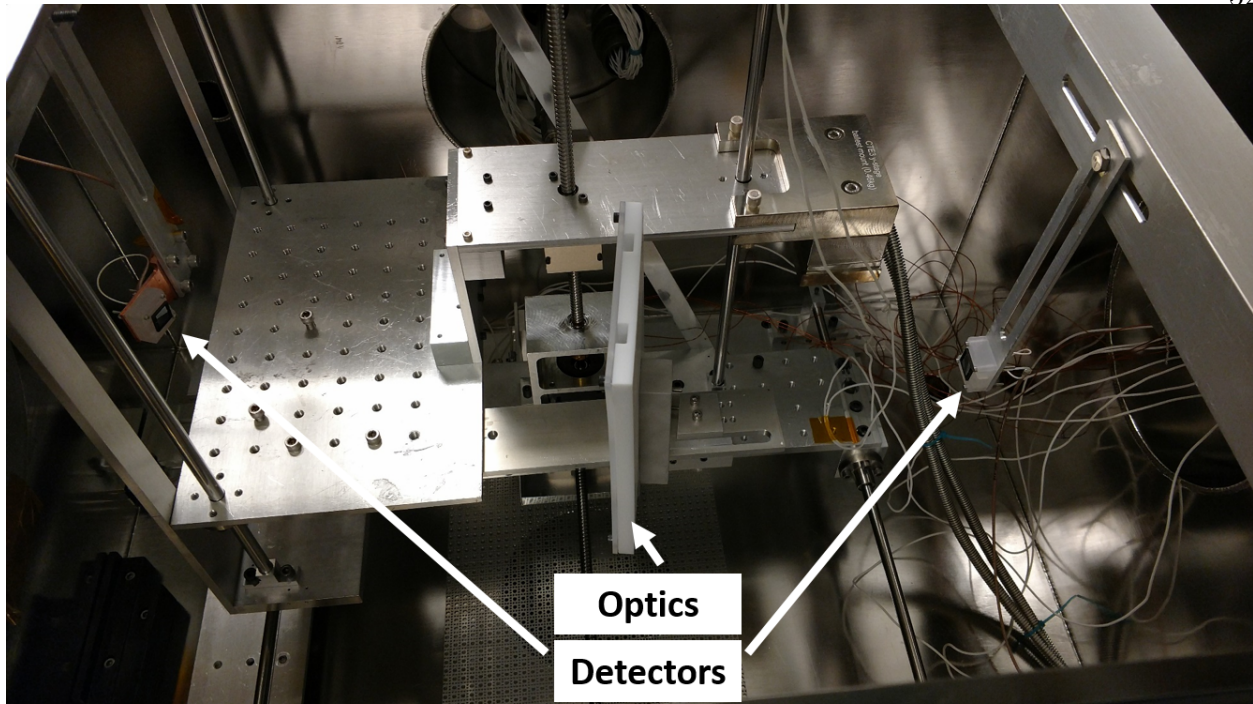
Figure 5.9: Inside the LASP CTE3 chamber. The Si-photodiodes are Opto Diode AXUV100G and flight spares.

a mean near 2 x $10^{(-12)}$ A and a standard deviation around 3 x 10^{-13} A. Thus, we need signals of at least $10^{(-11)}$ A for our reflected light signal to obtain a signal-to-noise of at least 5. Measured reflected signals greater than this will improve measurements accuracy. If are signal is at least $10^{(-11)}$ A, we can obtain precise measurements with oscillations less than $\sim 3\%$.

Figure 5.11 displays spectral scans using a D_2 and a HCL light source with a variable mix of H/Ar. The majority of the gas is H. The D_2 lamp has all-so-common MgF_2 window and thus has limited throughput below 115 nm. Thus, to measure reflectance down to 90 nm, the HCL is used. Both light sources produce reasonable signal to noise. It must be noted that the D_2 measurement was conducted with an aperture that was a factor of 4 larger than the HCL light source aperture. The intensities of the light sources are not one-to-one as a function of wavelength due to the different operation principles. There are two sets of measurement in Figure 5.11 to assess the repeatability of the input and reflected signals.
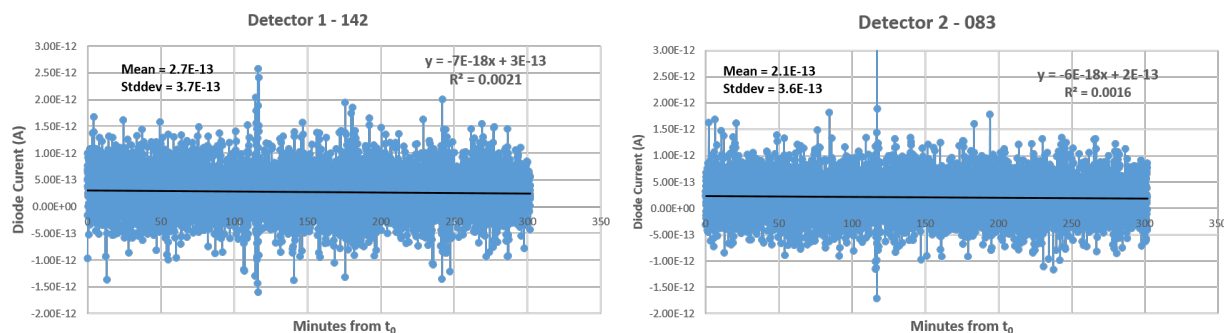
Figure 5.10: Dark current stability study measurements of the two Si-photodiodes. Dark measurements where performed over 5-hours to check for dark current systematic drifts, differences between the two detectors or non-random noise.

The blue and green (input - 'incident') symbols and the red and yellow (reflected) symbols almost completely overlap for currents larger than 4 x 10^{-12} A (signal-to-noise $\sim$2). Thus the measurements are highly repeatable. The reflected measurements were made on a bare gold mirror.
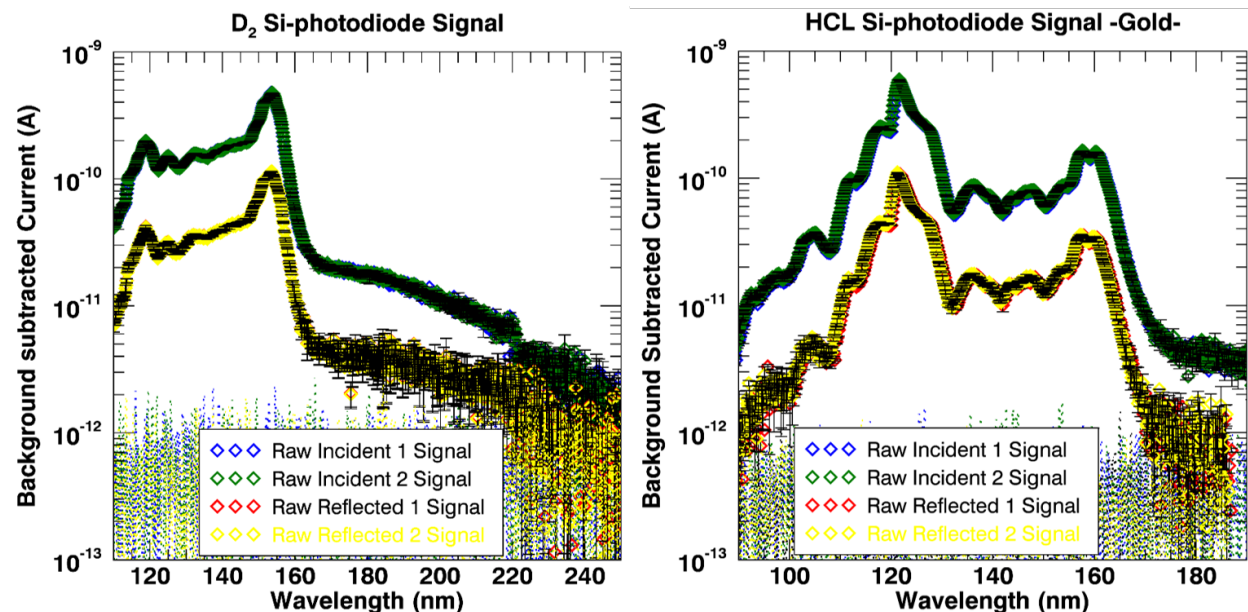
Figure 5.11: LASP CTE3 D_2 and HCL (H/Ar) light source spectral scan with the Si-photodiode. The input (I_0) and reflected (I_r) signal is large enough for reflectance calculations with moderate signal-to-noise (S/N $\geq$ 5). There are two sets of spectral scans and they agree very well. The ratio of this example raw signal is used for the reflectance measurement result.

To calibrate the performance of the refurbished CTE3 chamber, gold, bare Si and bare Al reflectances were measured. All 'reference' samples had either been measured by another system of can be modeled fairly well with optical constants. The samples were chosen due to the expected variability in dynamic range. Si-photodiodes generally have good dynamic range and can measure signals from $10^{-12} - \sim 10^{-5}$), depending on the electronics used. The gold sample was chosen for low reflected signal values, Si wafer for medium values and Al with native oxide for spanning low and high values in the wavelength range.

Figure 5.11 demonstrates the exceptional performance and good agreement between the measurements. The gold and black solid lines are reflectance calculations based on optical constants. Gold is kept as just bare gold (no oxide layer). The Si wafer measurements were fit with an optical model to include a native silicon oxide (SiO_2). The Al measurements were fit with a nominal aluminum oxide (Al_2O_3) thickness. The results of the oxide fits yield thicknesses consistent with literature and good agreement with the measurements.
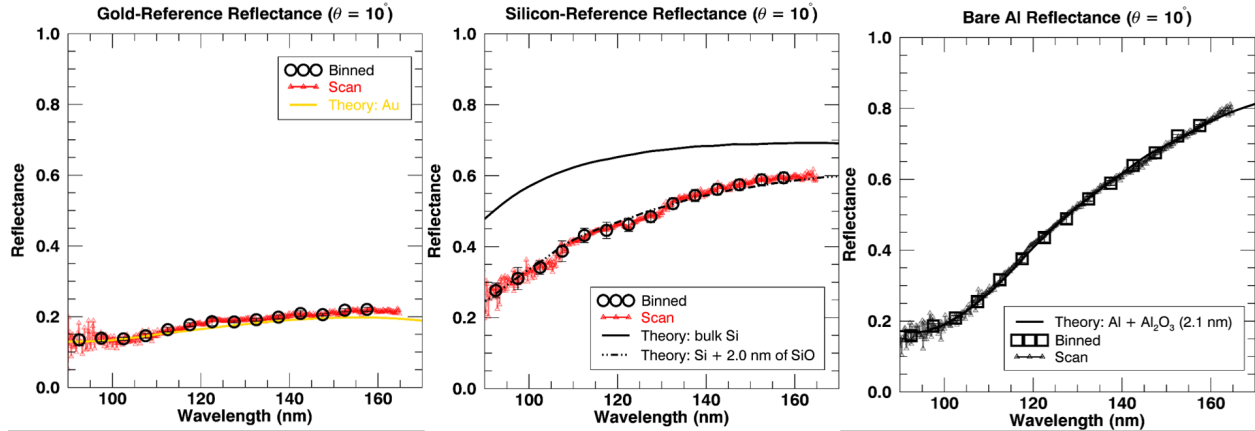
Figure 5.12: LASP CTE3 reflectance measurements of reference sample if gold (Au), silicon (Si) and bare aluminum with native oxide (Al). The yellow and black lines are calculations based upon optical constants. The red lines is the raw reflectance calculated from the ratio of the spectral scans. The symbols are the binned raw reflectance data.

The measurements were conducted at an angle of incidence of 10 degrees. The red lines is the ratio between the raw reflected signal and the input signal. The symbols are the 5 nm wide binned data from the red line. The symbols indicate the center wavelength

of the evenly binned data. The uncertainty is overplotted with error bar but are not clear. The measurement precision is roughly 1%, but the accuracy is +/- 2%. What is important for the CTE3 chamber reflectance measurements is the relative reflectance value between different sample. This is what the UV coatings project need to differentiate to assess the capability of ALE Al_2O_3 to improve the LUV and FUV reflectance of Al mirrors.

The LASP CTE3 chamber provided improvements on the measurement precision and accuracy in the UV coatings project.

- The repeatability of measurements is pristine, for our standards (within 1 - 2 % per binned data point).

- The precision and agreement between subsequent wavelength data points is much improved.

- The accuracy of the relfectance estimates are the best that were attained by a CU based system on this project.

5.1.5   Reflectance of ALE-ALD UV Mirrors

The next step combine the near-normal incidence ($\theta \leq 10°$) reflectance measurements of the CU-LASP CTE3 chamber (90 - 160 nm), JPL Filmetrics system (190 - 1,000 nm; JPL-Long), JPL ACTON VM 502 FUV (120 - 200; JPL-Short nm) and the NIST SURF reflectometer (80 - 500 nm) of the Al only, Al + ALD AlF_3, and Al + ALE Al_2O_3 + ALD AlF_3 sample set. The details on the atomic layer processes and motivation are in Chapter 4. I only discuss the reflectance results and implications here. Two sets of ALE-ALD series mirrors were fabricated on Si wafers. One set was measured by the CU-LASP system ASAP and the witness samples from this deposition measured by the JPL Filmetrics and JPL ACTON VM 502 FUV. The second set was prepared, shipped directly to NIST in Gaithersburg, Maryland. U.S.A. and measured ASAP.

The reflectance results are in Figure 5.13. The top panel is Set A, measured at CU and JPL. The bottom set is Set B measured at NIST. The sets are expected to be very similar optically as the etch and deposition procedures were duplicated for consistency. The main difference is the time lag of roughly 1 week ($\sim 7 - 10$ days) for the NIST measurements vs. the $2 - 3$ day delay for the CU-LASP measurements and the 1 day measurements at JPL.
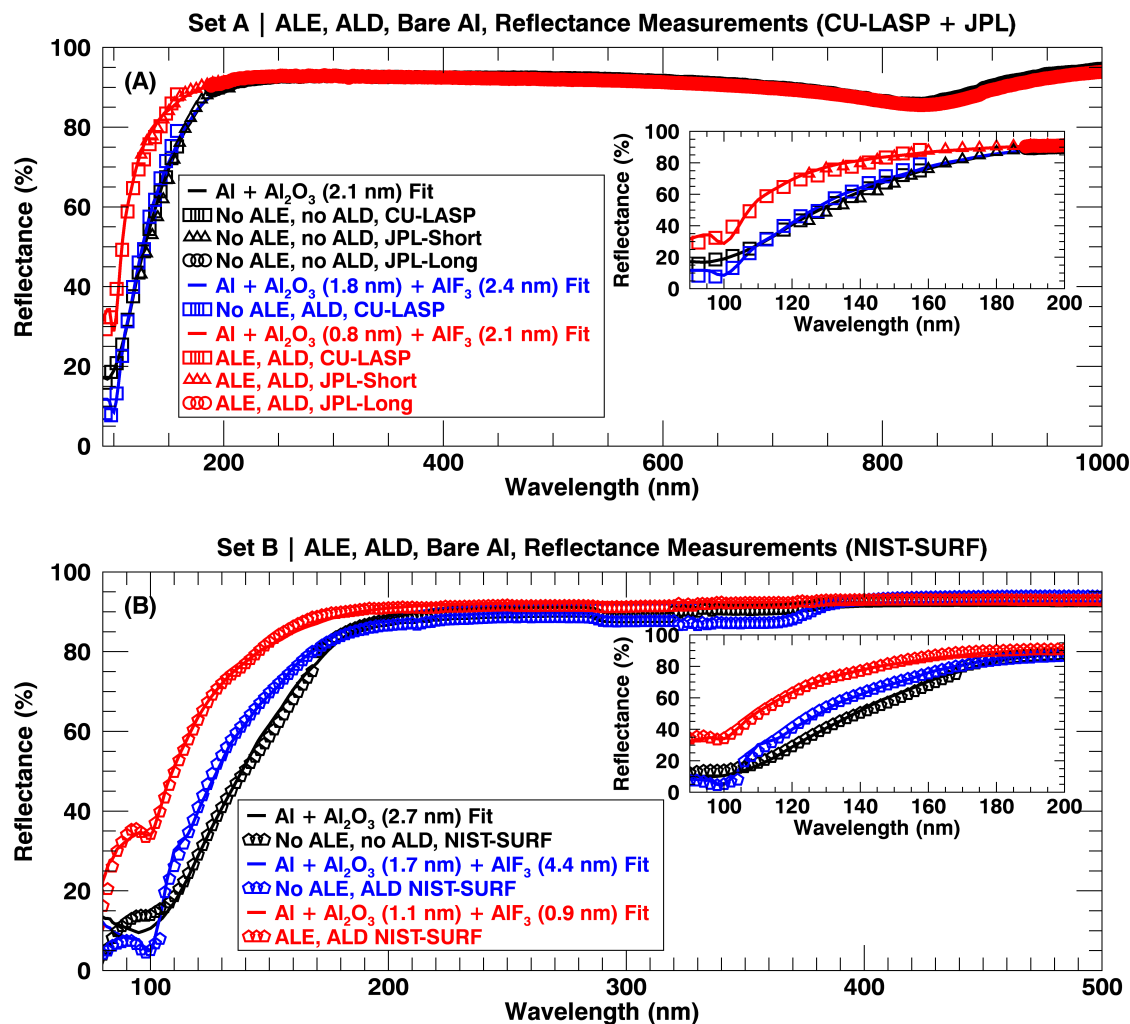
Figure 5.13: (A) Set A CU-LASP and JPL reflectance measurements (symbols) of Al-only (black), Al-ALD-AlF$_3$ (Blue) and Al-ALE-ALD-AlF$_3$ (red) show the etched sample achieves values near 30% at 90 nm while maintain high reflectance out to 250 nm. (B) Set B NIST-SURF reflectance measurements reaffirm the CU-LASP and JPL results and prove repeatability of improved performance. The lines in both (A) and (B) are film thickness fits to the respective measurements.

Figure 5.13 demonstrates that the ALE-ALD processed samples (red symbols) have higher reflectance at all wavelengths below 200 nm than the ALD-only (blue symbols) and unprocessed sample (black symbols). This is a huge step forward in this project! The intrinsic AlF_3 absorption is clearly observed, where the ALD-only sample reflectance is less than unprocessed sample for $\lambda > 105$ nm, which is the location of the AlF_3 absorption bands and an increase in k. The ALE-ALD sample demonstrate reflectance improvements on the Al plus ALD only sample with an increase from $\sim 8\%$ up to $\sim 30\%$ near 95 nm, from $\sim 5\%$ up to $\sim 30\%$ near 100 nm and from $\sim 10\%$ up to $\sim 40\%$ near 105 nm. These results prove that the ALE removal of Al_2O_3 and subsequent coating of ultra-thin layers of AlF_3 by ALD can mitigate absorption loses in the LUV and FUV.

Further improvements in the ALE-ALD process (better temperature control, optimization of etch and growth rates, etc.) can lead to additional reflectance improvements from 90 - 120 nm and be a prime candidate for future UV/Optical/IR astronomical space missions. The ideal reflectance performance would be R $\geq$ 50% between 90 - 105 nm. Even with the current results the reflectance gain between the ALD only sample and ALE-ALD sample I_S significant. The light throughput in a reflective optical system can be no greater than the product of the reflectance of all the components (with N reflections). For the application of space mirrors there will likely be a Cassegrain, RitcheyChrétien, or similar model. Thus, there will probably be at least four light reflections, the primary, secondary and tertiary (probably a fold mirror) mirrors before dispersion off a reflective grating. If all components a coated with this ALE-ALD process, for this system (N = 4) the gains in throughput compared to the ALD only coating at 95 nm would be roughly $(R_{ALE-ALD}/R_{ALD})^4 \approx 198$. The additional ALE processing in current coatings provide an increase in throughput of a factor of 198, with potential to be improved further.

This factor of increased throughput I_S similar in comparison to improvements over the traditional Hubble Space Telescope (HST) coating of Al + 24 nm of MgF_2 and even the new hot LiF depositions, as both coatings currently have reflectance near or below 10% at and

below 100 nm. Finally, the self-limiting, conformal, near stoichiometric film characteristics of ALE and ALD process allow for the scalability to large area substrates. This I_S vital for the proposed multi-meter sized mirrors for future astronomical space telescopes. This study has demonstrated one of many applications of atomic etch-growth or even a growth-etch processes for modifying the optical properties of systems.

5.2 UV Coatings Summary

We have produced ALD AlF_3 films on Si wafers and explored their surface roughness, UV-Vis-IR reflectance at two angles of incidence (10° and 45°, in segments), polarization, deposition temperature and environmental storage sensitivities. Thicker layers (d > 20 nm) have performed well in each of these investigations and have proven to be model-able for $\lambda >$ 120 nm. We have also developed a process that can remove native aluminum oxide. The ALE removal of Al_2O_3 also improve the surface roughness over ALD AlF_3 process alone. The subsequent ALE of Al_2O_3 and capping with ALD of AlF_3 has been proven to enhance the reflectance for $\lambda < 200$ nm. This is another breakthrough. The improvement of this process and scalability of ALD and ALE open an array of possibilities not limited to mirror coatings. I now summarize the main aspects of this UV coatings project and the first half of my PhD research.

(1) An atomic layer etch of Al_2O_3 procedure has been modified (with LiF preconditioning) to create mirrors capped with ALD AlF_3.

(2) E-beam Al + ALE of Al_2O_3 + ALD of ~2 nm of AlF_3 has been proven to improve the reflectance over e-beam Al + ALD of ~2 nm of AlF_3 from 90 - 200 nm. Increases from ~8% up to ~30% near 95 nm, from ~5% up to ~30% near 100 nm and from ~10% up to ~40% near 105 nm were observed. These results prove that the ALE removal of Al_2O_3 and subsequent coating of ultra-thin layers of AlF_3 by ALD can mitigate absorption loses in the LUV and FUV.

(3) High quality reflectance measurements were performed via the refurbishing of the LASP CTE3 chamber.

(4) The NIST SURF reflectometer was commissioned, systematic effects uncovered and improvements were made to conduct quality unpolarized reflectance measurements from 80 - 500 nm.

(5) The CASA Square Tank system was characterized, modified, used to perform initial project and degradation study measurements.

(6) ALD ALF$_3$ film surface roughness on Si wafers are consistent with ~15% increase in RMS as indicated by AFM.

(7) Unpolarized reflectance measurements from 90 – 800 nm have proven that ALD ALF$_3$ films are consistent with extracted optical constant calculations, which are similar to values listed in literature from thermal evaporation (90 – 124 nm) and magnetron sputtering (190 – 700 nm) except for higher than predicted reflectance near 110 – 120 nm. The absorption band of our films appears to occur at shorter wavelengths than calculations based upon Bridou optical constants predict.

(8) ALD AlF$_3$ has good Optical properties for deposition temperatures between 100 – 200 °C. Films deposited at different temperatures of 100 °C and 200 °C show small differences in UV reflectance, but still within measurement uncertainties.

(9) Polarization sensitivity was explored via ellipsometric angles. Polarization changes induced can be beneficial depending on the optical system and the film substrate choice. SE measurement agreement with optical constant calculations from 200 – 800 nm at multiple angles of incidence ($\theta = 45°$, $55°$ and $65°$) confirm favorable optical characteristics of the ALD AlF3 films. Furthermore, the optical predictability attained will allow ALD AlF3 implementation in optical designs to modify the polarization states induced by uncoated mirror properties.

(10) Our ALD AlF$_3$ on Si films exhibit minimal UV reflectance sensitivity to the MDL 'glove; box storage conditions of ∼40 °C and 1% relative humidity for 2 months, as compared to samples measured immediately. With continued development, ALD AlF$_3$ can be a viable coating material candidate for many optical systems, and not limited to smooth mirror surfaces and conformal diffraction grating coatings which have motivated our initiation of this project.

The long term objective is to development of ultra-thin (∼few nm) layers of metal fluoride films. Future results should include further analysis of film structures (crystalline vs. amorphous) via measurements such as X-ray Diffraction (XRD). Surface roughness vs. film deposition temperature derived from AFM. Film surface structure and composition from X-ray Photoelectron Spectroscopy (XPS), Time of Flight Secondary Ion Mass Spectroscopy (TOF-SIMS) and/or TOF Electron Recoil Detection Analysis (TOF-ERDA).

Chapter 6

The Solar Corona

The corona is the outermost layer of the solar atmosphere. Not all stars are expected to have coronae. Before a deep discussion into what the solar corona is and its properties, it is important to understand why a star would be expected to have a corona or not. Discussion of stellar and solar structure is imperative.

6.1   Stellar and Solar Structure

Figure 6.1 is the famous Hertzsprung-Russell diagram that shows the large variation of star types. It was noticed that the apparent visible light colors of stars varied as a function of surface temperature [27]. The relation between the colors of stars and the atmospheric structure has profound implications on our understanding of the process that fuel stars. The energy generation process in the core of stars directly relates to their luminosities and spectral classifications. The spectral classifications were originated to define the absence or presence of certain features in the spectrum. In particular, the appearance of lines (absorption or emission) of an element can yield information on the effective temperature at the visible light 'surface' of a star. In general stellar surfaces are not in solid form (like the crust on Earth), but the word 'surface' for stars relates to the region where the change in opacity allows photons to stream freely into interplanetary space. The properties of these 'surfaces' can vary among stars.

The stellar classifications range from O, B, A, F, G, K, and M (and L and so on),
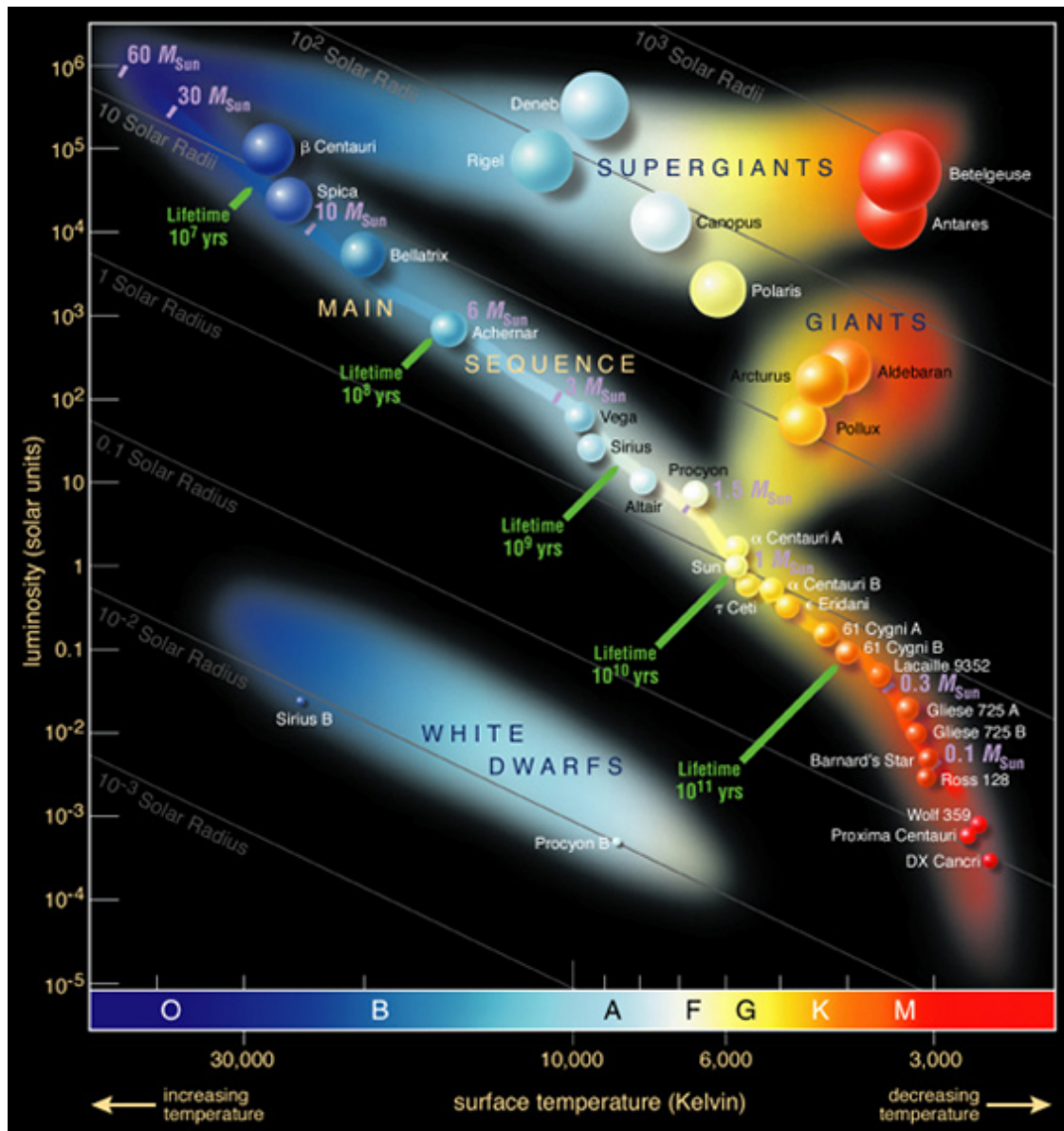
Figure 6.1: Hertzsprung-Russell (H-R) diagram depicting the relationship between a star's surface temperature (spectral class) and their luminosity (absolute magnitude). Image credit: European Southern Observatory (ESO). Source: https://commons.wikimedia.org/wiki/File: Hertzsprung-Russel_StarData.png under the Creative Commons Attribution 4.0 International License (https://creativecommons.org/licenses/by/4.0/deed.en)

which vary in surface temperature from over 30,000 K to below 3,000 K. The most massive stars are the O types and the least massive the M types. In general, the more massive a star is, the more efficiently it burns through its fuel (via gravitational contraction), the hotter

its photosphere and the bluer the spectrum. The emergent intensity is used as a proxy for the interior energy generation rate and is encapsulated in the mass-luminosity relation L $\propto$ M$^{3.5}$.

The main diagonal strip from high luminosity and hot surface temperature to low luminosity and cool surface temperature indicate the Main Sequence. The Main Sequence is when stars are primarily fusing hydrogen into helium in their cores. The majority of stars in the universe are currently 'on the Main Sequence' and will spend the majority of their 'lives' on the Main Sequence. These stars eventually evolve off the Main Sequence upon the commencement of fusing heavy elements in their cores. These are the Giants and Supergiants which reside in the higher luminosity sections per spectral type in the H-R diagram. Stars with masses less than 1.4M$_\odot$ will eventually go nova, expel their outer atmospheres and leave their cores radiating in space, supported under electron degeneracy pressure. These are the White Dwarfs on the H-R diagram.

The star of interest of this dissertation is the G2V star closest to Earth, the Sun. Thus, the discussion will transition from the array of star types and evolutionary possibilities to focus on the specifics of the Sun, its energy generation process and its atmosphere. The letter G indicates the effective temperature range, the Arabic number 2 classifies the pressure and the Roman numeral V is the luminosity class (dwarf) [27]. Stars generate energy via gravitational contraction. The pressure from the mass at higher layers in the star compact the core and increase the density and temperature to high enough temperatures that nuclear fusion can occur (T $\geq 10^7$ K). In stars like the sun, the conversion of hydrogen to helium is primarily through the proton-proton chain (p-p chain). While for more massive stars, there is enough force, and thus higher temperatures, to fuse hydrogen to helium via the more energetic pathway of the carbon-nitrogen-oxygen (CNO) cycle. This difference in the energy generation process has profound effects on the stellar atmosphere [69].

There are three main energy transport mechanisms conduction, convection and radiation. Conduction is the transport of energy by individual interaction of the atoms, molecules

and or ions with their neighbors. Conduction is normally an efficient energy transport mechanism for solids. Convection is the transport of energy by moving material. Radiation is the transport of energy via light. Stars transport the nuclear energy in the core out to the stellar surface using either convection, radiation or a combination of the two.

Figure 6.2 shows that in general, stars with mass greater than $\sim$1.5M$_\odot$ have convective lower interiors and radiative outer interiors. Because these stars do not have convective motions in the outer interior and X-ray flux has not been measured (aside from shocks in the hot stellar wind plasma) like the Sun, they are not expected to have temperature inversions (temperature increases as a function of height in the atmosphere) in their atmospheres. Stars with masses near the Sun ($\sim$0.5M$_\odot$ $\leq$ M $\leq$ $\sim$1.5M$_\odot$) have radiative inner interiors and convective outer interiors. Thus, these stars have confirmed temperature inversions in their atmospheres and hence coronae. Stars with mass less than $\sim$0.5M$_\odot$ have fully convective interiors, strong magnetic fields, known temperature inversions in their atmosphere and coronae.

I will give a brief summary of the solar structure here and full details are in Hansen and Kawaler 1994 [69]. One of the main effects that dictate whether radiation or convection transports the energy depends on the local opacity, chemical composition and temperature gradient in comparison to the adiabatic gradient. Basically, radiation dominates the energy transport outward until the recombination of heavy elements causes an increase in opacity (in addition to the electron scattering opacity). Thus, radiation is not as effective to transport the energy outward. Convection takes over and plasma is moved in large cells. These manifest in granules on the Sun Figure 6.3. This continues until the opacity changes such that the mean free path for visible light photons is on the order of 1 astronomical unit or larger. This region is the photosphere, which is dominated by the $^{-}$H opacity. $^{-}$H has an ionization potential of just 0.75 eV, and thus once it is formed it is destroyed (extra electron liberated) by any photon with energy greater than 0.75 ev ($\sim$1,653 nm).

A satellite image of the solar photosphere is in Figure 6.4. The appearance of a sharp

Heat Transfer of Stars
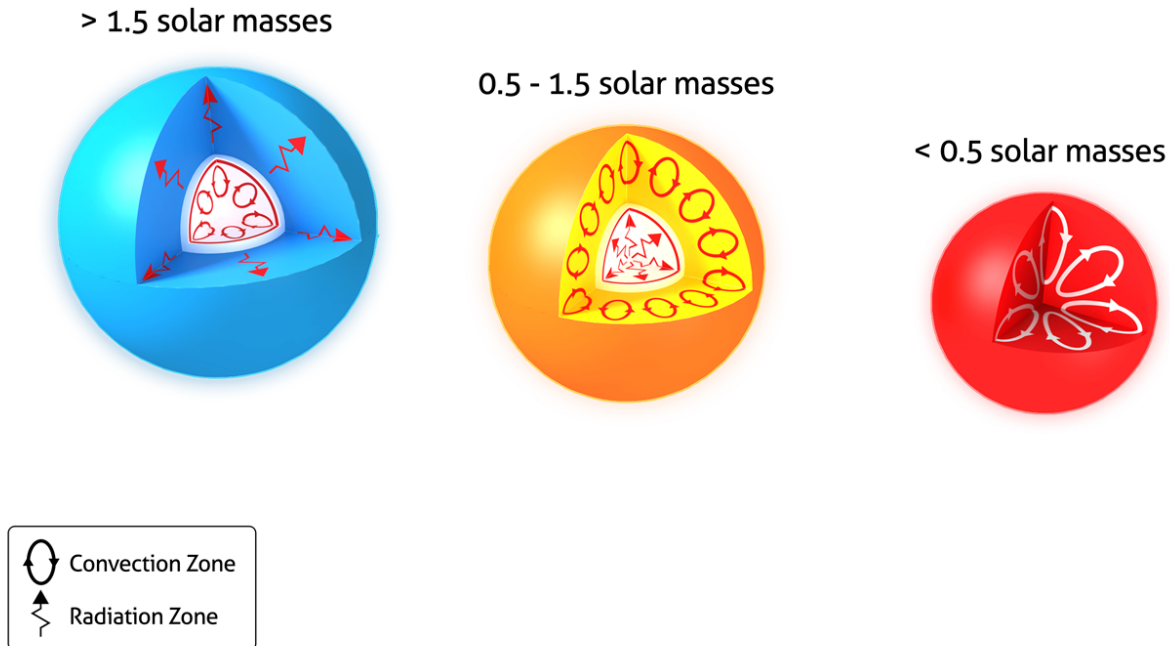
Figure 6.2: Stars with masses less than roughly $0.5M_\odot$ have fully convective interiors. Stars with $0.5M_\odot \leq M \leq 1.5M_\odot$ have a radiative inner portion and a convective outer portion. The most massive stars ($M > 1.5M_\odot$) have a convective inner portion and a radiative outer portion. The dynamics of the energy transport inside of stars have direct and profound implications on the atmospheric structure. Source: https://commons.wikimedia.org/wiki/File: Heat_Transfer_in_Stars.png under the Creative Commons Attribution-Share Alike 3.0 Unported Liscence (https://creativecommons.org/licenses/by-sa/3.0/deed.en)

disk is the consequence of the gradient in the opacity (sudden decrease). At this spatial resolution, the granule cells are hard to observe. What is not too difficult to detect is the dark spot on the solar disk. This feature is called a sunspot and are locations of strong magnetic field that inhibits the effectiveness of convection. While the photosphere has an average temperature near 5,700 K, sunspots can be as cool or cooler than 4,000 K. The lower energy transport rate leads to a lower intensity with respect to the rest of the photosphere. There is strong evidence that sunspots are generated by the convective fluid motions near
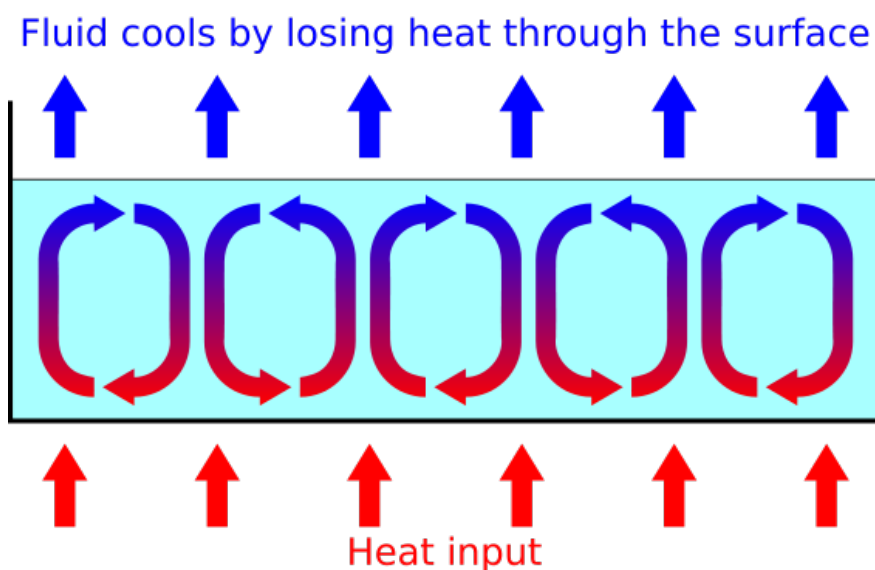
Figure 6.3: Convection transports energy by fluid motions. In gravitationally stratified convection, a hot parcel of material flows upwards due to buoyancy forces (adiabatic process), expands as it rises (pressure equilibrium), losses heat at the 'surface' (generally taken as a scale height), cools, and migrates downward, to be heated and return to rise. Source: https://commons.wikimedia.org/wiki/File:ConvectionCells.svg under the Creative Commons Attribution-Share Alike 3.0 Unported Liscence (https://creativecommons.org/licenses/by-sa/3.0/deed.en).

the surface. I will later discuss that the sunspots and the hottest regions of the solar corona called active regions are the same phenomena. Thus, there is a link between near surface stellar convection, starspots (active regions) and stellar coronae.

The emergent intensity of the solar spectrum originates from different layers of the solar atmosphere. There is not necessarily a one-to-one connection between the emergence of a photon from a specific height in the atmosphere to a portion of the electromagnetic spectrum. The solar atmosphere is highly dynamic, with material constantly moving to higher and lower layers, moving transversely (at nearly a constant altitude), and of varying temperatures. Thus, one cannot simplify the atmosphere to be solely isothermal concentric shells of various radii. Figure 6.5 demonstrates what regions of the atmosphere contribute the most to emission at portions of the electromagnetic spectrum. The processes that contribute to the opacity vary depending on the elemental composition, pressure, density, plasma tem-
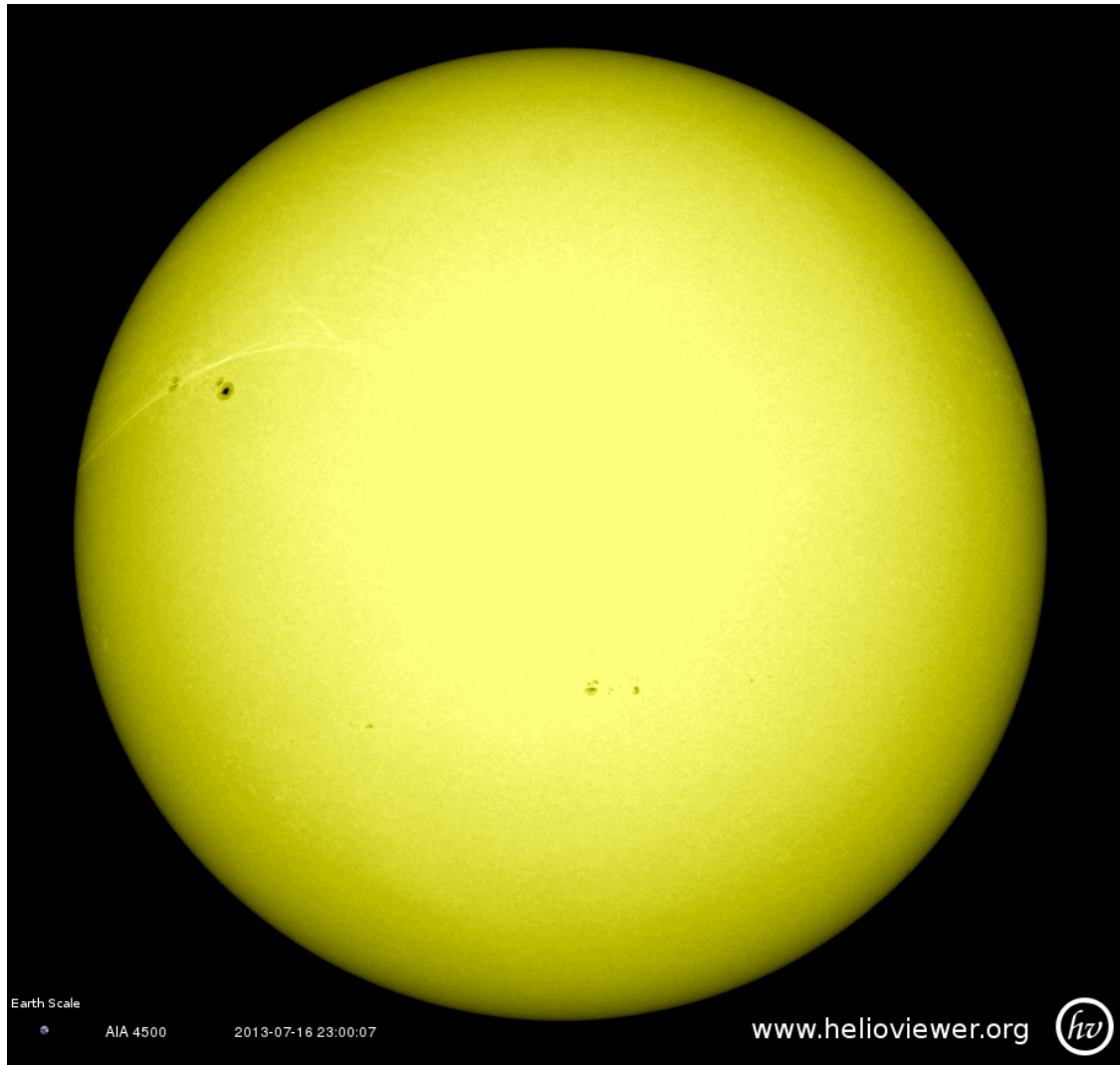
Figure 6.4: Visible light satellite image of the solar photosphere from the Solar Dynamics Observatory (SDO) and Atmospheric Imaging Assembly (AIA).

perature, plasma velocity, etc. along the line of sight. The differences in the dominant contributors to continuum and line opacity give the Sun its emergent intensity.

Because of the solar surface temperature is near 5,700 K, the dominance of the $^-$H opacity, change in density, lead to a blackbody (Planck Function) like spectrum modified by the gas at the layers directly above the 'surface', but beneath most of the chromosphere. The chromosphere has a temperature rise into the 10^4 - 10^5 K range. The hydrogen, aluminum, silicon, magnesium and carbon contribute substantially to the opacity [59]. A large portion
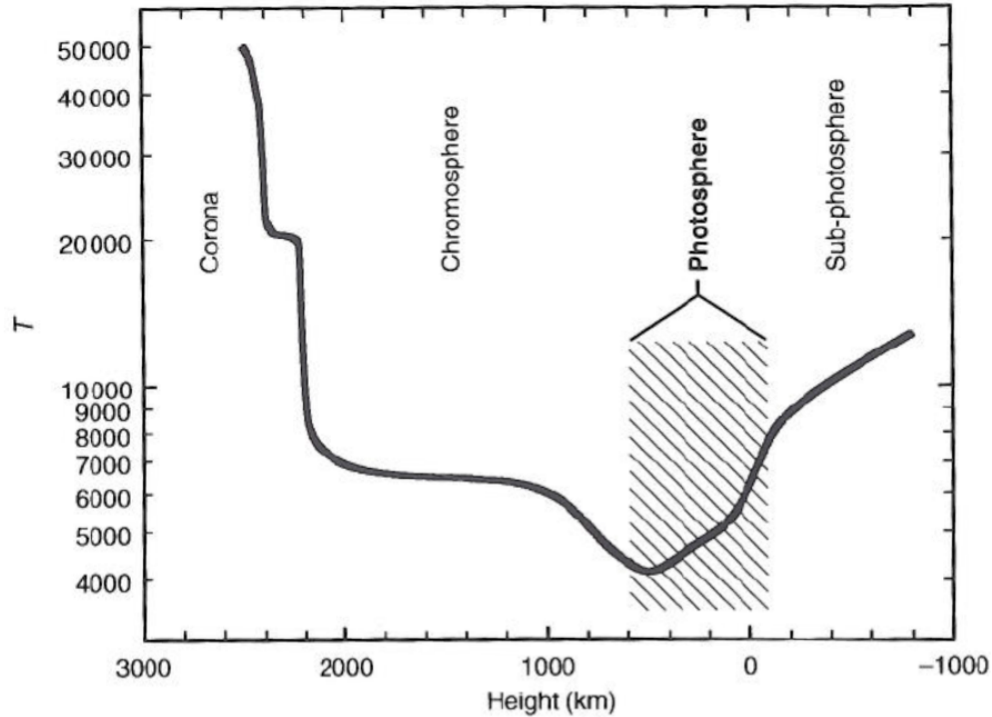
Figure 6.5: 1D approximation of the Solar atmospheric temperature profile. The photosphere has temperatures near $\sim$ 6,000 K down to the minimum 4,000 K. The chromosphere temperature increases up to the 10^5 K. The temperature of the corona is well in excess of 10^5 K.

of the chromospheric emission is in the UV. The transition region is where the average temperature rises to 10^6 K over roughly 200 km. The outermost layer of the solar atmosphere at over 10^6 K, called the corona, has relatively minimal opacity to radiation in the visible, UV and X-ray wavelengths, due to its extremely low average density (in contrast to the lower layers). The high temperatures result in high ionization states of heavy elements (elements other than H and He) and this ion line emission and free-free emission in the EUV and X-rays.

6.2   Coronal Details

In Section 6.1 the fact that stars with masses between roughly 0.5 - 1.5 M$_\odot$ have the energy transport of the outermost interior layer dominated by convection was discussed.

These convective fluid motions contain large amounts of energy and generate near surface magnetic fields which appear to be the critical conduit for transferring energy to the outer layers of the atmosphere. Thus, it seems that near surface convection $\Rightarrow$ surface magnetic fields $\Rightarrow$ energy propagation to the higher less dense atmosphere $\Rightarrow$ hot (T $\geq$ 1 MK) coronae. This brings us to the solar corona.

The solar corona is the interface between the solar surface (photosphere) and lower atmosphere (chromosphere), and the solar wind (interplanetary space), starting at roughly 2,000 km above the solar photosphere and extending to a few solar radii [6] (see Figure 6.7). The conditions in the corona are drastically different than the environment in the photosphere. The temperature in the corona reaches above 10^6 K in contrast to a photosphere temperature around 5,700 K. Furthermore, the density varies from as low as $\sim 10^8$ particles per cm^3 (e.g., in coronal holes) to as high as 10^{11} cm^{-3} (e.g., in flaring loops), as compared to a photospheric average density of $\sim 10^{17}$ cm^{-3}. Additionally, the plasma beta (see Equation 6.1), the ratio of gas pressure to magnetic pressure, which dictates what force dominates the dynamics, transitions from high (gas force dominated) in the photosphere, to low (magnetic force dominated) in the corona. This demonstrates the drastic changes in atmospheric conditions encountered in the corona even when eruptive transient processes are not considered.

The high temperature, low density, and dynamical conditions result in highly ionized plasma, emitting primarily UV and X-rays that is mostly optically thin to soft X-rays (besides specific scattering events) and confined by magnetic fields. The soft X-ray emission includes both spectral lines (bound-bound emission) from the various ion species in the corona, and continuum emission including free-free, electron-ion bremsstrahlung and free-bound, radiative recombination emission. The specific spectral emissions depend uniquely on the coronal conditions. Thus, soft X-rays present a rich diagnostic data set, because the solar coronal soft X-ray flux yields insight on plasma densities, temperatures, chemical abundances, magnetic field structure and velocity flows. Spectrally, temporally and spatially

resolved measurements are necessary to answer fundamental questions such as:

- How do solar active region physical parameters evolve over time as inferred from soft X-rays?

    - Temperature distribution of emitting plasma (differential emission measure)

    - chemical abundance

    - magnetic field morphology

- What is the solar soft X-ray spectral energy distribution and how does it vary over a solar cycle?

- What is the solar flare soft X-ray energy distribution and how does it vary with flare size?

- What are the primary heating mechanisms contributing to the observed soft X-ray flux?

With this information, this dissertation will expand upon the details of the solar coronal magnetic field, coronal heating theories, elemental abundance variations, radiative diagnostics, quiescence, active regions and flares.

6.2.1 Magnetic Structure

When viewing the Sun during a solar eclipse such as the most recent total solar eclipse viewable by a large potion of the United States on 2017 August 21, it is clear that there is a dimmer visible light aspect of the Sun (see Figure 6.6). Also, realizable upon closer inspection and experience with bar magnets, is the bar-bell like pattern to the visible light emission when the Sun is in a state similar to the eclipse in Figure 6.6. The intensity pattern can be much more complex than this, but for simplicity, we will commence our explanation from this perspective of the Sun.

Figure 6.6: Solar eclipse by the Moon. Image credit [58].The visible light from the solar corona, specifically the so-called K corona, which is scattered photospheric light from free electrons in the corona. The magnetic nature of the corona is clearly visible.

The Sun is magnetically structured down to the smallest currently observable size scales [119, 134]. The coronal visible light emission patterns observed during total solar eclipse are dictated by the current solar magnetic field configuration. The larger dipolar magnetic field is theorized to be generated deep in the interior of the Sun. This large scale (many solar radii, $R_\odot$) structure does not appear to reconnect on the Sun. These field lines are commonly referred to as 'open'. In general, plasma with enough kinetic energy to overcome the gravitational potential of the Sun propagating in a radial direction from regions where the open field lines originate leave the Sun and constitute the 'fast' solar wind. These regions are
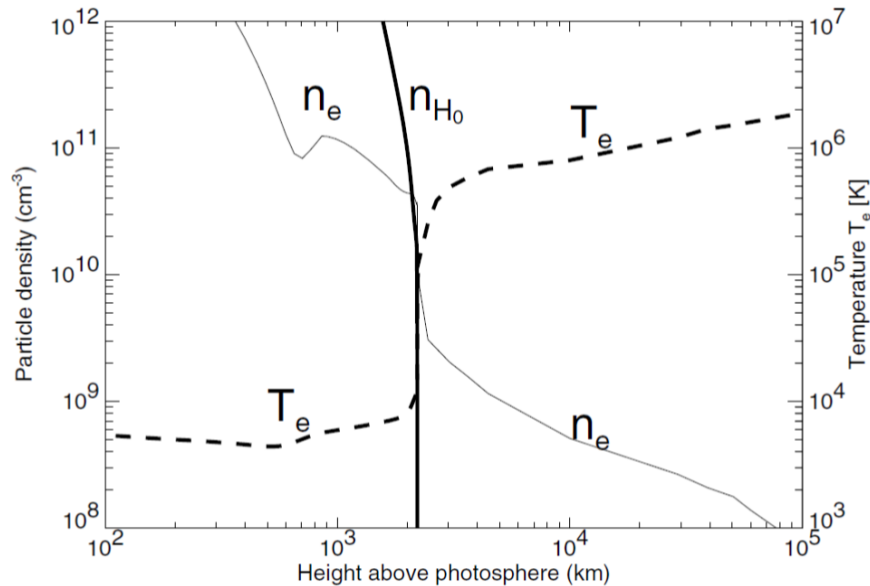
Figure 6.7: Approximated electron density and temperature as a function of height in the solar atmosphere. Figure adopted from [6].

more concentrated near the poles of the solar rotational axis. The regions where there appear to be connectivity (using radiation as a proxy for the magnetic field orientation) between magnetic field lines leaving the solar surface and returning (generally near the equatorial regions) to the solar surface are regarded as 'closed'. This is an important clarification for this dissertation. Active regions are locations of very strong concentrations of magnetic field and are deemed closed field phenomena.

The magnetic field's role in the physical processes that occur in the solar atmosphere is dependent upon the relative strength of the magnetic forces to any other competing forces. Equation 6.1 is one common metric, $\beta(\vec{B}, n_e, T_e, \xi)$, the ratio of gas pressure to magnetic pressure in cgs units. n_e is the electron density, T_e is the electron temperature, ξ is the ionization fraction, k_B is the Boltzmann Constant and $\|\vec{B}\|^2$ is the magnitude squared of the vector magnetic field. In general, one can use the plasma beta as a guide to uncover how

important magnetic fields are in the dynamics at particular locations in the solar atmosphere.

$$\beta(\vec{B}, n_e, T_e, \xi) = \frac{P_{gas}(n_e, T_e, \xi)}{P_{magnetic}(\vec{B})}$$

$$\approx \left[2\xi n_e k_B T_e\right] \left[\frac{\|\vec{B}\|^2}{8\pi}\right]^{-1}$$

(6.1)
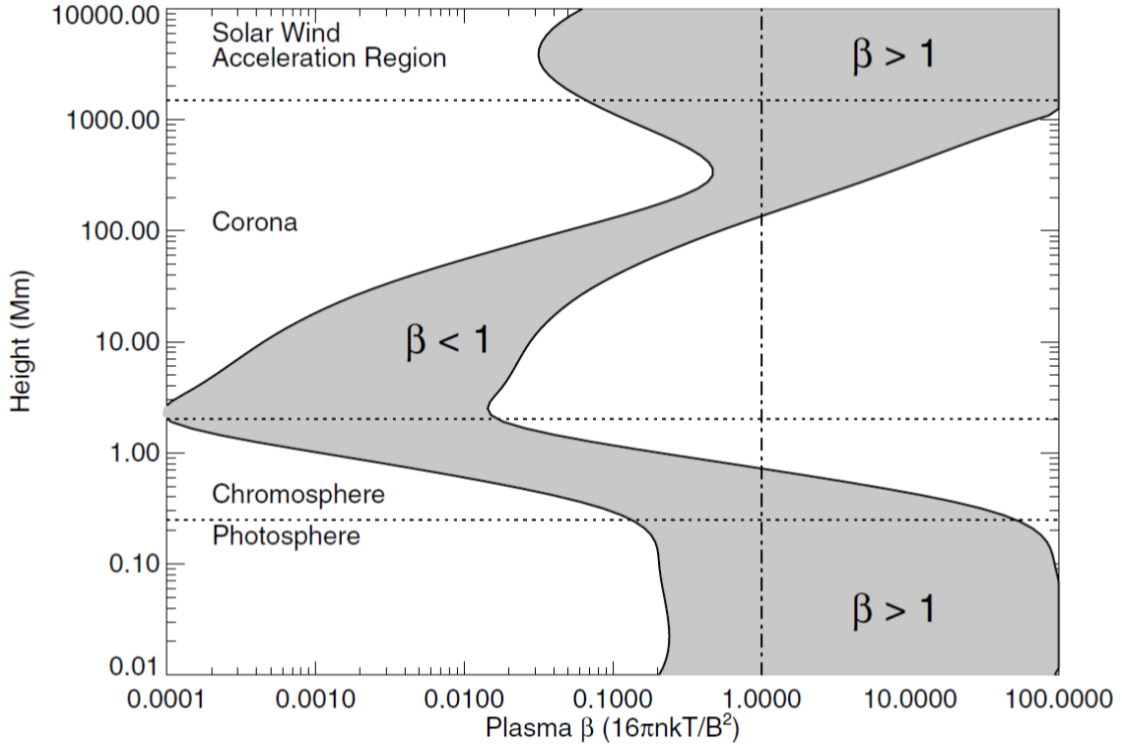
Figure 6.8: Plasma beta ($\beta = \frac{P_{gas}}{P_{magnetic}}$) as a function of height in the solar atmosphere. Image credit [6, 52]. The plasma beta is large in the photosphere (gas dominates the dynamics), smaller in the corona (magnetic field dominates dynamics) and large again in in the solar wind.

Figure 6.8 is the quintessential description of mapping a particular magnetic flux element plasma beta from the photosphere to the corona. In the photosphere where plasma densities are near $\sim 10^{17}$ cm^{-3}, β is much larger than unity and the gas force dominates. Magnetic fields (excluding Sun spots) are passively adverted (moved around) by the fluid flows. In the corona, where the densities can be as low as $\sim 10^9$ cm^{-3}, the plasma β is much less than unity, and the plasma (ionized gas) is confined by the Lorentz Force to follow the

field lines ($\overrightarrow{F} = q\overrightarrow{E} + q\left[\overrightarrow{v} \times \overrightarrow{B}\right]$), (when the magnetic field dominates over the large scales over the electric field which dominates the short range interactions). When this condition is satisfied, the plasma is said to be 'frozen' into the magnetic field lines. Thus, the plasma is confined to the field lines as it cools via radiation and conduction (but mostly along the field lines). This frozen in condition is why it is feasible to use the EUV and X-ray radiation as proxies for the magnetic field orientation.
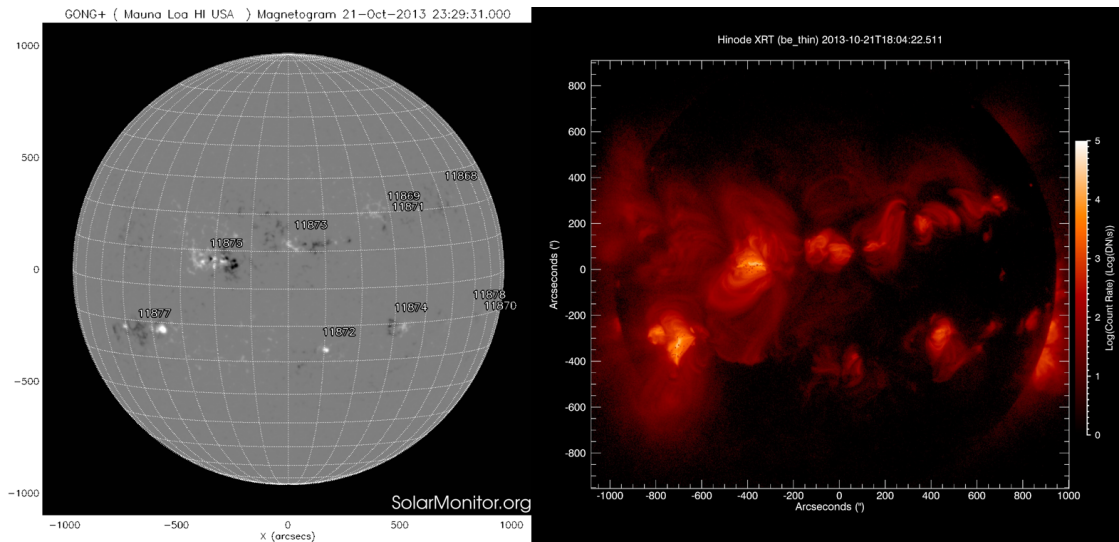
Figure 6.9: Left panel: GONG line-of-sight magnetogram showing the locations of sunspots on 2013 October 21. Right panel: Hinode XRT observations displaying active regions on 2013 October 21. It is apparent that the sunspots and active regions are co-spatial and originate from the same phenomena, magnetic fields.

Discussion on the coronal heating theories are in Section 6.2.2, for now we will progress with the understating that the corona emits mostly EUV and X-rays due to the plasma being hotter than 500,000 K. The closed field regions on the Sun harbor magnetic fields that are stronger than 500 G over large areas (bigger than Earth, diameter of Earth is ~1.3 $\times 10^7$ m). These magnetic fields can inhibit the effectiveness of energy flow via convection, radiate less, and appear dimmer then the rest of the solar disc in visible light. These are called sunspots. Sunspots line-of-sight magnetic field strength have been inferred routinely by various magnetogram measurements. An example from GONG is in Figure 6.9. The

sunspot magnetic fields protrude up into the corona where they radiate and appear bright in EUV and X-rays. In this context they are called active regions, primarily because of this increased high energy radiation and the fact that many eruptive phenomena like flares and Coronal Mass Ejections (CMEs) appear to originate from them. As evidence, it is clear from the 2013 October 21 observations in Figure 6.9 that the line-of-sight magnetic flux (sunspots) are co-spatial with the active regions in X-rays.
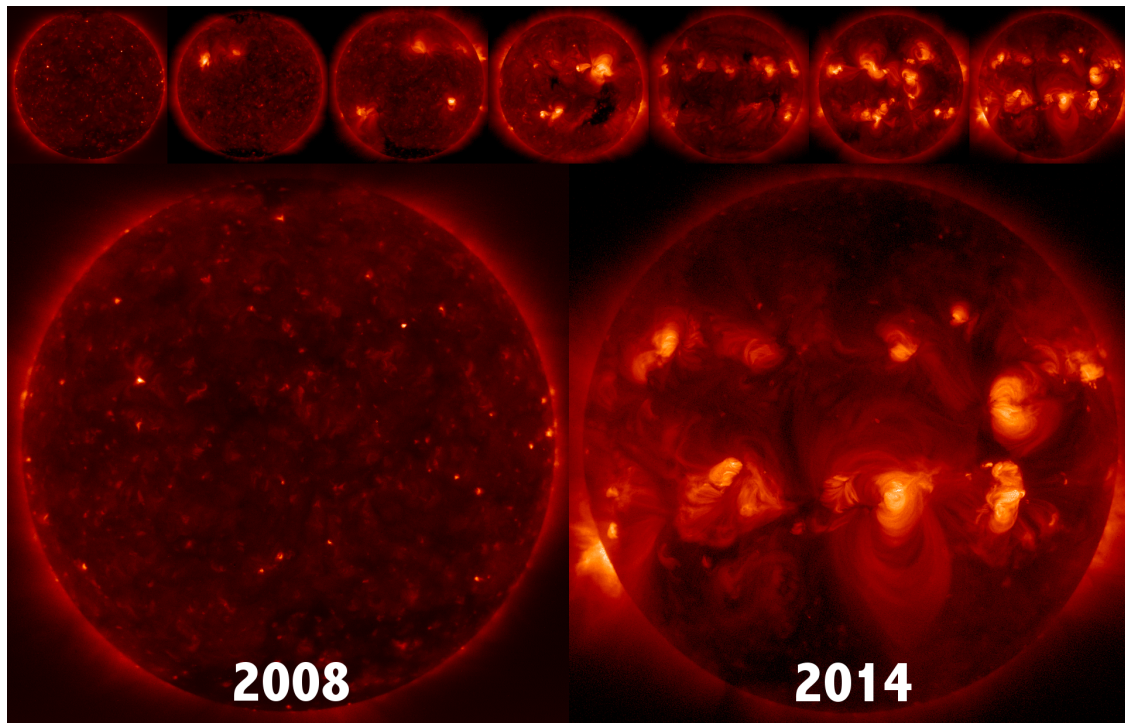
Figure 6.10: Hinode XRT images on 2008 and 2014. The change in the magnetic structure over the solar cycle is clear as the number of active regions (large scale magnetic structures) is much greater near the maximum of Solar Cycle 24. Image credit, the Hinode Team.

In addition to the magnetic spatial variability in the solar atmosphere, the quantity and pattern of large scale, closed field (active regions) magnetic field varies in time. In general there is a 22-year magnetic cycle where the polarity of the magnetic field reverses among the rotational axis poles. This reversal at the poles is between 9 and 13 years, but the duration of two reversals is close to 22 years. There is an 11-year activity cycle in the number of sunspots that appear on the solar disc. The peak in the number of sunspots

present for a given time is used to signify 'solar maximum', while the continual period where there are minimal sunspots present is called 'solar minimum'. Since sunspots and active regions originate from the same phenomenon, this cycle is also true for active regions and the solar X-ray flux.
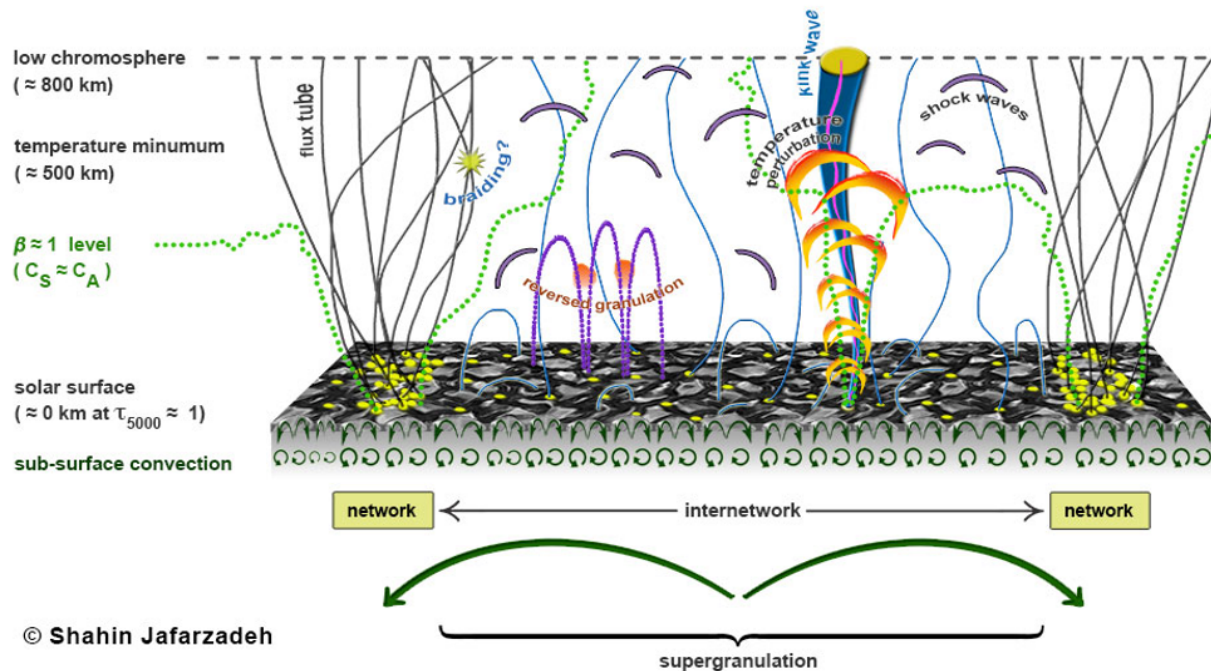
Figure 6.11: Figure by Shahin Jafarzadeh on the many phenomena (non-exhaustive) in the solar atmosphere. The solar atmosphere is extremely complex. Affects from granulation in the subsurface photosphere, in general propagate upward to the less dense chromosphere and corona. There are many phenomena actively being investigated like spicules, Alfvén waves, magnetic network, wave-mode conversion, shocks, Sun spots, active region dynamics, mass flow, magnetic reconnection, acceleration of the solar wind, etc., etc...

There are many solar phenomena that are continually present. This dissertation will only discuss two of the main atmospheric phenomena that generate X-ray flux changes, active regions and solar flares. Figure 6.11 depicts the many simultaneous processes occurring in the Sun. The solar atmosphere is very complex because many of these physical processes interact with one-another and cannot be decoupled and analyzed in pure isolation. This is encouraging, because it is reminder that even one of the more 'basic' stars has a wealth of phenomena to learn about and study.

6.2.2   Heating Theories

Why is the solar corona so hot? The current answer is that we do not *really* know at this time. It is most likely a combination of effects that contribute to the general coronal temperature profile. One of the current quests among solar physicists is to reduce the number of viable candidates, to narrow the possible prospects. The energy input into the corona needed to sustain quiet Sun temperatures (1 - 2 MK) is $\sim$3 x 10^5 ergs s^{-1} cm^{-2}. This must balance radiation (conduction to chromosphere also) losses and can be compared to measurements. The energy input needed to sustain active region temperatures (3 - 4 MK), is $\sim$1 x 10^7 ergs s^{-1} cm^{-2} and must be able to account for the temporal and spatial variability of the high energy photon emission observed. Any theory suggested, must pass these two initial tests.

Many theories have been proposed over the years, some include heating the corona by suprathermal particles (the tail of the Maxwellian) [142], spicules [162], shock dissipation of sound waves or magneto-hydrodynamic (MHD) waves, Landau damping of waves, plus others [58]. These have lacked significant observational backing and thus it seems that the current debate on coronal heating revolves around a couple of themes.

The two most prominent theories were originally proposed (or publicized effectively) by Hannes Alfvén and Eugene Parker. Both of these coronal heating theories revolve around kinetic energy generated by photospheric convective fluid motions that jostle kilogauss magnetic field lines rooted between granules (intergranular lanes) in the photosphere. The kinetic energy is converted to magnetic energy, which is either dissipated by reconnecting magnetic field lines that create small-scale, quickly occurring impulsive events [124], or by the interaction of waves on the magnetic field lines causing small-scale turbulence that leads to heating of the plasma [3]. Both processes are likely to be occurring, thus the determination of the relative contribution of each is critical in better comprehending the solar coronal heating question.

The timescale of the shuffling and entanglement of kilogauss magnetic flux tubes is vital in partitioning the Alfvén wave dissipation vs. impulsive heating contributions. If the footpoint motion timescale is fairly short, $\tau_{fp} < \frac{L}{V_A}$, where V_A is the local Alfvén velocity ($V_A = \frac{\|\vec{B}\|}{\sqrt{4\pi\rho}}$) and L is the loop length, then the disturbances will propagate fast enough to dominate the dynamics. The interaction of outward propagating Alfvén waves from the jostling of photospheric magnetic flux tubes and reflected (from the radial density gradient in the solar atmosphere) inward propagating Alfvén waves results in a leakage of energy to lower density plasma (the corona) [150] (see Figure 6.12). Turbulence is commonly invoke to cascade the energy to smaller size scales where it is eventually dissipated (possibly restively via currents). Only about 10% of the Alfvén wave energy is believed to reach the corona, but this appears to be enough to create 1 - 3 MK plasma [8], which can explain the quiet Sun and the majority of the active region plasma.

If the timescales of the footpoint motions are relatively long, $\tau_{fp} > \frac{L}{V_A}$, then the loops (or magnetic strands that compose the loops) can became entangled. These entangled field lines build stress and thus will 'reconnect' (rearrange themselves to a lower energy state). How this process exactly occurs is currently still unclear. But like the Alfvén wave dissipation model, the energy is transported to smaller scales and converted to heat (random particle motions). Accompanying the impulsive heating theory is possibly the flow of chromospheric plasma to the corona. The episodic heating theory of the solar corona envisions small-scale magnetic processes (called nanoflares) that dissipate magnetic energy that has been converted from the kinetic energy associated with photospheric convection [124]. Each bursty event is postulated to release small amounts of energy ($< 10^{24}$ ergs), that for low frequency events, near-instantaneously heats the local plasma to above 5 MK ($\log(T) \sim 6.7$). This plasma is theorized to quickly cool and thus spend the majority of time below 5 MK [87].

But, the ensemble of randomly occurring impulsive events could continuously generate coronal plasma at temperatures above 5 MK, with only dim emission - perhaps 3 orders of magnitude fainter than the cooler component (< 5 MK; see Figure 12.2.1). Thus, the
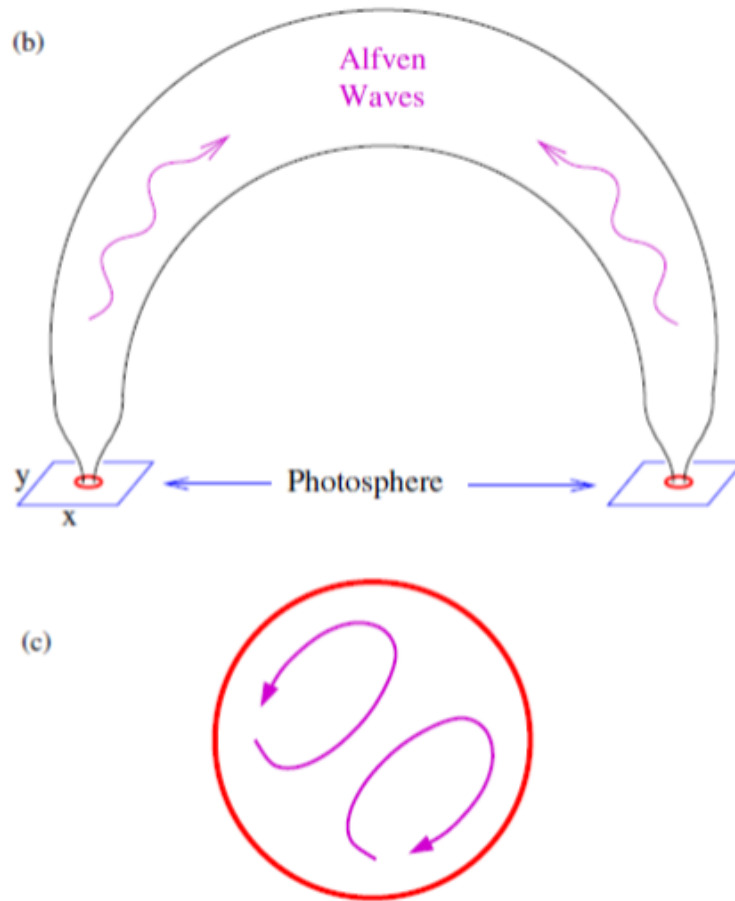
Figure 6.12: (b) Diagram of alfven wave propagation in magnetic loops from van Ballegooijen et al. 2014 [149]. (c) proposed velocity motions inside of magnetic flux elements.

direct detection of the predicted hot-dim plasma has been elusive with current solar soft X-ray instrumentation, which lack the necessary intensity sensitivity and extreme ultraviolet (EUV) instrumentation which can suffer from cooler plasma contributions in their respective passbands.

6.2.3   Elemental Abundance Variations

The chemical elemental abundances in the atmosphere of the Sun appear to vary as a function of height (photosphere vs. corona), a function of time (active region age), and a function of the phenomena (flares, CMEs, spicules, coronal holes, etc.). Thus, there has

been large interest in deducing the elemental abundance trends of the solar atmosphere. Because the outer layers of the solar interior are primarily convective, the interpretation is that the majority of the chemical elements created in the interior will be almost fully mixed and will eventually reach the photosphere. Thus, if one can accurately assess the photospheric abundance, one has a firm handle on the solar interior abundances, abundances of the initial composition of the solar system and an abundance estimate of the local stellar population formed roughly 4.5 billion years ago. The elemental abundance is critical for opacity calculations, which folds into energy transport processes and hence stellar evolution models.

The solar photospheric abundance has been an important topic and the estimated values have been highly dynamic over the past 30 years. Recent inclusion of new physics, improved atomic parameters, and the inclusion of magnetic fields [64, 10, 9, 63, 11, 4, 119, 110, 45, 46, 47], have advanced the understanding of the photospheric abundance further than current understanding of the solar coronal abundance. The first ionization potential (FIP) and hence probably the first ionization timescale, has been identified as a key parameter in the deviations between photospheric and coronal abundances. In general, it was postulated that elements with first ionization potentials less than 10 eV can be enhanced in the corona with respect to the photosphere. These have been called 'low' fip elements (low-fip). An important aspect in these studies are that comparisons are generally made with the ratio of a coronal measurement of a low-fip element to the coronal measurement of a high-fip element. This ratio is then compared to the photospheric ratio of similar low-fip and high-fip elements, but not necessarily the same element set, and definitely not the same ionization states. There are problems with this. First, the photospheric abundance estimates have been volatile and have varied substantially since the well referenced Feldman 1992 study. Second, it is not clear if the low-fip elements are enhanced, or are the high-fip elements depleted, or a combination of both. There has been evidence for both and a new modified set of abundances have been suggested [138]. There are no hydrogen nor helium lines to compare

to in the corona (because it is fully ionized), thus comparisons are commonly drawn between other high-fip elements like O, Ne, or Ar.

Again the temporal variation of the elemental abundances further complicates the issue, a few studies of EUV lines similar to [156] yield strong evidence of elemental abundance variations in ARs (see Figure 12.4). Within a few days an emerging AR can have an enrichment of low first ionization elements, such as Mg, Fe and Si, from photospheric abundance values ($A_{photospheric} = 1$), to the so called coronal abundance ($A_{coronal} \sim 4^*A_{photospheric}$) or even greater. There is a lack of literature of similar studies in the soft X-ray. If coronal heating processes like the impulsive nanoflare scenario are similar to their larger counterparts, then it is postulated that photospheric material would be driven up to the corona in active regions. This change could possibly be inferred from soft X-ray spectral measurements. Thus, there could be a connection between active region heating processes and the active region elemental composition.

6.2.4 Radiative Diagnostics

On average through out the Earth year, the Sun is 1.49 x 10^{11} meters away from Earth. That is a huge distance. Thus, for centuries humans have primarily studied the Sun and other astronomical objects, via the radiation they emit. The spectrum of radiation contains vital information on the physical conditions from which the photons were created. In particular for the study of the solar corona, detection and understanding of processes that generate X-rays is imperative. Even though X-rays account for less then 10^{-6} of the Sun's bolometric luminosity [58] (see, Figure 6.13) it provides a key diagnostic for the corona, particularly its variability, temperature distribution and elemental abundance. X-rays provide unambiguous inferences of plasma greater than 1 MK. Because the densities in the corona are so low, on average, the emergent radiation from the Sun propagates unimpeded to Earth. This is called the optically-thin approximation, when a gas opacity is extremely low to its own and surrounding radiation. Radiative analysis following this scenario has been deemed the

'coronal' approximation because of its applicability to the solar corona (and other stellar coronae).
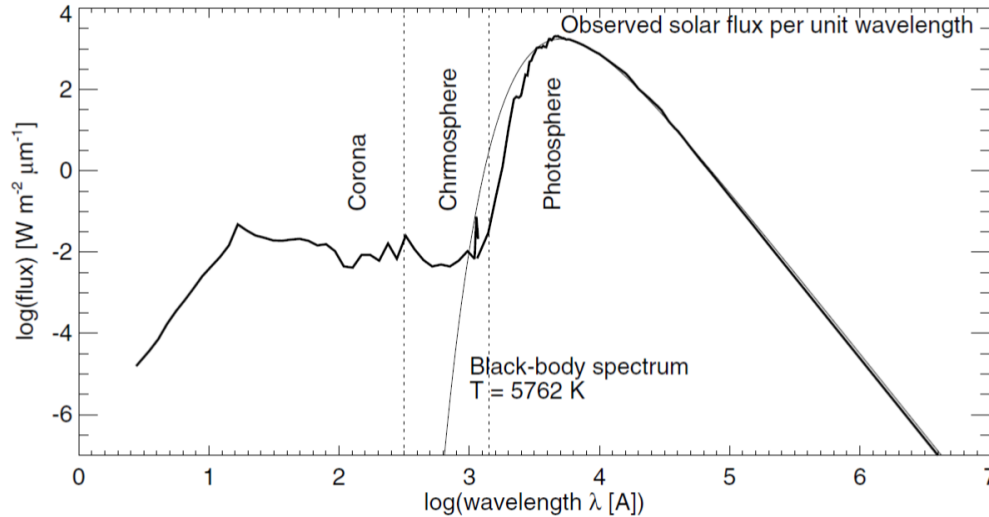
Figure 6.13: Composite spectral energy distribution (SED) from X-rays to infrared for the Sun. The majority of the visible light emission originates in the photosphere, the UV mostly created in the warmer chromosphere and X-rays (and EUV) are birthed, generally in the corona.

CHIANTI is an atomic database that applies the optically-thin approximation to synthesize spectra from $\sim$ 124 nm - 0.1 nm from plasma with temperatures ranging from 10^5 - 10^8 K [36, 161]. CHIANTI has been vital in the expediency of generating synthetic spectra in comparison to spectral observations. In this dissertation, the CHANTI atomic database is the only spectral synthesis employed. Following the methodology of CHIANTI derivation of a few critical expressions and few terms that will be utilized throughout the remainder of this dissertation. An important concept for the optically-thin plasma is that the intensity observed is dependent upon two-body interactions. These interactions primarily occur between free electrons and ions or protons. The reader is referred to Chapter 2 for a review of the full array of relevant processes. One of the most likely processes is electrons colliding (or interacting) with the ions and changing the ions ionizations state, and/or exciting the ion to a higher energy state. Assuming that the velocity distribution of these electrons arises from

thermal processes, ionization states as a function of plasma temperature can be calculated. This combined with the assumption that the ionization rate, balances the recombination rate is called collisional ionization equilibrium (CIE). Figure 6.14 displays the CHIANTI CIE calculations of the Fe ionization states as a function of temperature. Radiation detected from different ionization states for Fe (for example) can be used to probe the plasma temperatures.
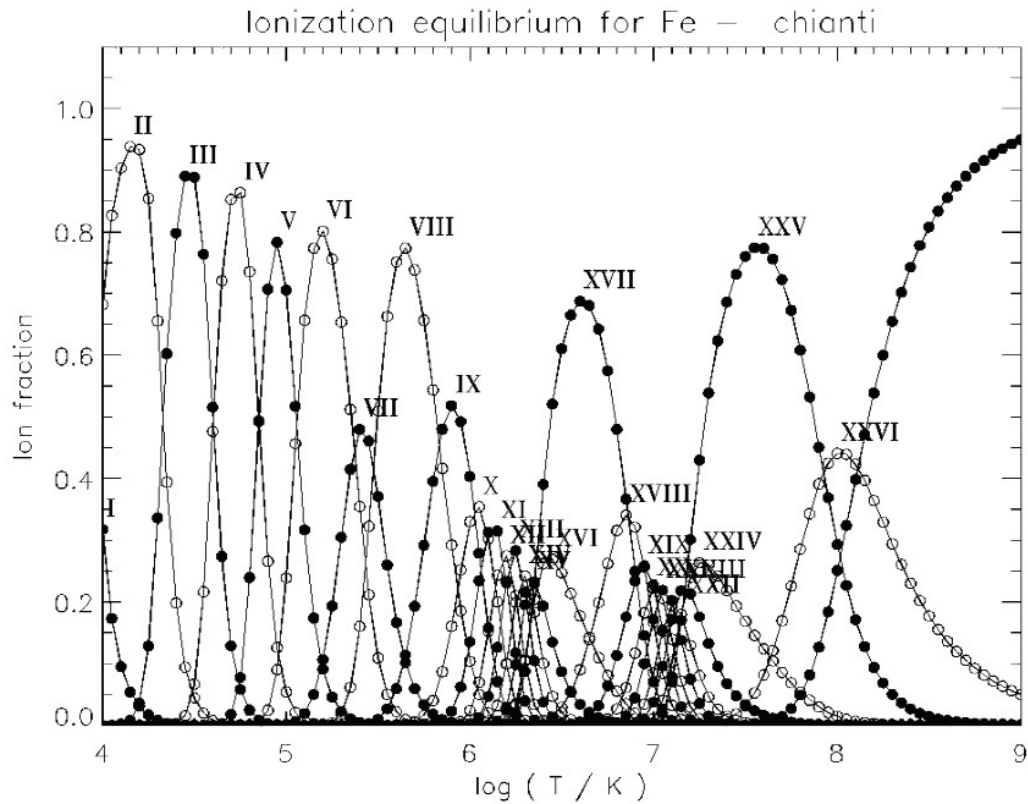
Figure 6.14: CHIANTI Atomic Database calculation of Fe ionization states as a function of temperature assuming collisional ionization equilibrium (CIE). The radiation from different ionization states can be used to probe the temperatures present in a plasma.

This excited ion discussed earlier can then de-excite radiatively, emitting a photon. This bound-bound transition results in a photon of a discrete wavelength (ionization, bound-bound transition). The free electron and ion/proton can also interact, the free electron can lose energy radiatively, and have a photon of no greater energy than the change of the

electrons kinetic energy (free-free transition). Finally a free electron can be captured by an ion, changing the ionization state of that ion and eventually de-exciting via photon emission (recombination). All of these process involve the electron and proton/ion and thus the emergent intensity from the optically-thin gas is proportional to the number density squared for fully ionized plasma. So in the corona, in general, the more light that is observed from a given region, the more material is present.

Because the product of the number density appears so often in optically-thin radiative calculations, a new quantity will be defined called the emission measure, EM. The column isothermal emission measure, $EM_C(T=T_0)$ or CEM, is the amount of plasma along the line-of-sight, ds, that is radiating (see Equation 6.2). The plasma is assumed to be all at one temperature, $T=T_0$, a delta function in temperature. n_e is the electron number density and n_p is the proton number density. Instruments that conduct spatially resolved observations normally utilize the CEM interpretation.

$$EM_C(T = T_0) = \int_s n_e n_p ds \ [\text{cm}^{-5}] \tag{6.2}$$

Sometimes it is more suitable to integrate the plasma over a segment of the radiating volume, dV. Thus, the definition of the volume emission measure, $EM_V(T=T_0)$ or VEM, (see Equation 6.3). Instruments that integrate the emission across the entire Sun must impose VEM analysis unless supplementary information on the area of the emitting plasma in the measured spectral bandpass is provided.

$$EM_V(T = T_0) = \int_V n_e n_p dV \ [\text{cm}^{-3}] \tag{6.3}$$

The solar coronal is not isothermal. The emission measure definition can be expanded to include contributions from a range of temperatures. This is called the differential emission measure (DEM). The formulations in column units, $DEM_C(T)$, and volume units, $DEM_V(T)$,

are in Equation 6.4 and Equation 6.5 respectively.

$$DEM_C(T) = \frac{dEM_C(T)}{dT}$$
$$= \int_s n_e n_p \frac{ds}{dT} \ [\text{cm}^{-5} \ \text{K}^{-1}] \tag{6.4}$$

$$DEM_V(T) = \frac{dEM_V(T)}{dT}$$
$$= \int_V n_e n_p \frac{dV}{dT} \ [\text{cm}^{-3} \ \text{K}^{-1}] \tag{6.5}$$

The Sun is mostly composed of hydrogen, thus, $n_p \sim n_H$ and because the corona consists of highly ionized plasma, it is common to observe the $n_e n_H \sim n_e^2$ nomenclature. With the concept of emission measure in mind, the discussion can turn to analyzing the intensity from a region of plasma. Equation 6.6, calculates, $I(E_{ij}, \Omega)$, the amount of energy (or light) per area, per time, per angle in the sky (the definition of intensity or radiance in this dissertation) from a particular atomic transition from state i, to state j (or interaction). This can be converted to a flux or irradiance (per area, per time) by integrating over the angular distribution of the emission, $d\Omega$.

$$I(E_{ij}, \Omega) = \frac{\int_s E_{ij} n_j A_{ji} ds}{\int_\Omega d\Omega} \ [\text{erg} \ \text{cm}^{-2} \ \text{s}^{-1} \ \text{sr}^{-1}]$$
$$= \int_s A(X) G(T, E_{ij}, n_e) n_e n_p ds \tag{6.6}$$
$$= A(X) G(T, E_{ij}, n_e) EM_C$$

E_{ij} is the energy difference between state i and state j, where the energy in state j > state i and $E_{ij} = \frac{hc}{\lambda_{ij}}$. A_{ji} is the Einstein A coefficient. It is the probability that an atomic transition will occur and is in units of s^{-1}. The higher the frequency the more probable the transition. A(X) is the abundance of element X relative to hydrogen. $G(T, E_{ij}, n_e)$ is the line contribution function which includes the atomic physics of collisional line strengths, cross sections, etc and is defined in Equation 6.8. n_j is the number density of atoms with

electrons in the excited state j. The population levels, $N_j(X^{+m})$ for an ionization state, m, are defined in Equation 6.7.

$$N_j(X^{+m}) = \frac{n_j(X^{+m})}{n(X^{+m})} \frac{n(X^{+m})}{n(X)} \frac{n(X)}{n(H)} \frac{n(H)}{n_e} n_e \tag{6.7}$$

$$G(T, E_{ij}, n_e) = \frac{E_{ij}}{4\pi} \frac{A_{ji}}{n_e} \frac{n_j(X^{+m})}{n(X^{+m})} \frac{n(X^{+m})}{n(X)} \; [\text{erg cm}^3 \text{ s}^{-1} \text{ sr}^{-1}] \tag{6.8}$$

$n(X^{+m})$ is the number density of atoms of element, X, in ionization state, m. $n(X)$ is the number of atoms of element, X. $n(H)$ is the number density of hydrogen. Examples of DEMs for the quiet Sun (QS), active region (AR), coronal hole (CH) and a solar flare are in Figure 6.15. These DEMs are nominally supplied in the CHIANTI software and exemplify the temperature structure differences in certain solar features. The coronal hole has very little plasma at or above 1 MK. Coronal holes would be generally located by the solar poles during quiescence, and migrate during solar maximum. The quiet Sun has plasma between 1 - 2 MK and is dominated by smaller X-ray flux features (2008 time in Figure 6.10), such as X-ray bright points.

The active regions have plasma generally up to 3 - 4 MK and are the most temporally persistent bright solar X-ray source. Active regions are very distinctive on the solar disc, such as the 2014 time in Figure 6.10. Solar flares are the most transient phenomena discussed in this dissertation and can create the hottest plasma on the Sun, with temperatures well over 10 MK. The DEMs can alter shape, depending on the elemental abundances in the Sun. As scientist we are always trying to include the most physics when describing a phenomena. Abundances will be discussed more throughout this dissertation. I will elaborate a little more about the quiet Sun, active regions and flares in the following sections and describe them in depth in the analysis Chapters of this dissertation.
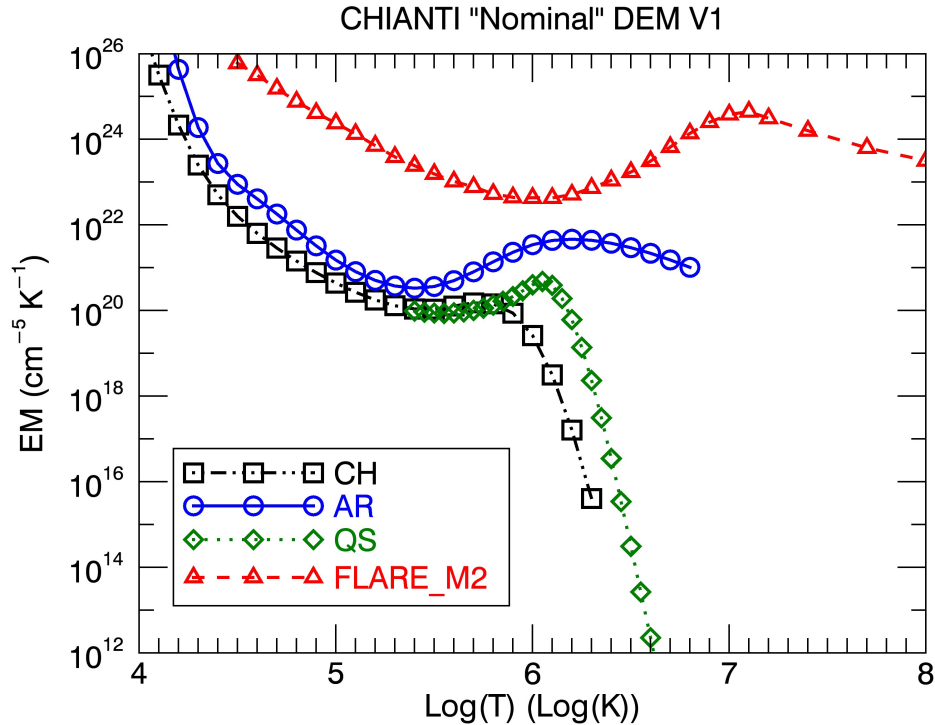
Figure 6.15: Differential Emission Measure (DEM) nominally stored in the CHIANTI Atomic Database. The coronal hole (black) is fairly void of plasma greater than 1 MK that is radiating, the quiet Sun (green) has the majority of the radiating plasma between 1 - 2 MK (except for the chromospheric contribution for T $\leq$ 0.5 MK). Active regions (blue) have contributions from hotter plasma (3 - 5 MK) and solar flares (red) manifest the highest temperature plasma (well over 10 MK).

6.2.5   Quiescence

The Sun without any large concentrations of line-of-sight magnetic field, large flares occurring, nor other eruptive events is generally called the quiet Sun. The Sun during quiescence is probably one of the most interesting and the least studied condition of the Sun. The name 'Quiet' Sun is really a misnomer, because even in the absence of large flares, active regions and more, the Sun still has many dynamic phenomena occurring. Even though the Sun has plasma up to and over 3 - 4 MK in active regions, why the quiescent Sun, which is void of active regions, is still 1 - 2 MK is baffling. For nanoflares to create this haze of hot

plasma lacking strong emission (unlike active regions) in X-rays means that the occurrence of nanoflares would really have to be ubiquitous. Understanding the 'dormant' state of the Sun is critical in understanding mass flow, energy flow and the role magnetic fields play over the majority of the solar area and over different time scales. These solar processes have important applications throughout the universe.

6.2.6   Active Regions

Active regions are strong concentrations of magnetic field emerging through the photospheric surface. The belief is that these magnetic fields are rooted relatively close to the photosphere and rise to the surface via buoyancy. The emergence of a strong magnetic field complex usually produces two dark sunspots in the photosphere. Active regions confine plasma in the corona, which either heats up or simply 'stays hot' for a time frame. Active regions generally emerge with the magnetic footpoints in close proximity to each other and gradually disperse after flux emergence. Active regions can persist for months and eventually fade out into the larger more diffuse solar magnetic structure. Active regions, hence the name, are where numerous explosive phenomena originate powered by magnetic energy that has built up. Solar flares, CMEs, and flux cancellation are features that make active regions unique in addition to their dominant soft X-ray emission.

Active region's inherent connection to the photosphere and subsurface, make it evident that any complete study of active regions cannot solely assess the coronal or chromospheric components in isolation. Understanding the fluid flows, plasma waves and particle content are vital in advancing our comprehension of active regions. The ability of active regions to suspend plasma without significant gravitational draining of the plasma to lower portions of the atmosphere is another mystery.

6.2.7   Flares

One of the most energetic phenomena in the solar system are solar flares. They can release large amounts of energy in less than a few minutes. Solar flares are eruptions driven by a magnetic instability in the atmosphere (corona and chromosphere). The rapid re-arrangement of these magnetic fields can convert up to 10^{33} ergs (for large flares) of initial energy stored in the corona into the acceleration of particles, radiation, waves and sometimes Coronal Mass Ejections (CMEs) [44].
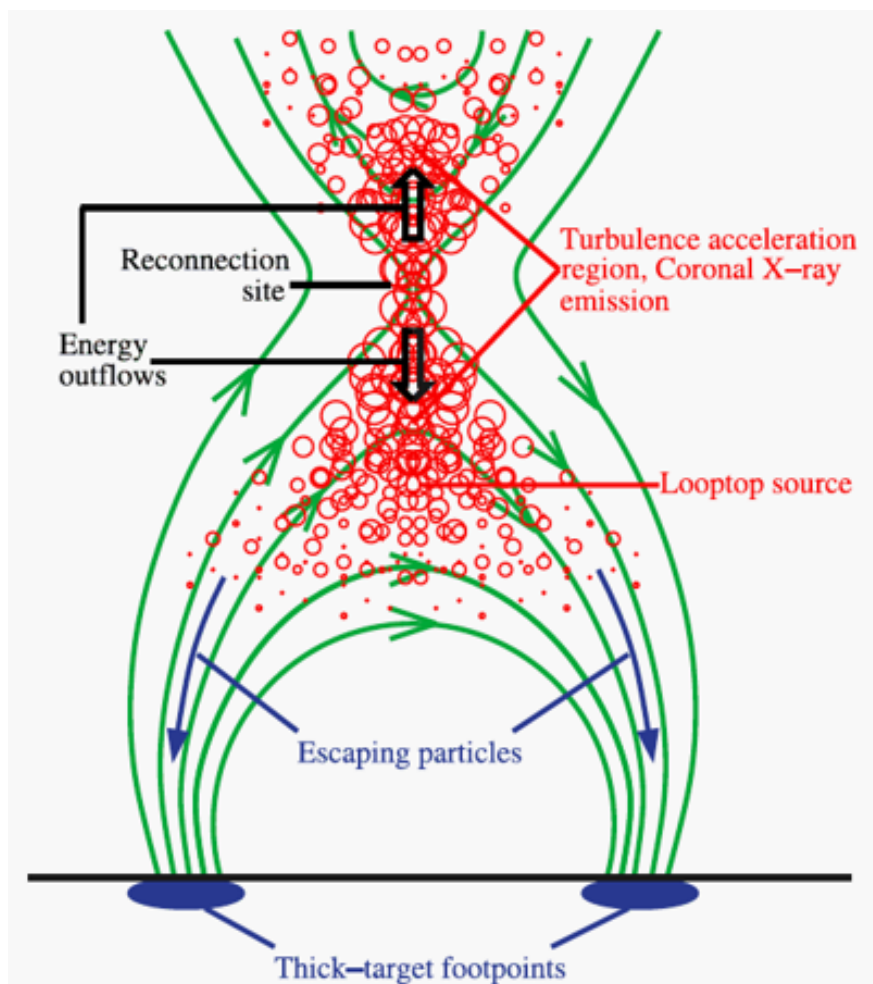
Figure 6.16: Diagram from Liu et al. 2008 [104] of possible reconnection set morphology for large solar flares. The green lines are the proposed magnetic field arrangement, red circles indicate possible turbulence, the blue disc would be the hard X-ray flare footpoint sources.

An example of the possible large solar flare eruptive process is depicted in Figure 6.16. Electrons are accelerated in the solar corona, possibly by a magnetic reconnection event. These non-thermally accelerated electrons propagate downward into the denser lower solar atmosphere (contain roughly $10^{31} - 10^{32}$ ergs), where they heat the plasma through Coulomb collisions (contain roughly $10^{30} - 10^{31}$ ergs) and produce bremsstrahlung hard X-rays (Impulsive Phase). The heated plasma evaporates from the chromosphere into the corona. This hotter plasma cools by conduction along the magnetic field lines to the lower temperature atmosphere and by radiation, primarily in soft X-rays and UV emissions (Gradual Phase). Precipitating particles in the lower atmosphere (chromosphere and maybe photosphere) can sometimes cause visible light enhancements (visible light dominates the total solar irradiance), which is how the first 'recorded' (by Eurocentric history) solar flare was observed by R. C. Carrington and R. Hodgson independently on 1859 September 1 ([26, 15]).

Chapter 7

The Miniature X-ray Solar Spectrometer CubeSats

7.1   Mission Overview

The objective of the *Miniature X-ray Solar Spectrometer* (MinXSS) CubeSats is to explore the highly variable solar soft X-ray (SXR) spectral distribution and reveal its impact on Earth's ionosphere and thermosphere. The MinXSS X-ray instruments consist of a spectrometer, called X123, with a nominal 0.15 keV full-width-half-maximum (FWHM) resolution at 5.9 keV and a broadband X-ray photometer, called XP. Both instruments are designed to obtain measurements from 0.5 - 30 keV at a nominal time cadence of 10 seconds. Solar soft X-rays are strongly absorbed by Earth's atmosphere in the E-region at an altitude of about ∼80 - 150 km. This energy input can strongly affect the energetics and dynamics of the ionosphere and thermosphere. These solar measurements can also be used to directly investigate the properties of the solar corona, which is dominated by magnetic field dynamics, resulting in tenuous, high temperature plasma of over 1 MK. The primary heating source or the relative contributions of the many components to coronal heating are still in question. While MinXSS data alone cannot address the root of this question, the spectrally resolved measurements from MinXSS, combined with other solar observations, can yield critical information on this and other compelling questions in solar physics. MinXSS is not the first spectrometer to conduct these type of measurements, but it has unique new capabilities that can be advantageous over previous full Sun flux (irradiance) measurements from spatially integrating spectrometers.

Figure 7.1 is a non-exhaustive list of EUV and X-ray space instruments that have conducted spectral measurements between 0.06 and 120 keV (updated from [107]). The majority of these measurements were of either high spectral resolution ($\Delta E > 0.1$ keV FWHM) over a narrow bandpass (e.g. Bragg crystal spectrometers) or low/no spectral resolution over a fairly large bandpass (e.g. integrating photometers). Currently, there are no solar instruments continuously conducting spectrally resolved soft X-ray measurements over a relatively large energy range. Fairly recent spectrally resolved, spatially integrated measurements have been conducted by *CORONAS-PHOTON Solar Photometer in X-rays* (SphinX) [53] and *MErcury Surface, Space ENvironment, GEochemistry, and Ranging* (MESSENGER) *Solar Assembly for X-rays* (SAX) [135]. SphinX conducted solar measurements over a time-frame of roughly 9 months in 2009 during a time of very low solar X-ray flux levels, including the lowest solar X-ray levels ever recorded. The SphinX designed spectral coverage was ∼1 - 15 keV at a nominal 0.4 keV spectral resolution. MESSENGER SAX performed solar measurements primarily at an orbit around Mercury from 1 - 10 keV at a nominal spectral resolution of 0.6 keV and has measured numerous solar flares [38] from 2011 March to 2015 April. Like the MinXSS solar X-ray measurements, both of these spectrometers generated spatially integrated spectra over the instruments' field of view (FOV).

MinXSS is designed to greatly improve upon these measurements and enhance the ability to determine emission line features with an improved spectral resolution (nominally ∼0.15 keV at 5.9 keV, due to detector architecture and electronics), a lower energy threshold ($E_{ph} \gtrsim 0.8$ keV, due to a slightly thinner Be window for MinXSS-2), and by providing near-continuous *dedicated* solar measurements over a ∼6 year period (MinXSS-1 1 year mission + MinXSS-2 5 year mission) during the declining phase of Solar Cycle 24, throughout solar minimum, and into the rising phase of Solar Cycle 25. MinXSS-1 was deployed from the International Space Station on 2016 May 16 and performed solar measurements until re-entry into Earth's atmosphere on 2017 May 6. MinXSS-2 is scheduled to launch no-earlier-than (NET) 2018 June.
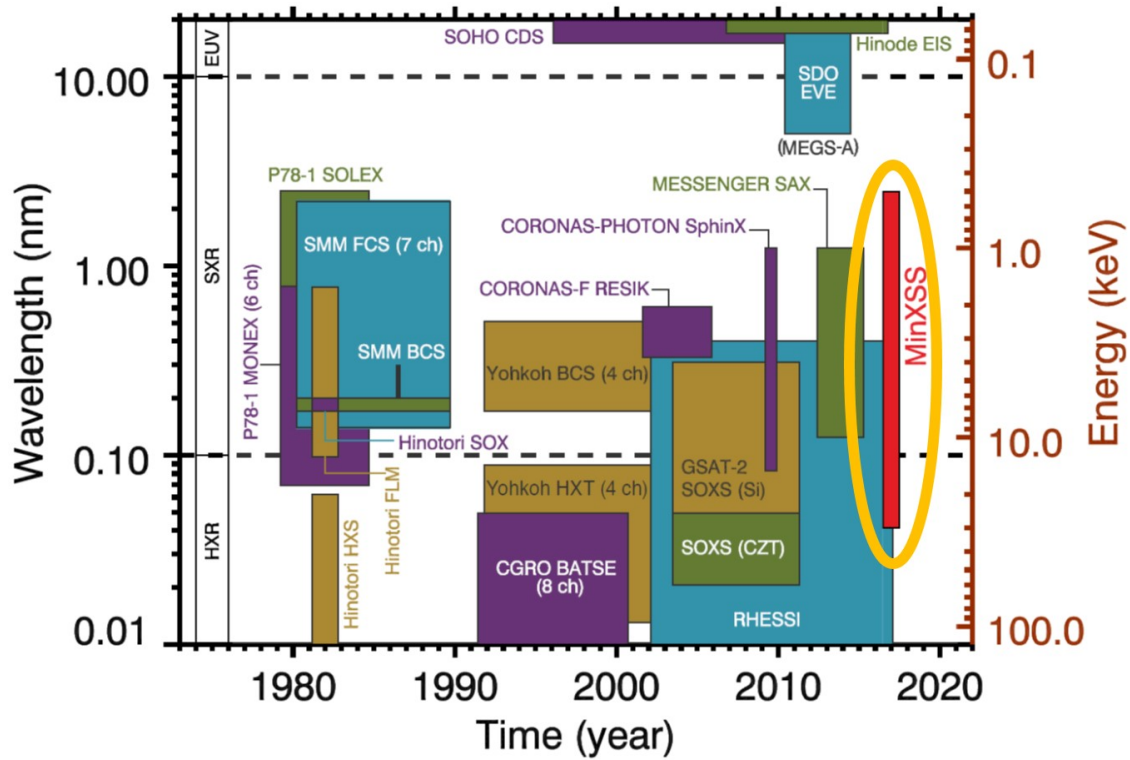
Figure 7.1: A non-exhaustive list of solar EUV and X-ray space borne instruments. The majority of soft X-ray missions conducted either high spectral resolution (< 0.1 keV) measurements over a narrow bandpass, had fairly low spectral resolution (> 1.0 keV) over a large spectral bandpass, or were integrating photometers. The MinXSS CubeSats will combine moderate spectral resolution (~0.15 keV FWHM at 5.9 keV) and a fairly large spectral bandpass (0.5 - 30 keV).

The aforementioned solar soft X-ray measurements lack direct spatial information. Combining spatially integrated, spectrally resolved measurements of MinXSS with data from other solar X-ray observatories can provide information on solar conditions. The Hinode *X-ray Telescope* (XRT) [90, 57] uses filters to create spectrally separated images of the soft X-ray intensity, but lacks fine spectral knowledge. The Geostationary Operational Environmental Satellite (GOES) *Soft X-ray Imager* (SXI) [77], exhibits similar qualitative spectral capabilities as XRT, but also suffers from the same issue of spectrally convolved images. The GOES *X-ray Sensor* (XRS) conducts spectrally [51] and spatially integrated measurements in two bands (0.1 - 0.8 nm and 0.05 - 0.4 nm). A ratio of these two bands can yield an isothermal

approximation to the coronal plasma temperature at the time of measurement [155]. The *Reuven Ramaty High Energy Solar Spectroscopic Imager* (RHESSI) [101] has provided spectral and spatial information using a Fourier imaging technique. RHESSI's primary spectral coverage extends from 6 keV - 17 MeV, with systematics-limited sensitivity below 6 keV. RHESSI's best spectral resolution in the 3 - 100 keV bandpass is ∼1 keV FWHM coupled with a 2.3 arcsecond FWHM spatial resolution. Additionally, the astronomy based *Nuclear Spectroscopic Telescope ARray* (NuSTAR) [70] satellite is sensitive to photons between 3 - 79 keV and has performed a series of solar measurements which have been summarized in [62] and [67]. The NuSTAR nominal 0.4 keV FWHM spectral resolution can produce spectral images with ∼18 arcsecond spatial resolution over its ∼11 arcminute field of view.

MinXSS data combined with the soft X-ray instrument data mentioned earlier, can be used in conjunction with other UV-Visible space observatories such as the Solar Dynamics Observatory (SDO) [126], the Hinode EUV Imaging Spectrograph (EIS) [33] and the Solar Optical Telescope (SOT) [147], the Interface Region Imaging Spectrometer (IRIS) [34], to mention a few, to address pertinent science questions about the solar atmosphere. Specifically, the corona's high temperature, low density, and magnetic conditions have been of keen interest for decades since the observations of 'coronium' lines in the solar spectrum [129, 143, 58]. Better understanding the solar soft X-ray energy distribution allow for improved inferences of plasma conditions present during various stages of the solar cycle and during solar flares. In addition, the MinXSS new observations will help improve the understanding of the solar soft X-ray influence on Earth's ionosphere and thermosphere. A few main solar science questions and tasks that MinXSS data will help address are:

- What is the solar soft X-ray energy distribution as a function of solar cycle phase (at least the falling and rising phases) for the following components?

    - flares

    - active regions (AR)

    - the quiescent Sun (QS)

- What is the AR variation in temperature, density, emission measure, chemical composition and magnetic complexity as a function of AR age and solar cycle phases?

- How are processes different between eruptive flares and non-eruptive compact flares?

- What is the soft X-ray spectral connection to magnetic complexity in the solar atmosphere?

In order to effectively include MinXSS data in any solar analysis, it is necessary to understand the performance capabilities of the MinXSS X-ray instruments. This paper describes the basic instrument characteristics and will be a reference for scientists interested in utilizing MinXSS. The remainder of this section of this dissertation includes basic descriptions of the MinXSS CubeSat mission in the folowing paragraphs, an overview of the instruments in Section 7.2, testing and capabilities of these instruments in Chapter 8 and Chapter 9, followed by examples of MinXSS-1 measurements from low solar levels (GOES A5) to an M5 flare and plasma inferences also in Chapter 9. Additional references for MinXSS include an overview of the MinXSS CubeSat and its subsystems by [107], pre-flight calibration results by [115], and early mission results by [158].

The MinXSS CubeSats development and testing involved extensive graduate student involvement in collaboration with the University of Colorado-Boulder's Laboratory for Atmospheric and Space Physics (LASP), and the Aerospace Engineering Sciences Department, with assistance from professors and professionals. The first of the twin satellites, MinXSS-1 was ferried to the International Space Station (ISS) from the Kennedy Space Center on 2015 December 6. MinXSS-1 was deployed from the ISS on 2016 May 16 (see Figure 7.3) to a Low Earth Orbit (LEO) with an initial altitude of ∼402 km. MinXSS-1 commenced

science operations on 2016 June 9 , and its mission ended on 2017 May 6 when it re-entered and burned up in Earth's atmosphere. The second CubeSat, MinXSS-2, is scheduled to launch to a Sun-synchronous orbit NET June of 2018 and to a higher altitude of 575 km for a longer-life mission. Figure 7.2 is a picture of the MinXSS-1 3U CubeSat, noting that 1 Unit (1U) is 10 cm × 10 cm × 11.35 cm in size. Even though they are small relative to *traditional* solar observing satellites, the MinXSS CubeSats are fully functioning satellites. They include triple junction GaAs solar cells from AzurSpace, Li-polymer batteries, Electrical Power System (EPS), an Attitude and Determination Control System (ADCS) supplied by Blue Canyon Technologies, a tape measure for a radio antenna, a Li-1 radio for communication, Command and Data Handling (CDH) microcontroller, and science instruments. The positions of these subsystems in the MinXSS spacecraft are shown in Figure 7.4. An overview of these subsystems is described in [107]. MinXSS-2 is an augmented version of MinXSS-1 with planned improvements in hardware, software and the implementations of lessons learned from the MinXSS-1 mission.

Scientifically, one of the most important upgrades of MinXSS-2 is a newer version of the X-ray spectrometer. The MinXSS-1 instruments are listed in Table 7.1 and MinXSS-1 in are listed in Table 7.2. The instruments consist of a visible-light Sun Position Sensor (SPS), an X-ray photometer (XP), and an X-ray spectrometer called X123. Nominally the MinXSS science data are composed of 10 second integrations, that can be decreased to 3 seconds or increased to 1 minute depending on the scientific objectives. The next section describes the full set of MinXSS instruments and their capabilities.

Table 7.1: MinXSS-1 satellite launch, orbit and mission lifetimes. A few instrument properties are also listed.

Satellite	MinXSS-1		
Orbit Insertion Date	16–May–2016		
Anticipated Mission Lifetime	~1 year		
Initial Orbit Altitude (km)	~400 km		
Instrument	SPS	XP	X123
Si Detector Depletion Depth (μm)	55	55	500
Aperture Area (cm^2)	4.0×10^{-2}	2.0×10^{-1}	2.5×10^{-4}
Window Type-Material	ND7[†]	Be	Be
Window Thickness (μm - uncertainty)	–	19.0 (0.1)	24.5 (0.6)
Full Field of View (FOV, °)	8	8	4

[†] Neutral density filter - 10^7

Table 7.2: MinXSS-2 satellite launch, orbit and mission lifetimes. A few instrument properties are also listed.

Satellite	MinXSS-2		
Orbit Insertion Date	NET[*] June–2018		
Anticipated Mission Lifetime	~5 years		
Initial Orbit Altitude (km)	~575 km		
Instrument	SPS	XP	X123
Si Detector Depletion Depth (μm)	55	55	500
Aperture Area (cm^2)	4.0×10^{-2}	$2 .0x\ 10^{-1}$	2.5×10^{-4}
Window Type-Material	ND7[†]	Be	Be + Zn
Window Thickness (μm - uncertainty)	–	18.0 (0.1)	11.2 (0.3) + 0.1 (0.1)
Full Field of View (FOV, °)	8	8	4

[*] NET = No Earlier Than

[†] Neutral density filter - 10^7
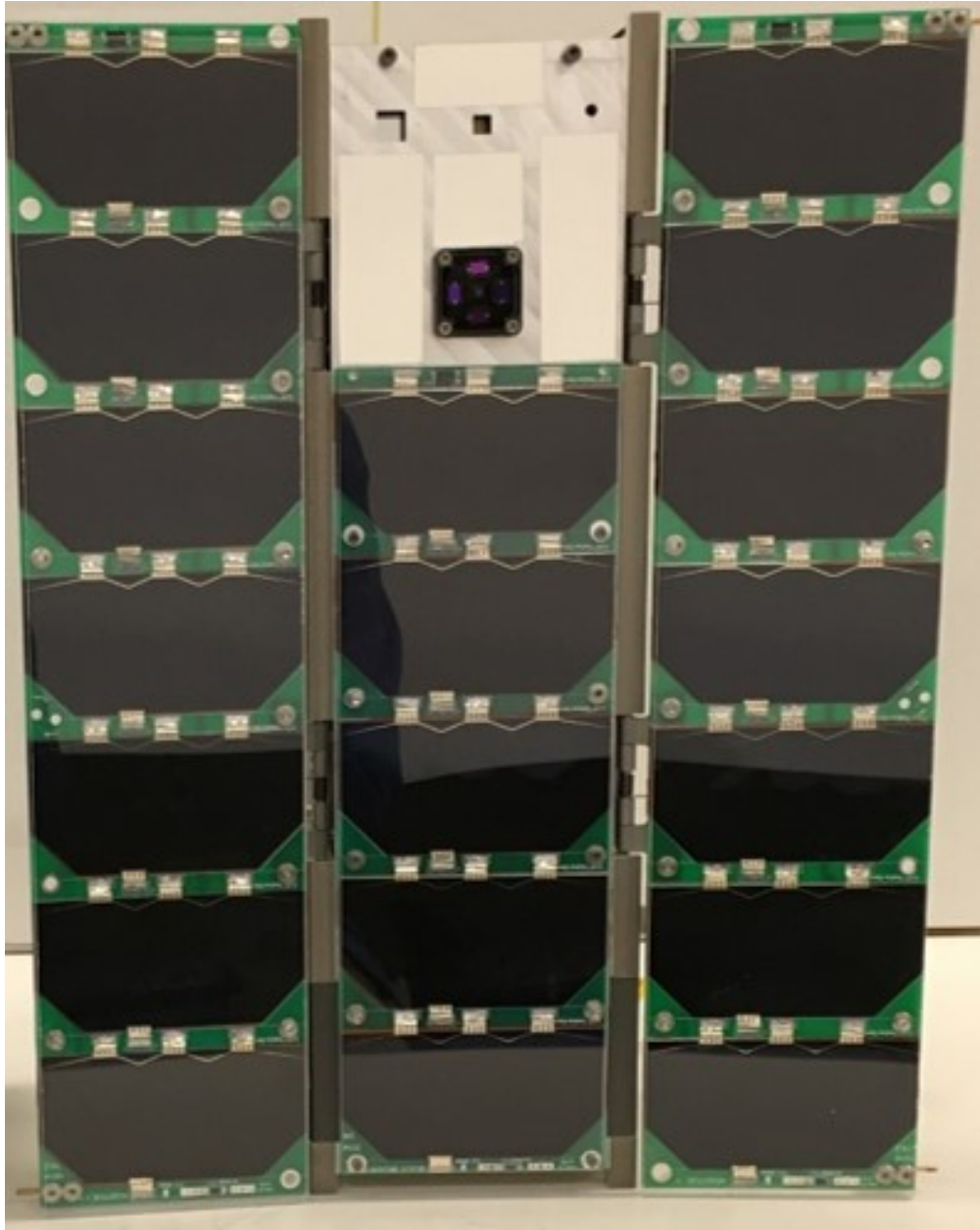
Figure 7.2: Picture of one of the twin Miniature X-ray Solar Spectrometer (MinXSS) 3U CubeSats. The CubeSat is oriented so that the solar panels and instrument apertures are facing the viewer (desired Sun facing side on-orbit). The MinXSS CubeSats are *designed* to measure the solar X-ray flux from 0.5 - 30 keV using the X-ray Photometer (XP) for spectrally integrated measurements across the entire energy band and the X123 spectrometer for energy resolved photon-counting measurements. The X123 spectrometer has a nominal spectral resolution of 0.15 keV full-width-half-maximum (FWHM). MinXSS-1 was deployed from the International Space Station on 2016 May 16 with an initial LEO altitude of ∼402 km and had an 11-month mission life before its re-entry on 2017 May 6. Mission lifetime is dependent upon solar activity. MinXSS-2 is to be launched to a Sun-synchronous orbit of ∼575 km NET June of 2018 for an anticipated 5 year mission.

Figure 7.3: MinXSS-1 deployment from the ISS on 2016 May 16 to a Low Earth Orbit (LEO) with an initial altitude of ∼402 km.
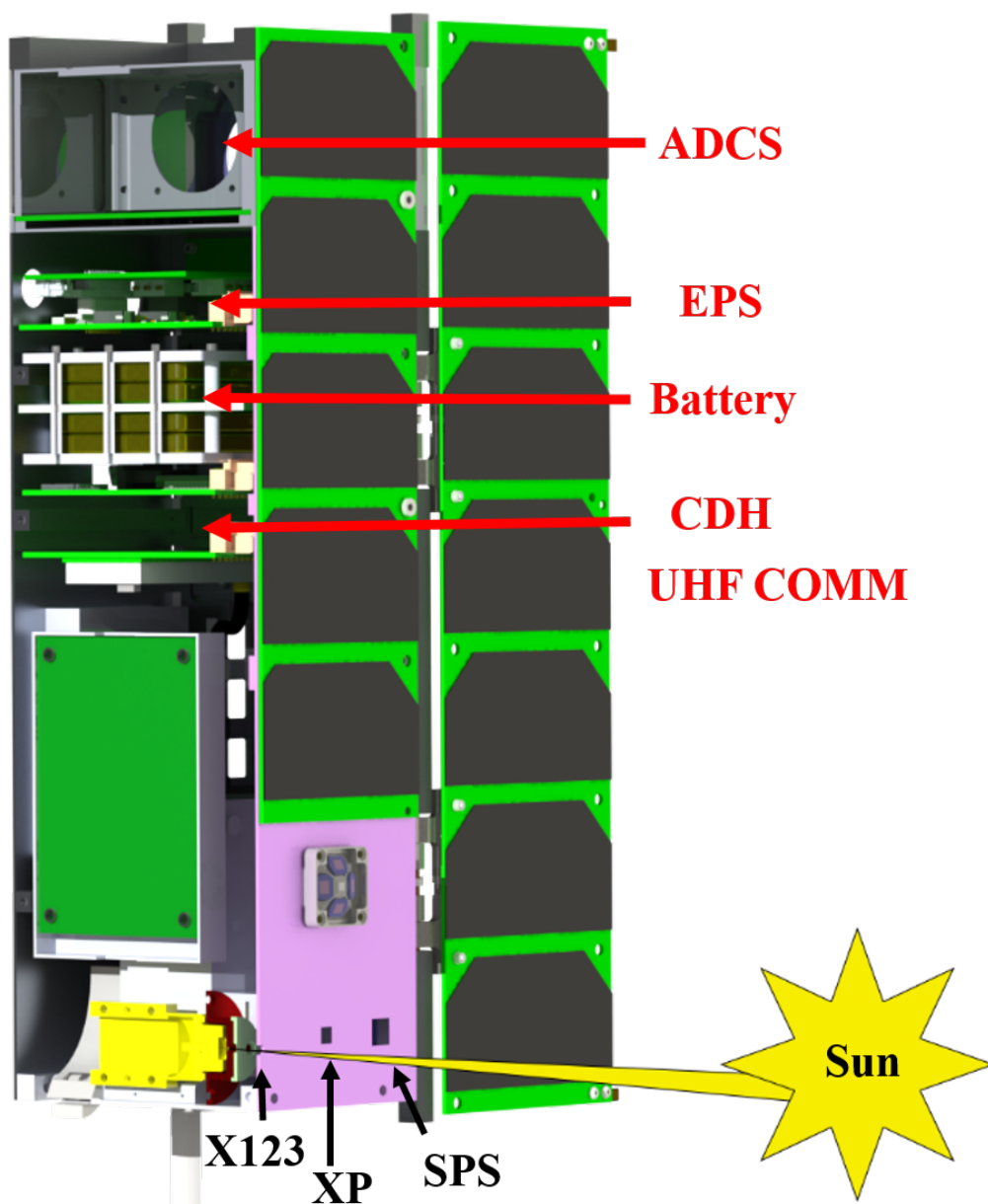
Figure 7.4: Cut out of the MinXSS CubeSat to demonstrate the optical path of the Sun (not to scale) through the field of view limiting aperture and housing for the X123 spectrometer. The X123, XP and SPS apertures, and other subsystem locations are labeled for clarity.

7.2   Instruments

7.2.1   Sun Position Sensor (SPS)

SPS is a visible-light sensitive quad silicon-photodiode (Si-photodiode) arrangement behind an ND7 (neutral density filter with an attenuation factor of 10^7). The Si-photodiodes have a 55 μm thick depletion depth. The SPS square aperture is 2×2 mm and the layout is discussed below and in Figure 7.5. The relative solar illumination on each of the four diodes is used to calculate the solar position within the MinXSS X-ray instruments' field of view (FOV). The absolute position knowledge is accurate to within 3 arcseconds and the pointing is controlled to a precision of 10 arcseconds, limited by the capabilities of the Blue Canyon XACT ADCS system.

The SPS quad Si-photodiode detector assembly is used to calculate the solar position in the MinXSS FOV. SPS sits behind a ND7 filter (attenuation of a factor of 10^7) to limit the visible-light flux and eliminate all other electromagnetic contributions to the signal. SPS relies on the visible-light emission from the Sun to estimate the solar location within the FOV position by calculating offset angles referred to as α and β. Figure 7.5 shows the basic SPS layout of the quad diode assembly with a square 2×2 mm aperture. SPS has no focusing optics and thus its operating principle relies upon measuring the relative light detected on each of the four diodes Q1, Q2, Q3, and Q4 to calculate solar disc location. Equation 7.1 and Equation 7.2 display the relation between the quad diode signal to the α and β coordinates, which must be scaled by the known maximum angular deviation α_{max} and β_{max}. The maximum angular deviation is set by the geometrical layout of the aperture with respect to the quad diodes. For an aperture of width, w, height, h and separation between the photodiode and aperture along the optical path, d, the maximum angles can be calculated from Equation 7.3 and Equation 7.4.

$$\alpha = \alpha_{max} \frac{(Q1 + Q4) - (Q2 + Q3)}{(Q1 + Q2 + Q3 + Q4)} \tag{7.1}$$

Figure 7.5: SPS quad diode layout demonstrating the orientation of the α and β angles. The SPS square aperture is 2 mm × 2 mm.

$$\beta = \beta_{max} \frac{(Q1 + Q2) - (Q3 + Q4)}{(Q1 + Q2 + Q3 + Q4)} \tag{7.2}$$

$$\alpha_{max} = \alpha tan\left(\frac{w}{2d}\right) \tag{7.3}$$

$$\beta_{max} = \beta tan\left(\frac{h}{2d}\right) \tag{7.4}$$

7.2.2 X-ray Photometer (XP)

The LASP designed XP unit consists of a Si-photodiode (55 μm thick depletion depth) with a beryllium (Be) window 19.0 μm thick for MinXSS-1 and 18.0 μm thick for MinXSS-2 to attenuate visible-light contamination. The XP aperture is 5 mm in diameter. The main purpose of XP is to serve as a consistency check to the detected photon flux and linearity of

the X-ray spectrometer X123, assesssing long term degradation trends, and comparison to the GOES XRS photometers. The Si-photodiodes in XP and SPS have been flown numerous times, such as on SDO [159], are known to be stable in space, and have linear response over the full range of solar flux levels after corrections to various influences. The XP photodiode response can have gain and dark current variations due to thermal fluctuations, and can possibly suffer noise from sources internal to the MinXSS spacecraft (e.g. emf, radio transmission, microphonics, etc.), which must be corrected for. After gain and dark current corrections, the XP product returns one spectrally integrated value for the solar X-ray contribution over its expected spectral response from $\sim$0.5 - 30 keV. This type of information is valuable, but of similar capability as the GOES XRS. The spectral information provided by the X-ray spectrometer, X123, can greatly enhance the interpretation of the XP data.

7.2.3   X-ray Spectrometer (X123)

The MinXSS main scientific instrument, X123, is an X-ray spectrometer purchased from Amptek (Amptek website: http://amptek.com/). Figure 7.6 displays the relatively small size of the X123 spectrometer, making it ideal for a CubeSat. The data returned from X123 will be the most important data product that MinXSS will provide to the scientific community. X123 is composed of a Silicon Drift Detector (SDD) with a 500 μm thick Si depletion depth behind a Be window 24.5 μm thick for MinXSS-1 and 11.2 μm thick for MinXSS-2. From pre-flight calibrations, there appears to be Zn contaminant in the MinXSS-2 Be filter with an approximate thickness of 0.1 μm for MinXSS-2. The X123 silicon sensor dead-layer is comprised mostly of SiO and has a nominal thickness around 0.15 μm. The deadlayer thickness was not measured and thus the nominal thickness value in included in the detector modeling. This thickness of SiO does not strongly impact the detector high energy efficiency, but could contribute to the low energy (< 1 keV) efficiency.

Amptek provides the X123 electronics for power regulation, high voltage for SDD operation, detection of individual X-ray photons and the energy of each photon, binning the
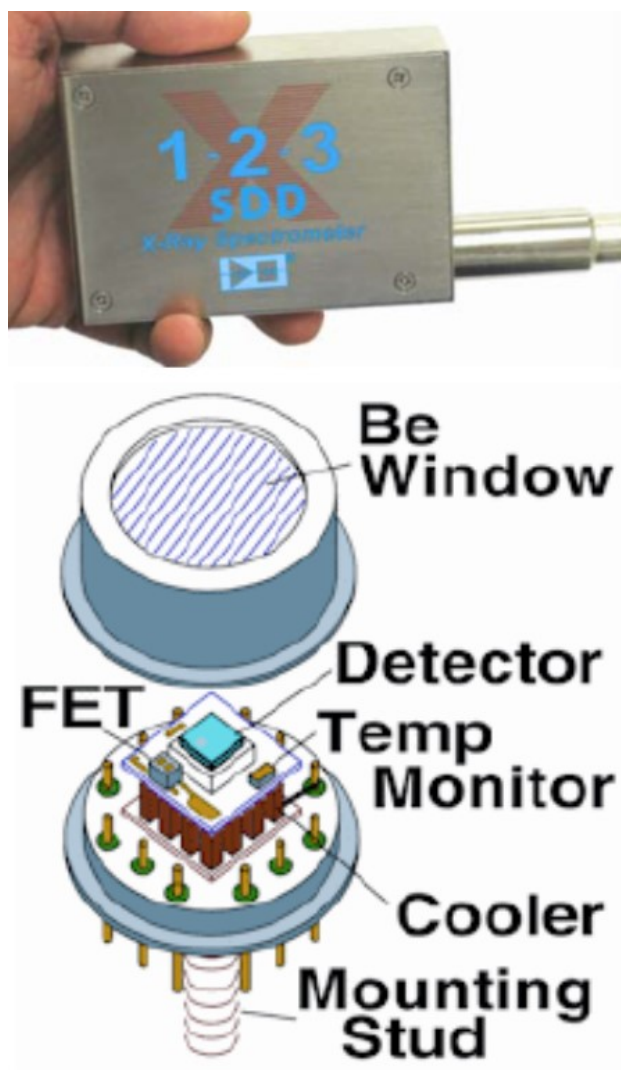
Figure 7.6: Basic layout of the X123 detector from the Amptek website. The MinXSS X-ray spectrometer is a commercial off the shelf (COTS) X123 silicon Drift Diode (SDD) from Amptek (http://amptek.com/). The detector package comes in various sizes and each can fit in the palm of an adult's hand, making X123 perfect for a CubeSat. The X123 consists of a beryllium (Be) window to attenuate visible light and transmit X-rays, the SDD detector, thermoelectric cooler (Peltier cooling) and a Field Effect Transistor (FET) pre-amplifier all in the detector head, that is attached to an external electronics box.

photon events into a spectrum, and embedded software for reading the spectrometer output. Thus, in addition to X-ray characterization, the main task remaining is to integrate the X123 output to the MinXSS CDH processor that compresses the data and formats it into data packets. The power draw from X123 is nominally ~2.8 W during normal operations

and at max $\sim$5.0 W (normally at turn on). The X123 spectrometer is actively cooled with a thermoelectric cooler (also provided by Amptek) to $\sim$224 K. The cooling is necessary to minimize thermal noise which will contribute to the lower energy bins ($E_{bin} \leq 1.0$ keV). The X123 sensor resides inside a stainless steel housing to protect the X123 sensor from energetic particles in space, and there is a tungsten FOV-limiting pinhole aperture out front with a $\sim$0.18 mm diameter to protect from solar hard X-rays.

7.2.4   Detector Operation

The X123 SDD, XP and SPS operation relies, in principle, on electron-hole pair generation in the Si lattice by the incident photon flux. Photons and any other energy sources (these contribute to the noise) that have more than the Si electron-hole pair generation energy ($E_{e-h} \gtrsim 3.65$ eV) can create a number of electron-hole pairs proportional to the energy of the incident photon. For the SPS and XP detectors, the liberated charges contribute to a current which is measured, amplified and converted to a digital unit. Depicted in Figure 7.7 is the difference for the X123 spectrometer. Electrons generated by this energy deposition process drift toward the readout anode and the resulting charge is integrated on a capacitor within the detector rise time (peaking time). These energy 'impulses' are deemed events. The preamplifier, which consists of a Field Effect Transistor (JFET for MinXSS-1 and MOSFET for MinXSS-2), that amplifies the signal, converts it to a voltage, and this voltage ramp is shaped to a trapezoid. The magnitude of these shaped signals are used to discern the energy deposited in the active detector volume for each incident photon 'event'. The performance capabilities of the X-ray instruments are discussed in the next Section.
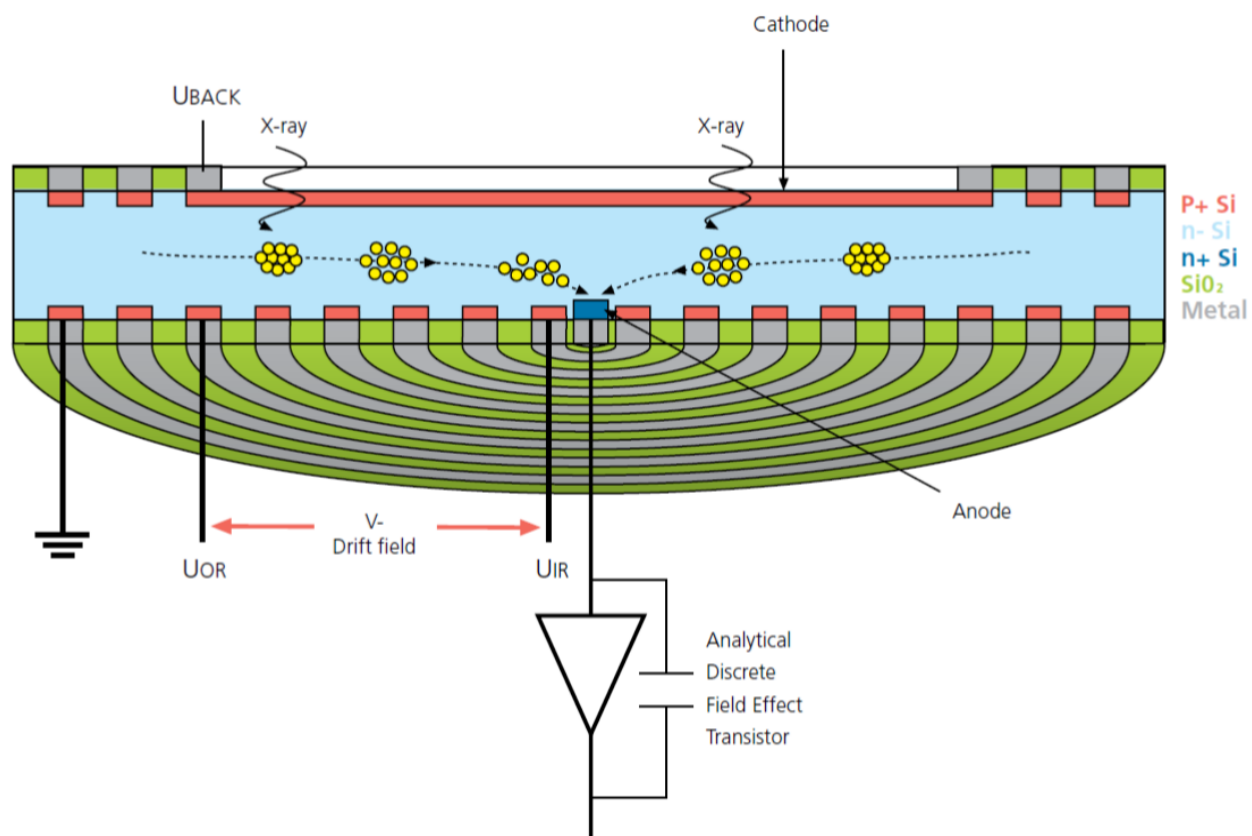
Figure 7.7: Schematic demonstrating the basic SDD architecture and principle operation. Adopted from the article "SDD Explained" (http://www.uni-export.com.pl/files/Akcesoria analityczne/SDD_Explained.pdf). Photons with energy greater than the Si electon-hole pair energy ($\sim$3.65 eV) incident on the biased bulk silicon structure will liberate electron-hole pairs. The negative charge is drifted towards the central capacitor. THe charge is integrated on the capacitor, converted to a voltage amd amplified by the Field Effect Transistor (FET).

Chapter 8

MinXSS Instrument Testing and Characterization

The MinXSS instrument suite was characterized using radioactive lab sources for spectral resolution, optimization of electronic settings, determining the gain and energy offset of the X123 spectrometer. SPS, XP and X123 field of views (FOV), XP and X123 window thicknesses, spectral efficiency, and linearity were determined from the National Institute for Standards and Technology (NIST) Synchrotron Ultraviolet Radiation Facility (SURF) measurements. MinXSS X123 spectrometer basic performance properties and characterization methodology are described in [115]. Accurate knowledge of the electron beam current, electron beam energy, magnetic field strength, and source distance allows for the precise calculation of the synchrotron light spectral intensity to enable calibration of the X123 and XP responsivities with about 10% accuracy [115].

8.1   Radioactive Line Sources, Gain and Energy Offset

The X123 energy bin gain, energy bin offset, and spectral resolution have been estimated using radioactive line sources of ^{55}Fe for the $\sim$5.90 and $\sim$6.49 keV line complexes, and ^{241}Am for the $\sim$11.87, $\sim$13.95, and $\sim$17.75 keV lines. The fit values for the both the MinXSS-1 X123 gain and MinXSS-2 X123 gain are 0.0297 keV/bin and are consistent with the nominal bin width (0.03 keV). The offset is dependent on the electrical grounding conditions at the time of operation, due to the fact that the pulse height analysis is computed on top of a baseline voltage, which can drift. Thus, the X123 energy offset in the lab at LASP

for radioactive source measurements, at NIST SURF and on-orbit may not be exactly the same. Nominally, the value for MinXSS-1 energy bin offset is around -0.076 keV and the MinXSS-2 energy bin offset is close to -0.265 keV.
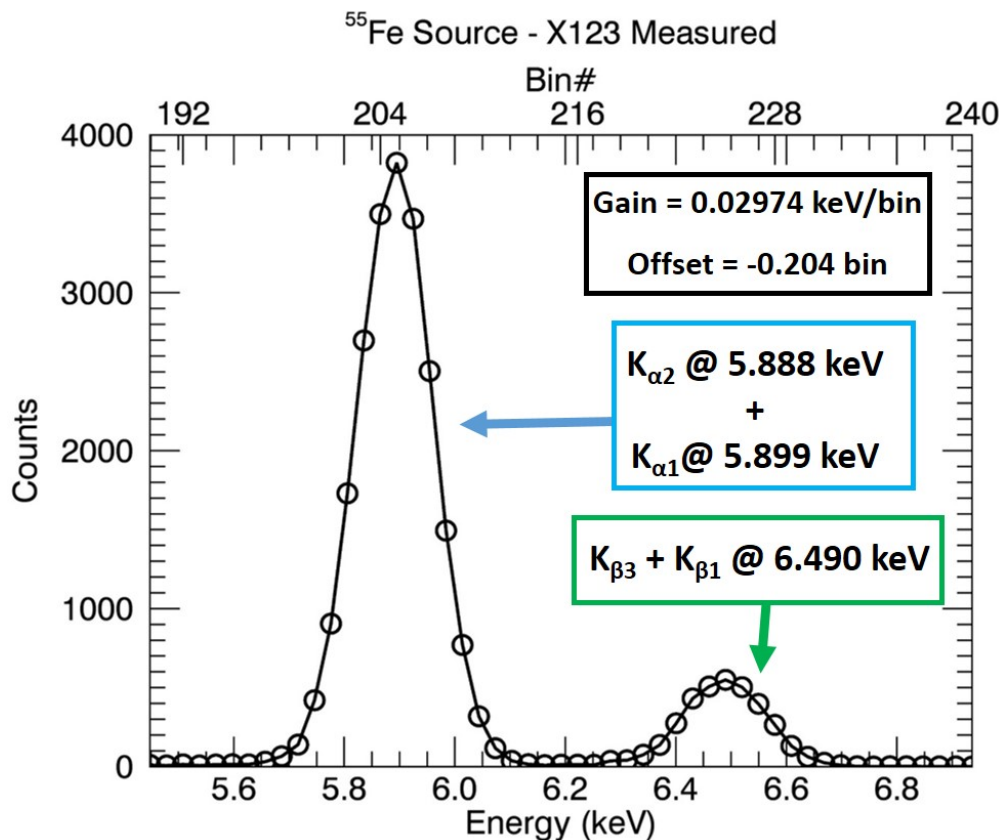
Figure 8.1: An example of an X123-measured ^{55}Fe source emission profile. The Kα and Kβ line complexes at ($\sim$5.9 and $\sim$6.5 keV respectively) are fully resolved from one another, but the individual components of these lines complexes are not, at the $\sim$0.15 keV FWHM nominal spectral resolution at 5.9 keV. The fitted energy gain of $\sim$0.029 keV/bin is consistent with the nominal binning of 0.03 keV bin.

8.1.1   Spectral Resolution

The X123 has a customizable peaking time, which dictates how long the photon liberated electron charge cloud is integrated on the readout capacitor. The longer the peaking time, the better the spectral resolution. MinXSS-1 has a fixed peaking time of 4.8 μs but we have tested the MinXSS-2 X123 detector for various peaking times between 0.6 - 9.6 μs. We

will operate the MinXSS-2 X123 for peaking times between 1.2 - 4.8 μs due to the tradeoff between spectral resolution and effective maximum count rate that can be recorded before photon pile-up begins to occur. We only show data for these 1.2 - 4.8 μs peaking times in this paper. The longer the peaking time, the lower the maximum count rate that can be accurately measured. Details on the maximum count rate are discussed in Section 8.2.4.

Figure 8.2 shows example MinXSS-2 X123 [55]Fe measurements from 1 - 10 keV and [241]Am measurements from 10 - 30 keV. The subset of lines used to assesss the spectral resolution at specific energies are signified by the vertical dotted line. The nominal spectral resolution near 5.9 keV was confirmed for the respective peaking times. The current on-orbit estimated MinXSS-1 X123 detector resolution is $\sim$0.24 keV, which is much broader than the nominal 0.15 keV spectral resolution at 5.9 keV for a 4.8 μs peaking time. We are currently assesssing the reasons for a degraded on-orbit resolution. MinXSS-2 has an improved version of the X123 spectrometer, the X123 Fast SDD. The X123 Fast SDD has an improved preamplifier, a MOSFET transistor instead of a JFET for the MinXSS-1 version. This has a lower effective capacitance, lower noise and results in improved spectral resolution for the same peaking times as the older version. An advantage is increased maximum count rate, which will be discussed in Section 8.2.4. The spectral resolution for MinXSS-2 at 5.9 keV is 0.137 keV for 4.8 μs, 0.162 keV for 2.4 μs, and 0.168 keV for 1.2 μs.
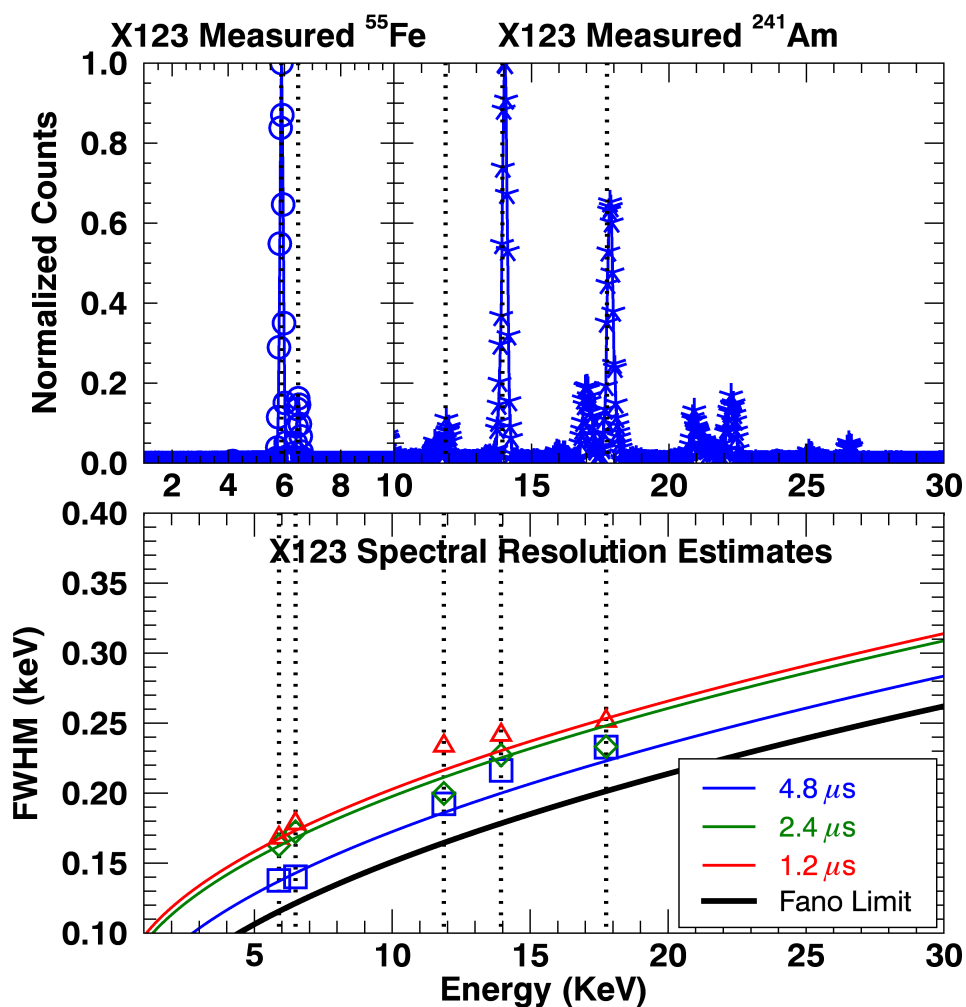
Figure 8.2: Example plot of MinXSS-2 X123 spectral resolution estimates vs. photon energy using radioactive X-ray sources. The top split-plot shows the normalized counts from the ^{55}Fe source from 1 - 10 keV and the ^{241}Am source from 10 - 30 keV. The ^{55}Fe ∼5.90 and ∼6.49 keV line complexes are easily detected. The ^{241}Am ∼11.87, ∼13.95, and ∼17.75 keV lines are used for spectral resolution estimates. The vertical dotted line emphasizes which spectral lines were used for FWHM resolution estimates for three different spectrometer peaking times. Longer peaking times yield better photon energy resolving power up to the combined electronic and Fano Limit. The Fano Limit is the intrinsic statistical limit of bulk Si semiconductor material to resolve energy differences, and is over-plotted with the black solid line. The colored lines are the Fano Limit (from Fano Noise) with an estimated electronic noise contribution from the ^{55}Fe measurements. These estimates depicted by the color lines are used to extrapolate the spectral resolution to *higher* photon energies. The extrapolation to lower energies is not expected to adhere to these lines due to other noise sources (microphonics, thermal noise, and other uncharacterized sources).

8.2   NIST SURF MinXSS Testing

NIST SURF is a highly accurate and precise ultraviolet photon source known to within 2% and with extension in to the visible and soft X-ray ranges (soft X-ray accuracy known to within 10%) [5]. The synchrotron radiation produced by the relativistic electrons bent by magnetic fields is beamed into the direction of motion and directed down a beamline for instrument characterization tests. Basic descriptions of synchrotron radiation are given in [14], [12] and references therein. The general proportionality relating the synchrotron beam current in milliamps, I_e, mean electron energy in mega-electron volts, E_e, and a photon spectral dependence function, F, involving modified Bessel functions, photon energy, E_{ph}, critical photon energy, E_c, and azimuthal (out of plane vertical angle), Ψ, to the number of generated photons, $N_{photons}$, in units of photons s^{-1} $mrad_{\Theta}^{-1}$ $mrad_{\Psi}^{-1}$, is given in Equation 8.1.

$$N_{photons} \propto I_e(mA)E_e^2(MeV)F(\tfrac{E_{ph}}{Ec}, \Psi) \tag{8.1}$$

Increasing the mean electron energy, E_e, changes the spectral distribution of the radiation (increasing E_e produces more photons at every photon energy, but proportionally many more at high photon energies than at low photon energies). It must be noted that the mean electron energy, E_e, appears in the critical photon energy, E_c, also. This leads to the discussion of our first SURF test to determine our X123 spectral response, Multienergy.

8.2.1   Field of View Sensitivity

The MinXSS X-ray instruments integrate the incident radiation across their FOVs to create their respective signals. While XP and X123 do not have spatial resolution per se, they do possess a sensitivity to light intensity across their respective FOVs. Based on the design of the housing baffles, XP nominally has an angular response across an 8° FOV and X123 has a FOV of 4°. An example of the alpha-beta (α-β) coordinate system used for the SURF calibrations is given in the SPS image in Figure 7.5. An extended source such as the
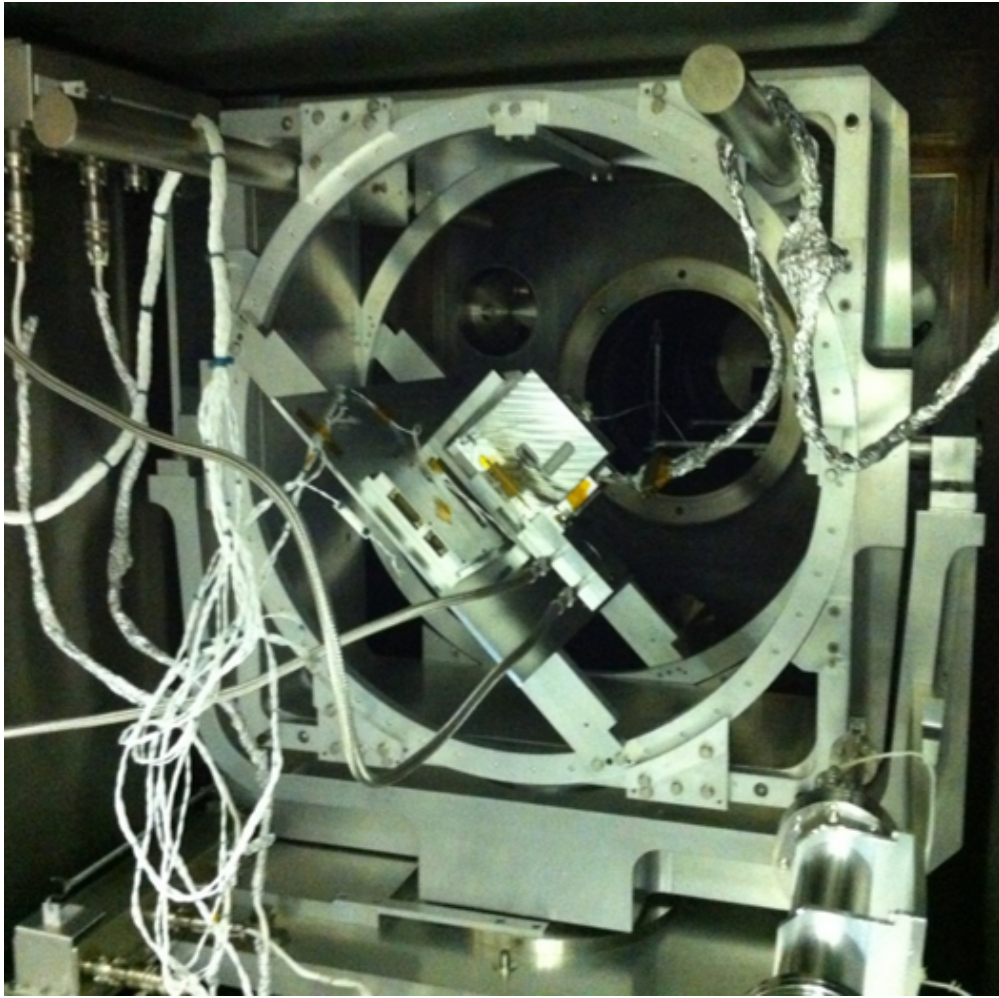
Figure 8.3: The MinXSS CubeSats in the Gimbal at NIST SURF.

Sun viewed from Earth will have an angular size of roughly 0.5°, but the response can vary strongly depending on the actual X-ray coronal structure during observations. This is well within the FOV of XP and X123. For the most accurate photometric measurements from MinXSS, it is important to correct for the solar disc position within the MinXSS FOV.

Figure 8.4 shows FOV sensitivity maps of MinXSS-1 and MinXSS-2 X123. The maps are a 1.4° × 1.4° subset, centered on the FOV of X123. The XP map yields similar FOV sensitivities. The values are the raw NIST SURF determined MinXSS response maps, convolved with the visible-light solar disc, and expressed as a percent difference in the total signal summed over all energies at that position with respect to the center, to estimate the

X-ray detection variation across the FOV. This pre-flight map serves as our baseline until on-orbit maps are created for comparison. The absolute variation across the centered $1.4° \times 1.4°$ FOV is around 8%. The MinXSS ADCS unit (XACT from Blue Canyon Technologies) has proven to keep the Sun within $0.3°$ of the center of the MinXSS FOV with a precision of 3 arcseconds ($\sim0.008°$). Thus, the inner $1°$ diameter annular region is the most important for MinXSS on-orbit performance and the absolute variation within this region is no larger than about 5%. We note that only mechanical alignment was implemented between the XACT ADCS unit and the instruments.
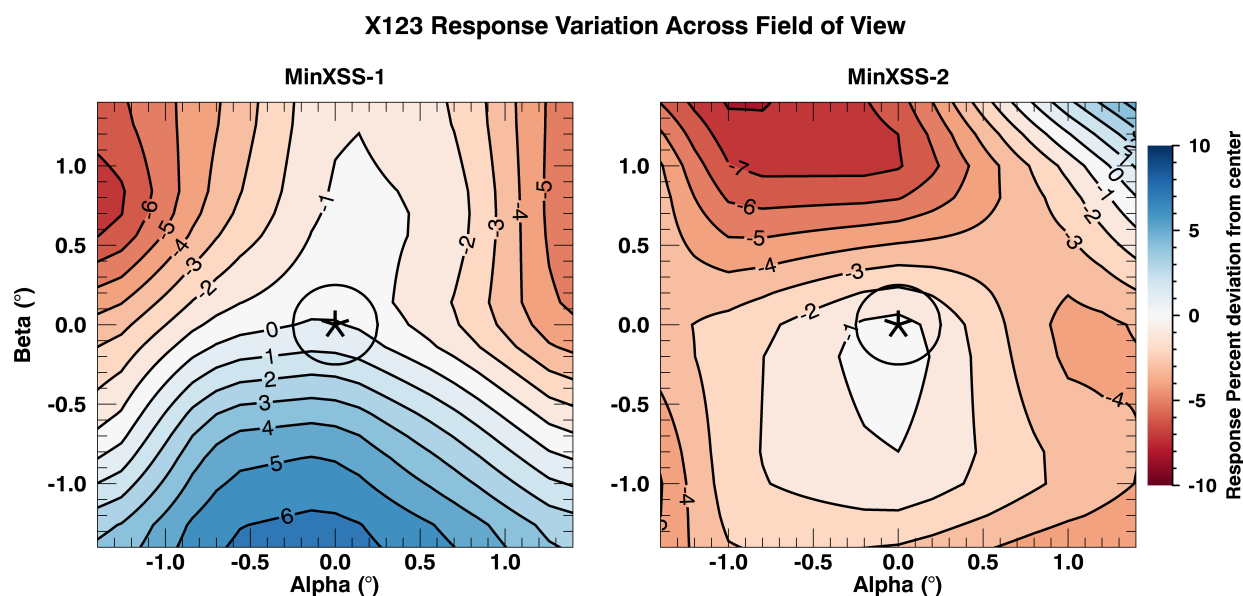
Figure 8.4: X123 Field of View (FOV) sensitivity maps constructed from pre-launch data at the National Institute for Standards and Technology (NIST) Synchrotron Ultraviolet Radiation Facility (SURF) for each CubeSat (left: MinXSS-1 and right: MinXSS-2). The maps displayed are the MinXSS spectral response convolved with the apparent visible-light solar disc. The asterisk denotes the center of the spectrometer FOV which mechanically aligned to the boresight of the spacecraft. The black circle represents the size of the visible-light solar disk in the FOV. The contours and color map signify the percent difference in the X123 response from the center (asterisk), which is a few percent in magnitude.

8.2.2　　　Effective Area

The XP 55 μm and X123 SDD 500 μm thick depletion depths for Si based X-ray detectors dictate the high energy cut-off efficiency. The window material and composition affect the high and low energy efficiency. For Be based windows only the lower energy photons are attenuated and thus the Be window thickness dictates the low energy photon response. Noise contributions, primarily electronic noise, limit the XP signal fidelity and the X123 lower energy contribution. The MinXSS instrument spectral efficiency was determined through a series of measurements conducted at NIST SURF and the details are listed in [115]. The SURF photon spectrum is known to within 10% near 1 keV and produces statistically significant counts up to about 3 keV. Model uncertainties in the fitted detector window thicknesses, depletion depth thicknesses and atomic coefficients yield uncertainties near 20% for the higher energies. Since the SURF spectrum is a continuum, it is not very useful for the spectral resolution estimates, such as those discussed in Section 8.1.1, but the absolute synchrotron photon spectral distribution can be used to determine the detection efficiency of the MinXSS X-ray instruments.

The MinXSS XP signal can be calculated from the following expression in Equation 8.2, where C$_{XP}$ is the XP count rate with units of $\frac{DN}{s}$, s is seconds, DN is the Data Number, which is converted from the femtoCoulomb (fC) signal by the XP gain, G_{XP}. The bracketed term is the femtoamps (fA) generated from the detected photon flux, from the source of photons, $S(E_{ph}, \Omega)$ with photon energy, E_{ph}.

$$C_{XP} = G_{XP} \int_0^\infty \left[\int^{\Omega_\odot} S(E_{ph}, \Omega) A_{XP} R_{XP}(E_{ph}, \Omega) d\Omega \right] dE_{ph}. \tag{8.2}$$

In the case of the Sun, there is a distribution of photons as a function of X-ray energy, and a function of position in the extended corona. The Sun appears as an extended object and its position can vary within the MinXSS FOV. The physical extent of the X-ray emission from the Sun is encompassed in the solid angle, Ω, which is not necessarily the simple conversion

of $\pi sin^2(\theta_\odot) \approx \pi\left(\frac{R_\odot}{1AU}\right)^2 \approx 6.8 \times 10^{-5}$ sterradians, because the X-ray emission is not confined to the visible-light solar disk. An example of the distribution of X-ray emission that MinXSS can detect is illustrated in the Hinode XRT images in Figure 9.15. Thus, $S(E_{ph}, \Omega)$ is an intensity or radiance, in units of photons s^{-1} keV^{-1} cm^{-2} ster^{-1} in this formulation. A_{XP} is the XP aperture geometric area, in units of cm^2. The XP detector response $R_{XP}(E_{ph}, \Omega)$ includes the XP detector efficiency, the conversion from photon energy to fC, ϵ_{ph}, and the FOV sensitivity which is encompassed in the Ω dependence. In theory, the integral of the bracketed term can include all photon energies from 0 to ∞ incident on the XP area, but the actual high and low energy limits are set by the XP detector response.

The combination of the XP detector response and geometric area constitutes an 'effective area'. The XP MinXSS-1 and MinXSS-2 effective area curves are displayed in Figure 8.5. The main XP photon response lies between 0.5 - 30 keV, with the actual count contribution depending on the solar X-ray spectrum, $S(E_{ph}, \Omega)$, during observations. Both MinXSS-1 and MinXSS-2 XP devices have similar responses as their Be windows are of similar thickness (19.0 μm for MinXSS-1 and 18.0 μm for MinXSS-2).

In a similar fashion to the XP calculation, the X123 count rate per energy bin denoted, j, is $\left(C_{X123}\right)_{bin,j}$, in units of $\frac{Counts}{s}$ can be calculated by Equation 8.3 and Equation 8.4

$$\left(C_{X123}\right)_{bin,j} = \int_{E_{min,j}}^{E_{max,j}} \left[\Upsilon(E_{det})\right] dE_{det} \tag{8.3}$$

$$\Upsilon(E_{det}) = \int_0^\infty \int^{\Omega_\odot} S(E_{ph}, \Omega) A_{X123} \overline{\overline{\Re}}_{X123}(E_{ph}, \Omega, E_{det}) d\Omega dE_{ph} \tag{8.4}$$

where A_{X123} is the X123 aperture geometric area. The main difference between XP and X123 in terms of the signal calculation is the spectral binning of the data and the response function. $\overline{\overline{\Re}}_{X123}(E_{ph}, \Omega, E_{det})$, which is the photon $\Leftrightarrow$ detected energy bin *redistribution* function and includes the FOV dependence thru Ω. The function $\overline{\overline{\Re}}_{X123}(E_{ph}, \Omega, E_{det})$ maps E_{ph} to E_{det} for forward modeling and vice-versa, for inverting detected counts to create an

incident photon flux estimate. Thus, the bracketed term in Equation 8.3 is only a function of dE_{det}, because of the operation of $\overline{\Re}_{X123}(E_{ph}, \Omega, E_{det})$ on the source intensity $S(E_{ph}, \Omega)$. Hence, the final integral over the individual energy bin energy limits, $E_{min,j}$ and $E_{max,j}$ to obtain a final count rate value in energy bin j. Again, in theory the integral over E_{ph} in the bracket is over all photon energies, but in reality, this is limited to the X123 spectral efficiency, high and low photon limits.
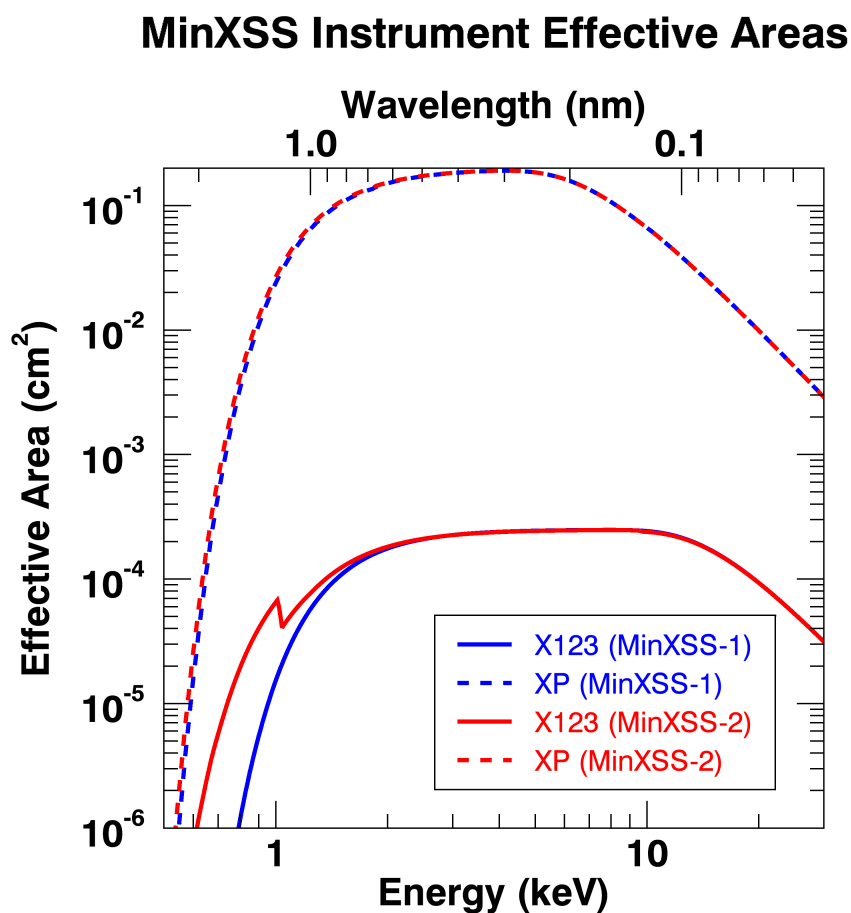
Figure 8.5: MinXSS-1 and MinXSS-2 X-ray instrument effective area vs. photon energy. The main difference between the XP (dashed line) and X123 (solid line) is due to the geometric area of their respective apertures. The XP aperture diameter is ∼5 mm, while the X123 pinhole diameter is ∼0.18 mm. MinXSS-2 has an undesigned Zn contribution to the Be window, which results in an edge in the response near 1 keV.

Similarly, for X123 the combination of the X123 spectral efficiency (the probability that a photon incident on the active area of the detector will be absorbed) and the aperture geometric area can be used to create the effective area curves for MinXSS-1 and MinXSS-2 X123 in Figure 8.5. The edge near 1 keV in the MinXSS-2 X123 detector effective area curve is due to a Zn contamination in the Amptek supplied Be window and has been included in the modeling. The primary spectral range is nominally 0.5 - 30 keV for both MinXSS spacecraft X123 detectors, but it is obvious in Figure 8.5 that the MinXSS-2 detector has a higher efficiency for the lower photon energies ($E_{ph} \leq 2$ keV). This is due to the thinner 11.2 μm Be window on the MinXSS-2 detector as compared to the 24.5 μm thick window on MinXSS-1. The choice of the thinner Be window X123 detector being on the second MinXSS was intended, because MinXSS-2 has an anticipated longer misson of $\sim$5 years vs. MinXSS-1 mission lifetime of $\sim$1 year. The higher efficiency for lower photon energies aids in extending the low energy limit of the MinXSS-2 X123 data product. Effective area curves are great for comparing both the spectral and intensity sensitivities between various instruments on different observatories. Details on the determination of these properties from the SURF Multienergy technique is discussed in Section 8.2.2.1

8.2.2.1   Multienergy Technique

Initially we do not know the spectral response of our X123 spectrometer, but we can determine it by illuminating our detector with known spectral flux and dividing the measured counts by this known input flux. This is the ideal process for determining the instrument spectral response but is not always feasible due to low count rates leading to increasingly large uncertainties in the determined response from this 'inversion' technique. Additionally, energy loss processes in the detector will yield counts at energies different than the initial photon energy (sometimes referred to as an off-diagonal response), which are not properly treated by a simple division. A more robust methodology is to use a model containing estimations of the dominant physical processes that influence the measured count flux and

fit the best parameter values of the physical model to the measured count flux. We follow this ideology to estimate our X123 spectral response for many different input photon spectral distributions and respective measured count fluxes, which we call Multienergy.

Figure 8.6. Demonstrates the basic Multienergy procedure and the main steps are listed below. This analysis was performed on both XP and X123 to estimate the Be window thicknesses, spectral response and effective areas but only the X123 processs is described here in detail.

(1) Shine a known photon spectral intensity on the X123 aperture at a certain SURF mean electron energy.

(2) Obtain the best fit parameters for the instrument response for that specific input photon flux that best reproduces the measured count flux.

(3) Perform a Monte Carlo simulation around the best fit parameters to obtain 10 other estimations of the best fit parameters. This helps determine the uncertainty of the best fit parameters.

(4) Repeat steps 1 - 3 for the next SURF mean electron energy.

(5) Compute final best fit parameter values by taking the mean of the main fit parameters per energy (result of 2).

(6) Compute the final uncertainty on each best fit parameter by combining the uncertainty estimations from the MC runs.

The MinXSS X123 modeled count flux from SURF is determined from Equation 8.3 and Equation 8.4, where the photon source function is now equal to the normalized SURF photon flux times the beam current, $S(E_{ph}, \Omega) = \mathrm{F}_{SURF}(\mathrm{E}_{ph})\mathrm{I}_e(\mathrm{mA})$. Best fit values are obtained by minimizing the residuals between the beam-current-normalized measured count

Fit Detector Response Model Parameters to the Measured Counts
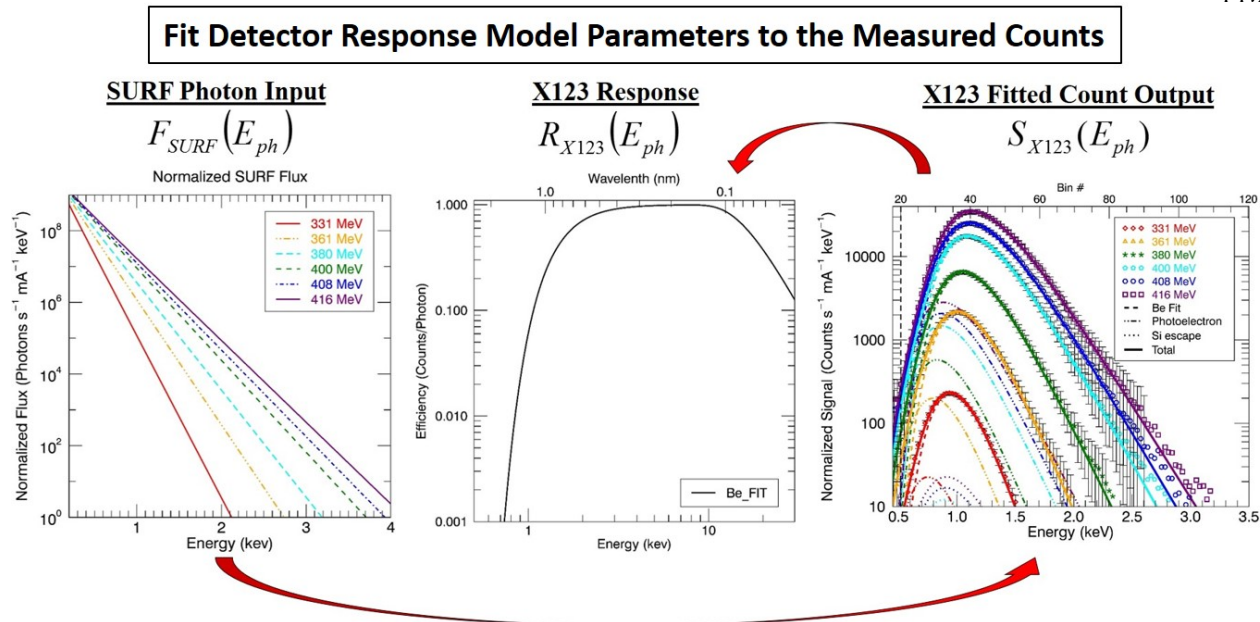
Figure 8.6: Outline of NIST SURF Multienergy technique to estimate the X123 spectral response. We fit a model of detector response parameters to the measured count flux from the SURF photon flux. Fitting the measured counts over the 0.5 - ∼3.0 keV spectral range allows us to estimate the entire spectral efficiency from 0.5 - 30 keV from the model parameters. The main fit parameter is the Be window thickness. Other subsidiary components include contributions from escape of Si fluorescence photons from K and L (2s and 2p) excitations and photoelectrons produced in the Be window.

flux and the model-estimated count flux, forward modeled from the beam-current-normalized input SURF flux convolved with the modeled instrument response.

Figure 8.7 displays the results of the Multienergy fit for the Be window thickness. The Be window thickness is the strongest dependent variable for the X123 spectral response. We compute the mass attenuation coefficient per photon energy following the analysis provided by Henke et al. 1993 [74] and proceed to fit the Be window thickness from transmission and absorption properties. The detector bulk silicon and silicon oxide transmission and absorption properties are also taken from Henke et al. 1993 calculations and are fixed at the Amptek stated nominal thickness (500 μm for the depletion depth of the SDD). Any uncertainties in the silicon absorption parameters would affect the response at the high energies ($\geq$10 keV), which we cannot measure with SURF.

SURF Multienergy Results		
Beam Energy (MeV)	**Best fit Be thickness (µm)**	**MC Best fit thickness (µm)**
331	24.62	25.09
361	24.74	24.42
380	25.08	25.18
400	25.34	25.50
408	25.35	25.53
416	25.48	25.43
Average estimate*	25.2	25.21
Uncertainty of energy fit type*	0.3	0.56
Final Estimate*	25.2	
Final Uncertainty*	0.42	

Figure 8.7: Beryllium (Be) thickness fit results from the Multienergy SURF flux input to the X123. 10 Monte Carlo (MC) trial analysis was performed about each beam energy best fit to improve estimates of the Be fit thickness uncertainty. The Final Estimate listed of the best fit Be thickness is the mean of the best fit values from 361 - 416 MeV. The Final Uncertainty is derived uncertainty from the best fit MC trials. * = signifies that all energies except 331 MeV where used to construct the final value

Other subsidiary components of the instrument response function, R_{X123}, include Si escape processes of fluorescence photons and an estimated photoelectron contribution from the Be window. The Si escape loss processes result in counts occurring at an energy bin that is the incident photon energy minus the Si edge energy ($\sim$1.8 keV for K, $\sim$0.15 keV for 2s, and $\sim$0.11 keV for 2p). These spectral detection shifts occur if the resulting Si escape photon actually leaves the active area of the detector without being absorbed, or else if the escape photon is reabsorbed by the detector, one retains the original photon energy in the detected energy bin.

The Si-K shell (1s) and Si-L shell (2s and 2p) photon escape processes are incorporated by computing the relative bulk mass (volume averaged rate) fluorescence photon escape rate for the active volume of the detector relative to the Si photopeak (all of the incident photon energy being absorbed in the Si active area and detected by the readout mechanism) efficiency (see Figure 8.8). Thus, the Si escape processes contribution changes dynamically for each

iteration of the detector response value during the fitting process. The probability for the Si escape process (mass attenuation coefficient contributions) are derived from Yeh and Lindau 1985 [160] and Henke et al. 1993 [74].
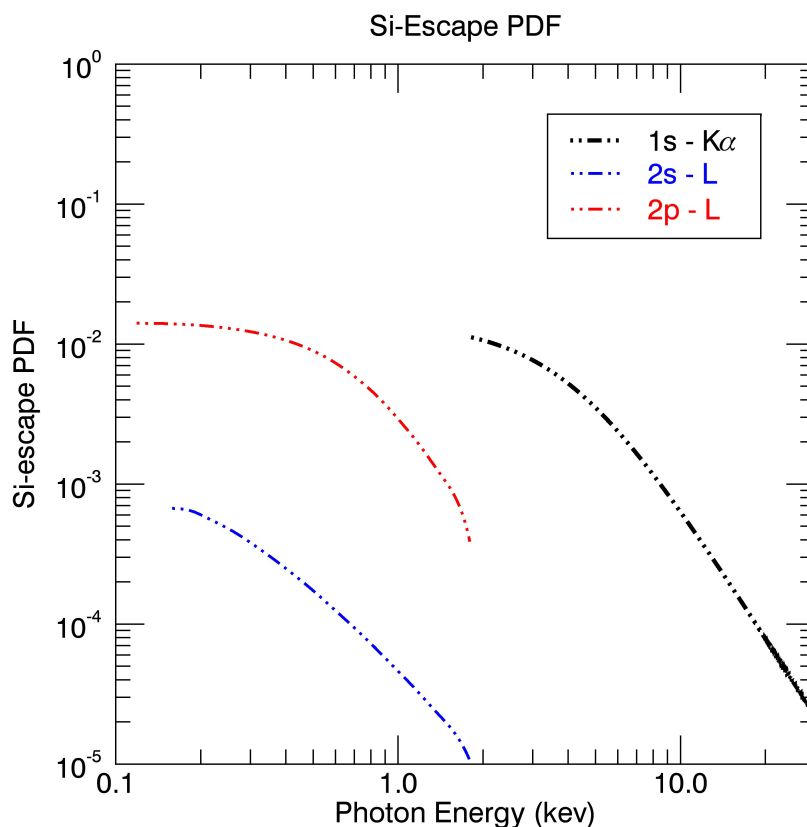
Figure 8.8: Si K, L (2s and 2p) escape probabilities normalized by the photopeak yield.

Figure 8.9 demonstrates that another process worth consideration is the liberation of photoelectrons in the X123 Be window that can eventually be detected and appear in the spectrum. These events will occur at lower energies than the initial photon distribution that created the photoelectrons due to the energy loss processes in migrating to the window surface, escape the surface and interact with the bulk Si if the electrons are energetic enough to overcome the negative detector surface bias voltage, the dead Si layer, and deposit their

energy in the active region of the SDD. The resulting contribution would be a continuum distribution at low energies ($E_{ph} \leq 1.5$ keV) for typical solar fluxes (peak in photon distribution) and window thicknesses (absorption probability spectrum of window) on our X123 units.
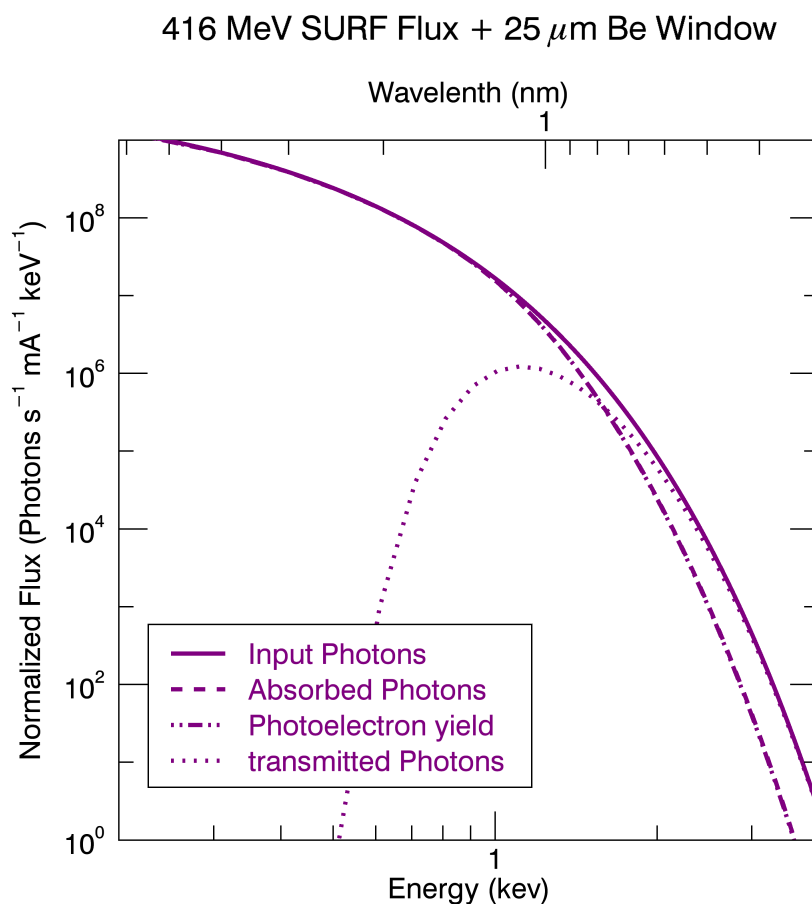
Figure 8.9: The photon fux propogated through an example 25 μm thick Be window clearly show the creation of photoelectrons below 3 keV. The challenging unanswered question is what is the electron energy distribution that interact with our detector. The mass attenuation coefficient for Be is taken from Yeh and Lindau 1985 [160].

Methods of repelling possible photoelectrons generated in the Be window by an additional electric grid have not been implemented in the MinXSS CubeSat architecture. Thus, we attempt to include Be photoelectrons in the X123 spectral response by dynamically in-

corporating this contribution via a simple model coupled to the fitted Be window thickness. The Spicer model [91, 41], is used to evaluate the probability of photoelectrons being created and eventually depositing their energy in the SDD active volume. The general procedure is outlined in Figure 8.10 and explained in depth below.

(1) A photon incident on the Be window is absorbed and liberates an electron (photo-absorption).

(2) This liberated electron is free to migrate the bulk Be and could travel to the detector side surface of the Be window.

(3) If the electron has more more energy than the bulk Be work function, Φ_{Be-WF}, then it can leave the surface and impact the detector.

(4) The electron can penetrate past the detector SiO dead-layer, deposit its energy into the detector Si active volume, generate electron-hole pairs and resister as an 'event'.

Equation 8.5 encapsulates all of these steps as the combination of the respective process' probability distribution functions. The most complete methodology in modeling all of these effects definitively for a specific detector-window apparatus is to construct a full 3D CAD model into software like GEANT4 [2] to work out the geometric dependence of specific interactions. We have not done such an elaborate investigation here, but have simply worked out the probabilities assuming all incident photons intercept the Be window aligned to the optic axis and average the effects over the azimuthal degree of freedom (cylindrical symmetry).

$$N_{pe}(E_{ph}, E_{pe}, x, \theta) = N_{ph}(E_{ph})A(E_{ph}, x)P(E_{pe})F_{ee}(E_{pe}, x, \theta, L)D(E_{ph}, E_{pe})a_{eff} \qquad (8.5)$$

$N_{pe}(E_{ph}, E_{pe}, x, \Theta)$ is the number of photoelectrons that leave the Be window and interact with the Si dift diode and combines the independent process of the Spicer formulation.
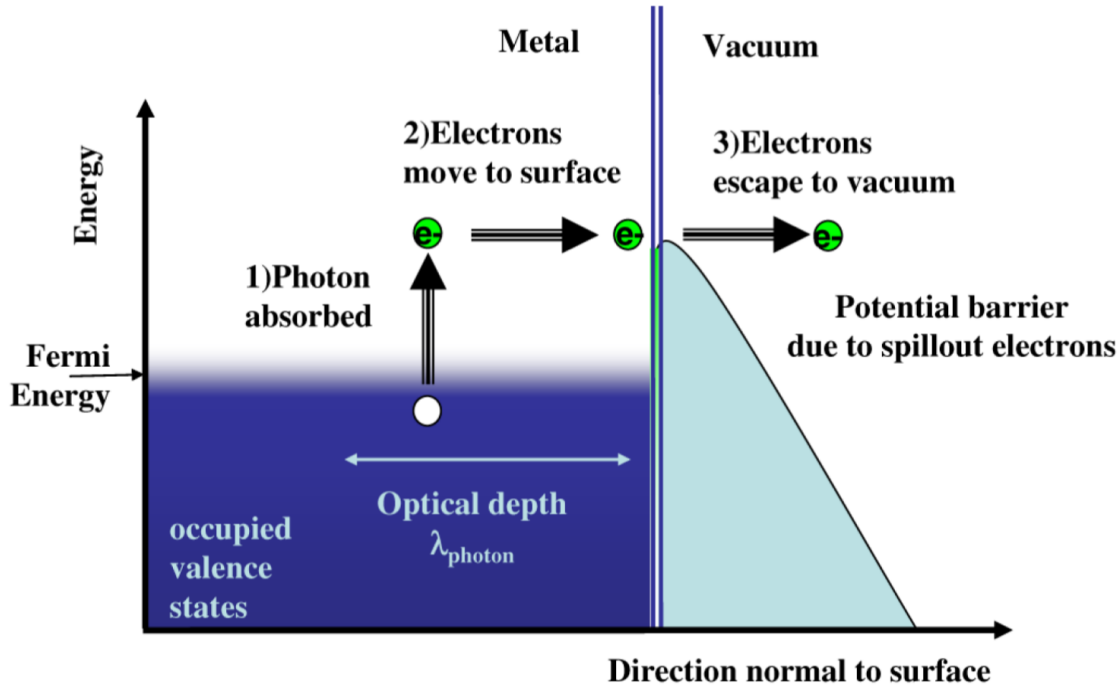
Figure 8.10: Diagram displaying the basic processes assumed in the Spicer model used to estimate the X123 Be window photoelectron contribution. Figure adapted from Dowell and Schmege 2009 [41].

E_{ph} is the photon energy, which must give the electron in the atom energy greater than the Fermi level ($E_{Be-Fermi} \approx 0.014$ keV) to contribute to free electrons in the lattice. E_{pe} is the photo electron energy, which is modified by the Be 1s binding energy, $E_{Be-1s-bind} \approx 0.112$ keV, ($E_{pe} \sim E_{ph} - E_{Be-1s-bind}$, because a dominant component of the Be photon absorption comes from the 1s bond). The electrons that make it out of the Be window must overcome the Be work function (ϕ_{Be-WF}) to leave the window surface. a_{eff} is an efficiency factor, to include photoelectron losses due to fringe fields, SiO dead layer, position in the detector, detection sensitivity, etc. The efficiency is determined by the Multienergy fit and constrained to be between $0 \leq a_{eff} \leq$. $N_{ph}(E_{ph})$ is the incident photon flux. $A(E_{ph}, x)$ is Beer 's Law, the fraction of photons that reach a depth x in the Be window, and defined in Equation 8.6.

$$A(E_{ph}, x) = e^{\frac{-x}{\lambda_{ph}(E_{ph})}} \tag{8.6}$$

$P(E_{pe})$, Equation 8.6, is the probability that photons at a depth x, will liberate electrons over an infinitesimally small incremental distance Δx (we take the limit as Δx $\to$ 0 and sum the contributions later).

$$P(E_{pe}) = 1 - e^{\frac{-\Delta x}{\lambda_{\chi e}(E_{ph})}} \tag{8.7}$$

$F_{ee}(E_{pe}, x, \theta, L)$, Equation 8.8, is the probability that a liberated electron at a depth x, will transverse a distance $\frac{(L-x)}{\cos\theta}$ (to make it to the detector side of the window) and reach the surface, where L is the total Be window thickness. Electron-electron scattering is taken as the dominant interaction process to inhibit the migration of electrons in the respective media with the mean free path calculated from asymptotic fits from Zjaja et al. 2006 [163] and displayed in Figure 8.11.

$$F_{ee}(E_{pe}, x, \Theta, L) = e^{\frac{-(L-x)}{\lambda_{e-e}(E_{pe})\cos\theta}} \tag{8.8}$$

This requires an electron trajectory to fall within a cone angle that does not put the electron at the 'walls' of the window. Using the ratio of normal to total electron momentum $\cos\theta_{max} = \frac{P_{normal}}{P_{total}} = \left(\frac{\phi_{WF}}{E_{ph}+E_{pe}-E_{Be-Fermi}}\right)^{0.5}$. $D(E_{ph}, E_{pe})$ is the fraction of electrons that fall within the cone defined above, Equation 8.9.

$$\begin{aligned} D(E_{ph}, E_{pe}) &= \frac{1}{4\pi} \int_0^\theta \sin\theta' d\theta' \int_0^{2\pi} d\phi \\ &= 0.5\left(1 - \cos\theta\right) \\ &= 0.5\left(1 - \left[\frac{\phi_{WF}}{E_{ph} + E_{pe} - E_{Be-Fermi}}\right]^{0.5}\right) \end{aligned} \tag{8.9}$$

Technically, the integration of $D(E_{ph}, E_{pe})$ over the angle θ should occur over the entire expression of $N_{pe}(E_{ph}, E_{pe}, x, \Theta)$ because of the θ dependence in $F_{ee}(E_{pe}, x, \Theta, L)$, in the exponential. We neglect this contribution in the exponential because the of the strong dependence of the electron mean free path. The majority of photoelectrons that will be

Be Electron Mean Free Path
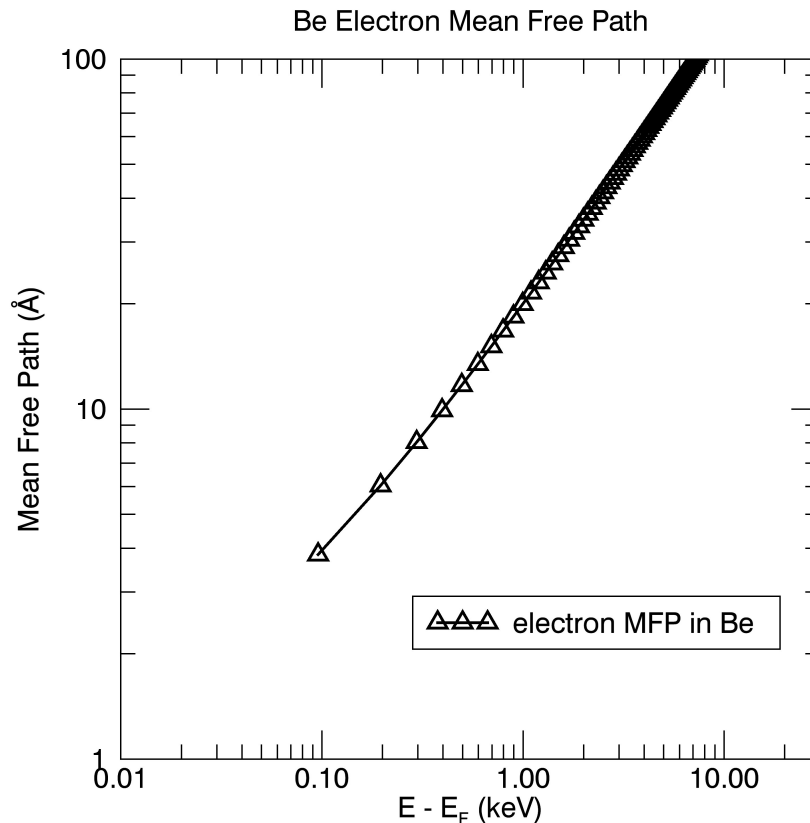
Figure 8.11: Calculations of the electron mean-free-path in Be, assuming that the main interation is electron-electron scattering [163].

generated and be able to interact with our detector to create a signal will be liberated by photons in roughly the last 1 μm of the window (due to the electron-electron scattering displayed in Figure 8.11).

Equation 8.5 is evaluated (numerically) by taking the limit of $\Delta x \to 0$ and integrating the photoelectron contribution over each iteration of a Be window thickness during the fitting process. I have implemented many approximations to obtain the final expression of Equation 8.5 to obtain an estimation of the photoelectron contribution. This is not an exact expression. Even with all the considerations here, there are still large uncertainties in the

Be Photoelectron Escape Cone Angle PDF
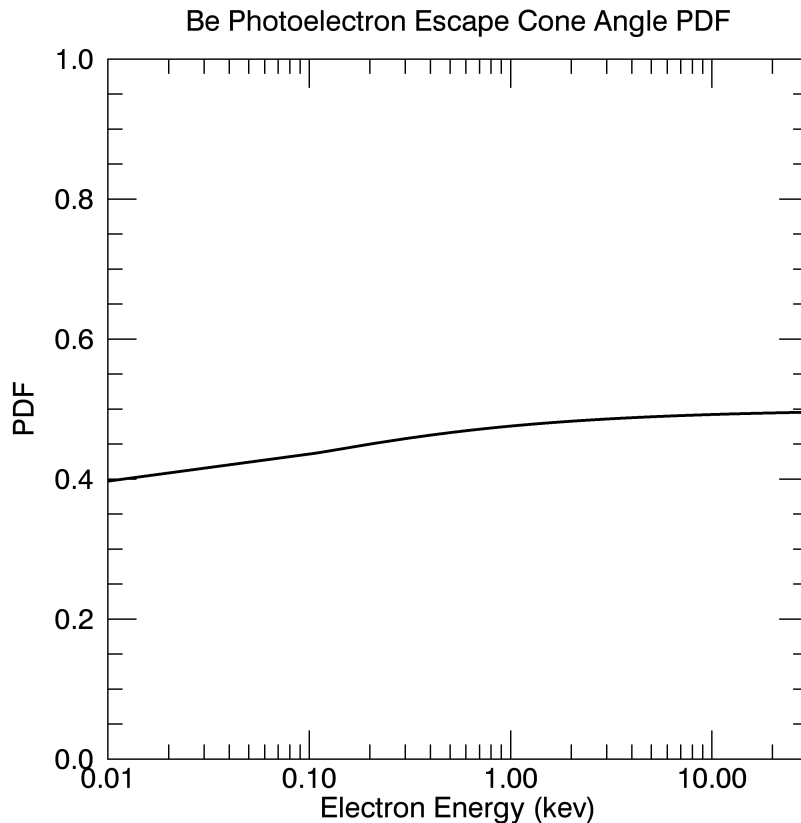
Figure 8.12: Be photoelectron cone angle dependence, Equation 8.9. The probability that an electron of a certain energy (created from a near collimated photon - aligned with the optical axis) will propagate in the forward direction inside a cone angle towards the X123 detector.

exact geometry of any fringe electric fields on the detector, the exact dead-layer thickness, and the propagation direction into the detector active area. The negative bias near the front end of the detector will act to de-energize the impinging Be window liberated electrons and shift their energy spectrum that will be recorded by the X123. Thus in the Multienergy fitting process this photoelectron energy centroid is allowed to vary in addition to the overall photoelectron yield (giving a fixed electron energy distribution shape, but with a variable energy position and amplitude). This procedure results in Figure 8.6 fits which are consistent

across the SURF electron beam energies for a consistent paring of Be photoelectron yield (amplitude) and electron group energy loss (energy offset). Futhermore, the results all give similar Be window thickness results, owing to the validity of the approximations assumed here. Again, future characterization should implement full 3D CAD modeling like GEANT4.

8.2.3   Detector Response Matrix

In reality, the resulting count space is discrete and not continuous after the integration of the bracketed quantity in Equation 8.3 to create the binned data. Thus, one can interpret the photon-count *redistribution* function as a Detector Response Matrix (DRM) for the X123 spectrometer, with columns, k, that connect the incident photon energy to the row, j, which are the loses recorded in the X123 energy bins. This is listed in Equation 8.10, where $\overrightarrow{C}_\mathbf{j}$ is the detected count rate spectrum, $\overline{\overline{\Re}}_{\mathbf{k,j}}$ is the X123 DRM and $\overrightarrow{S}_\mathbf{k}$ is the source intensity. The DRM contrubutions were estimated from the NUST-SURF multienergy technique.

An example of the MinXSS X123 DRM is displayed in Figure 8.13. The DRM incorporates the detection efficiency, the probability that a photon stopped in the detector by a photo-electric interaction will be recorded. The probability of the full-energy being deposited in the detector gives the diagonal response or photopeak efficiency. Additionally, there are loss processes such as fluorescence emission [88], which result in an event being recorded at a lower energy. These are the off-diagonal terms in the DRM and include loss processes such as Si K and L (2s and 2p) escape. Also included are signal contributions from Be window photoelectrons. These model contributions are included in the functional form of $\overline{\overline{\Re}}_{X123}$ and are also discussed in [115].

$$\overrightarrow{C_j} = \overline{\overline{\Re}}_{\mathbf{k,j}}\overrightarrow{S_k}. \tag{8.10}$$

Another effect in MinXSS spectra is Compton scattering, but to a much smaller degree than Si-escape (both because of the lower probability and the lack of *detectable* higher energy
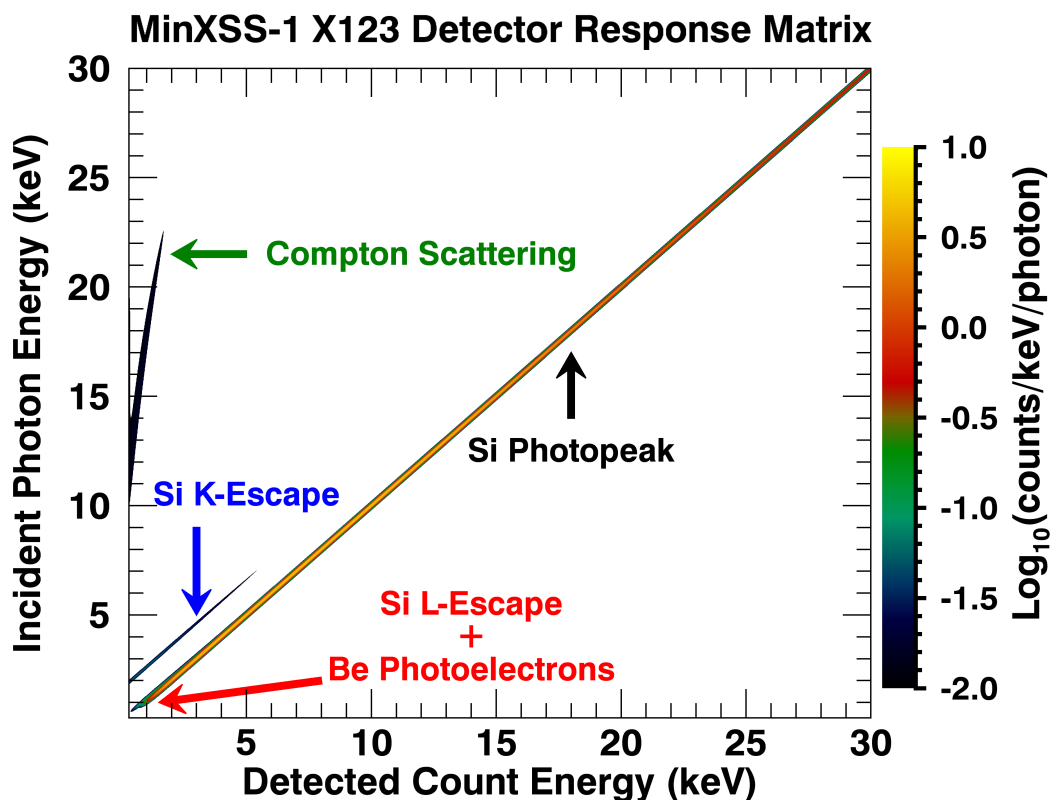
Figure 8.13: Example of the X123 Detector Response Matrix (DRM) which includes Si photopeak, Compton scattering, Be window generated photoelectrons, and Si K and L (2s and 2p) escape processes. The DRM gives the probability that an incident photon of energy E_1 will deposit energy E_2 in the detector.

photons greater than 10 keV). Compton scattering is unlikely to be a major contaminant in the quality of MinXSS spectra due to the small effective area of X123 coupled with the steeply decreasing solar spectra at high energies. Only large X-class flares could produce large enough signal at photon energies greater than 10 keV to make Compton scattering important, but other issues such as photon pile-up and X123 dead-time will occur before that becomes relevant. We have used a flux linearity test at SURF to quantify when pile-up and detector dead-time will become severe and discuss this in Section 8.2.4
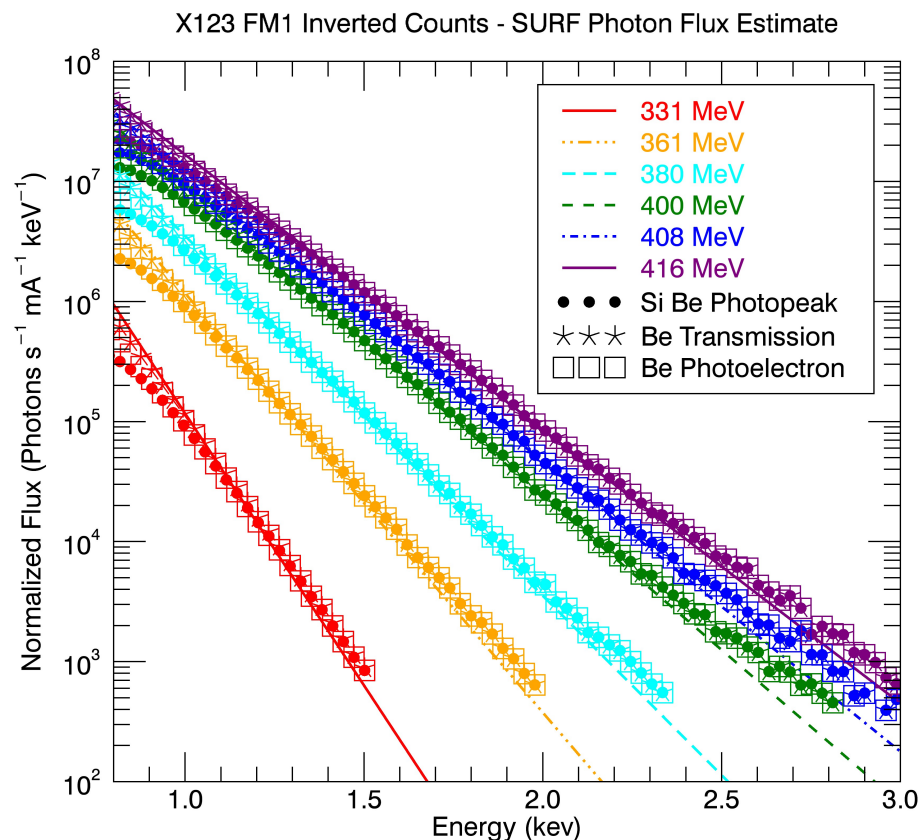
Figure 8.14: Estimation of the SURF flux incident on the X123 aperture, inverted from measured counts. The solid lines are the known SURF input flux, the symbols are three different response model aspects used for the inversion. The photopeak component (corrected for Si escape effects and Be photoelectrons) are the filled circles, the Be transmitted photon flux component are the asterisks and the Be photoelectron component are the open squares. All three model component inversions agree well down to 1 keV. Thus, we can confidently invert to estimate the photon flux over these energies.

To verify the validity of the X123 estimated spectral response we have 'inverted' the measured NIST SURF X123 counts to extract the incident photon flux. The result should agree reasonably well with the known input photon flux from SURF, where the spectral response is well determined and the measurement signal to noise is high. This inversion technique is independent of forward fitting a spectral model to the measured count flux,

where many spectral models are dependent on assumed plasma parameters (temperature, densities, chemical abundances, etc.), the spectral lines included in the model and experimentally determined atomic parameters (like oscillator strengths). Thus, MinXSS measurements can be used as an irradiance product and to help improve spectral models such as the CHIANTI Atomic Spectral Database [37, 161]. Figure 8.14 demonstrates that confidence in estimating the photon flux incident upon MinXSS-1 X123 down to 1.0 keV. Inverted photon flux estimates are created from the individual X123 response function components listed in Figure 8.6.

8.2.4   Linearity of Response

It is desired to have a linear response vs. light source intensity levels for the MinXSS instruments. The linearity of response for XP and X123 were assesssed at NIST SURF (Figure 8.15) plus early data from the MinXSS-1 mission (Figure 8.16). The count rates discussed here are the measured counts summed over the spectrum during an accumulation divided by the accumulation time. We took advantage of Equation 8.1, the SURF flux linearly scaling with the beam energy, to test the linearity of the X123 response by increasing input SURF photon flux. Figure 8.15 shows the X123 fast and slow counter responses to the SURF increasing photon flux. The measurements in Figure 8.15 are used to estimate the input count rate in Figure 8.16 and are not corrected for dead-time effects for the various peaking times of the slow and fast counters which can impact results. These have been accounted for in the data in Figure 8.16 and through the rest of this dissertation. The procedure to correct for these effects is discussed below.

MinXSS data products contain many types of time parameters, but it is best to use the actual measured count rates (counts per second; cps) to deduce the severity of dead-time and pile-up effects vs. directly using the time parameters in the data sets. The X123 spectral data can be corrected for dead-time losses up until a maximum input count rate for the slow counter, $[C_s]_{max}$, which depends on the slow counter peaking time, τ_s. The
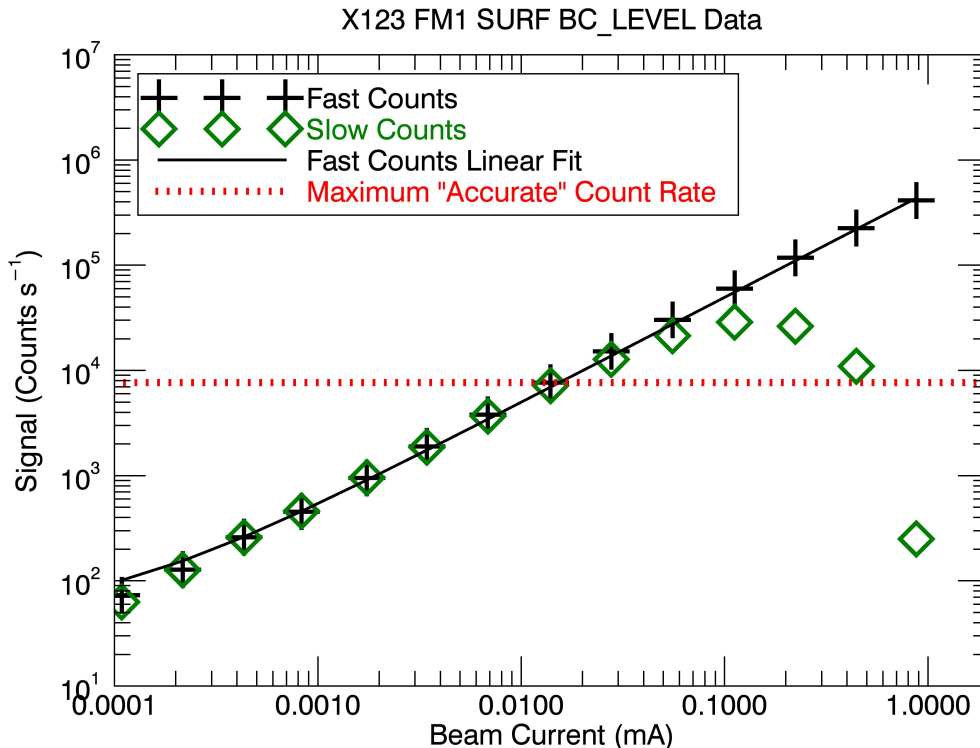
Figure 8.15: NIST SURF X123 linearity test shows a maximum count rate limit of $\sim$8,000 counts s^{-1}, for an accurate spectrum. Maximum count rate is deduced from the last measured count rate, the red dotted lines, where the X123 slow counter (peaking time = 4.8 s), the green diamonds, and fast counter (peaking time = 100 ns), the black pluses, begin to diverge. The black solid line is a linear fit to the fast counts. The SURF flux spectrum depends linearly with the SURF beam current (I_e), so a linear increase in the SURF beam current leads to a linear increase in the SURF photon flux.

slow counter peaking time directly effects the slow counter dead-time, τ_{ds}, via the relation $\tau_{ds} = B(\tau_s + \tau_{flat})$, where B is a constant (over the mission) per detector, and τ_{flat} is the trapezoidal shaping flat top time. The maximum input count rate that the slow counter can be corrected for is $[C_s]_{max} = \frac{1}{\tau_{ds}}$. This corresponds to $\sim$85,000 cps for MinXSS-1 (4.8 μs peaking time) and $\sim$255,000 cps for MinXSS-2 (1.2 μs peaking time). Below, we discuss the dead-time correction process with the NIST SURF data and the on-orbit specific correction process.
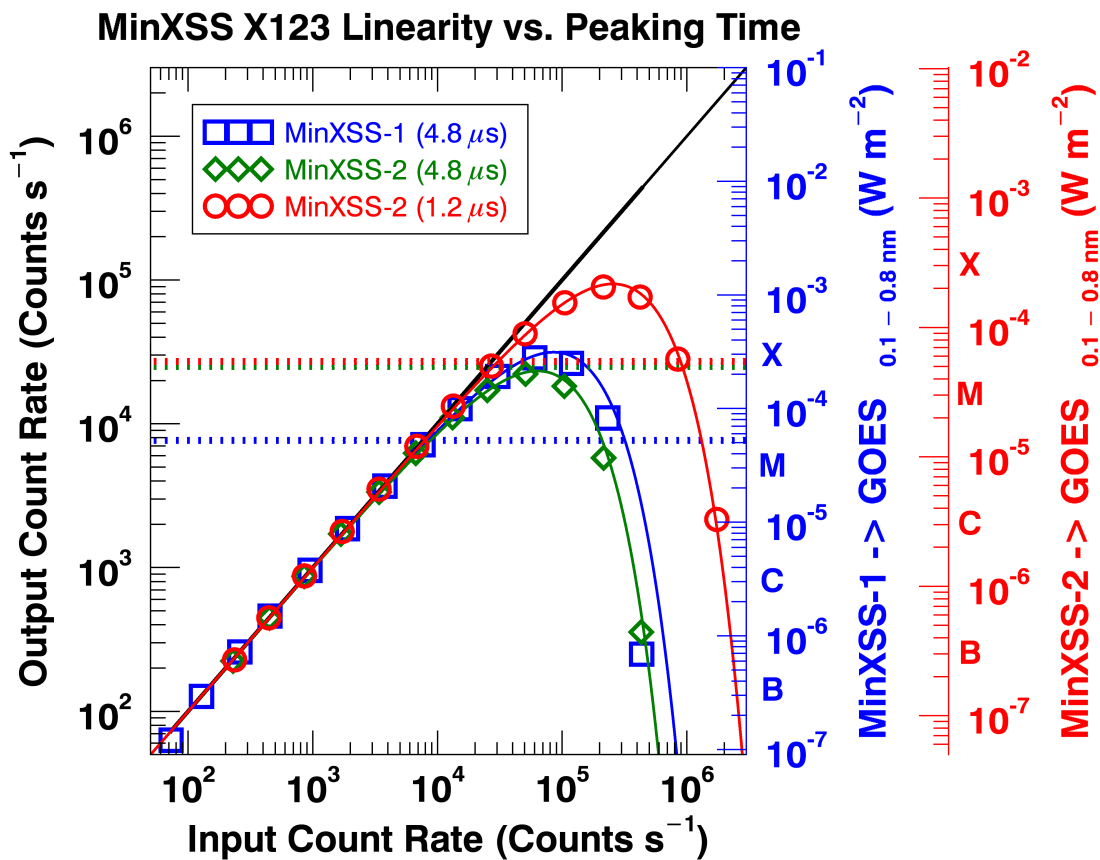
Figure 8.16: X123 detected (output) count rate for an input (actual) count rate, for the MinXSS-1 (blue symbols) and MinXSS-2 (green and red symbols) expected operating peaking times. The lines indicates the dead-time model fit. Comparison of a MinXSS-1 observation based scaling to GOES flux levels (blue vertical axis) and model estimations for MinXSS-2 (red vertical axis). The horizontal dotted lines indicate the count rate where dead-time effects, pile-up effects and detector paralysis begin to occur. Spectra above these count rates must be heavily processed prior to analysis.

The MinXSS-1 X123 has a JFET preamplifier and MinXSS-2 with the X123 Fast SDD unit has a MOSFET preamplifier, allowing for lower noise and improved utility for shorter peaking times. The deduced non-dead-time corrected maximum count rate for MinXSS-1 is ~8,000 cps for its chosen 4.8 μs peaking time. The deduced non-dead-time corrected maximum count rate for MinXSS-2 is ~7,000 cps for the 4.8 μs peaking time and ~27,000 cps for the 1.2 μs peaking time. The latter will be the MinXSS-2 nominal operational peaking

time. The horizontal thick dotted lines in Figure 8.16 display these non-dead-time corrected spectrally integrated maximum count rates. These listed count rate values (C_s) are from the slow counter, which creates the X123 spectrum. The 'input' count rate (C_{in}) is determined from the measured fast counter count rate (C_f) corrected for fast counter dead-time (τ_{df}). The fast counter has a shorter peaking time of 100 ns (τ_{pf}) and an effective pair resolving time of ~120 ns ($\tau_{pair} = \tau_{df} = 120$ ns). The fast channel is used to determine if each event is 'valid', if the X123 slow channel and hence the Digital Pulse Processor should include it in the spectrum. This helps minimize photon peak pile-up, where more than one photon is absorbed by the detector within the peaking time and the event is recorded as the sum of the photon energies. As a consequence of the much shorter peaking time, the fast channel has much lower spectral resolution and thus is not the preferred channel for accurate spectra accumulation.

All photon-counting X-ray detectors exhibit some form of count rate loss due to dead-time [88]. At high count rates losses due to dead-time can become significant and expressions to approximate the true count rates for X123 are provided by [131]. The linear black solid line in Figure 8.16 displays the relation between the input and dead-time corrected fast counter output count rates. The dead-time correction for the fast counter count rate follows the non-paralyzable model, $C_{in} = \frac{C_f}{(1 - C_f \tau_{df})}$. C_{in} resembles the 'true' input count rate. This expression is accurate to within 5% for true count rates $\leq$ 500,000 cps. For the NIST SURF calibrations we calculate C_{in} directly from the fast counter and use $C_{model} = C_{in} e^{-C_{in} \tau_{ds}}$, the paralyzable model, to directly estimate the count rate in the slow counter (C_s). The expression for C_{model} assumes a Poisson arrival probability for photons and registered events. The blue (MinXSS-1, $\tau_s = 4.8$ μs) , green (MinXSS-2, $\tau_s = 4.8$ μs) and red (MinXSS-2, $\tau_s = 1.2$ μs) solid lines in Figure 8.16 are the calculated dead-time suppressed slow counts (C_{model}). The corresponding measured slow counts (C_s) are the symbols.

Overall, these predictions agree with the measured data until pile-up effects cause the measured count rate to lie below the calculations. The resultant pile-up effects depend on

the shape of the photon flux spectrum, but in general, will be noticeable for input count rate values greater than the peak modeled count rate distribution C_{model} (the solid lines in Figure 8.16). This occurs for $C_{in} > \frac{1}{\tau_{ds}}$. τ_{ds} will be included in the MinXSS processing software release. Thus, in theory, if one has quality fast and slow counter measurements during an observation the true count rate can be deduced to within 5% until 500,000 cps. Unfortunately, this NIST SURF procedure to correct the slow counter for dead-time effects is not directly applicable on-orbit because (1) the low energy thresholds for the fast and the slow counter may not be (and currently are not) at exactly the same energy, and (2) on-orbit the MinXSS-1 fast counter has exhibited high noise (radio beacons, reaction wheel momentum changes, etc.) and thus cannot be used quantitatively, only qualitatively. MinXSS-2 ground testing does not exhibit the same noise characteristics and should have reduced fast counter noise on-orbit.

As an alternative to estimate the true spectrum count rate on-orbit one can use the merit function in Equation 8.11, $\mathcal{L}$, where n is the variable to estimate the spectrally integrated slow counter count rate without dead-time depression, in units of cps. The minimum of $\mathcal{L}$ with the restriction that, $C_s < n < \frac{1}{\tau_{ds}}$ should yield the input count rate (n_{min}), or 'true' count rate that best estimates the measured spectrally integrated slow count rate, C_s. It is apparent from Figure 8.16 that the model function C_{model}, is not monotonic nor uniquely defined for input count rates in the interval $0 < n < \infty$. Thus, to obtain a feasible result one must restrict the search domain to be between $C_s < n < \frac{1}{\tau_{ds}}$. For $n > \frac{1}{\tau_{ds}}$ other effects like pile-up must also be corrected for. Additionally, the quantity of the difference between the observed count rate and model count rate is squared to ensure positive concavity and thus the realization that n_{min} will be the best fit result. The ratio of the best fit value to the actual spectrum summed count rate yields a correction factor P, $(P = \frac{n_{min}}{C_s})$ that can be multiplied by each binned count rate in the spectrum to adjust for dead-time during the respective integration. Using this technique, the MinXSS data utility range can be extended to counts rates determined by $C_s < \frac{1}{\tau_{ds}}$. As a proxy to indicate when these correction will

be needed, correlated XP data or the GOES XRS flux levels can be used.

$$\left[\pounds(C_s < n < \tfrac{1}{\tau_{ds}}, C_s, \tau_{ds}) \right]_{min} = \left[\left[C_s - C_{model}(C_s < n < \tfrac{1}{\tau_{ds}}, \tau_{ds}) \right]^2 \right]_{min}$$
$$= \left[\left[C_s - n e^{-n\tau_{ds}} \right]^2 \right]_{min} \tag{8.11}$$

Early MinXSS-1 data from different GOES levels has been used to estimate the blue vertical axis in Figure 8.16, which roughly relates the GOES 0.1 - 0.8 nm (W m^{-2}) flux levels to the spectrally integrated MinXSS counts. The X123 counts are totaled across the *entire* operational spectral bins ($E_{ph} \gtrsim 0.8$ keV,) and not limited to the corresponding GOES 0.1 - 0.8 nm band (1.55 - 12.4 keV). This relation is to serve as a general guide of what count rates one would expect for specific GOES levels and can plan for X123 effects as necessary (photon peak pile-up, dead-time, etc.). The MinXSS-2 estimates are *modeled* counts based on the response functions and process described in Section 8.2.2, in Equation 8.3, where the photon source term, S is generated from inverting the MinXSS-1 measured count spectrum. These rough estimates are displayed as the red vertical axis in Figure 8.16. Examples of the count rate, and estimated photon flux as a function of GOES levels from the early aspects of the MinXSS-1 mission are discussed in Section 8.2.4.

8.3   MinXSS Data Products

The publicly available MinXSS data can be accessed on the MinXSS website http://lasp.colorado.edu/home/minxss/. These data include Level0d, Level1 - 4 products with one of the most relevant products being the Level1 spectral irradiance (photons s^{-1} cm^{-2} keV^{-1}). Measured count rates, spacecraft position, Sun-Earth distance, pointing information, etc. are also included. MinXSS data processing software to convert raw data to science quality data will be incorporated into SSW soon.

In detail we expound upon the data product types, some of which will be released to the public.

- Level0C - Not publicly available. Raw housekeeping data and X123 science packets on their native time grid.

- Level0D - Publicly available. Interpolated housekeeping data to the MinXSS instrument science packets times. The majority of unit conversions have been performed.

- Level1 - Publicly available. MinXSS instrument data filtered for 'science quality' data. All data deemed 'not adequate' for scientific analysis has been removed. These data include the native 10 second integrations, 1, 15, and 60 minute averages.

- Level2 - Not currently publicly available. Level 1 data corrected for degradation and long-term 'instrumental' trends.

- Level3 - Daily average (1440 minute) of the Level 1/Level 2 product.

- Level4 - Publicly available. Level1 data fit with the OSPEX Suite to derive 1TCoronal, 2TCoronal, 1TFree, 2TFree, 1TAllFree and 2TAllFree model estimations.

Chapter 9

MinXSS Plasma Diagnostic Capabilities and Instrument Performance

Most traditional astrophysicists that soley care about the science of an astrophysical object ('pure' scientist) will not care much about the instrument architecture, testing and details that I mention in Chaper 8. They just want to know a few basics about an instrument. 1) what type of measurement does it make (imaging, spectra, spectral-imaging and their respective resolutions), 2) what time scale can it make measurements on (integration times, temporal resolution), 3) how often does it conduct observations and probably most importantly, what diagnostic capability does this instrument have for astrophysical objects. In the case of the Sun and scientist interested in the properties of the solar corona, this means what kind of temperature and chemical composition discrimination is possible. To address these valid concerns, I have constructed temperature response functions for the MinXSS X-ray instruments. I have also implemented spectral fitting models for the MinXSS X123 data and performed cross-calibrations with other instruments. Let's begin with the temperature response functions.

9.1   Temperature Response Functions

To connect the MinXSS instrument spectral response to the ability to detect plasma of differing temperatures, one can calculate a temperature response curve. The temperature response curve is the signal expected in an instrument from the plasma photon emission. This response curve is built as a function of plasma temperature iteratively, by using many

isothermal emission models of differing temperatures. The temperature response curve is generated by using a spectral syndissertation model to create an X-ray emission profile from physical parameters (temperature, density, plasma emission measure, elemental abundance, etc.) vs. photon energy, folding this through the MinXSS instrument response and totaling the counts over a specified number of energy bins (creating an effective energy bin width for this model) for X123 and the estimated XP total current (in fC units). In general, the spectral emission model used is computed for a range of isothermal plasma temperatures. This grid of input temperatures leads to a grid of MinXSS instrument counts per isothermal temperature. Equation 9.1, Equation 9.2, and Equation 9.3 show the functional form of the calculation to compute the temperature responses for XP and X123 respectively.

$$F(T)_{XP} = G_{XP} \int_0^\infty \left[\int^{\Omega_\odot} S(E_{ph}, \Omega, T) A_{XP} R_{XP}(E_{ph}, \Omega) d\Omega \right] dE_{ph}. \tag{9.1}$$

$$F(T)_{X123\ bin,j} = \int_{E_{min,j}}^{E_{max,j}} \left[\Upsilon(E_{det}, T) \right] dE_{det} \tag{9.2}$$

$$\Upsilon(E_{det}, T) = \int_0^\infty \int^{\Omega_\odot} S(E_{ph}, \Omega, T) A_{X123} \overline{\overline{\mathfrak{R}}}_{X123}(E_{ph}, \Omega, E_{det}) d\Omega dE_{ph} \tag{9.3}$$

An example of the MinXSS XP and X123 temperature response curves are in Figure 9.1. There are differences in the temperature response function depending on the abundances used in spectral emission model for the soft X-rays are primarily due to the variance in the low first ionization potential (low-FIP) elements of Fe, Mg, Si, Ca and the mid-FIP element S. Elements with a first ionization potential less than 10 eV have been measured to be overabundant with respect to the high-FIP elements in the solar corona when compared to photospheric values. This has become known as the FIP effect in the Sun. Summaries of the variations in Solar abundance are given by [93] and [138]. Thus, we calculate the temperature response for a range of abundances and display the abundance values corresponding to 'common' reference values in literature. Results displayed are for traditional 'Coronal' [48]

(4 times photospheric for the low-FIP elements), 'Hybrid' [138] ($\sim$2.1 times photospheric), and one of the latest photosphere [23] abundances. The MinXSS instrument temperature response begins to deviate for plasma temperatures greater than 2 MK, primarily due to the ions of the low-FIP elements.
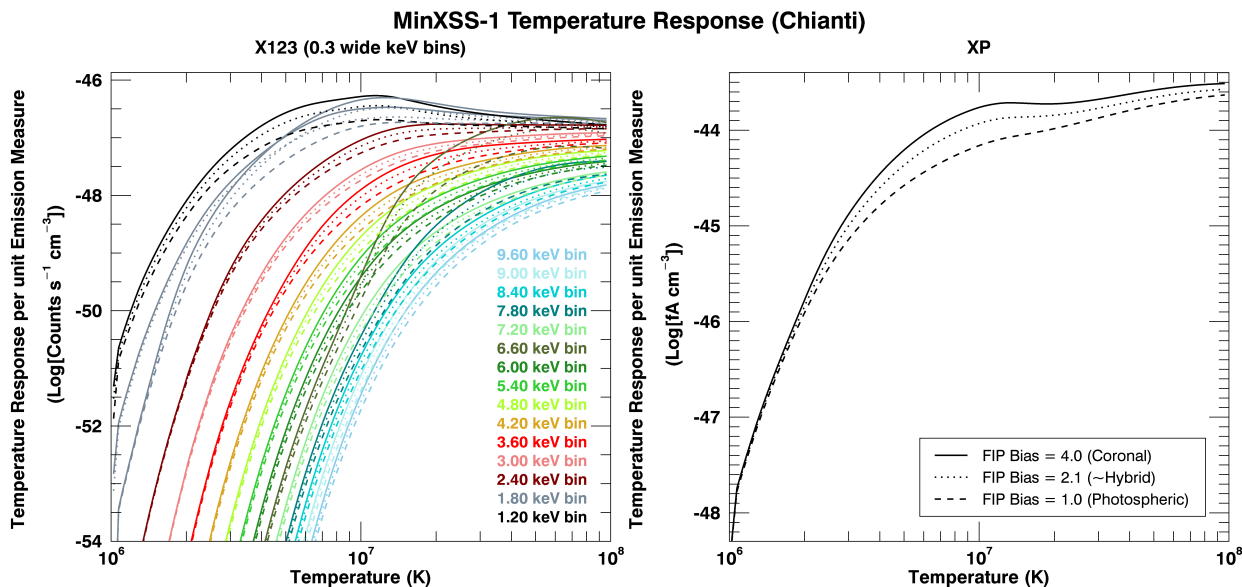
Figure 9.1: An example of the X123 and XP temperature response functions for a spectrum summed to 0.3 keV wide bins for X123 (ten 0.03 native bins). The temperature response is in volume emission measure units of cm^{-3}. The isothermal spectral emission model used to compute the spectral response of the MinXSS instruments per plasma temperature is a spectrally extended version of the SolarSoftware (SSW) f_vth function (which uses the Chianti Atomic Database). The temperature response in soft X-rays can vary due to differences in the abundance of the low-FIP elements of Fe, Mg, Si, Ca and the mid-FIP element S used in the spectral emission model. Thus, we display the temperature response for traditional 'Coronal' [48] (4 times photospheric for the low-FIP elements), 'Hybrid' [138] ($\sim$2.1 times photospheric), and one of the latest photospheric [23] abundances. The MinXSS instrument temperature response begins to deviate for different abundances for plasma temperatures greater than 2 MK, due to the ions of the low-FIP elements.

Figure 9.1 demonstrates the temperature range over which MinXSS X123 and XP can reliably extract information. X123 and XP inferences are biased towards the plasma temperatures greater than 2 MK. The dominant emission for non-large-flaring-times is expected to be around 2 - 4 MK. Thus, MinXSS will be able to infer non-large-flaring Sun properties

between 1.5 - ∼4 MK with high confidence, but limited capabilities for temperatures below 1.5 MK. The temperature response flattens for the X123 lower energy bins (≤ 3 keV) for temperatures greater than ∼4.5 MK. Due to this flat nature and with limited significant counts from energy bins greater than 3 keV (which is not expected from the X123 relatively small effective area), X123 can only set upper limits on the emission measure, but cannot definitively constrain the temperature values for plasma hotter than ∼5 MK during non-large-flaring times. Plasma temperatures above ∼5 MK are expected for C, M and X class GOES flares. The higher energy bins (≥ 3 keV) are mostly sensitive to plasma temperatures greater than ∼5 MK, but need substantial photon flux for statistically significant signals. All these attributes demonstrate that MinXSS has the greatest diagnostic capability for large flares on the Sun.

9.2 Emission Measure Loci

Emission measure loci (em loci) provide a powerful diagnostic and a useful visualization tool to understand a spectral instrument's capability to infer plasma temperature distribution from a specific set of observations [153, 94]. Em loci can be calculated by taking the measured data (summed counts over a specified energy range for X123 or the total signal for XP) and dividing by the instrument's temperature response calculated for that energy range, for the corresponding best fit elemental abundance and emission model, $emloci = \frac{Counts}{F(T)}$.

Figure 9.2 displays the MinXSS-1 X123 (solid colored lines) and XP (dashed black line) em loci for the pre-flare and flare peak on 2016 July 23. The different colors show the em loci of the various summed 0.3 keV wide energy bins (counts from ∼10 X123 bins summed) with a significant count rate (≥ 0.05 counts per second per nominal bin), which depict the energy ranges that best restrict the emission at specific temperatures. In general the higher X123 energies are better for inferring the hotter plasma conditions.

The em loci in Figure 9.2 scale up and down with the MinXSS signal (comparison of non-flaring and flaring times). If the plasma was isothermal, then one would expect an

isothermal fit to 'touch' (or overlap with) the em loci at the corresponding temperature value. This is because all of the radiant energy would be comming from plasma at this one temperature. Additionally, where the various em loci curves for different energy bins intersect is roughly the location that yield the isothermal temperature and emission measure that best describe the plasma. More importantly, the collective minimum of all the em loci provide an envolope indicating the maximum amount of light radiated from all plasma temperatures. This property is extrmely valuable, as the solar coronal is multi-thermal and hence, DEMs are best at describing the plasma temperature distribution from radiation measurements.
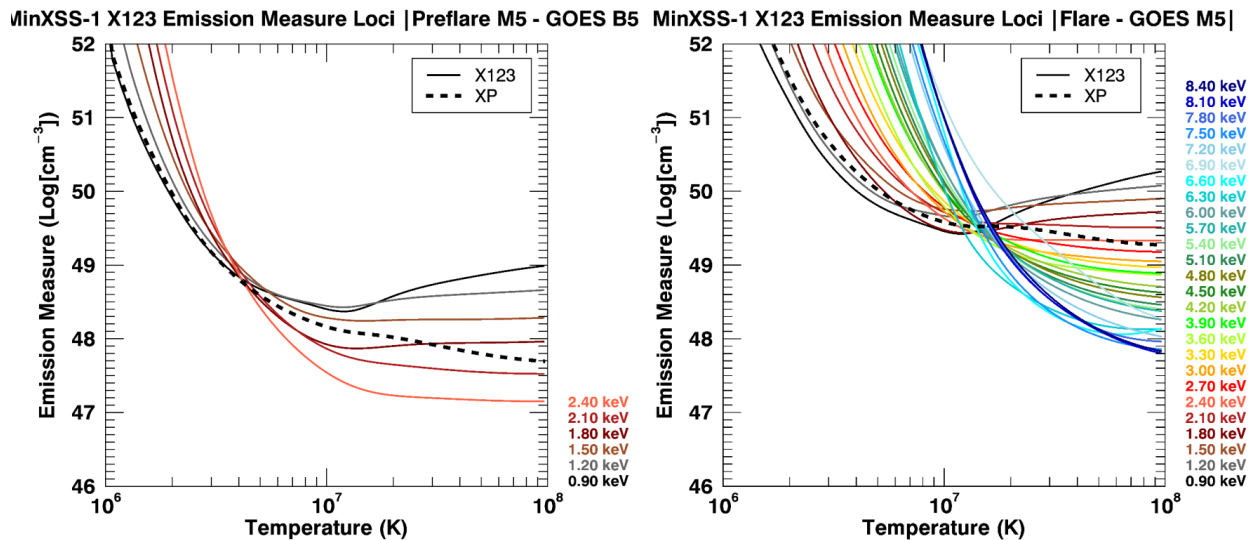
Figure 9.2: MinXSS-1 X123 and XP emission measure loci for pre-flare emission at roughly a GOES B5 level before the M5.0 flare on July 23, 2016 (left) and the actual flare (right). The solid colored lines correspond to X123 counts summed to 0.3 keV wide energy bins and the dash-dotted lines are the XP loci. The rainbow keV values in the top left plot indicate the color code for the minimum energy bin use for each X123 em loci. The em loci indicate the maximum emission if all the plasma was isothermal for each summed energy bins. The near convergence of the em loci curves in emission measure and temperature space indicate that the flare (right plot) is much hotter and more dense than the pre-flare spectrum (left plot)

9.3   1T, 2T and multi-T Spectral Fits

The unique spectrally resolved measurements of MinXSS are suitable for parametric fits of single temperature (1T), two temperature (2T), multi-temperature (multi-T) and differential emission measure (DEM) models to estimate the plasma conditions. QS, AR and flare data over the possible total 6 year MinXSS mission combined with data from the observatories mentioned in Chapter 7 can be used to address current questions in solar physics. To test out the diagnostic capabilities of MinXSS and to compare results with GOES XRS and RHESSI, we have performed a series of parametric fits using the OSPEX (https://hesperia.gsfc.nasa.gov/ssw/packages/spex/doc/ospex_explanation.htm) programming suite in Solar Software, which utilizes the Chianti Atomic Database [36, 161], on the seven sets (includes pre-flare times) of data from GOES A5 to M5 levels during 2016 June - July. The uncertainties calculated on the fit parameters in this dissertation are basic OSPEX returned fits uncertainties, based on the curvature matrix, which assumes that the curvature has a local Gaussian shape.

We have used four models to fit the respective observations for comparisons between models. The best fit values are listed in Table 9.1, Table 9.2, Table 9.3, Figure 9.9, Figure 9.10 and Figure 9.11. In this analysis we denote a FIP-Bias value of 1 equal to photospheric which would have values similar to those in [23] and FIP-Bias of 4 equal to the traditional 'Coronal' abundance and are those of [48]. The first model is a simple one temperature, fixed coronal abundance (1TCoronal; $A_{low-fip} = 4$) model, which did not fit the data suitably for any of the seven data sets. There were large discrepancies for the elemental features labeled in Figure 9.7. The second model is a single temperature model in which the abundance of low FIP elements is allowed to vary through a single multiplicative factor, called the FIP-Bias. This model is called 1TFree, but it underestimates the pre-flare flux for photon energies greater than ~2.5 keV. The same 1TFree model did not fit the flare components well neither. For the times where there is not substantial counts for X123 energy bins > 2.5

keV, like the QS flux (GOES ∼A5) the 1TFree model provides an adequate fit.

The third model is a two temperature component with a single multiplicative factor for the FIP-Bias (2TFree). These fits consistently produce satisfactory results with reduced χ^2 between 1 - 4, except for the M5.0 flare. All pre-flare spectra in this dissertation are fit over the times listed in Table 9.1 with a 2TFree model. The flare-peak fits include an additional 2TFree model that is fit to account for the additional radiation on top of the fixed model pre-flare values. In this methodology the fixed pre-flare model during the peak-flare times serves as a background estimate. Thus, the result is a separate FIP-Bias for the 2TFree pre-flare and the flare-peak functions. Values near 4 for this fit class resemble traditional coronal values and values near 1 are photospheric.

The abundance models are sensitive to the 'humps' from emission line groups of Fe, Mg, Si, S, Ar, Ca, and Ni (where applicable) around ∼1.2 6.7 and 8.1, 1.7, 2.1, 2.7, 3.0, 4.0, and 8.1 keV respectively. For the 2TFree model, a FIP bias value of 3.48 is found for the QS spectra, for the pre-flare times values between 2.0 - 3.5 are obtained and lower values between ∼1 - 1.41 are obtained for the peak-flare spectral fits. It is clear that there is a difference in the estimated abundance from pre-flare to flare-peak and the lower abundance during the flare is consistent with recent literature [138, 38, 158]. The availability of the Fe and Fe+Ni complexes at 6.7 and 8.1 keV respectively, provide clear diagnostics for the abundance factors and in turn are weighted more heavily for the flare abundances. The lower abundance is also in line with the theory of plasma from the lower atmosphere flowing up to the higher layers of the atmosphere and radiating in X-rays and UV.

The forth model type is a two temperature component where each of the elements, Fe, Ca, S, Mg, Si, Ar and Ni are allowed to vary (2TAllFree) as long as there are sufficient counts in the X123 energy bins for the respective element's line group features in the spectrum. It is important to note that the Ni abundance scale factor is coupled to the Fe abundance scale factor. Thus, the Ni abundance is not a true independent inference. This is heritage in the fitting routine for the Fe+Ni complex near 8.0 keV and does not strongly skew the fits. The

2TAllFree temperature and emission results are in Table 9.2, the elemental abundance results in Table 9.3, the spectral fits in Figure 9.9 and the comparison to em loci in Figure 9.11. The separate abundance values are in abundance ratio units of coronal/photospheric, where the coronal values are from [48] and the photospheric values are from [23].

9.3.0.1   MinXSS-1 Mission Length Data

I have computed 1TFree, 2TFree, 1TAllFree and 2TAllFree fits over the entire MinXSS-1 science mission length (2016 June 9 - 2017 May 20) averaged over 15 minutes (where there is data downlinked) to observe basic trends in the solar corona. The temperature, Figure 9.3, is consistent with a 2 - 3 MK component (which is dominated by active regions) during quiescent times except for transients due to flares. When flares occur there is a large spike in th temperature, sometimes up to and above 10 MK. For times where a single temperature is an adequate representation of the soft X-ray spectra, the 2T temperature components merge to the 1T value and general each of the 2T components get half of the same emission measure.

The volume emission measure for both the 1T and 2T models are consistent around 10^{48} - 10^{49} cm^{-3}. The MinXSS-1 total counts above 0.9 keV is very consistent to the GOES 0.1 - 0.8 nm flux. The low-fip multiplicative bias varies, but stays near 'coronal' values ($A_{low-fip} \sim 1$) but commonly drops below this value during flares. The change in elemental abundance values dropping during flare times is consistent with the interpretation of chromospheric plasma rising to the corona due to the influx of particles and energy (chromospheric evaporation).

These spectral fits show consistent results during the MinXSS-1 mission length. The 1T and 2TFree fits are a certain class of models to describe the solar X-ray flux. The solar flux is not necessarily at one or two main temperatures, but commonly is a range of temperatures. This is why differential emission measure (DEM) are employed and are discussed in Section 9.6.1.
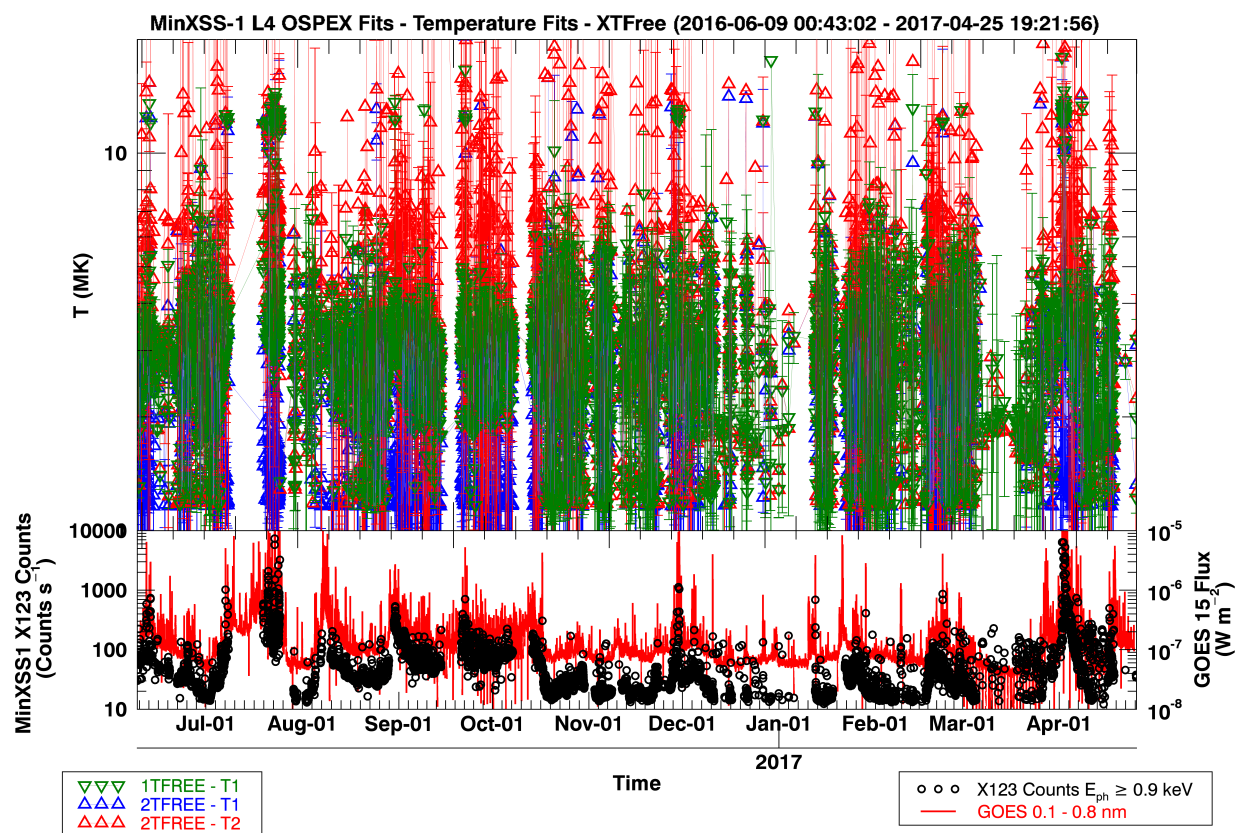
Figure 9.3: Temperature results over the MinXSS-1 mission of 15 minute averaged X123 data fit by OSPEX 1TFree (green) and 2TFree (red-hotter and blue-cooler) class models. The X123 detected spectral flux is dominated by active regions and flares, thus the 2 - 3 MK active region plasma is clearly observed plus transients due to flares. The GOES 0.1 - 0.8 nm flux is plotted as the red line below to serve as a reference for the solar activity level.
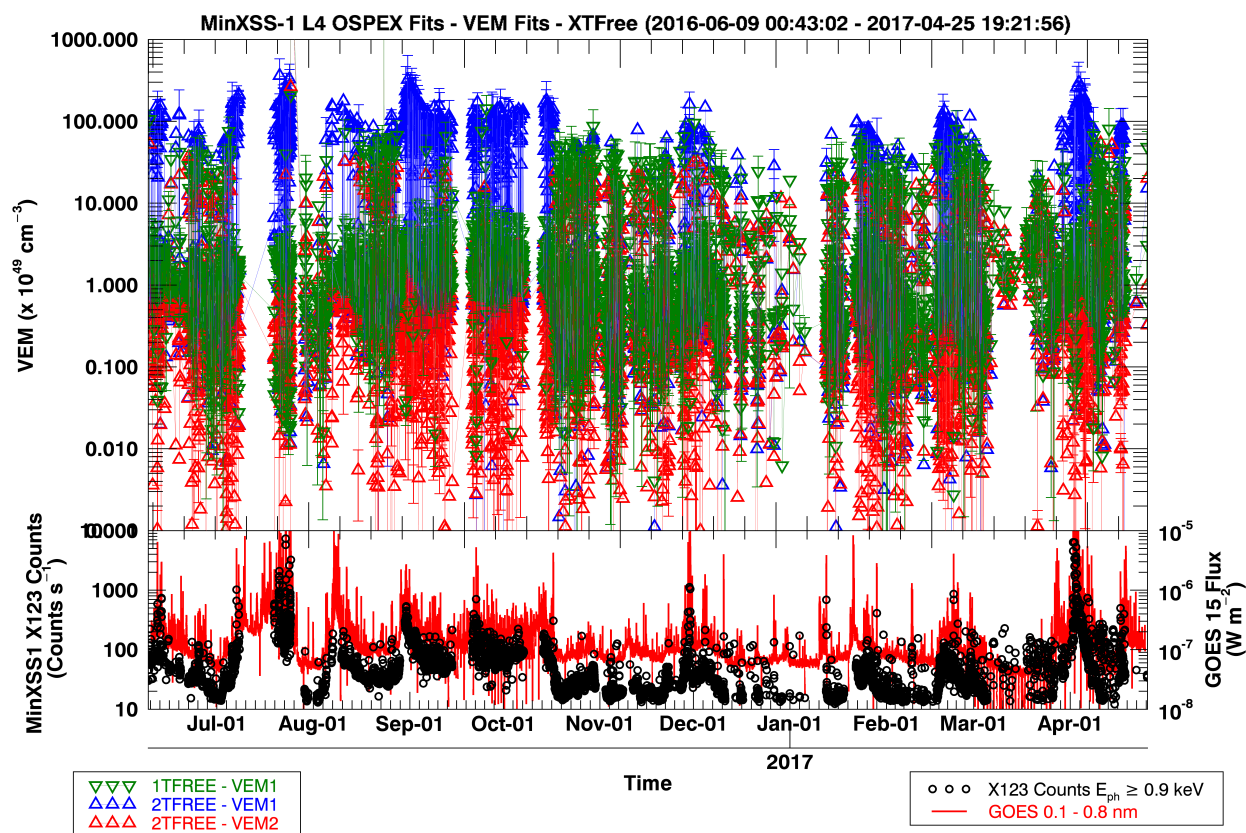
Figure 9.4: Volume emission measure (VEM in units of 10^{49} cm^{-3}) results over the MinXSS-1 mission of 15 minute averaged X123 data fit by OSPEX 1TFree (green) and 2TFree (red-hotter and blue-cooler) class models. The emission from active regions for these 1T and 2 T models is consistently near 10^{48} - 10^{49} cm^{-3}. The GOES 0.1 - 0.8 nm flux is plotted as the red line below to serve as a reference for the solar activity level.
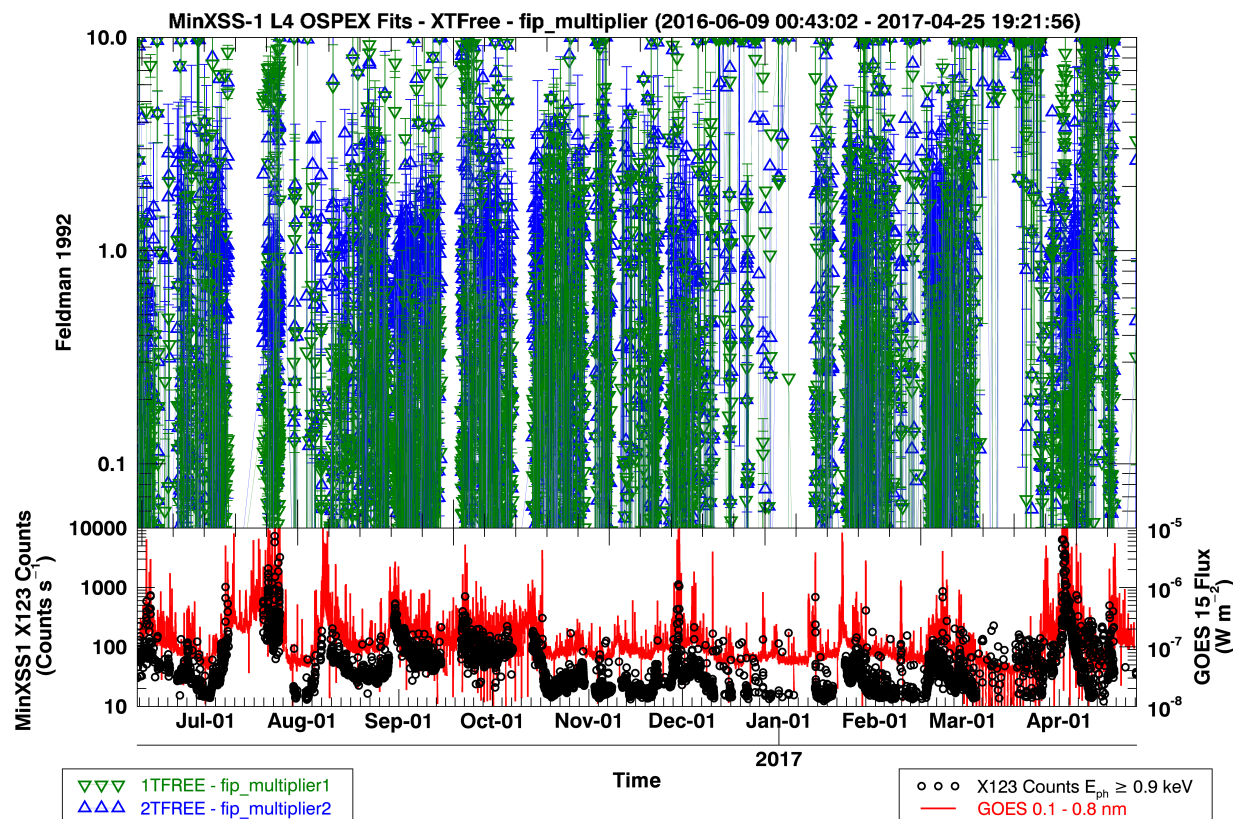
Figure 9.5: Multiplicative factor for the low-fip elements (scaling units of Fe, Ni, Ca, Si, Mg and 0.5*S from Feldman 1992 values) results over the MinXSS-1 mission of 15 minute averaged X123 data fit by OSPEX 1TFree (green) and 2TFree (blue) class models. The values hover near 'traditional' coronal values for quiescent active regions and drop precipitously during flare times (possibly due to chromospheric evaporation). The MinXSS-1 X123 counts for $E \geq 0.9$ keV are plotted as the black circles in the bottom panel. The GOES 0.1 - 0.8 nm flux is plotted as the red line below to serve as a reference for the solar activity level.
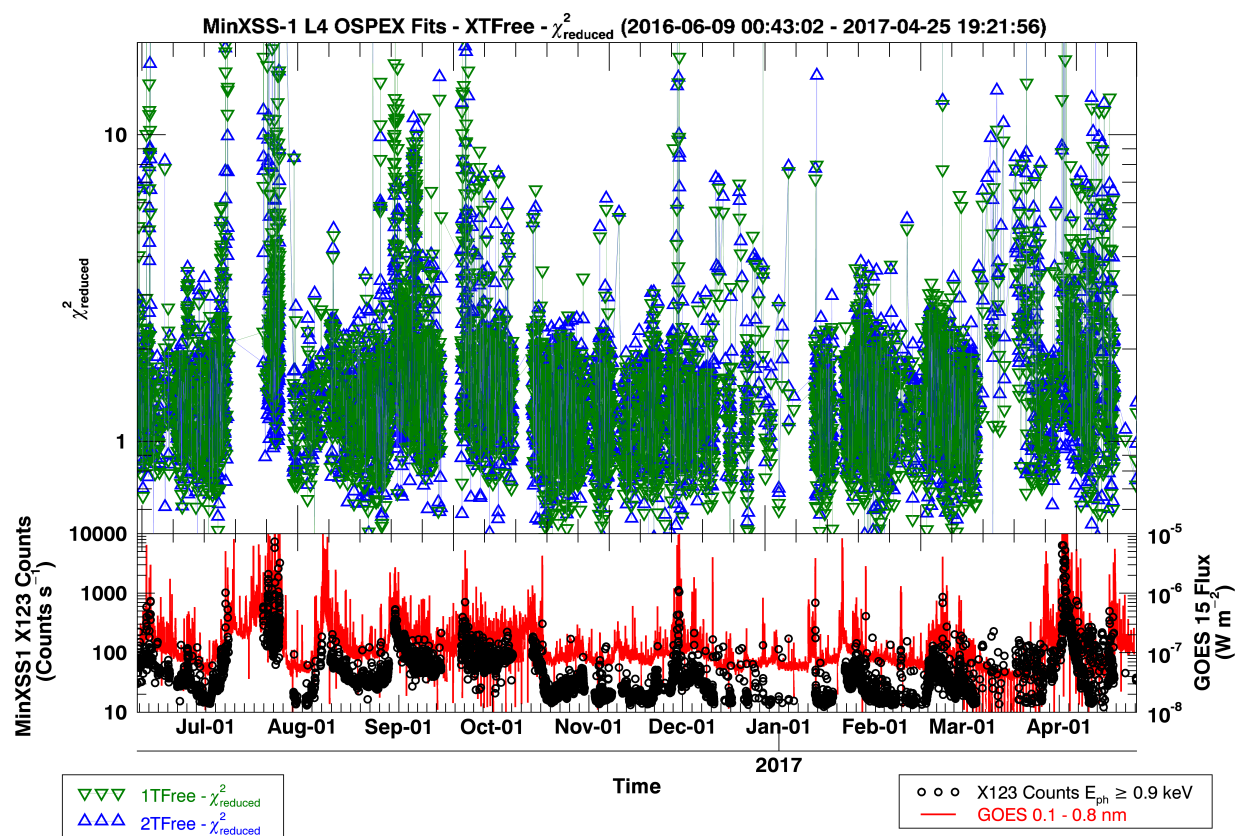
Figure 9.6: Reduced Chi-square ($\chi^2_{reduced}$) over the MinXSS-1 mission of 15 minute averaged X123 data fit by OSPEX 1TFree (green) and 2TFree (blue) class models. Values near unity are desired. The $\chi^2_{reduced}$ is around 2 - 6 for most fits, which is OK. The MinXSS-1 X123 counts for E $\geq$ 0.9 keV are plotted as the black circles in the bottom panel. The GOES 0.1 - 0.8 nm flux is plotted as the red line below to serve as a reference for the solar activity level.

9.4 MinXSS X123 and XP Cross-Calibration

The MinXSS X123 spectrometer prototype was space-flight verified on two NASA Sounding Rocket flights for the calibration of the *SDO Extreme Variability Experiment* (EVE) [159] and returned high quality science data for two 5 minute periods [28]. Thus, we have confidence in the MinXSS CubeSat versions of the X123 spectrometers to return high quality data. This was reaffirmed with the first few months of data downlinked from the MinXSS-1 mission. Over the early phases of the mission the X-ray flux has been as low as GOES ∼A5 and as high as GOES M5.0 during a flare. The times of the corresponding GOES levels are:

- **A5** from 2016 June 29 10:29:32 - 2016 July 01 22:55:53,

- **B5** from 2016 July 23 01:15:05 - 01:39:45,

- **C2.7** from 2016 July 08 - 00:55:04 - 00:58:44,

- **M1.2** from 2016 July 21 - 01:50:01 - 01:53:31,

- **M5.0** from 2016 July 23 - 02:10:05 - 02:13:46

These data have been filtered and only data that pass our 'science quality' check (minimal background levels, particle events, non-SAA times, etc.) are analyzed below. These filter checks also isolate eclipse time data with only thermal noise apparent in the spectrum which result in ∼ 2 - 5 cps across the entire spectrum. Other external (astronomical) soft-X-ray flux contributions to the MinXSS X123 background are negligible due to the small instrument aperture. The solar flare times are centered on the flare peak total count rate in the MinXSS X123 spectrum. These solar fluxes have all been corrected for dead-time losses using Equation 8.11 and result in MinXSS-1 X123 count rate levels of 26 - 9 100 cps. The dead-time losses were ∼11% for the M5.0 flare, ∼3% for the M1.2 flare, ∼0.7%

for the C2.7 flare, and less than $\sim 0.5\%$ for B GOES levels and lower. This demonstrates the MinXSS spectrometer capability to cover a wide range of solar X-ray flux levels. XP responds identically to the increasing GOES flux, with background subtracted signals in the range of 801 - 616 928 fC. This provides a confirmation of XP and X123 nominal operation.
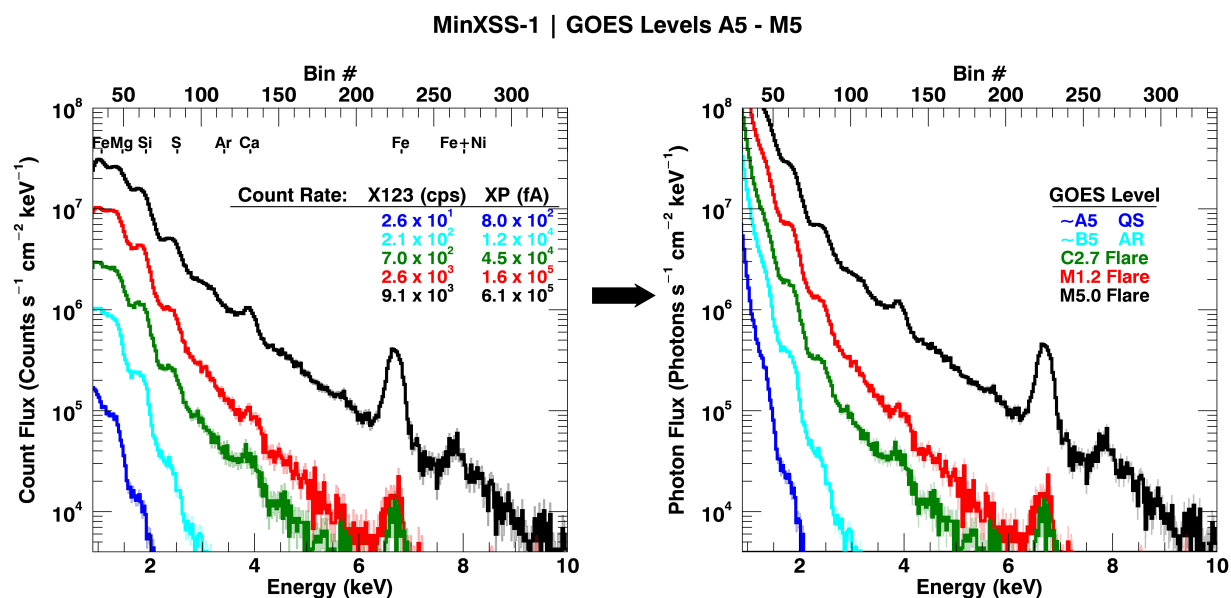
Figure 9.7: MinXSS-1 X123 solar measurements (solid lines) from GOES A5 to M5 levels ($\sim 5 \times 10^{-8}$ - 5×10^{-5} W m^{-2}). The left plot is the mean count flux and the right plot is the estimated photon flux. The uncertainties are depicted as the shaded region around the measurements. This demonstrates the dynamic range of the MinXSS-1 spectrometer, and the variation in spectral features for increasing solar flux levels. The 'bumps' in the spectrum are due to groups of dominant emission lines from ionized Fe near 1.2 keV and 6.7 keV, Mg near 1.7 keV, Si around 2.1 keV, S by 2.7 keV, Ar (or lack thereof) near 3 keV, Ca by 4 keV, and the Fe+Ni complex at 8 keV. These features can be used as elemental abundance probes to assesss deviations from the traditional 'Coronal' abundance values during various solar conditions.

Due to the X123 noise sources mentioned earlier, Be window thickness and uncertainties in the photon inversion process, and to the off-diagonal elements of the X123 response, the lower end of the MinXSS-1 X123 spectra valid for scientific analysis is ~ 0.8 keV. The sharply decreasing solar flux for the higher energies limit and the MinXSS small aperture result in an effective high energy limit of ~ 12 keV. Even for flares as large as M5.0, the flux is not

large enough to produce a statistically significant count rate above 12 keV before effects such as detector dead-time and pile-up hinder the accuracy of the spectra. Thus, our MinXSS-1 X123 has an effective solar flux energy range of 0.8 - 12 keV and should return quality data up to low X-class flares if corrected for dead-time and pile-up effects. The MinXSS-2 X123 Fast SDD spectrometer with a nominal slow channel peaking time of 1.2 μs, is four times faster than the nominal 4.8 μs peaking time, thus one would expect roughly four times the count rate before inaccurate spectra. But the MinXSS-1 Be window is much thicker than the MinXSS-2 window (24.5 vs. 11.2 μm), making comparisons non-linear. Early estimates put the MinXSS-2 X123 maximum GOES level at X-class solar flares. Future data will reveal the full relation, keeping in mind that the axis on Figure 8.16 are rough estimates and that the spectral distribution of photons is non-linear vs. GOES flux levels.

The spectral photon flux estimates in Figure 9.7 demonstrate the drastic change in the soft-X-ray spectra. The X123 soft X-ray spectrum measured change by orders of magnitude over a few GOES level changes. Additionally, the XP fA signal (converted from the measured DN signal) scales with the GOES flux levels of A5 to M5. This provides a consistency check for the X123 spectral signal. While the qualitative nature of this change is not new, the quantitative determination of the magnitude of this change is relevant. Table 9.1 lists the X123 and XP count rates as a function of GOES class and is plotted in Figure 9.7. The measured XP signal was compared to the X123 estimated XP signal, by taking the X123 estimated photon flux and computed the XP signal from this flux. The resultant 'X123 modeled' XP signal is then compared to the measured XP signal. The XP measured and 'X123 modeled' XP signal agree to within ~4% except for the GOES A5 measurement. At low GOES levels the XP signal becomes comparable to the thermal photodiode noise and leads to underestimated signals. This is apparent in the QS emission measure inferences.

A particularly interesting feature in the X123 spectrum is the presence of two 'humps' near 1.7 keV due to Mg XI and Mg XII line groups, and 2.1 keV from Si XIII and Si XIV lines. These hump features persist for all GOES levels and provide useful diagnostics for element

abundance estimations. The Fe XXIV and Fe XXV line complex near 6.7 keV is prominent for the GOES flares of levels C2.7 and higher. This line complex is well suited to estimate the Fe abundance modification during solar flares vs. the QS (non-large-flaring Sun). Only for the brightest flares (M5.0 and M1.2 in this dissertation) is the Fe-Ni complex near 8.0 keV pronounced and suitable for analysis. For smaller flares the signal is not statistically significant to infer physical properties from this feature. These measurements demonstrate the MinXSS dynamic range of its solar measurements.

The consistency between X123 and XP em loci provide further confidence that both instruments are performing nominally. The minimum of all the em loci for the MinXSS-1 X123 energy bins provides an upper limit to any multi-temperature and DEM fits. The energy must be spread over a range of temperatures and thus could not 'touch' the em loci at any point. Thus em loci provide firm upper limits to the temperature distribution for a particular measurement from a particular instrument. Em loci are not a new tool, they have been used most notably in XRT, EIS, AIA, FOXSI, RHESSI and NuSTAR analysis to name a few. Em loci can be a valuable aid in MinXSS data analysis.

9.5 MinXSS and GOES X-ray Sensor (XRS) Cross-Calibration

A main benefit of conducting routine spectrally resolved soft X-ray measurements is the ability to calculate and track the spectral distribution of energy flux. This information is important for models of Earth's atmospheric response to solar radiative forcing, solar flare analyses and comparison of the solar X-ray flux to other stars. Table 9.1 lists the integrated soft X-ray energy flux (multiplying the energy flux by the X123 bin width and summing over photon energy bins) above 1 keV estimated at 1 AU from MinXSS-1 X123 measurements for the main five GOES levels. This information is also in Panel A of Figure 9.8. Panel B displays the fitted power law relationship, y = a(x^b), between the MinXSS-1 X123 total counts and the total radiative energy greater than 1 keV energy, which is not quite linear. The data in the scatter plots (Panels B, C and D) are from 2016 June 10 - 2016 November

30. The coefficient of 2.2×10^{-8} J counts^{-1} m^{-2} can be used to obtain a rough estimate of the energy content from the X123 total counts alone. A large portion of this energy (up to an order of magnitude) resides below 2 keV and this is apparent when comparing to the corrected (divided by 0.7) GOES XRS 0.1 - 0.8 nm flux, see Panel A in Figure 9.8.

There is a correlation between the 0.1 - 0.8 nm ($\sim$1.55 - 12.4 keV) energy flux calculated from MinXSS-1 X123 and GOES XRS (Panel D of Figure 9.8). The XP count rate (DN s^{-1}) has a near linear relationship to the GOES XRS 0.1 - 0.8 nm flux, especially above GOES B1 levels and is useful as a proxy to the GOES XRS measurements. This is expected as XP tracks the total soft X-ray energy incident on the MinXSS-1 aperture (number of electron-hole pairs generated is proportional to E$_{ph}$). Exact linearity is not expected between X123 count rate and GOES XRS energy flux because X123 is photon counting. These results validate the dynamic response of the MinXSS-1 X123 and XP to the solar flux. The next section discusses the feasibility of extracting physical information from model fits of the MinXSS X123 data to estimate plasma temperature, density, emission measure and elemental abundances.

For the QS spectra, there are not enough counts for energies $\geqq$ 2.5 keV and not 'strong enough' features for a consistent fit and thus the individual element abundance parameters are poorly constrained. But for the pre-flare spectra and flares statistically significant abundance values can be deduced. Again the trend is clear that there is a decrease in the abundance majority of the low-FIP elements (Fe, Si, Mg, Ni) during the flare-peak vs. the pre-flare fits. Additionally, the individual element abundance variation observed provides further evidence for a more complicated fractionation process than a simple single FIP-Bias scaling for all the low-FIP elements. Similar conclusions about abundances being more complex than a FIP-Bias scaling have been expressed in recent studies, such as in [138] and [38].

This is further complicated by the postulated decrease in abundance from the nominal

Table 9.1: MinXSS-1 count rate and photon energy flux of observations from GOES A5 - M5 levels. Ratio$_{B5}$ is the count rate value of the corresponding row divided by the B5 count rate.

GOES Level	X123$_{measured}$ (counts s^{-1})	Ratio$_{B5}$ X123	X123 Total Photon Energy Flux $\geq$ 1 keV at 1 AU (W m^{-2})	XP$_{measured}$ (fA)	Ratio$_{B5}$ XP	XP$_{X123-predicted}$ (fA)	100*(Δ_{XP}/XP$_{measured}$)
QS ~A5	2.63×10^1	1.25×10^{-1}	4.6×10^{-6}	8.01×10^2	6.67×10^{-2}	1.33×10^3	-66.35%
AR ~B5	2.10×10^2	1.00×10^0	4.6×10^{-5}	1.20×10^4	1.00×10^0	1.15×10^4	4.2%
C2.7 flare	7.01×10^2	3.33×10^0	1.5×10^{-4}	4.53×10^4	3.77×10^0	4.36×10^4	3.7%
M1.2 flare	2.60×10^3	1.23×10^1	5.5×10^{-4}	1.65×10^5	1.37×10^1	1.61×10^5	2.7%
M5.0 flare	9.1×10^3	4.38×10^1	2.1×10^{-3}	6.18×10^5	5.14×10^1	6.16×10^5	0.3%
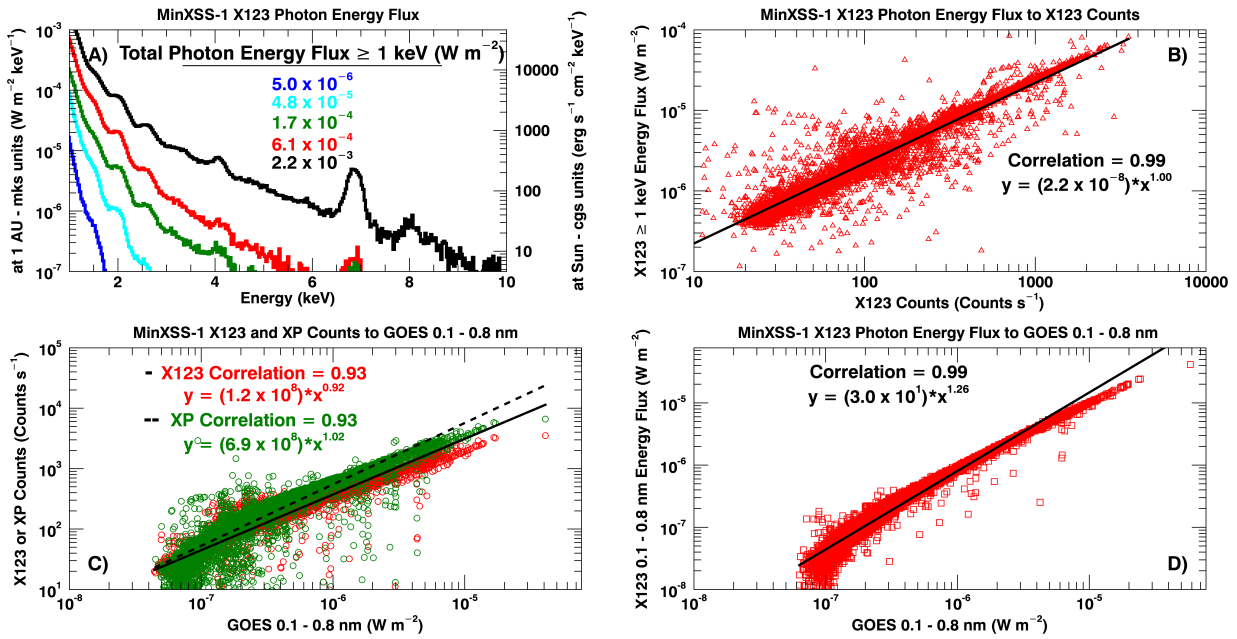
Figure 9.8: Panel A shows the MinXSS-1 X123 derived photon energy flux at 1 AU (in mks units - W m^{-2} keV^{-1}) and scaled back to the Solar surface (in cgs units - erg s^{-1} cm^{-2} keV^{-1}). The total energy flux at 1 AU as measured by MinXSS-1 for photon energies ≥ 1 keV is listed for the GOES $\sim$A5 (blue), B5 (cyan), C2.7 (green), M1.2 (red) and M5.0 (black) class observations. Panels B - D contain scatter plots, correlation coefficients and linear fit of MinXSS-1 X123 photon energy ≥ 1 keV to count rate (Panel B), MinXSS-1 X123/XP count rate to GOES 0.1 - 0.8 nm flux (Panel C) and MinXSS-1 X123 photon energy flux integrated from 0.1 - 0.8 nm ($\sim$1.55 - 12.4 keV) to GOES XRS 0.1 - 0.8 nm flux (Panel D) all show very strong correlations, validating the MinXSS data.

coronal/photospheric ratio of Ar for the three flares here and Ca for two of the three flares. The abundances of Ar and Ca have been of recent interest in Hinode EIS spectrum [40, 39] and MinXSS can provide an additional diagnostic in investing any anomalous behavior. A more rigorous analysis of elemental abundance variations, solar flares, quiescent conditions and active region evolution comprising DEM fits and are planned for the future.

The MinXSS-1 X123 spectral fits of the non-flaring Sun are consistent with a dominant emission component between 1 - 3 MK with volume emission measure values near 10^{49} - 10^{50} cm^{-3}, which is not surprising. To highlight the limit of inference in these simple 2T

models, we include the more uncertain hotter ($\gtrsim 4.5$ MK), dimmer ($\lesssim 10^{48}$ cm^{-3}) secondary component. With this secondary component, the model fits the data well with reasonable χ^2 values. Without this secondary temperature component, the 1T models underestimate the measured count rate above 2.5 keV, albeit a DEM fit could reconcile this excess. The ability of MinXSS data alone to constrain this contribution is limited (due to the small effective area) and can only provide upper limits to the emission measure. We caution against the existence of this hot-dim component (we signify this with ** in Table 9.2 and Table 9.3 on the fit parameters and a dash-dot delta function without a black outline in Figure 9.11) without conclusive evidence provided by simultaneous observations from other more sensitive instruments. The purpose of this dissertation is to highlight the MinXSS capabilities, but this also encompassess uncovering the limitations.

We checked the estimated GOES XRS 0.05 - 0.4 nm flux for the MinXSS 2T inferred pre-flare secondary hot-dimmer components using the goes_fluxes.pro IDL code. The measured fluxes from the GOES 0.05 - 0.4 nm channel would have to be between at least 2.2, 2.9, and 4.2×10^{-9} W m^{-2} (for photospheric abundances) for the pre-flare times of C2.7, M1.2 and M5.0 for this component to have the emission measure similar to the MinXSS 2TAllFree fits. All measured GOES 0.05 - 0.4 nm fluxes were at about factor of 2 below the estimated values. Spectral fits to accommodate the measured count rate above 2.5 keV is most likely reconciled by DEM fits of MinXSS data coupled with other soft X-ray data. This will be done soon.

There has been numerous literature discussing active region hot components (T $\geqq 5$ MK) inferred from soft X-ray data (see [28, 111, 130, 139, 137, 136] to state a few and references therein). All of these aforementioned studies had their respective limitations. Future measurements from the MaGIXS [89] sounding rocket and continued measurements from FOXSI [78] sounding rockets, plus the NuSTAR satellite [67] will provide additional data to validate or further the case to rebuke the previous claims of the hot-dim plasma's presence, or at the very least, provide firm upper limits on its emission measure. The only
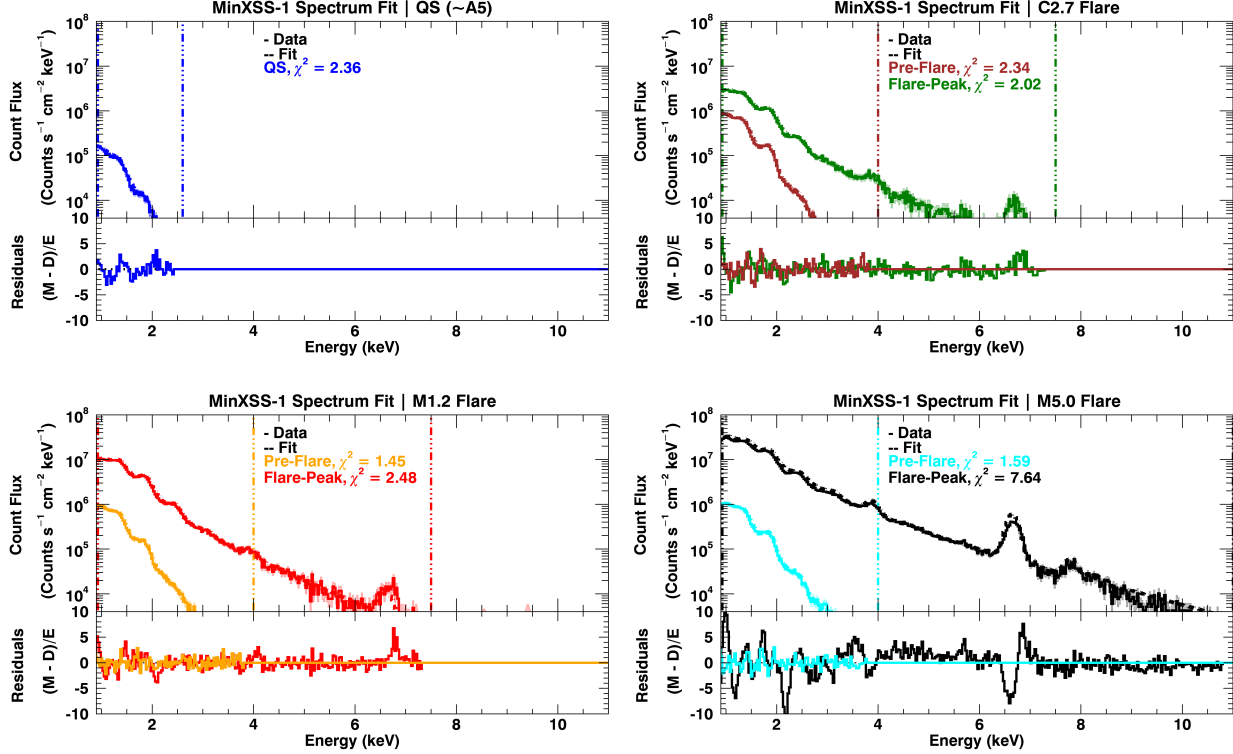
Figure 9.9: MinXSS-1 X123 count flux solar measurements (solid lines) with the best fit spectra overlaid (dashed lines), for temperature and emission measures derived using the OSPEX suite. The residuals are listed also (M = model, D = data, and E = uncertainty). The shaded regions indicate the uncertainties in the count flux. A 2T model with select elemental abundance fit separately (2TAllFree). The best fit parameters with their uncertainties are listed in Table 9.3 and Table 9.4. There is a 2T model used for non-large-flaring times (QS and pre-flare) and an additional 2T model is added to compensate for the radiative enhancement during the flare-peak times. The vertical dash-dot-dot-dot lines show the high and low energy limits for the spectral fits.

substantial inkling seems to be from the Extreme Ultraviolet Normal Incidence Spectrograph (EUNIS-13) rocket flight [21]. MinXSS data combined with the other soft X-ray and UV observatories can help to further constrain the existence of hot-dim and investigate the solar plasma temperature distribution.

We will now refer back to the em loci for an intuitive understanding of the measurements for the case of large flares during peak emission times, we expect the flaring plasma to dominate the solar spectral emission. Thus, a 1T model result would peak near this value
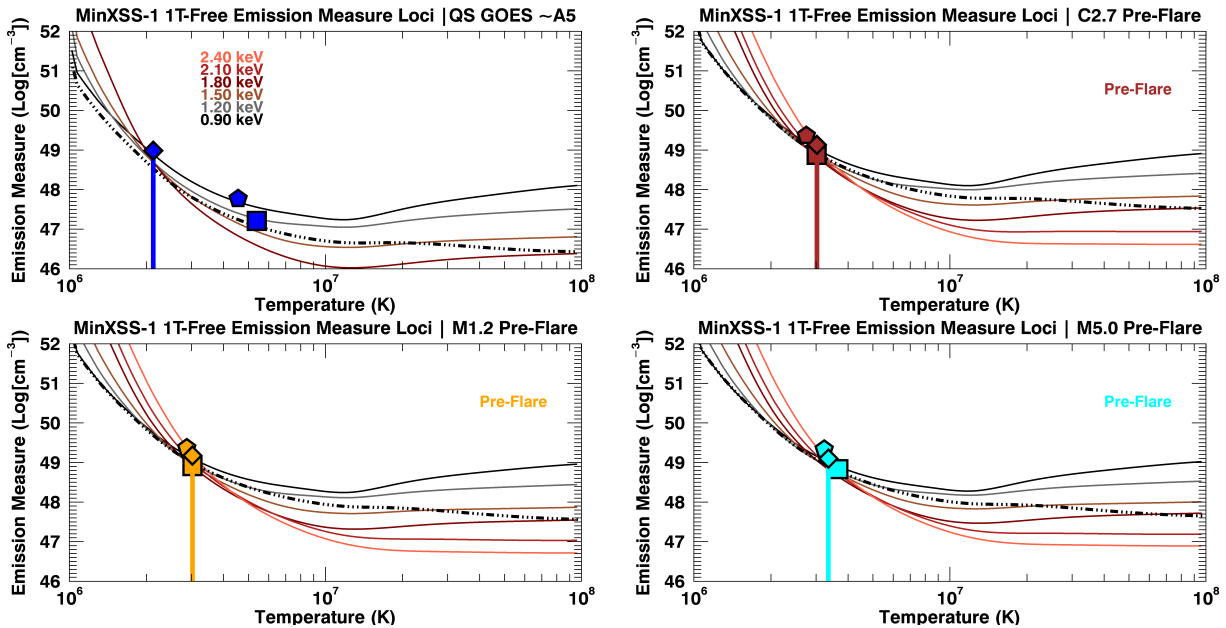
Figure 9.10: Volume emission measure loci (em loci) plots with MinXSS-1 OSPEX 1TFree fit parameters over-plotted as delta functions in temperature with filled diamonds indicating the emission measure value for the non-large-flaring sun (pre-flare). These MinXSS-1 em loci and fit parameters correspond to the spatial distribution captured by Hinode XRT in Figure 9.15. The solid colored lines correspond to X123 counts summed to 0.3 keV wide energy bins and the dash-dotted lines are the XP loci. The rainbow keV values in the top left plot indicate the color code for the minimum energy bin use for each X123 em loci. The em loci indicate the maximum emission if all the plasma was isothermal for each summed energy bins. GOES averaged values are listed for photospheric (pentagon) and coronal (square) abundances. The plot of X123 1TFree fits are to demonstrate, 1) the agreement with the overlapping X123 em loci, 2) agreement with the overlapping XP em loci and 3) consistency with the GOES XRS isothermal estimation except for low GOES levels like the ~A5 levels (due to the non-linearity of GOES for low flux levels).

and this is what was observed for the 1T models. The 1TFree model for the QS and 3 pre-flare times are displayed in Figure 9.10 to exemplify this (the diamond symbols). The values for all the pre-flare times are near 3 MK and coincide with the GOES XRS isothermal estimates for coronal (squares) and photospheric (pentagons) abundances. Moreover, the X123 1TFree values lie in between the GOES XRS coronal and photospheric estimates, as they should because the fit results for X123 reside in between coronal and photospheric FIP-Bias values. The 3 MK isothermal plasma temperature is consistent with the inferred

active region DEM peak from the combined Hinode EIS and SDO AIA study of [35].

The peak-flare emission in this exploratory study of MinXSS-1 consistency with GOES is best described by a persistent cooler component between 3 - 7 MK plus a hotter contribution ($\geqq$ 13 MK) that dominates at the higher energy flux. All flare data analyzed in this dissertation cover about a 3 - 4 minute time-frame centered about the peak soft X-ray emission times. Refinement of the MinXSS-1 spectral responses is a continual endeavor, particularly for high flux times, such as the M5.0 flare (which is currently the highest flux observation that we have analyzed thoroughly). The deviations near values of 5 between the uncertainty normalized difference between the model and observations for the Si 2.1 and the Fe 6.7 keV features exhibit the need for further improvement.

The 2TAllFree em loci results are displayed in Figure 9.11. The best fit emission measure and temperatures are the delta functions with stars at the emission measure value. The [158] M5.0 flare fit results are overlaid as the dashed histograms in the bottom right panel. The thick black em loci is for the M5.0 flare and the thick cyan em loci for the pre-flare, both are the minimum of all the individual energy bins corresponding to the spectral model used in the [158] analysis. The GOES XRS average flare-peak time 1T emission measure and temperature results for photospheric and coronal elemental abundance are over-plotted for comparison.

Table 9.2: MinXSS-1 2TFree (one FIP-Bias scale factor) spectral fits of observations from GOES A5 - M5 levels. The uncertainties in the fit parameters are in parendissertation. ** highlights that the pre-flare data inferred dimmer and hotter second component is near the limit of the MinXSS plasma diagnostic capabilities and thus not as well constrained.

GOES Level	Observation Times	EM_1 (10^{49} cm^{-3})	T_1 (MK)	EM_2 (10^{49} cm^{-3})	T_2 (MK)	FIP-Bias$_{12}$ (1 = photospheric) (4 = coronal)
QS ~A5	2016-Jun-29 10:29:32 - 2016-Jul-01 22:55:53	19.9 (9.2)	1.17 (0.08)	0.21 (0.07)	2.43 (0.12)	3.48 (0.46)
C2.7 PreFlare (~B3)	2016-Jul-07 23:41:03 - 2016-Jul-08 00:04:24	10.8 (0.75)	1.70 (0.02)	*0.12 (0.01)*	*4.58 (0.08)*	2.89 (0.10)
C2.7 flare	2016-Jul-08 00:55:04 - 2016-Jul-08 00:58:44	1.21 (0.04)	4.28 (0.07)	0.10 (0.005)	14.91 (0.27)	1.41 (0.06)
M1.2 PreFlare (~B3)	2016-Jul-20 18:04:13 - 2016-Jul-20 18:28:53	8.73 (0.81)	1.82 (0.04)	*0.13 (0.02)*	*4.68 (0.14)*	2.17 (0.09)
M1.2 flare	2016-Jul-21 01:50:01 - 2016-Jul-21 01:53:31	6.21 (0.11)	4.05 (0.03)	0.46 (0.01)	12.97 (0.12)	1.41 (0.03)
M5.0 PreFlare (~B5)	2016-Jul-23 01:15:05 - 2016-Jul-23 01:39:45	7.68 (0.80)	1.86 (0.05)	*0.18 (0.02)*	*4.80 (0.12)*	2.21 (0.09)
M5.0 flare	2016-Jul-23 02:10:05 - 2016-Jul-23 02:13:46	17.10 (0.13)	4.86 (0.02)	2.22 (0.02)	19.67 (0.08)	0.98 (0.01)

Table 9.3: Temperature and emission measure values from MinXSS-1 2TAllFree (separate elemental abundance scale factors) spectral fits of observations from GOES A5 - M5 levels and plotted in Figure 9.9. The best fit abundances are listed in Table 9.4. The uncertainties in the fit parameters are in parendissertation. ** highlights that the pre-flare data inferred dimmer and hotter second component is near the limit of the MinXSS plasma diagnostic capabilities and thus not as well constrained.

GOES Level	EM_1 $(10^{49}$ cm$^{-3})$	T_1 (MK)	EM_2 $(10^{49}$ cm$^{-3})$	T_2 (MK)
QS $\sim$A5	15.2 (0.21)	1.93 (0.05)	–	–
C2.7 PreFlare ($\sim$B3)	7.29 (0.59)	1.91 (0.04)	*0.05 (0.01)*	*5.25 (0.23)*
C2.7 flare	1.91 (0.12)	3.82 (0.08)	0.09 (0.006)	15.92 (0.45)
M1.2 PreFlare ($\sim$B3)	11.90 (2.5)	1.69 (0.08)	*0.18 (0.03)*	*4.45 (0.16)*
M1.2 flare	8.27 (0.41)	3.61 (0.05)	0.57 (0.02)	12.38 (0.16)
M5.0 PreFlare ($\sim$B5)	5.44 (0.78)	2.04 (0.08)	*0.11 (0.03)*	*5.19 (0.26)*
M5.0 flare	8.16 (0.11)	7.18 (0.02)	1.38 (0.02)	20.78 (0.16)

9.6   MinXSS and Reuven Ramaty High Energy Solar Spectroscopic Imager (RHESSI) Comparison

The *Reuven Ramaty High Energy Solar Spectroscopic Imager (RHESSI)* has been producing spectral resolved images of the Sun from soft X-rays (3 keV) to Gamma rays (17 MeV) with its cooled germanium detectors soon after its launch on 2002 February 5 [101]. RHESSI spins at a rate of 15 revolutions-per-minute and use it's arrangement of front and rear grids to generate spatial Fourier components of the emitting source on the Sun to locate the emission. Via this in-direct imaging, RHESSi can reconstruct the spatial distribution of the source via a back-projection method and further improve the image spatial resolution with various image reduction techniques such as Clean, MEM, etc. RHESSI has been an influential NASA small Explorer Mission and has provided unprecedented data on solar flares across the high energy domain. I solely compare the spectral data from simultaneous RHESSi and MinXSS observations of a couple of flares previously discussed in the initial MinXSS-1 cross comparisons.

A further check of the MinXSS-1 flare measurements is provided with a comparison to near simultaneous RHESSI measurements. RHESSI results are overlaid as 'R' in Figure 9.11 for the M1.2 and M5.0 flares, which were the only flares in this dissertation simultaneously observed by both MinXSS-1 and RHESSI. The RHESSI fits were performed in OSPEX, composed of a 1T thermal and a non-thermal (thick2) bremsstrahlung component. The spectra were fit from $\sim$6 keV to the maximum photon energy with signal above the background ($\sim$30 keV). The RHESSI thermal fit components yield values near GOES estimates [155] and the MinXSS-1 em loci curves (discussed in Section 9.2). RHESSI estimates a temperature of 15 MK for both flares and emission measure values of 0.1 and 2.5×10^{49} cm^{-3} respectively for the M1.2 and M5.0 flare. RHESSI fits indicate an elemental abundance FIP-Bias factors of 2.1 and 1.3 for the M1.2 and M5.0 flares respectively, both below 'traditional' coronal values.

Table 9.4: Separate abundance values are in abundance ratio units of coronal/photospheric, where the coronal values are from [48] and the photospheric values are from [23] from MinXSS-1 2TAllFree spectral fits of observations from GOES A5 - M5 levels that are plotted in Figure 9.9. Elemental abundances that were fixed during fitting have a 'fixed' in parendissertation in place of an uncertainty. These values were fixed during fitting when there were not sufficient counts in the corresponding spectral feature to ascertain an abundance. The abundances of He, C, O, F, Ne, Na, Al and K were fixed at photospheric values. The best fit temperatures and emission measures are listed in Table 9.3.

Element	Fe	Ca	S	Mg	Si	Ar	Ni*
FIP (eV)	7.90	6.11	10.36	7.65	8.15	15.76	7.64
QS ∼A5	0.06 (1.75)	4.00 (fixed)	1.29 (fixed)	1.43 (0.18)	3.90 (0.89)	1.20 (fixed)	0.06 (1.88)
C2.7 PreFlare (∼B3)	2.26 (0.28)	4.00 (fixed)	1.32 (0.64)	2.60 (0.10)	3.39 (0.20)	1.20 (fixed)	2.43 (0.30)
C2.7 flare	0.78 (0.08)	3.18 (0.47)	1.11 (0.69)	1.06 (0.07)	1.38 (0.07)	0.81 (0.28)	0.84 (0.08)
M1.2 PreFlare (∼B3)	1.94 (0.23)	4.00 (fixed)	0.98 (0.74)	2.30 (0.13)	1.80 (0.14)	1.20 (fixed)	2.08 (0.25)
M1.2 flare	1.00 (0.06)	1.64 (0.26)	1.05 (0.67)	1.59 (0.06)	1.34 (0.04)	0.75 (0.16)	1.08 (0.06)
M5.0 PreFlare (∼B5)	2.39 (0.28)	4.00 (fixed)	1.37 (0.64	2.26 (0.12)	2.41 (0.17)	1.20 (fixed)	2.56 (0.29)
M5.0 flare	1.85 (0.02)	4.23 (0.11)	0.90 (0.65)	1.62 (0.03)	0.80 (0.01)	1.10 (0.01)	1.98 (0.02)

* The Ni abundance was linked to the Fe abundance. So this is not a truly independent estimate of the Ni abundance.
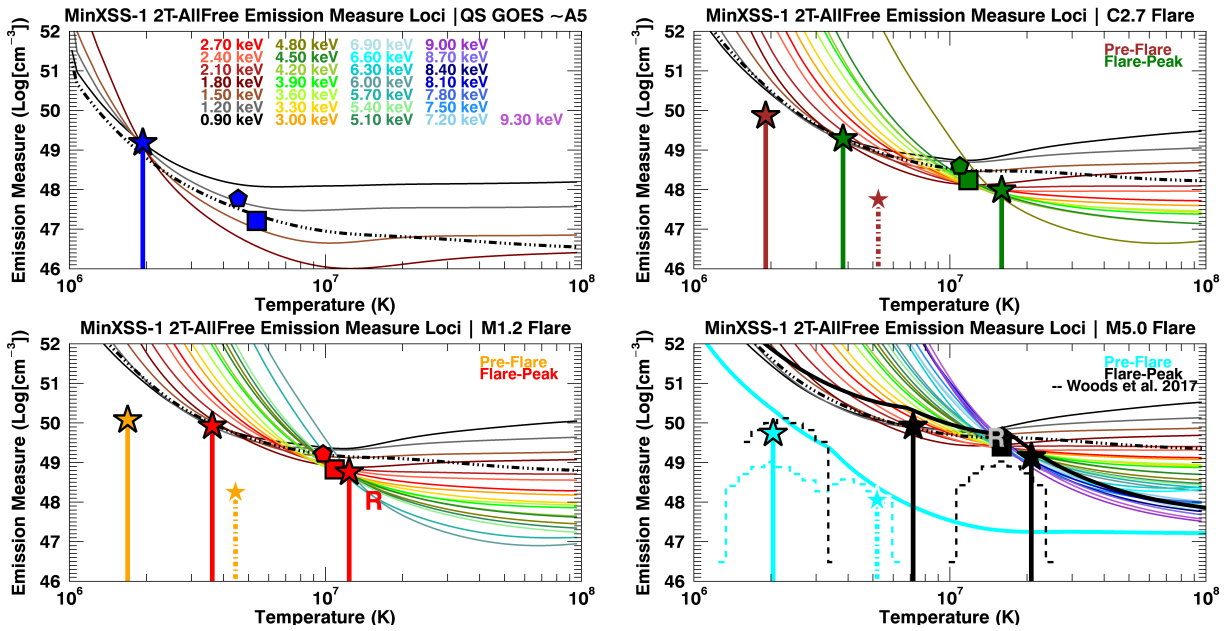
Figure 9.11: Em loci plots with MinXSS-1 OSPEX 2TAllFree fit flare-peak and QS parameters over-plotted as delta functions in temperature with filled stars indicating the emission emission measure value. The solid line delta functions are well constrained by the MinXSS data. The pre-flare dash-dot delta function without the black outline indicates that the hotter-dimmer component is less constrained by MinXSS data. The thin solid colored lines correspond to X123 counts summed to 0.3 keV wide energy bins and the dash-dotted lines are the XP loci. The rainbow keV values in the top left plot indicate the color code for the minimum energy bin use for each X123 em loci. The X123 and XP em loci are consistent. The [158] M5.0 flare fit results are overlaid as the dashed histograms in the bottom right panel. The thick black em loci is for the M5.0 flare and the thick cyan em loci for the pre-flare, both are the minimum of all the individual energy bins corresponding to the spectral model used in the [158] analysis. GOES averaged values are listed for photospheric (pentagon) and coronal (square) abundances. RHESSI values for the M1.2 and M5.0 flare are indicated by the 'R'.

It is not expected for MinXSS-1 and RHESSI to return the exact same temperature and emission measure values due to the different spectral responses, spectral resolution, effective areas and consequential temperature sensitivities, but one expects consistencies in RHESSI plasma parameters with MinXSS em loci and inferred photon flux. MinXSS-1 and RHESSI photon flux in Figure 9.12 provides one of the few spectrally complete flare measurements from 1 keV to at least 15 keV. The combined MinXSS-1 and RHESSI dynamic range spans nearly eight orders of magnitude of photon flux and there is overlap near the 6.7 keV Fe

complex. The ~8 keV Ni feature is also apparent in the MinXSS-1 spectra. Similarly, RHESSI data can be used to extract non-thermal contributions to the MinXSS-1 spectra for large flares. The discussion of the instrument complexities, and cross-calibration between MinXSS and RHESSI is reserved for a future dissertation (Amir et al., in prep).
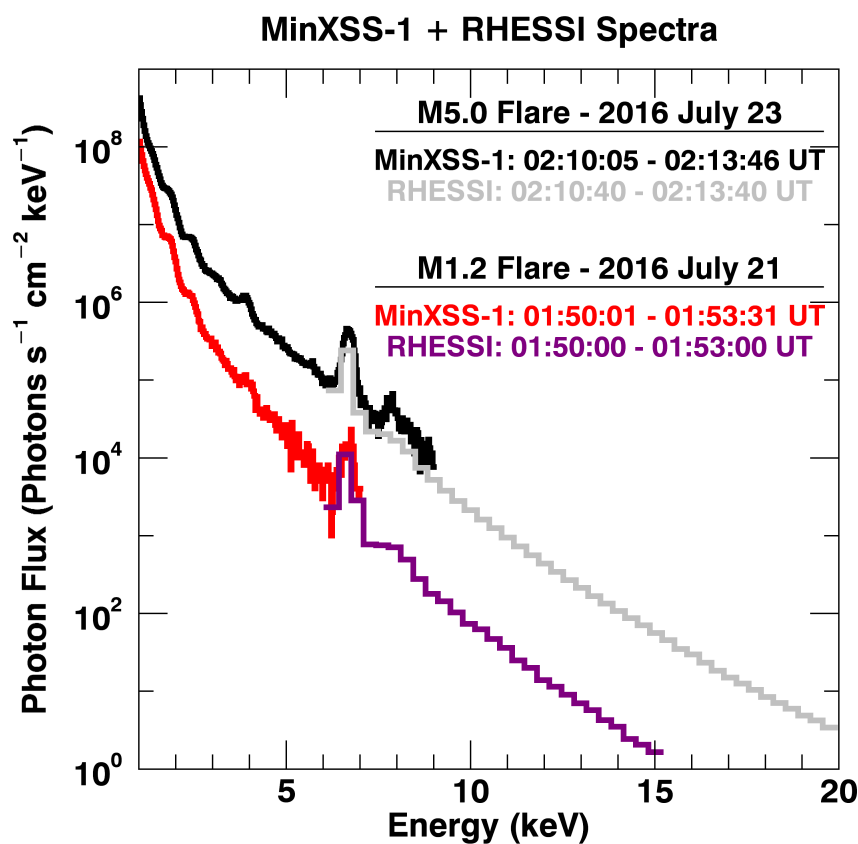
Figure 9.12: MinXSS-1 M1.2 and M5.0 flare photon flux spectra with overlaid RHESSI spectra. These near simultaneous measurements provide complete spectral coverage from 1 keV to the minimum detected flux from RHESSI and spans eight orders of magnitude in flux. The main overlap between instruments for flares is near the 6.7 keV Fe complex. This comparison helps validate the MinXSS observations.

9.6.1   Differential Emission Measure (DEM)

The Solar corona is not isothermal, and thus we implement a new tool to aid in analysis of the solar corona. In Section 6.2.4 DEM were mentioned as one of the most physically realistic interpretations of the radiation detected from the optically-thin solar corona. DEM analysis is extremely tricky and filled with nuance.

(1) Given a set of observations (counts in a data set, C_i), there may be no solution that satisfies Equation 9.4 within the given uncertainties (δ_{C_i}).

(2) A solution can consist of DEM results that have negative emission measures, which is mathematically consistent, but non-physical.

(3) If a solution exits, it may be non-unique, meaning that there can be multiple realizations of DEMs that give the same predicted count rate, depending on the form of the temperature response, $F_{ij}(T)$ (ith data set and jth temperature bin).

(4) The solution could be unstable, meaning that small perturbations of the measurement (C_i) on the order of magnitude of the measurement uncertainties (δC_i)) can lead to large deviations in the DEM solution (noise amplification).

Furthermore, there are intrinsic limitations to using X-ray observations alone to extract DEMs [32]. This basically stems from the exponential in the kernel in the contribution function, $G(T, E_{ij}, n_e)$. The exponential dependence arises from the Maxwellian electron velocity distribution. In low density, high temperature plasma, the 'coronal' approximation is commonly employed for radiative analysis [58, 6]. The approximation assumes that the plasma is optically-thin surrounding radiation and that the radiation is primarily driven by electron collision with an ion/atom, that subsequently de-excites via spontaneous emission. The electrons velocities and ion states are assumed to be dominated by thermal processes, and thus the radiation will have limited diagnostic capabilities. The temperature dependence

in the kernel, $\frac{e^{\frac{-E}{kT}}}{T^{0.5}}$, *desensitizes* the radiation to changes in the plasma temperature, T. In general, small changes in T, do not lead to large changes in the radiation profile. These intricacies hamper broadband filter data (like XRT) and course resolution spectrometers (like MinXSS X123), in the ability to extract the DEM *structure*, because the signal is dominated by the X-ray continuum emission, but these class of instruments can still set upper limits on the emission measure vs. temperature over broad temperature ranges.

High spectral resolution spectrometers still suffer from the radiation temperature *desensitizing* effects from the Maxwellian kernel, but are better at confining the temperature *structure*. The ionization state of ions calculated by from collisional ionization equilibrium (CIE), which again have an exponential dependence due to the Maxwellian distribution of electron energies, can have large 'wings' in temperature space of the fractional abundance for a particular ion state. Thus, the CIE predicted ion fraction can peak at a temperature T_{peak}, but still have detectable emission from that ion if the actual plasma DEM much lower or higher than T_{peak}. An example of this is discussed in Del Zanna 2013 [35], where emission from Fe XVIII (with $T_{FeXVIII-peak} \approx 7$ MK for CIE) is detected from methods using Hinode Extreme Imaging Spectrometer (EIS) and AIA data, but the results from a comprehensive DEM extraction yield that the majority of plasma has $T \leq 3$ MK. Further, observations similar those of EUNIS-13 for hot ions like Fe XIX ($T_{FeXIX-peak} \approx 8.9$ MK) [21] help refine our knowledge of the coronal DEM. Ionization equilibrium can be broken when the heating process heats the ions or electrons at different rates and much faster than the ion-electron collisional timescale, τ_{ie} (which is dependent upon the ion-electron collisional frequency, ν_{ie}). An important note is that ionization non-equilibrium is important for flares (especially in the early phases) [13].

With these caveats in mind we implement DEM fitting processes to determine the plasma temperature structure throughout the rest of this dissertation. There are many methods of using the information from Equation 6.6 to solve for the plasma DEM from the

measured signals via Equation 9.4.

$$C_i = \int_T DEM(T)F(T)dT$$
$$= \sum_j DEM(T)_j F_{ij}(T)\Delta T_j$$

(9.4)

.

The main DEM method utilized in this dissertation is a forward model iterated until χ^2 is minimized. All DEM results in this dissertation will be displayed as emission measure vs. temperature plots, where the DEM has been integrated over each corresponding temperature bin, to demonstrate the total emission per temperature. The xrt_dem_iterative2.pro (XIT, [154]) uses spline points in $\log(T_e)$ space (here we will assume that that the ions and electrons are in thermal equilibrium, $T = T_e$, which in reality is not always the situation). To estimate the uncertainty of the XIT realization, many Monte Carlo (MC) runs can be computed. The MC trails solve the forward fitting spline methods with the observational values perturbed about the input values within 1-σ of the given uncertainties. The forward modeling guarantees a positive solution in DEM space, but many forward fitting techniques must assume a functional form a priori. Another method is to assume a Gaussian shape for the temperature structure along the line of sight. This methodology has been implemented on AIA data assuming each pixel has a Gaussian temperature distribution and returns limited, but satisfactory results [7] (see Figure 9.13)

Direct inversion methods, $DEM(T) = F_{ij}^{-1}(T)C_i$, like Regularized Inversion (RIT, [68]), can return negative emission measures, which while mathematically is a viable solution, is not physically realistic. RIT uses singular value decomposition with a 'tweaking' parameter, to return a 'smoothed' DEM solution (minimizes oscillatory behavior). The RIT technique was explored in this dissertation work, but is omitted in this dissertation document. Another inversion technique, called the Sparse DEM ([30] obtains a DEM by minimizing the number of zero emission measure temperature bins subject to constraints set by the data

and corresponding measurement uncertainties.

To explore the DEM solutions using MinXSS-1 data alone with XIT, MinXSS-1 observations on 2016 September 5 (cross-calibration data with XRT) is displayed in Figure 9.14. because MinXSS instruments sum the solar signal across the field of view, this represents the 'average' DEM solution that can best recreate the MinXSS-1 XP and X123 measurements. The first thing to notice it the lower emission measure values in the XIT DEM solution as compared tot he 1T and 2TFree fits at the same temperatures (see Figure 9.27). The 1T and 2TFree solutions are basically at the same emission measure magnitude (per temperature) as the MinXSS-1 em loci. The XIT DEM solution (black thick line) is much lower than the minimum of all the MinXSS-1 em loci. One can envision this as conservation of energy. For each MinXSS-1 measurement, a total radiative energy can be inferred in the soft X-rays. When the plasma is assumed to be primarily at one or two temperatures, the amount of radiation is only coming from those corresponding delta functions in temperature. As more temperatures contribute to the spectral flux, less radiation is needed at the original 1T or 2T values to generate the amount of energy determined by the observation. Thus, as more temperatures are included the emission measure profile spreads out and will always be lower than the collective minimum of the broad (in temperature space) emission measure loci from MinXSS (broadband spectrometer), XRT or AIA (filters with broad temperature responses). Now for spectral line DEM results from spectrometers like Hinode EIS, the DEM results will be very close to the minimum of each spectral line em loci used to constrain the DEM. This is the main reason that spectral line DEM analysis can better constrain the temperature *structure* and not simply set upper limits to the DEM.

The pixel-by-pixel DEM solutions obtained from the 1 Gaussian and Sparse techniques on AIA data alone are displayed in Figure 9.13 The DEM results supplies an intuitive comprehension of the variability of temperature and emission for different solar features. Consistencies between the 1 Gaussian and Sparse include:

(1) active regions have the highest total emission,

(2) active regions also harbor the highest emission measure weighted temperatures

(3) coronal holes are really void of emission, hence the name

(4) the majority of the solar coronal defined by area (not active regions) is near 0.5 - 2 MK and has a substantial diffuse component that dominates the emission in this temperature range

The spatially averaged 1 Gaussian and Sparse DEMs (over positive pixels) are over-ploted in Figure 9.14 to compare with the XIT results. The AIA only DEMs have substantial high temperature (T $\geq$ 10 MK) contributions that over estimate the MinXSS-1 X123 observations. While in contrast the MinXSS-1 only XIT DEM accurately recreates the MinXSS-1 measurements. MinXSS-1 X123 em loci mitigate the realization of this hotter contribution, but have a large amount of plasma at cooler temperatures (T $\leq$ 10 MK), where MinXSS is poor at constraining the emission. We will see that the inclusion of AIA data with MinXSS removes the spurious low temperature emission and confines the hotter portion.
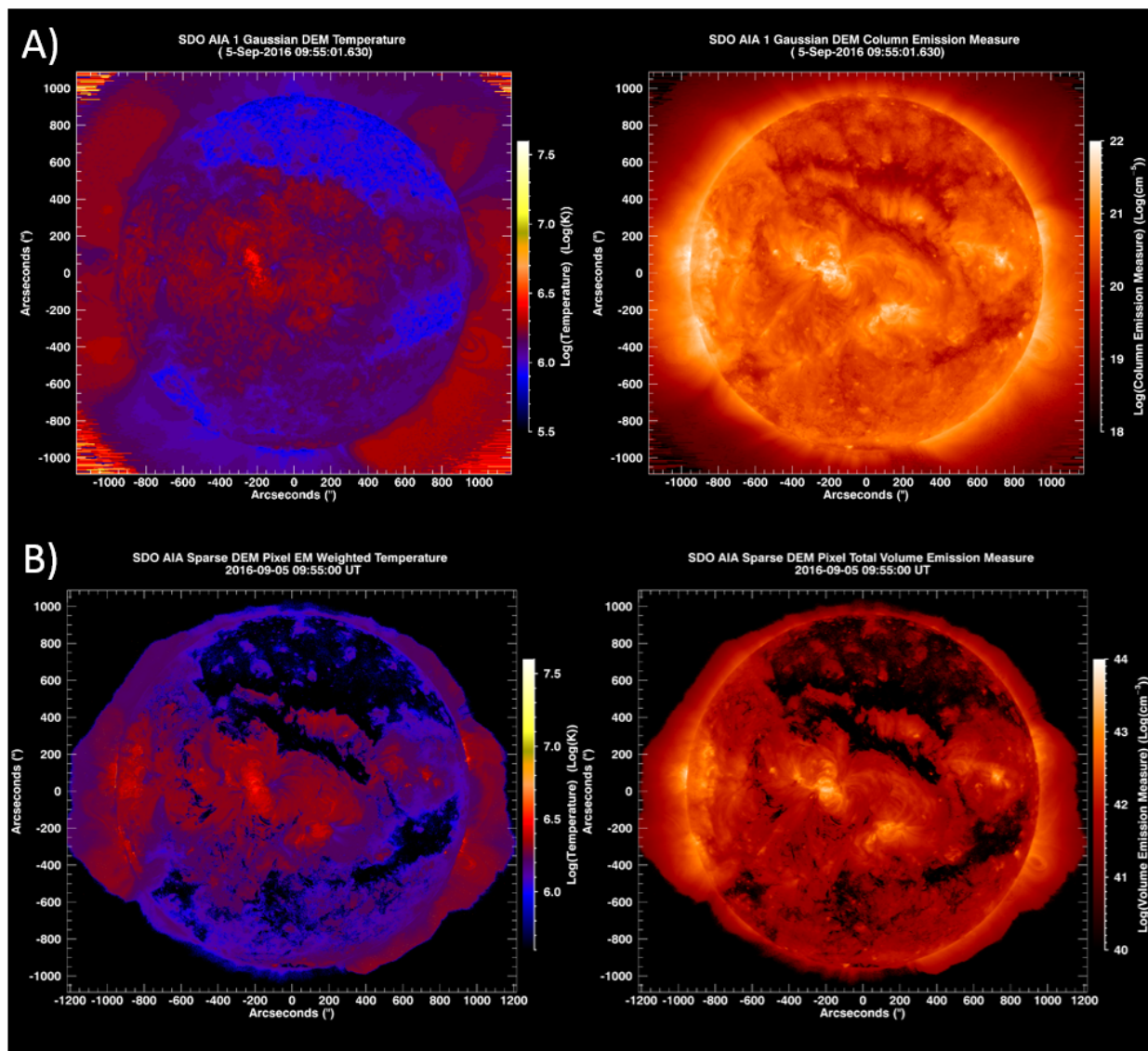
Figure 9.13: MinXSS-1 ⇔ XRT cross-calibration on 2016 September 5. (A) 1 Gaussian DEM map for emission weighted temperature (left) and peak column emission measure (right). (B) Sparse DEM map for emission weighted temperature (left) and total volume emission measure (right). Both maps are fairly consistent (where there are valid Sparse results).
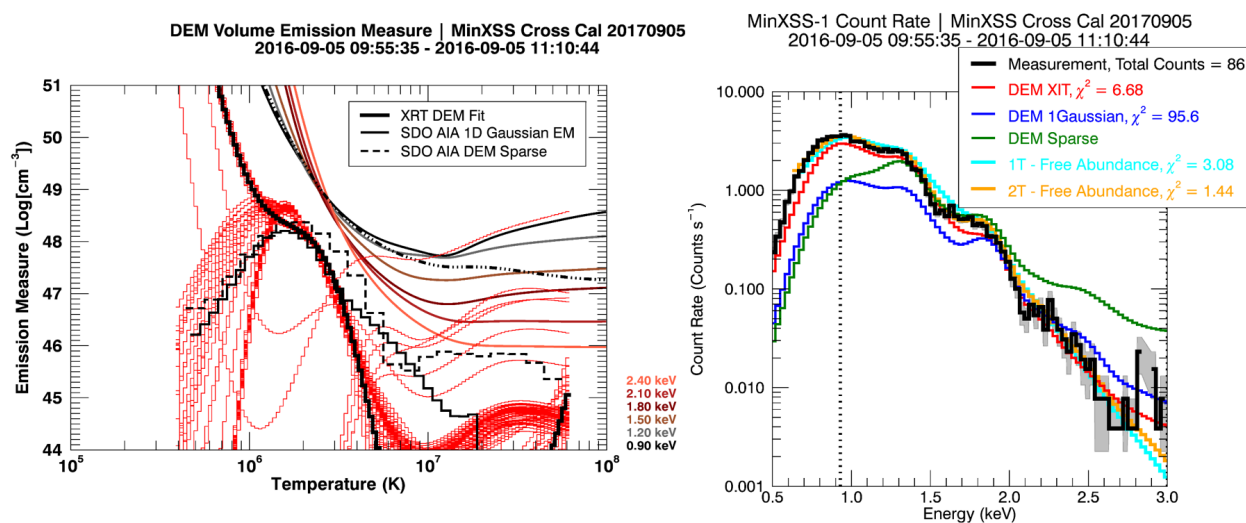
Figure 9.14: MinXSS-1 ⇔ XRT cross-calibration on 2016 September 5. Left plot: MinXSS-1 XP and X123 only DEM fit results. VEM vs. temperature using the XIT method (black thick histogram line). The thin red histogram lines are 100 Monte-Carlo realizations and give an indication of the fit uncertainty. The XIT DEM is from the spatially integrated MinXSS-1 data. The thin black histogram line is the 1 Gaussian DEM result using AIA data only. The thin black histogram dashed line is the Sparse DEM result using AIA data only. The AIA only DEMs will be discussed in detail in the AIA calibration section. Both AIA only DEMs have substantial very hot plasma (T *geq* 10 MK) inference that over estimate the observed X123 count rates. The 1 Gaussian and Sparse DEM are solved per pixel grouping and averaged over the positive pixels. The colored solid lines are the X123 em loci and the dash-dot-dot-dot black line is the XP em loci. Right plot: MinXSS-1 X123 measured and DEM count rates. The XIT predicted MinXSS-1 count rates agree very well given all the uncertainties in the DEM fitting process.

9.7   MinXSS and Hinode X-ray Telescope (XRT) Cross-Calibration

Hinode X-ray Telescope is a grazing incident focusing optic telescope (Wolter I) with relatively broadband filters and a charge-coupled-device (CCD) detector operating in integrating mode (vs. photon counting mode) [57, 81]. Hinode has been in operations observing the Sun regularly since its launch in 2006 September 22 [90]. XRT also has a co-aligned optical telescope to serve as a reference for the solar disc. This dissertation will only discuss the X-ray portion of the XRT instrument. XRT has a nominal 2,048" x 2,048" field of view with a 1" pixel size. The focusing optics give XRT a much larger collecting area (XRT max effective area ~1 cm^2) than MinXSS and hence sensitive much much dimmer plasma for the same exposure time. But many of the exposures are fairly short (on the order of 1 second, except for the thickest filters) and the MinXSS-1 nominal integration time is 10 seconds. So in theory, combining many 10 second integrations from MinXSS-1 can probe similar intensity plasma as XRT. The relatively short exposure times for XRT images are to mitigate saturation of the CCD pixels. To enhance dynamic range long, medium and short exposure times can be combined to make a composite image with increased dynamic range, after normalization by the exposure time (DN s^{-1}). The long exposures allow detection of dimmer plasma, the medium exposure replaces the saturated pixels in the long exposure and the short exposure replaces the saturated pixels in the medium exposure. All XRT data discussed in this dissertation are composite images where applicable and in count rate units (DN s^{-1}).

XRT Be-thin images are displayed in Figure 9.15 to provide qualitative spatial context for the X-ray emission that MinXSS detects for non-large-flaring times. The XRT Be-thin serves as the closest XRT synoptic filter analog to the MinXSS spectral response. The four panels in Figure 9.15 are the closest XRT full-Sun synoptic images in the times discussed in the earlier study for the QS (Panel A), pre-flare C2.7 (Panel B), pre-flare M1.2 (Panel C) and pre-flare M5.0 (Panel D) times. It is clear that active regions are present, their emission

dominate the MinXSS count rates (due to the hotter plasma content).
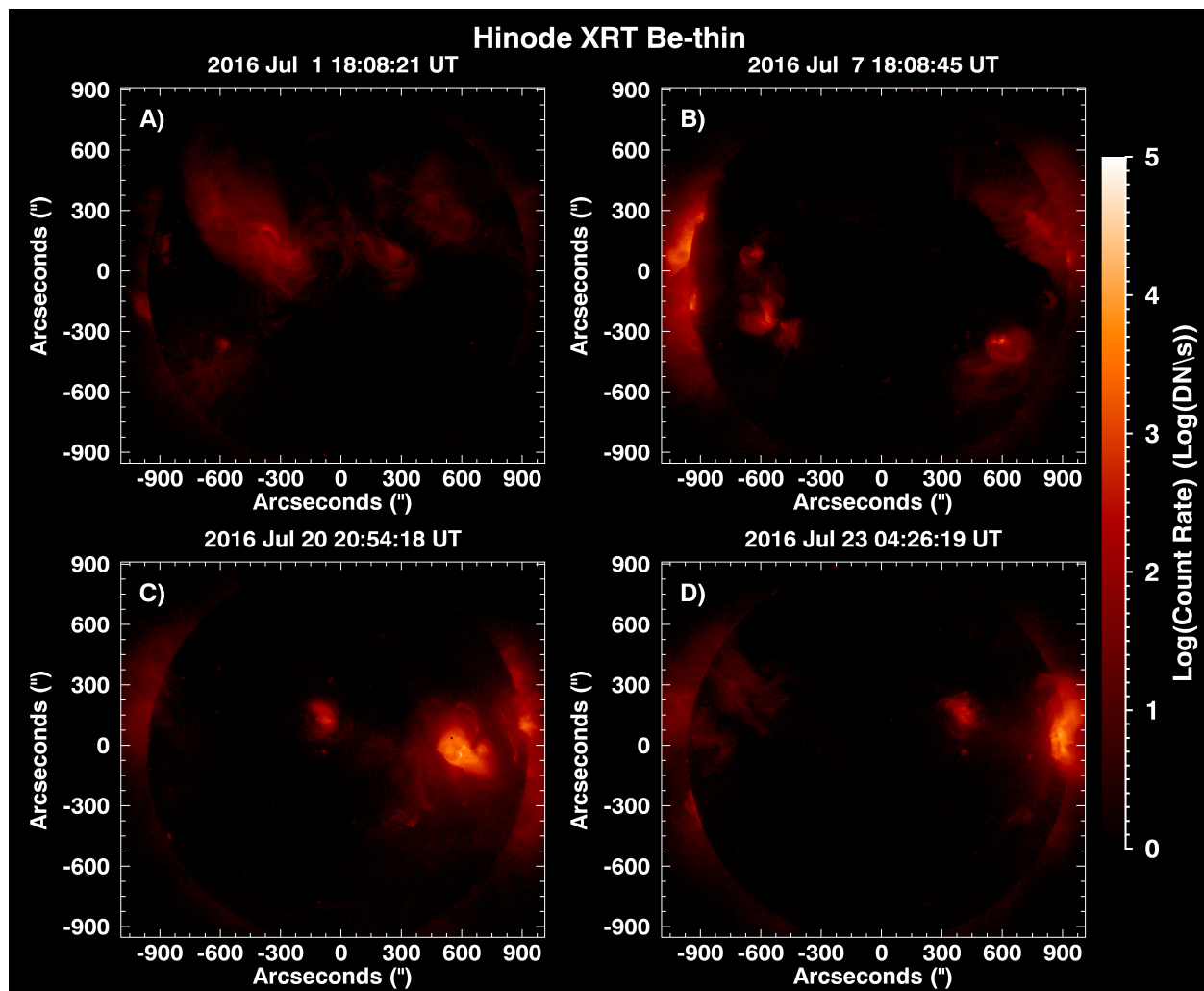
Figure 9.15: Log-scaled count rate Hinode X-ray Telescope (XRT) Be-thin full Sun images near the time of the MinXSS-1 observed QS (Panel A), Pre-flare times for the C2.7 (Panel B), M1.2 (Panel C) and M5.0 (Panel D) flares. The XRT images provide information on the spatial distribution of the soft X-ray emitting plasma, since MinXSS measurements are integrated across the entire FOV.

Reference XRT effective area curves are displayed in Figure 9.16. XRT has a contamination that is diminished during repetitive bake-outs, but re-accumulates [117, 118]. Thus, the contamination varies as a function of time and the latest version of the XRT spectral responses must be used during analysis. Fortunately, for the purpose of MinXSS and XRT cross-calibration, the filter that have spectral responses peaked closer to the MinXSS

bandpass ($\sim$ 0.9 - 12 keV), Be-thin, Be-med, Be-thick, Al-med, Al-thick. These are the so-called 'thick' filters. The so-called 'thin' filters, Al-mesh, Al-poly, Ti-poly and C-poly have significant effects due to the contamination.
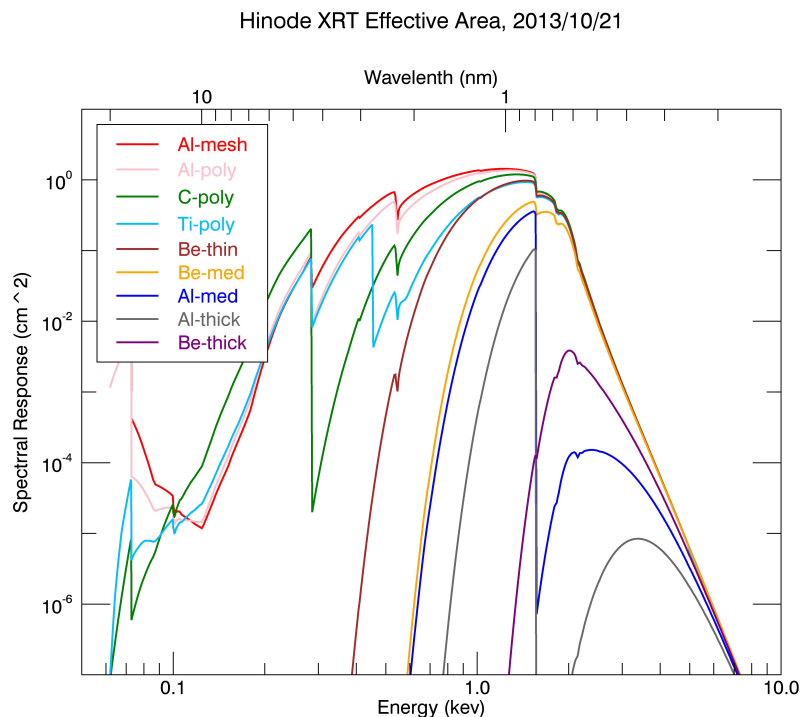
Figure 9.16: Example of the Hinode XRT filter effective areas (cm^2). It is clear that the 'thick' filters of Be-thin, Be-med, Be-thick, Al-med and Al-thick should yeild the most consistent results with MinXSS XP and X123 signals, because of the similarities in spectral responses.

As discussed earlier an analogous procedure to the MinXSS-1 XP calculation Equation 9.1, is used to create the XRT temperature response, F(T). It is clear in Figure 9.17 that the temperature responses depend on the elemental abundances used in the photon emission model. Again this is due to the location of numerous bound-bound transitions from Fe, Ni, Si, Ca, Mg and S in the soft X-ray portion of the electromagnetic spectrum. The solid lines in Figure 9.17 correspond to the Feldman 1992 'coronal abundances', dotted lines are the Schmelz et al. 2012 'Hybrid' and the dash and dash-dot-dash are the Caffau et al. 2011

and Asplund et al. 2009 (respectively) photospheric abundances. All XRT results in this dissertation use the best fit (either 1T or 2TFree) abundance estimates from MinXSS-1 X123 data.
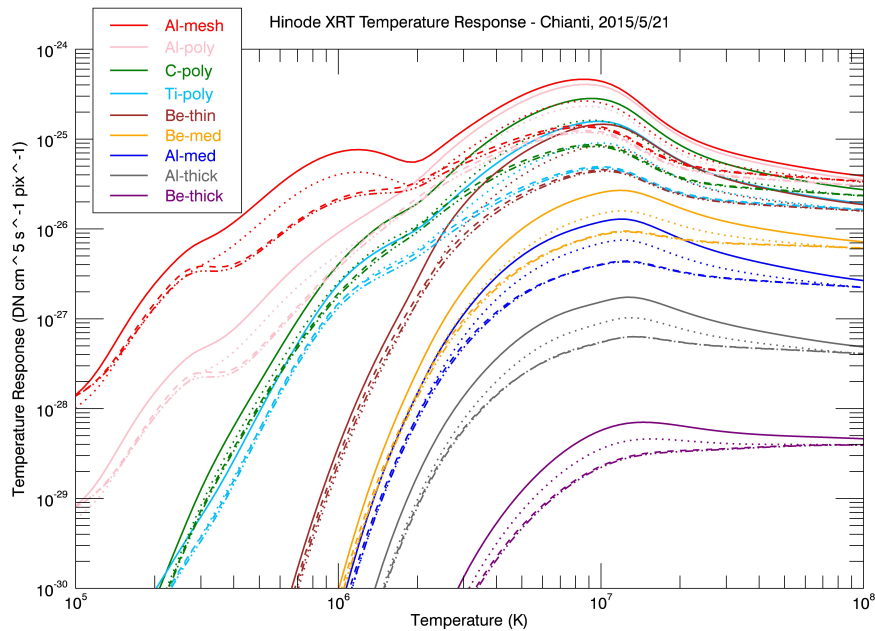
Figure 9.17: Example of the Hinode XRT filter temperature responses, F(T), (DN s^{-1} cm^5 pixel^{-1}) in column emission measure units (CEM) for various abundances. The solid line is the nominal 'coronal' abundances of Feldman 1992 (A$_{low-fip}$ ≈ 3 - 4), the dotted line is for the 'Hybrid' abundances from Schmelz et al. 2012 (A$_{low-fip}$ ≈ 2), the dashed and dash-dot lines are for the photospheric derived abundances from Caffau et al. 2011 and Asplund et al. 2009 respectively (A$_{low-fip}$ = 1). It is obvious in the XRT temperature response curves, like the MinXSS curves that the X-ray emission is very sensitive to the elemental abundances of the emitting plasma.

To quantify the connection between MinXSS-1 and XRT I undertook a cross-calibration over the MinXSS-1 mission length (2016 June 9 to 2017 April 25). Because MinXSS-1 instruments integrate over the entire field of view ($\sim 4°$ x $4°$). Thus, all XRT data in this cross-calibration is from the full Sun XRT images ($\sim 2,048$" x $2,048$") over the mission length and for a subset of measurements (2016 September 5). Comparisons between XRT and MinXSS-1 are between:

(A) MinXSS-1 X123 inverted photon flux ($E_{ph} \geq 0.9$ keV), OSPEX 1TFree and 2TFree fit photon fluxes (using the xrt_flux.pro) predicted DN s^{-1} to measured XRT DN s^{-1} (see Figure 9.19).

(B) Pearson linear correlation coefficients of MinXSS-1 X123 measured count rate ($E_{ph} \geq 0.9$ keV), interpolated to the XRT measurement times (see Figure 9.19).

(C) Spectral Pearson linear correlation coefficients of MinXSS-1 X123 measured count rate per 0.3 wide keV bin, interpolated to the XRT measurement times (see Figure 9.20).

(D) XRT filter ratio emission measure vs. temperature predicted MinXSS-1 X123 count rates, to the measured X123 count rate on 2016 September 5 (see Figure 9.29).

(E) Em loci of XRT and MinXSS in VEM units on 2016 September 5 (see Figure 9.29).

(F) XIT DEM fits of MinXSS-1 only data, XRT data only and combined MinXSS-1 and XRT on 2016 September 5 (see Figure 9.31 and Figure 9.32).

We shall start with the MinXSS-1 mission length time comparison between the X123 count rate and OSPEX fits. The photon flux estimated from the MinXSS data or model fits are folded through the XRT spectral response curves given in Figure 9.16, the photon-electron gain and other effects are accounted for to create the estimated XRT signal. Be-thin and Al-med have the best consistency between the X123 data and the 1T and 2TFree fits. The ratios between the X123 inferred DN rate and actual DN rate in Figure 9.18 and Figure 9.19 are no more than a factor of 10 and mostly within a factor of 2. With the uncertainties of X123, and XRT spectral responses this is an acceptable agreement. The Pearson linear correlation coefficient is the largest for these two filters for the MinXSS total counts ($\rho_{Be-thin}$ = 0.63 and ρ_{Al-med} = 0.69) of all displayed in Figure 9.20.

There are are not many full Sun Be-med and Al-thick measurements, thus a mission length comparison is either very limited (with only a few observations with Be-med filter)
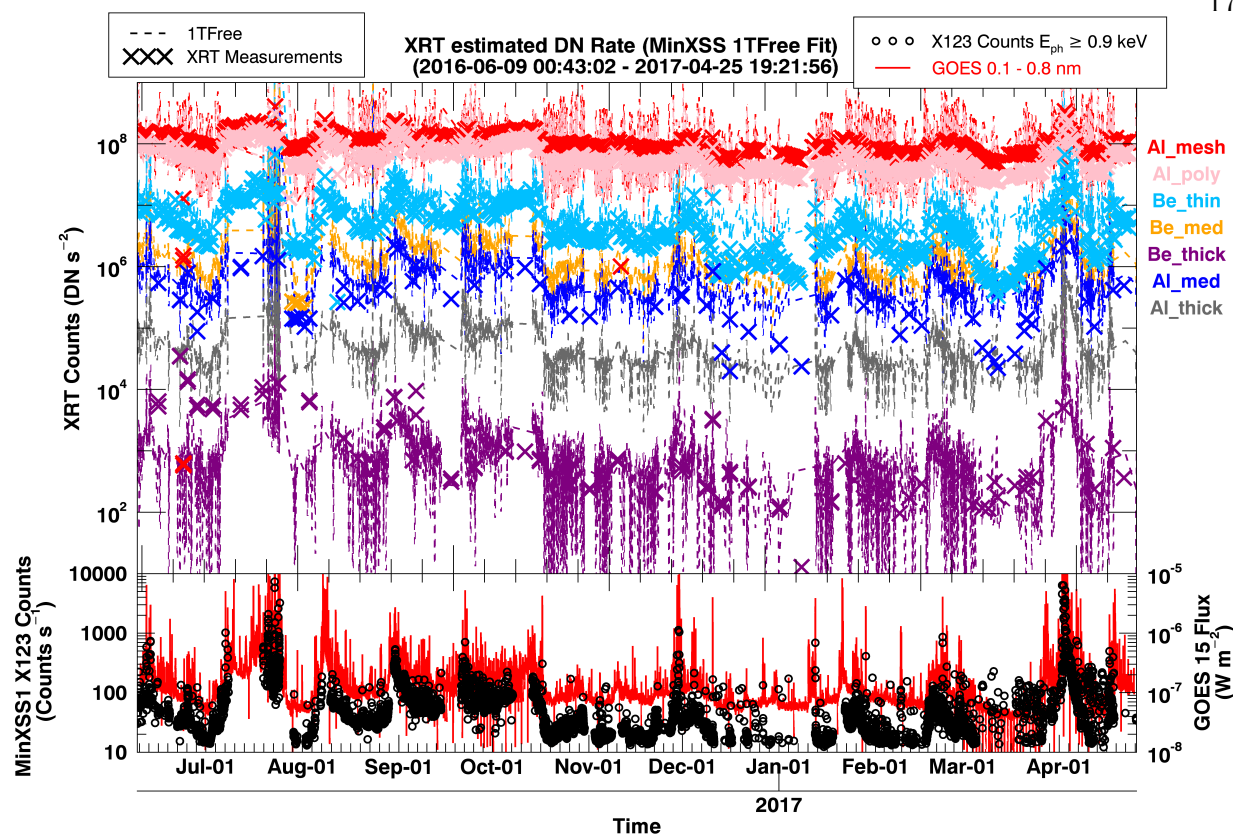
Figure 9.18: MinXSS-1 1TFree OSPEX fits (lines) estimated XRT count rates with the actual XET count rates overploted (X's) over the entire MinXSS-1 mission. The bottom panel is X123 count rate for $E_{ph} \geq 0.9$ keV (black symbols) and the GOES 0.1 - 0.8 nm (red lines).

or not possible (Al-thick). The Be-thick data normally has an extremely low signal ($\sim$ few DN s^{-1}, even for the longest exposure times for quiescent solar conditions), leading to large noise. Thus any correlation must be proceeded with caution. Al-mesh and Al-poly are underestimated by generally a factor of 0.5 or more for the X123 measurements above 0.9 keV. Using the spectrally extended 1T and/or 2 T Free fits the comparison moves much closer to unity. This is expected and occurs for two reasons. First, the majority of the solar flux resides below 2 keV and the Al-mesh and Al-poly filters have much larger effective area at those wavelengths than the 'thick' filters. Secondly, any variance significant uncertainty

in the contamination thickness will directly effect these filters. The fact that MinXSS-1 measurements correlate best with the thicker filters further strengthen the postulation that the X123 and XP instruments are most sensitive to active regions on the Sun, which contain the hottest non-flaring plasma and hence the most X-ray photons.
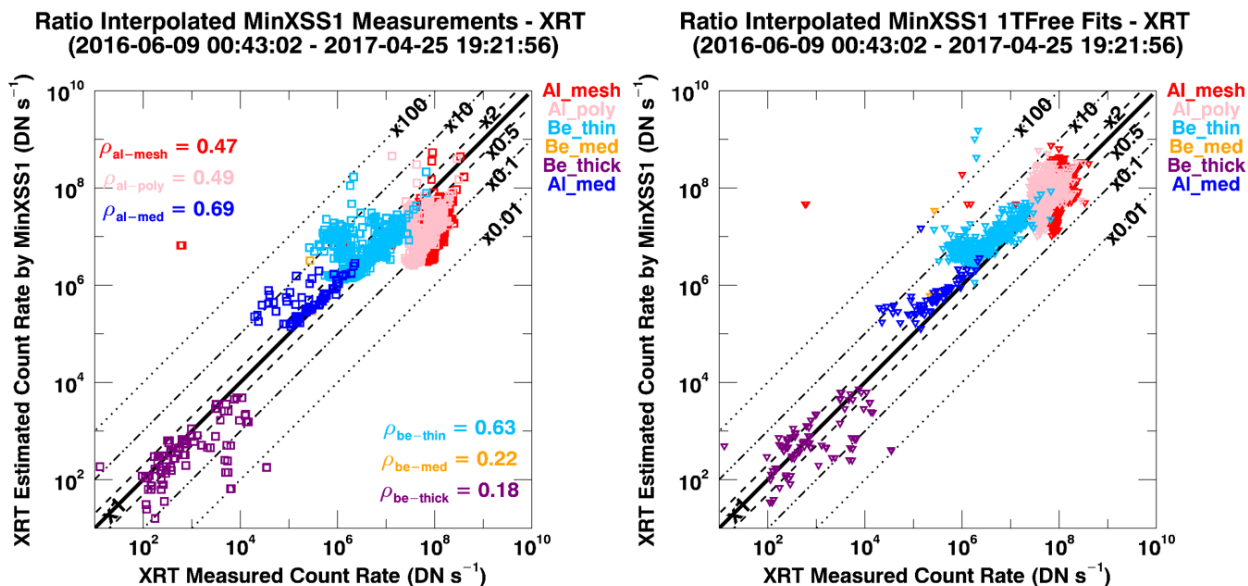
Figure 9.19: MinXSS-1 X123 estimated XRT count rate from the 15 minute averaged data interpolated to the XRT synoptic time frame. The Be-thin and Al-med are the most consistent for the actual X123 data (left) and the OSPEX 1TFree fit (right).

The spectral correlation is consistent with the majority of X123 counts occurring above 0.9 keV and that most of the noise being below 1.0 keV (the sharp rise in the correlation coefficient for all filters above 1 keV). The mission length data is vvery useful for observing long term connections between the two instruments, but XRT synoptics nominally are not in all the important filters. Thus to include a special Be-med and Al-thick observation we have coordinated a special observation series with XRT.

We have worked to cross-calibrate the two instruments to develop quantitative relationships. We have four coordinated observations with MinXSS-1 and XRT on 2016 August 29, 2016 August 30, 2016 September 5 and 2016 September 6. The August observations suffered
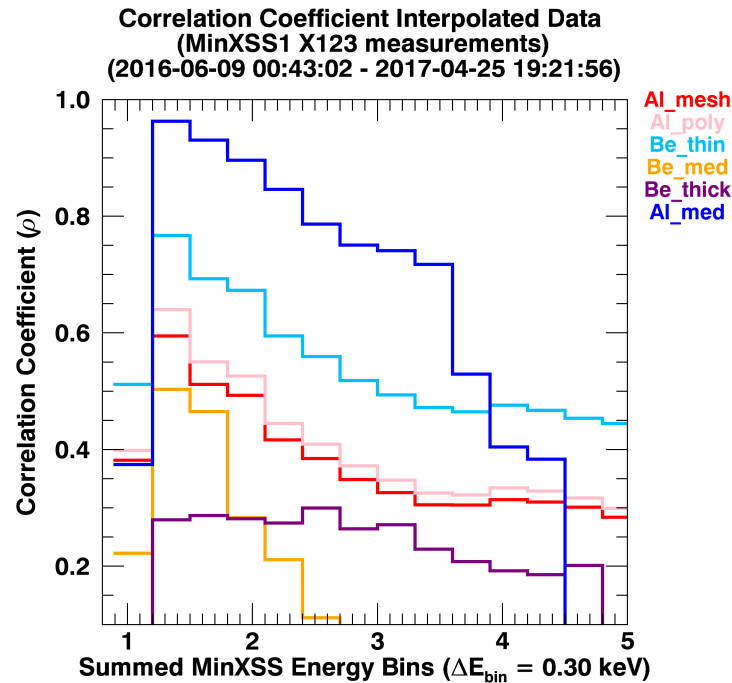
Figure 9.20: MinXSS-1 correlation spectrum (binned at 0.3 keV) with XRT filters for the entire MinXSS-1 mission. The MinXSS-1 data is the 15 minute average and the XRT images are the full Sun synoptics.

saturation in some of the XRT filter images, making direct comparisons difficult. A solar flare occurred during the 2016 September 6 XRT exposures, thus a comparison for this date delayed until after the analysis of the one saturation free, non-flare simultaneous observation on 2016 September 5. The following cross-calibration is from data on 2016 September 5.

Count rate images between 2016 September 5 09:55:00 and 09:59:59 UT of the Be-thin (Figure 9.21), Be-med, Be-thick (Figure 9.23), Al-med, Al-thick (Figure 9.24), Al-mesh and Al-poly (Figure 9.22) show a fairly mundane Sun with a small, older active region and a 'haze' of diffuse coronal emission. Histograms in Figure 9.25 of the count rate clearly demonstrate that the thinner filters have the highest count rate and give an intuitive interpretation of the image data. The histograms also show that the active regions account for a relative small portion of the Al-mesh and Al-poly count rates and almost all of the Be-med, Be-thick,

Al-med and Al-thick filters.
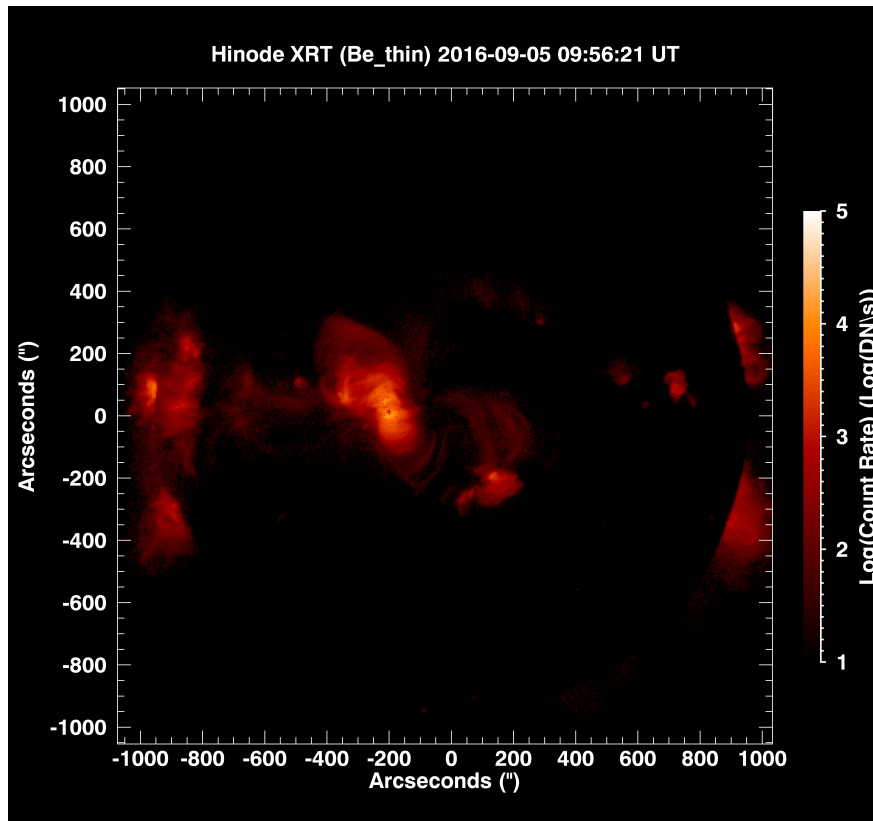
Figure 9.21: MinXSS-1 ⇔ XRT cross-calibration on 2016 September 5. Log-scaled count rate XRT Be-thin full Sun image. Be-thin is the regularly taken full Sun synoptic that best displays the X-ray emitting regions that contribute to the MinXSS signal.

MinXSS-1 observations were averaged (where there was valid data) from 2016 September 05 09:55:35 - 11:10:44 UT to maximize signal-to-noise (SN). Figure 9.26 shows that the GOES XRS level was near 1.4×10^{-7} W m^{-2} ($\sim$B1 level) and fairly steady over this time frame. So averaging MinXSS-1 data over this time frame is valid. The XP data has been background subtracted and the fA signal agreed with the X123 predicted XP fA signal to within 1%. The X123 data was fit in OSPEX with 1T and 2TFree models with good agreement ($\chi^2_{reduced}$ = 3.08 and 1.44 respectively). The spectral fits and em loci in Figure 9.27 show consistency among the fits and the data. GOES XRS inferred photospheric and coronal abundance emission measure and temperature values are higher in temperature than
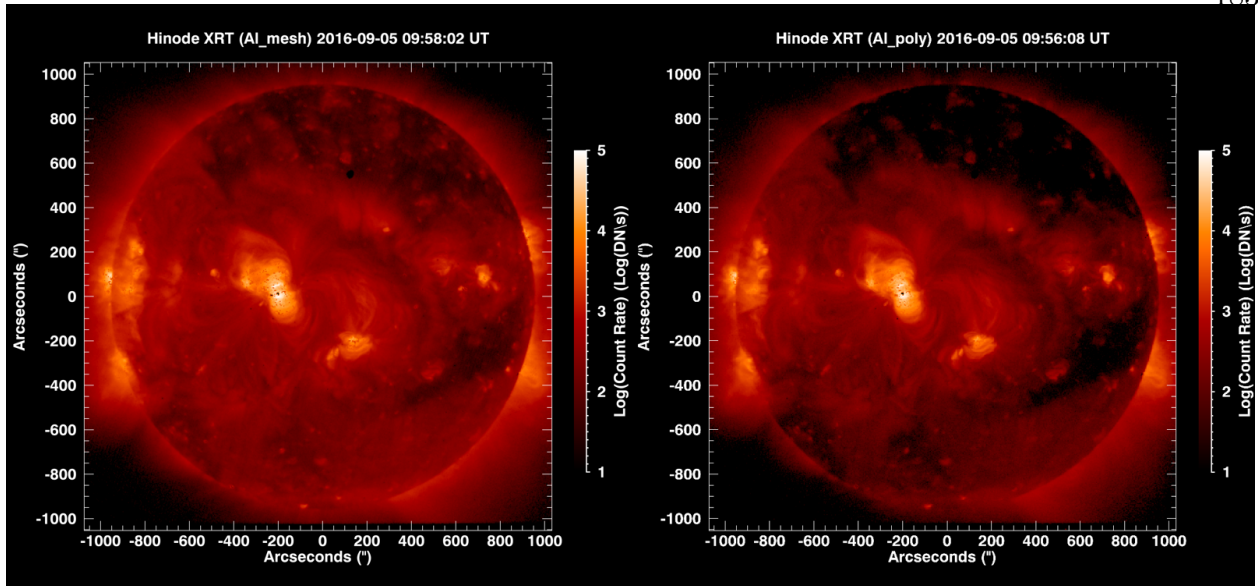
Figure 9.22: MinXSS-1 ⇔ XRT cross-calibration on 2016 September 5. Log-scaled count rate XRT Al-mesh and Al-poly full Sun images. These 'thin' aluminum filters have significant spectral contribution from photons less than 0.6 keV, contributions from cooler plasma and hence emission is observed from the majority of the ~1 MK corona.

MinXSS (due to the GOES XRS high temperature spectral bias) but still consistent with the MinXSS em loci.

These measurement and OSPEX spectral fits were used to compute the expected XRT count rates as discussed earlier and similar results as the MinXSS-1 mission length analysis were observed. Figure 9.28 lists the good agreement between X123 and Be-thin, Be-med, Be-thick, Al-med and Al-thick (within a factor of 2) for the measurement photon flux above 0.9 keV and an underestimation of the Al-mesh and Al-poly count rates. The Al-mesh and Al-poly discrepancy is mitigated with the 1TFree photon flux and a strong overestimation is observed with the 2TFree photon flux. This is further validation that the MinXSS-1 extracted emission measure for temperature components less than 2 MK is normally too large and not an accurate realization of the solar conditions.

Using spectral models like Chianti, ratios of the signal in one filter pixel to the signal in another filter in the same pixel can yield an approximation of an isothermal spectrum. These
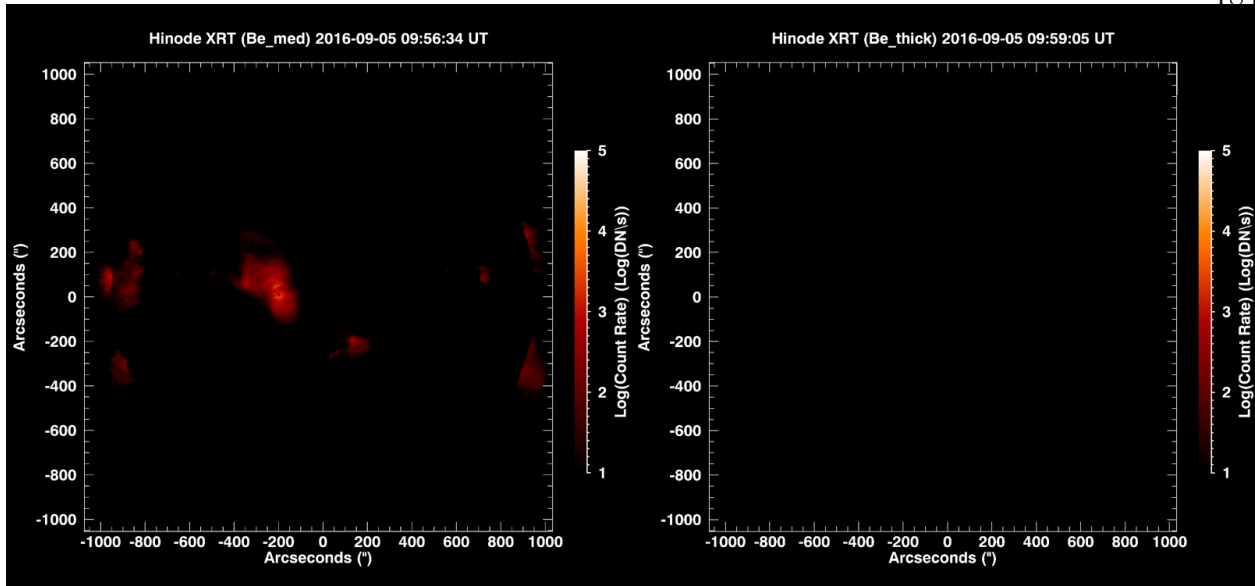
Figure 9.23: MinXSS-1 ⇔ XRT cross-calibration on 2016 September 5. Log-scaled count rate XRT Be-med and Be-thick full Sun images. These 'thicker' beryllium filters are some of the hottest plasma generally fount in active regions. Be-med is sensitive to plasma for T ≥ 2 MK and Be-thick is a great diagnostic for plasma with T ≥ 4 MK if the emission measure is strong enough.... Many stacked exposures of Be-thick images normally show active region cores and transient quiet Sun features.

isothermal approximations are computed by forward modeling the signal in XRT filters for an range of isothermal spectra and computing the signal ratios. Thus a temperature vs. filter ratio curve is created and only temperature ranges that have a large enough slope (non-degeneracy) and monolithic behavior are employed. The emission measure value that best recreates both filer signals is used. Following this methodology, given a signal ratio per filter set, one can approximate an isothermal temperature and emission measure per pixel. An example emission measure and temperature map for the Be-thin and Al-poly ratio is displayed in Figure 9.29.

Emission measure maps, temperature maps, emission measure vs. temperature distributions and predicted MinXSS-1 X123 signals were computed for all filter ratios possible (with adequate signal-to-noise). The later two are displayed in Figure 9.30. The emission measure vs. temperature distributions are consistent with the XRT volume emission measure
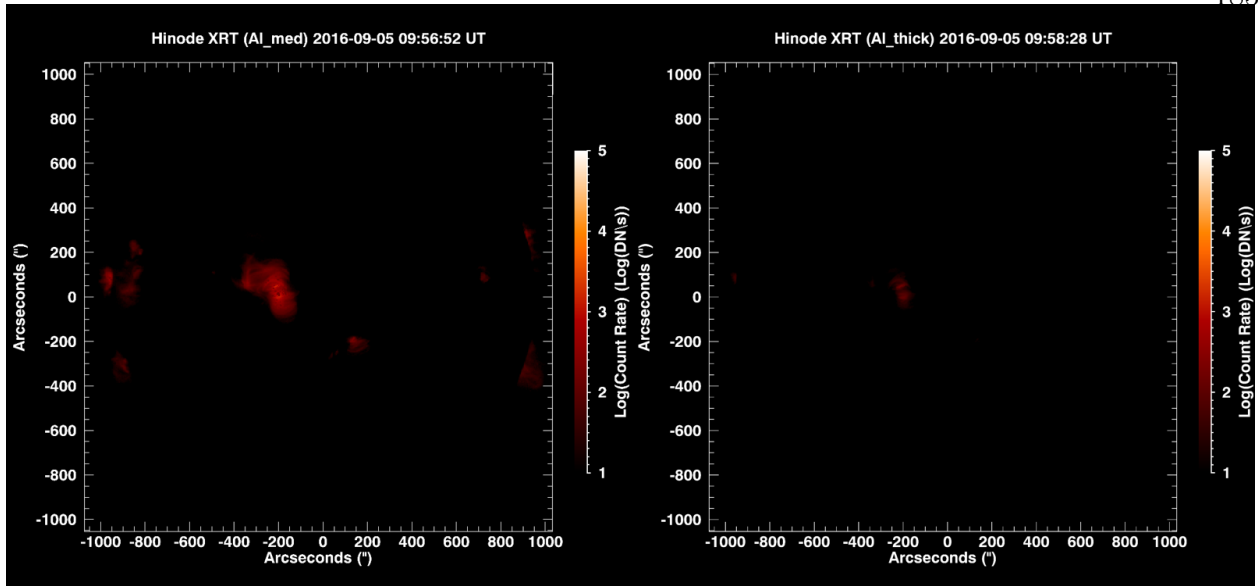
Figure 9.24: MinXSS-1 ⇔ XRT cross-calibration on 2016 September 5. Log-scaled count rate XRT Al-med and Al-thick full Sun images. These 'thicker' aluminum filters are mostly sensitive to photons between 0.6 - 1.6 keV and generally probes plasma for T ≥ 2 MK. Active region emission is readily observed in these filter images.

loci and a few filter ratios yield spurious hot (T ≥ 10 MK) components. These can clearly be debunk when one compares their predicted X123 count rate to the measured count rate. There is a clear over estimation of the high energy counts ($E_{ph} \geq 2$ keV). Furthermore the low energy counts do not come close to estimating the magnitude of the X123 low energy counts. This is primarily due to the photon noise and temperature noise flags, removing many pixels where the count rat is either too low or the inferred temperature is too uncertain. Thus, there are not enough valid pixels to recreate the magnitude of the X123 spectrum. This is expected and so are the spectral inconsistencies because the Sun is not isothermal. There can be many contributions to the emission by the various temperature components along the line of sight. Thus, I implement the XIT DEM fitting algorithm to further compare the MinXSS-1 and XRT capabilities.

When using the DEM XIT on MinXSS-1 data alone, extremely large emission measure distribution below 2 MK that accurately recreates the MinXSS-1 X123 count rate (see

Hinode XRT composite norm Histograms, 2016-09-05
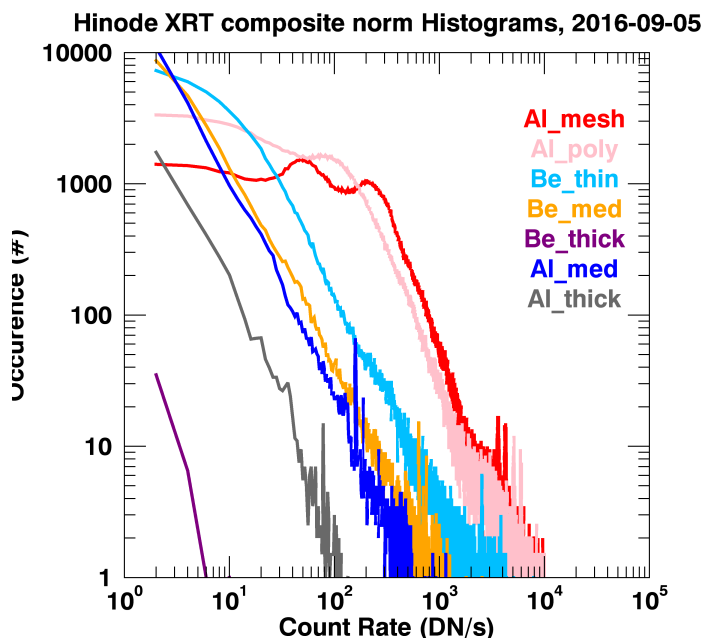
Figure 9.25: MinXSS-1 $\Leftrightarrow$ XRT cross-calibration on 2016 September 5. Histograms of the full Sun composite images.

Figure 9.14) is inferred. This is because X123 and XP have little sensitivity to plasma below 2 MK. When this MinXSS-1 only derived DEM is folded through the XRT responses it recreates the thick filters (Be-thin, Be-med, Be-thick, Al-med and Al-thick) fairly well but drastically overestimates the counts in the thin filters Al-mesh and Al-poly) by factors over 300. This is due to the higher sensitivity to cooler plasma of the thinner filters (see Figure 9.32). Thus, we know that the magnitude of this cooler plasma is not accurate. Conversely, XRT only XIT DEM predicts all the XRT count rates to within a factor of 2 (except Be-thick, a factor of 3, but Be-thick had a very small signal and relatively large uncertainty), and the MinXSS-1 X123 signals up to 2.1 keV to within a factor of 3, but overestimates the higher energy counts, due to a hot plasma tail. **Even though XRT has higher effective area than MinXSS, the lack of pure spectral discrimination hinders XRT's ability to adequate constrain hotter plasma (T $\geq$ 6 MK).** This is known as the XRT (and
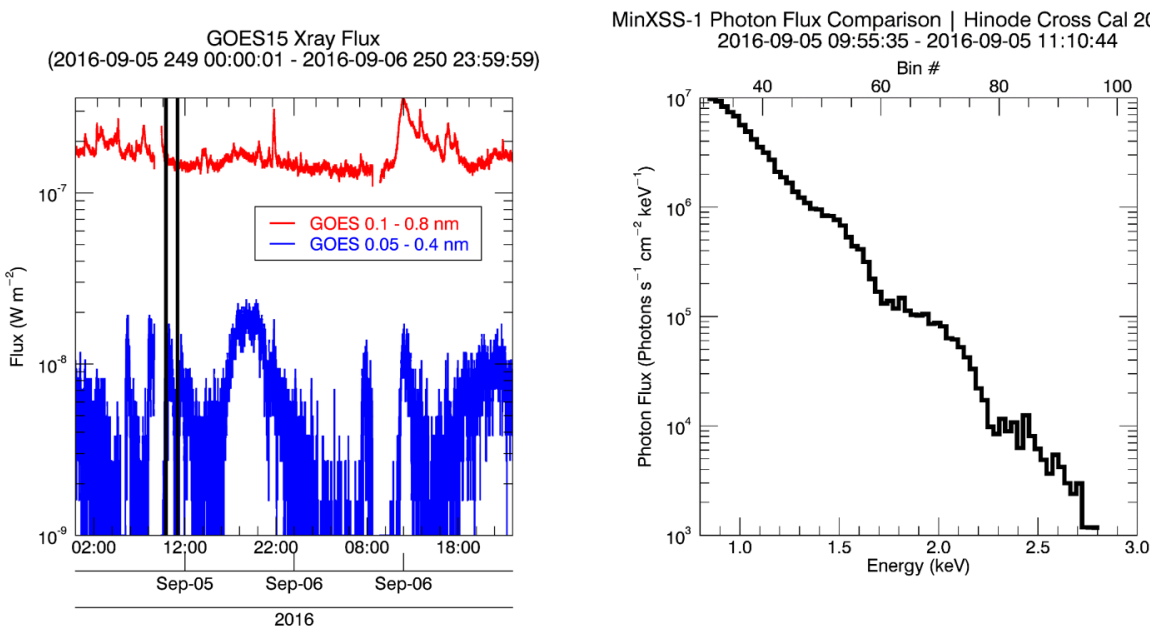
Figure 9.26: MinXSS-1 ⇔ XRT cross-calibration on 2016 September 5. Left plot: GOES 0.1 - 0.8 nm (red) and 0.05 - 0.4 nm (blue) energy fluxes vs. time. The black vertical lines indicate the time range that MinXSS-1 observations were averaged over. The Sun was fairly 'quiet'. Right plot: X123 directly derived ('inverted') photon flux incident on the X123 aperture.

EIS) high temperature 'blind spot', coined by Winebarger et al. 2012 [157] and reaffirmed here by MinXSS-1.

Using combined MinXSS-1 and XRT data to constrain the XIT DEM results in improved count rate estimations (all within roughly a factor of 1.5!) of all XRT and MinXSS-1 data sets, diminished hot components (T $\geq$ 5 MK) and a slightly lower cool component (T $\leq$ 2 MK) (see Figure 9.31). Consequently the overlap of the minimal sensitivity to plasma less than 2 MK lead to large uncertainties in the *shape* of the DEM below 2 MK under the em loci envelope. When this DEM result is folded through instruments that have cooler plasma sensitivity like SDO AIA and Hinode EIS, the XRT and MinXSS-1 derived DEM overestimates their respective signals. This realizations leads to the fact that instruments more sensitive to plasma less than 2 MK need to be included to refine the DEM to a more realistic shape.
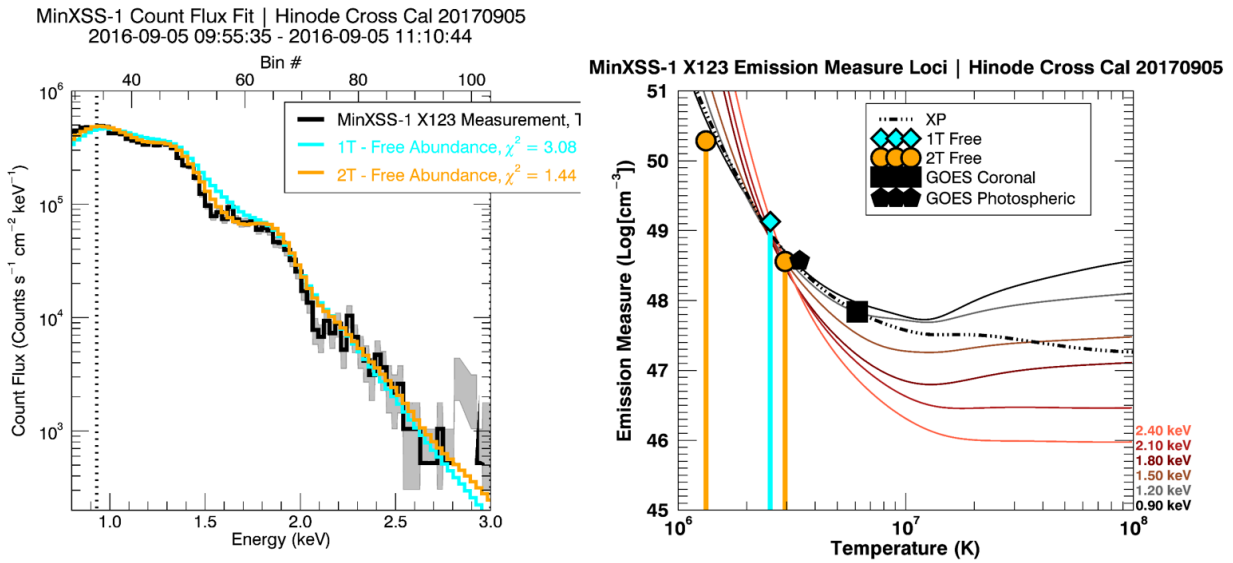
Figure 9.27: MinXSS-1 ⇔ XRT cross-calibration on 2016 September 5. Left plot: MinXSS-1 X123 count flux and OSPEX 1T and 2T spectral fits. Right plot: X123 and XP em loci with the 1T, 2T Free OSPEX fits and the GOES photospheric (pentagon) and coronal (square) values overploted.

XRT Filter		Al-mesh	Al-poly	Be-thin	Be-med	Be-thick	Al-med	Al-thick
# of arcsrconds^2 XRT Data	("^{2})	4.2E+06	3.9E+06	1.3E+06	8.6E+05	7.3E+04	1.7E+06	5.8E+05
XRT Measurement All positive pixels	(DN/s)	1.3E+08	8.9E+07	7.9E+06	1.4E+06	9.0E+02	6.7E+05	5.3E+04
X123 Measurement estimated XRT count rate	(DN/s)	1.2E+07	1.1E+07	5.6E+06	1.2E+06	6.1E+02	6.4E+05	7.9E+04
	Ratio	0.09	0.12	0.70	0.87	0.68	0.97	1.49
XRT_Flux.pro Chianti V8.0 MinXSS 2TFree Fit - abundance	(DN/s)	5.4E+08	3.4E+08	2.0E+07	1.8E+06	8.0E+02	9.5E+05	1.1E+05
	Ratio	4.17	3.83	2.49	1.30	0.88	1.43	2.02
XRT_Flux.pro Chianti V6.0 MinXSS 2TFree Fit Feldman 1992 abundance	(DN/s)	1.1E+09	3.3E+08	2.0E+07	1.8E+06	8.4E+02	9.9E+05	1.1E+05
	Ratio	8.47	3.75	2.46	1.35	0.93	1.48	2.09

Figure 9.28: MinXSS-1 ⇔ XRT cross-calibration on 2016 September 5. Table comparing MinXSS-1 X123 estimated XRT filter count rates from 1) X123 data alone, 2) X123 OSPEX spectral fits using the best fit elemental abundance and 3) nominal XRT spectral emission model.
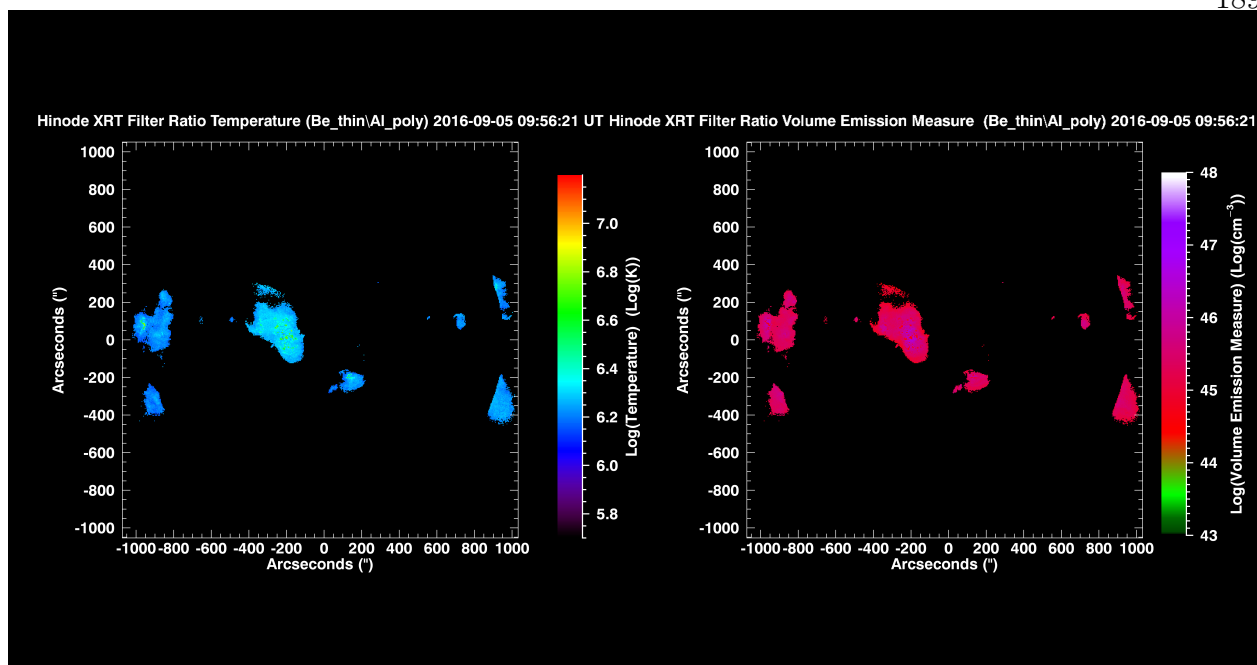
Figure 9.29: MinXSS-1 ⇔ XRT cross-calibration on 2016 September 5. Left plot: XRT Be-thin and Al-poly filter ratio temperature map. Each pixel is assumed to be isothermal in this filter ratio formulation. Right plot: XRT Be-thin and Al-poly filter ratio VEM map.
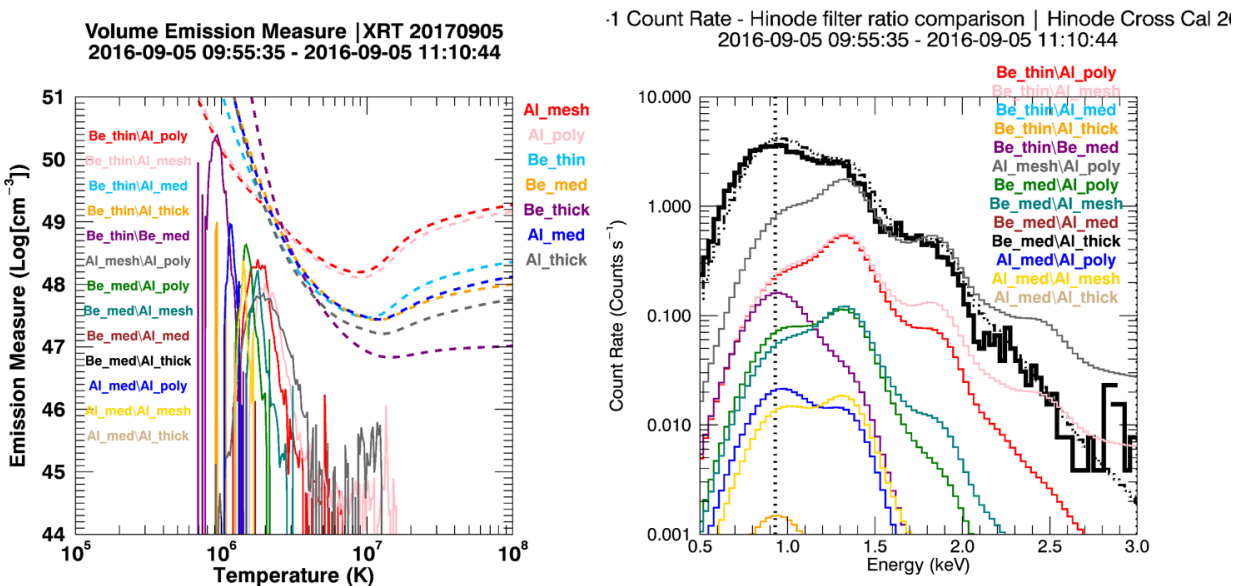
Figure 9.30: MinXSS-1 ⇔ XRT cross-calibration on 2016 September 5. Left plot: VEM vs temperature distribution for various XRT filter ratios. Different ratios emphasize different temperature ranges. Right plot: MinXSS-1 X123 measurements (black histogram) and XRT filter ratio predictions (color histograms). None of the XRT filter ratios can recreate the X123 spectrum. This is expected because the Sun is not isothermal.
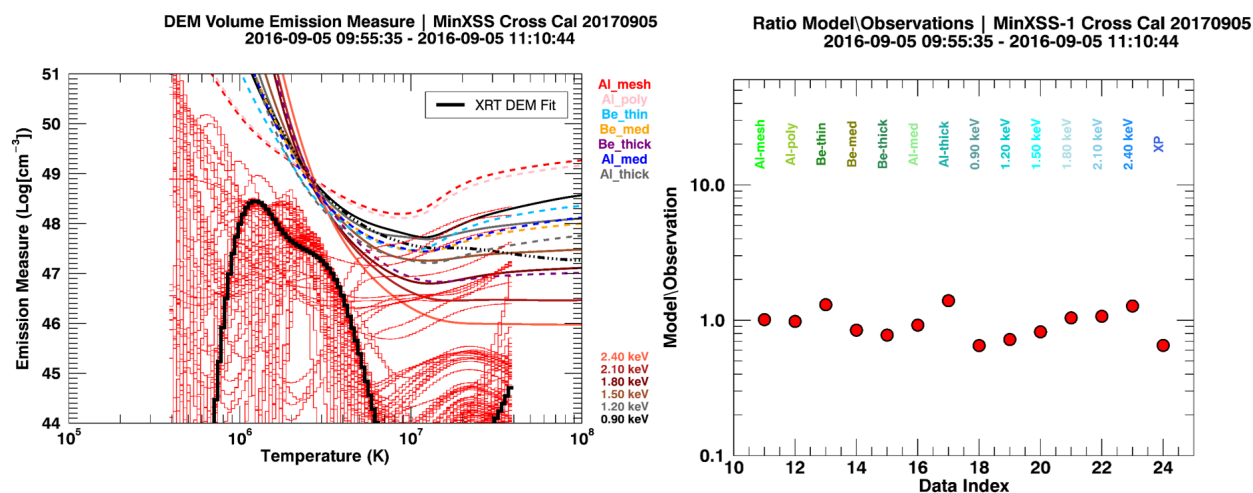
Figure 9.31: MinXSS-1 ⇔ XRT cross-calibration on 2016 September 5. Left plot: MinXSS-1 and XRT DEM fit results. VEM vs. temperature using the XIT method (black thick histogram line). The thin red histogram lines are 100 Monte-Carlo realizations and give an indication of the fit uncertainty. The uncertainty in the DEM has decreased and the hot plasma ($T \geq 5$ MK) is better constrained. The colored solid lines are the X123 em loci and the dash-dot-dot-dot black line is the XP em loci. The dashed color lines are the XRT em loci. Both em loci agree quite well. Right plot: MinXSS-1 X123 measured and DEM count rates. The lower temperatures ($T \leq 2$ MK) are poorly constrained because both MinXSS and XRT have low sensitivity to cooler plasma.

XRT Filter/MinXSS		Al-mesh	Al-poly	Be-thin	Be-med	Be-thick	Al-med	Al-thick	0.9 keV	1.2 keV	1.5 keV	1.8 keV	2.1 keV	2.4 keV	XP
Actual Count Rate	normalized (counts/s)	3.05E+01	2.27E+01	6.06E+00	1.57E+00	1.24E-02	3.98E-01	9.15E-02	3.06E+01	1.97E+01	5.72E+00	2.58E+00	4.97E-01	1.46E-01	5.19E+03
DEM XRT-MinXSS (VEM units)	Ratio	1.01	0.98	1.30	0.84	0.78	0.92	1.39	0.65	0.72	0.82	1.04	1.07	1.27	0.65
DEM XRT Only (VEM units)	Ratio	1.00	1.00	1.00	0.97	2.93	0.97	1.63	0.55	0.66	1.39	3.25	6.37	15.27	0.85
DEM MinXSS Only (VEM units)	Ratio	362.19	363.55	3.40	1.17	0.76	1.30	1.93	1.00	1.00	0.99	1.02	0.96	1.04	1.00

Figure 9.32: MinXSS-1 $\Leftrightarrow$ XRT cross-calibration on 2016 September 5. Table comparing the DEM MinXSS-1 X123 estimated XRT filter count rates. XRT DEM alone results in over estimating the X123 counts above 2 keV, the MinXSS-1 DEM alone results in over estimating the XRT Al-mesh and Al-poly count rates, but the combined XRT and MinXSS-1 DEM yield good results for all filters and MinXSS-1 energies (within a factor of 2).

In summary, MinXSS-1 and XRT thick filters yield consistent results within the factor of 3 uncertainty in both instruments spectral responses and other effects. MinXSS-1 and XRT thick filters are sensitive to similar populations of plasma and when MinXSS-1 derived elemental abundances are used for the XRT responses the two satellites can be combined for reliable high temperature discrimination. While XRT has a larger effective area and is more sensitive to flux changes on a short time scale, the highe temperature 'blind spot' limits the effectiveness of XRT to constrain relatively dim plasma hotter than 6 MK, which was uncovered by Winebarger et al. 2012 [157] and validated with MinXSS-1 in this study. MinXSS-1 course spectral resolution allows for the separation of spectral bins with hotter temperature sensitivity and can set lower limits on the hot-dimmer plasma content in the quiescent Sun than the XRT broadband filters.

9.8 MinXSS and Solar Dynamics Observatory (SDO) Atmospheric Imaging Assembly (AIA) Cross-Calibration

The *Solar Dynamics Observatory (SDO) Atmospheric Imaging Assembly (AIA)* is a series of telescopes with special mirror coatings and filters to separate numerous spectral bandpasses [100]. AIA can create images in 94 $\mathring{A}$ (Fe XVIII), 131 $\mathring{A}$ (Fe VIII, XXI), 171 $\mathring{A}$ (Fe IX), 193 $\mathring{A}$ (Fe XXIV), 211 $\mathring{A}$, 304 $\mathring{A}$ (He II), 335 $\mathring{A}$ (Fe XVI), 1600 $\mathring{A}$ (C IV), 1700 $\mathring{A}$ (continuum) and 4500 $\mathring{A}$ (continuum) with temperature coverage from 6 x 10^4 K to 2 x 10^7

K. AIa was launched as part of NASA's Living with a Star program on 2010 February 11 to provide an unprecedented cadence of full Sun images at the densest EUV filter coverage to date. AIA nominally returns some of its filter images at a cadence of ∼12 seconds with roughly a 2460" x 2460" field of view with a nominal 0.6" spatial resolution.

The Heliosiemic Magnetospheric Imager (HMI) created line of sight magnetograms, allowing the inference of the photospheric magnetic field distribution [140]. The nominal data units are Gauss, which can be combined with the projected pixel area to extract the magnetic flux. I only display HMI magnetograms in this dissertation to display the photospheric magnetic structure and qualitatively compare the strong positive and negative polarity regions to active regions and their link to the X-ray flux.

We have seen that DEM results using AIA data alone yield overestimations of the hot plasma content (T ≥ 10 MK, see Figure 9.14). Moreover, when comparing the XRT and MinXSS-1 only DEM predicted count rates of AIA to the actual full Sun values there are overestimations by factors of 3 ($171\mathring{A}$ and $211\mathring{A}$) and 4 ($193\mathring{A}$ and $335\mathring{A}$). Thus, I attempted to refine our determinations of the full Sun temperature structure by including AIA data into the DEM fitting constraints. We focus on the MinXSS-1 and XRT cross-calibration data set on 2016 September 5.

To understand the advantage of adding AIA to the DEM analysis, the AIA temperature responses are plotted in Figure 9.33). 335 $\mathring{A}$, 211 $\mathring{A}$ 193$\mathring{A}$, 171 $\mathring{A}$ and 131 $\mathring{A}$ will help constrain the cooler (T ≤ 2 MK) plasma significantly when combined with XRT and MinXSS-1. 94 $\mathring{A}$ has a large contribution from Fe XVIII, which has peak formation temperature near 7 MK, but substantial contribution from plasma up to 20 MK. To better comprehend the contibution of the Fe XVIII emission, one can extract this component from the 94 $\mathring{A}$ signal following the algorithm of Del Zanna 2013 [35] in Equation 9.5.

$$C_{FeXVIII} = C_{94\mathring{A}} - \frac{C_{211\mathring{A}}}{120} - \frac{C_{171\mathring{A}}}{450} \tag{9.5}$$

Where C, is the count rate (DN s^{-1}) in the corresponding filter image pixel. The extraction of the Fe XVIII component has proven reliable in many studies and is included in this one, but because the Fe XVIII count rate is not linearly independent from the other AIA filter images, I will not invoke it as a constraint in the DEM fitting. Representative count rate images of 94 $\mathring{A}$, 131 $\mathring{A}$, 171 $\mathring{A}$, 193 $\mathring{A}$, 211 $\mathring{A}$, 335 $\mathring{A}$, Fe XVIII and HMI data are during the MinXSS-1 and XRT cross-calibration study in Figure 9.34 and Figure 9.35, with t histograms of the data in Figure 9.36).
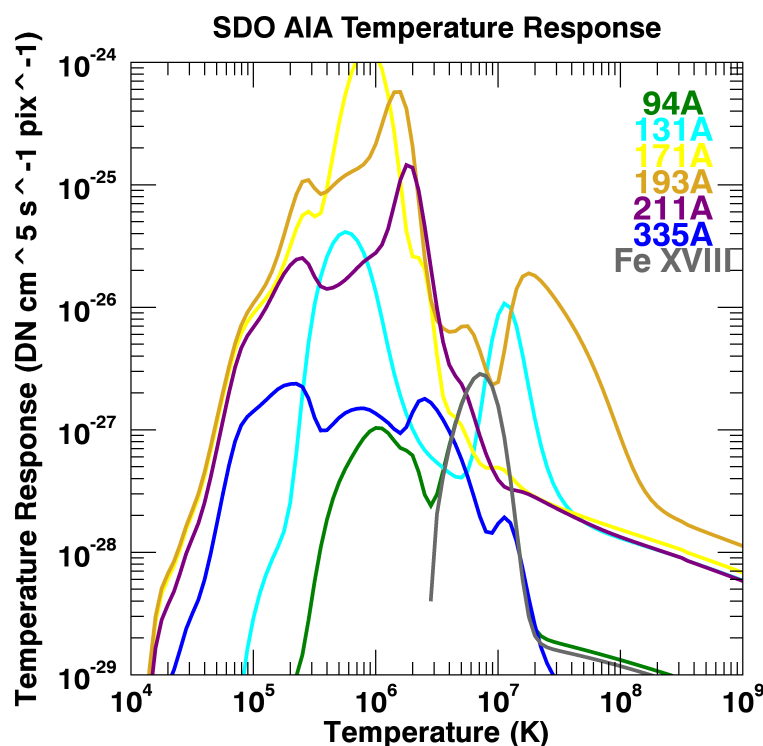
Figure 9.33: Example of the SDO AIA filter temperature responses, F(T), (DN s^{-1} cm^5 pixel^{-1}) in column emission measure units (CEM) for various abundances. In general, the filters have broad temperature responses except for 94$\mathring{A}$ and the derived Fe XVIII component.

The total positive pixels were summed and normalized by the number of positive pixels. The resultant values were used to constrain the XIT DEM. Figure 9.37) shows the dramatic

improvement in constraining the DEM structure below 2 MK. The inclusion of AIA data is vital for accurate DEM estimations using XRT and MinXSS-1 data. All predicted count rates are within a factor of 3 and the DEM has now morphed to have significant (emission measure $\geq 10^{44}$ cm^{-3}) between 0.4 and 4 MK. The small increase by T $\sim$ 40 MK is an artifact of the XIT procedure, is not real and can be ignored.
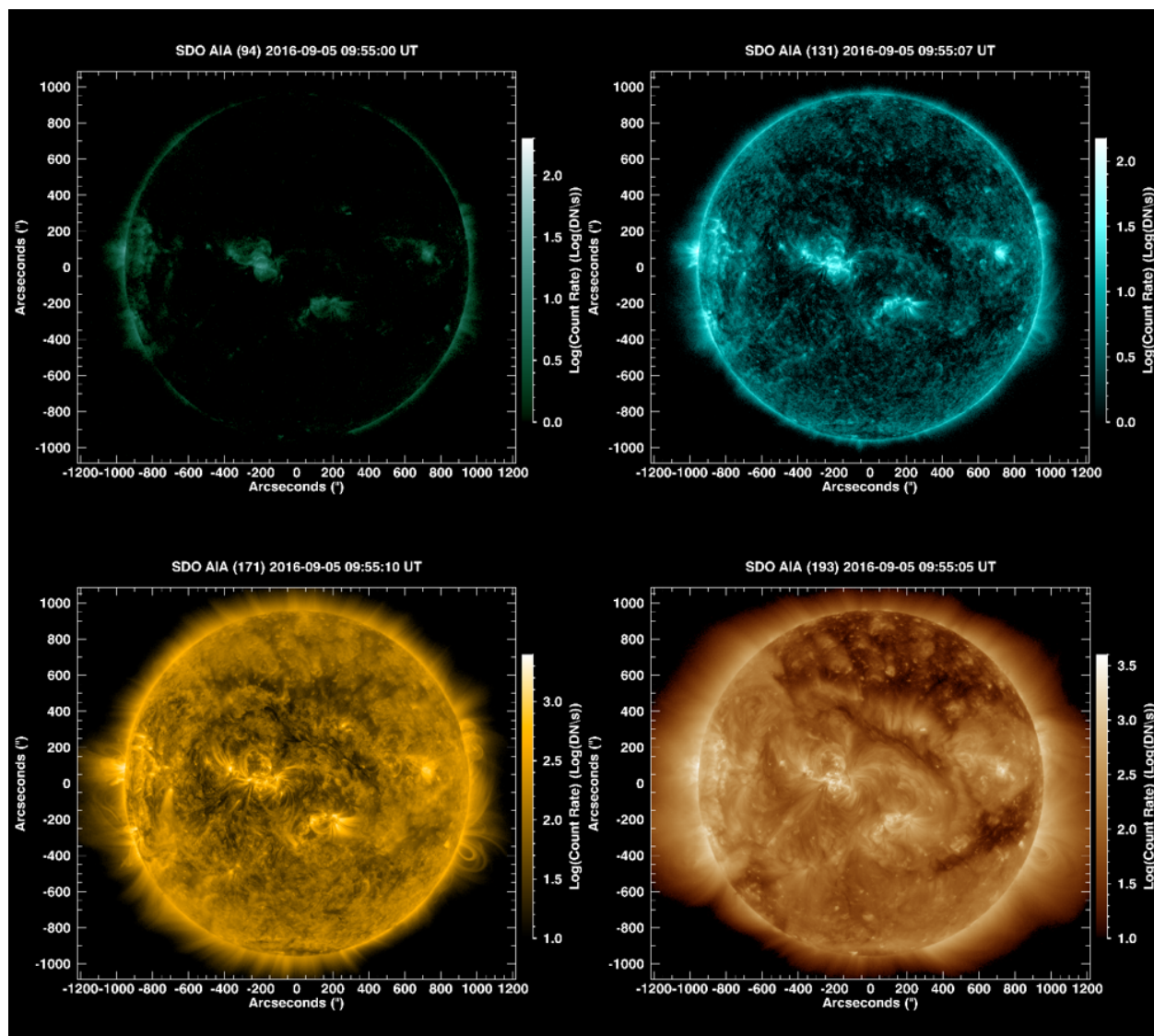
Figure 9.34: Log-scaled count rate AIA 94$\mathring{A}$, 131$\mathring{A}$, 171$\mathring{A}$ and 193$\mathring{A}$ images on 2016 September 5.

The AIA em loci show how important the inclusion of AIA data can be. In summary,
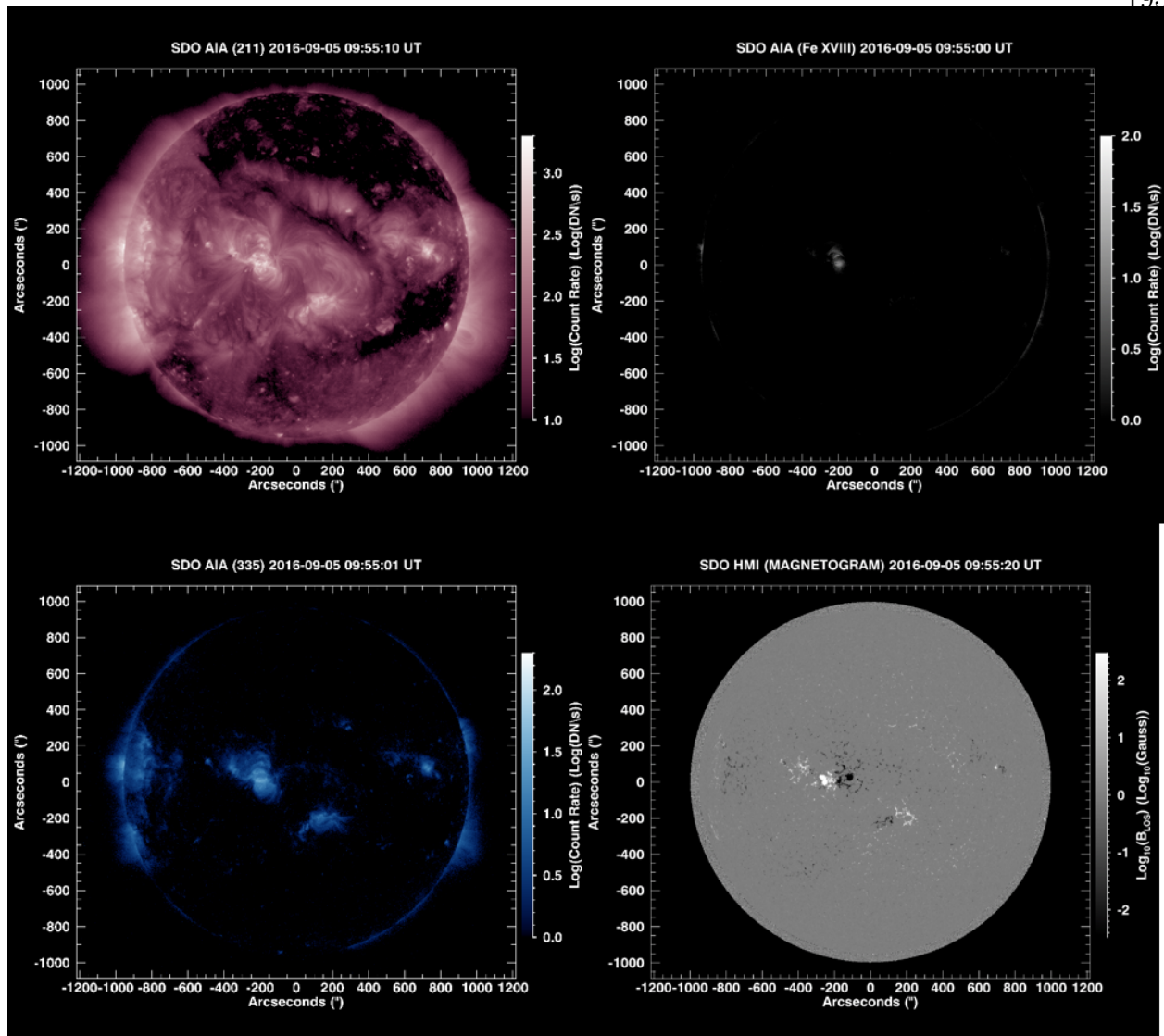
Figure 9.35: Log-scaled count rate AIA 211$\mathring{A}$, 335$\mathring{A}$, Fe XVIII and HMI images on 2016 September 5.

the inclusion of AIA data to the XRT and MinXSS-1 full Sun observations is essential for a much improved DEM estimation from 0.4 to 100 MK. MinXSS-1 with the aid of XRT constrain the high temperature portion of the DEM while AIA bolster confidence in the low temperature end. AIA performs regular measurements without any significant eclipse periods, XRT conducts daily synoptic full Sun images and MinXSS, when in orbit regularly observes the Sun. Thus, inclusion of SDO Extreme Variability Experiment (EVE) data to

this data set can provide daily DEMs to determine the temporal variability of the Sun-as-a-Star. The Sun is vary unique, due to its proximity to Earth. This close proximity can allow us to connect features in the full Sun DEM to solar intricacies. These DEMs can then be used as a guide in future stellar DEMs that will be extracted, especially with the new X-ray astrophysics missions launching soon.
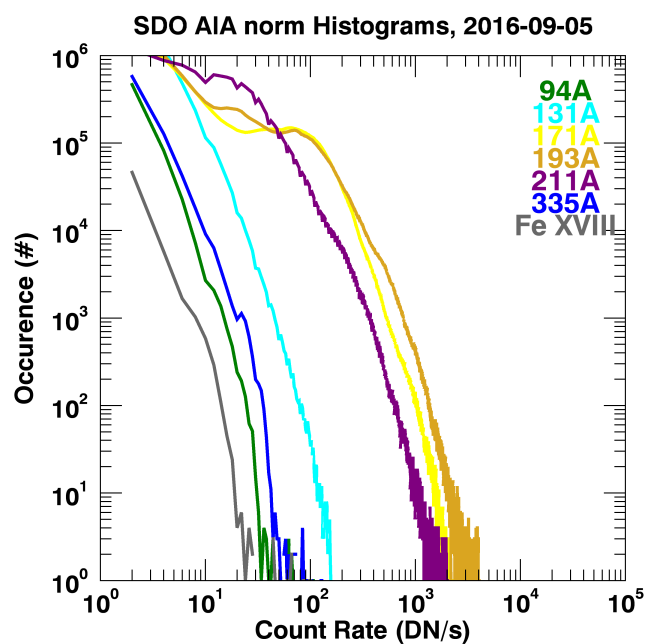
Figure 9.36: Histograms of the full Sun SDO AIA images on 2016 September 5.
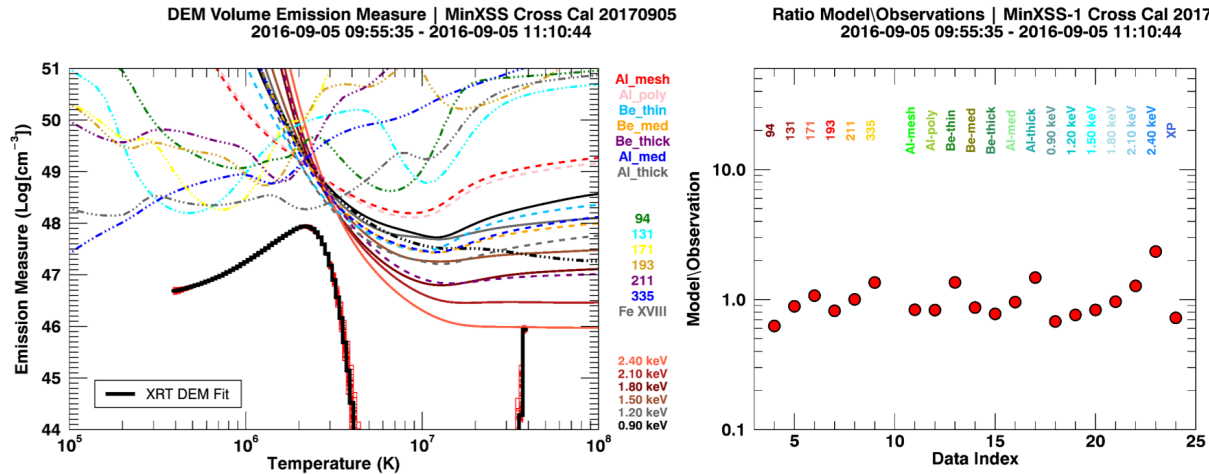
Figure 9.37: MinXSS-1 ⇔ XRT cross-calibration on 2016 September 5. Left plot: MinXSS-1, XRT and AIA DEM fit results. VEM vs. temperature using the XIT method (black thick histogram line). The thin red histogram lines are 100 Monte-Carlo realizations and give an indication of the fit uncertainty. The uncertainty in the DEM has diminished drastically. The DEM is strongly constrained over the fit temperature range. AIA greatly improves the cool plasma inference. Right plot: MinXSS-1 X123 measured and DEM count rates.

9.9   MinXSS and the Hinode EUV Imaging Spectrometer (EIS)

The *Hinode EUV Imaging Spectrometer* conducts very high spectral resolution measurements (nominal $\Delta\lambda \approx 47$ mA FWHM) 170 - 210 $\mathring{A}$ and 250 - 290 $\mathring{A}$ [33]. The slit spectrograph has slit settings of 1", 2", 40" and 266". EIS generally raster over a region of interest, so semi-simultaneous images over an effective field of view are acquired. EIS regularly (roughly every 3 weeks) rasters its 40" slot over the entire Sun in patches. The patches are combined and co-aligned (optimally using the 195 $\mathring{A}$ EIS image to align with the AIA 193 $\mathring{A}$ image) to create a full Sun mosaic in all of the nominal data sets. An example of a few of the full Sun mosaics from the MinXSS-1 and XRT cross-calibration are displayed in Figure 9.38.

The Hinode EIS full Sun mosaics were also coordinated with MinXSS-1 observations to serve as a cross check for studies discussed through out this Chapter. The full EIS mosaic data set include images probing a range of temperatures and are:
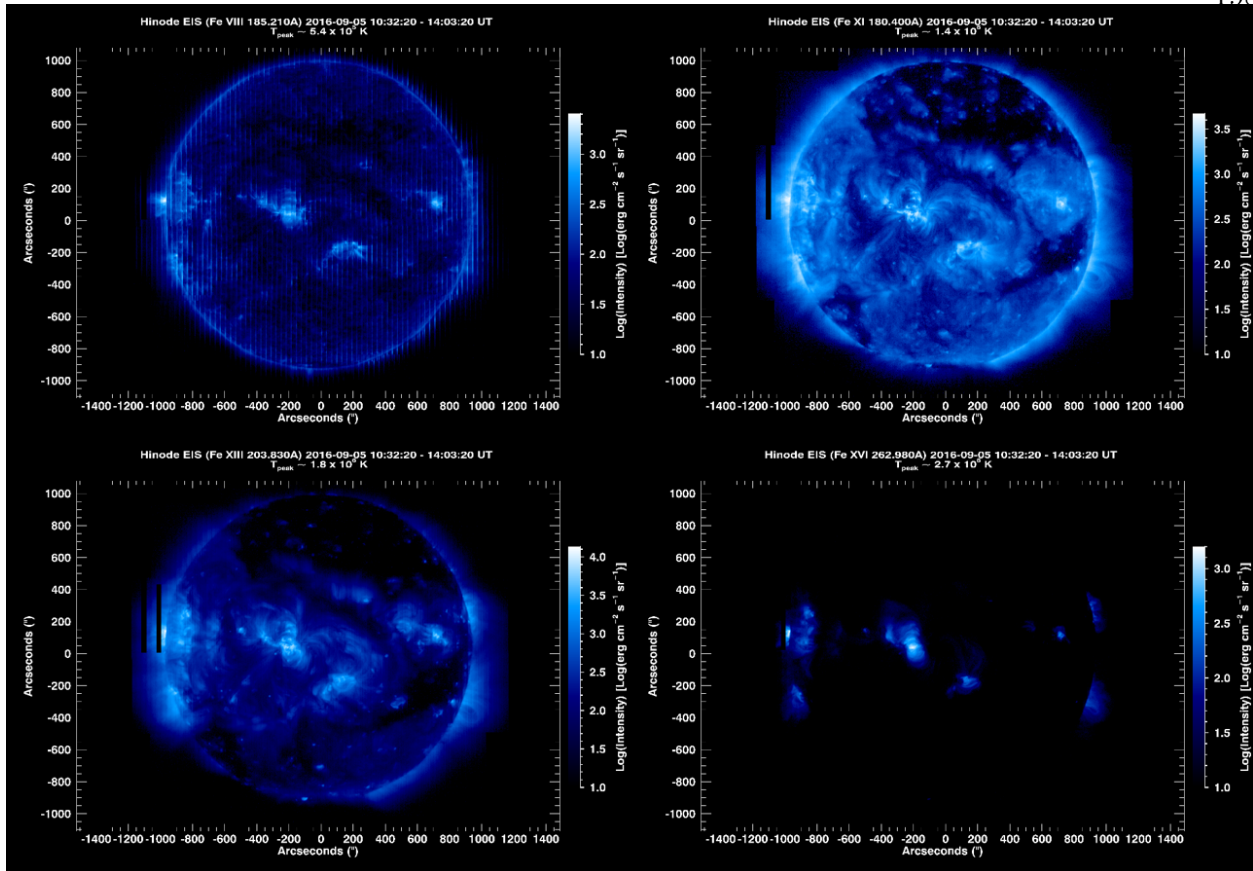
Figure 9.38: Log-scaled energy intensity (ergs cm^{-2} s^{-1} sr^{-1}) of Fe VIII (185.21 Å, T$_{peak}$ ∼5.4 x 10^5 K), Fe XI (180.40 Å, T$_{peak}$ ∼1.4 x 10^6 K), Fe XIII (203.83Å, T$_{peak}$ ∼1.8 x 10^6 K) and Fe XVI (262.98Å, T$_{peak}$ ∼2.7 x 10^6 K) images on 2016 September 5.

- 180.40 Å (Fe XI - T$_{peak}$ ∼ 1.4 x 10^6 K)

- 185.21 Å (Fe VIII - T$_{peak}$ ∼ 5.4 x 10^5 K)

- 195.12 Å (Fe XII - T$_{peak}$ ∼ 1.6 x 10^6 K)

- 202.04 Å (Fe XIII - T$_{peak}$ ∼ 1.8 x 10^6 K)

- 203.83 Å (Fe XIII - T$_{peak}$ ∼ 1.8 x 10^6 K)

- 211.36 Å (Fe XIV - T$_{peak}$ ∼ 2.0 x 10^6 K)

- 256.32 Å (He II - T$_{peak}$ ∼ 8.5 x 10^4 K)

- 258.42 $\mathring{A}$ (Si X - $T_{peak} \sim 1.4$ x 10^6 K)

- 262.98 $\mathring{A}$ (Fe XVI - $T_{peak} \sim 2.7$ x 10^6 K)

- 264.23 $\mathring{A}$ (S X - $T_{peak} \sim 1.5$ x 10^6 K)

- 274.24 $\mathring{A}$ (Fe XIV - $T_{peak} \sim 2.0$ x 10^6 K)

- 275.37 $\mathring{A}$ (Si VII - $T_{peak} \sim 6.3$ x 10^5 K)

- 284.16 $\mathring{A}$ (Fe XV - $T_{peak} \sim 2.2$ x 10^6 K)

By visual inspection there are qualitative similarities between the features in the EIS 40" slot and the XRT filter images. The EIS 262.98 $\mathring{A}$ is centered on a bright Fe XVI with $T_{peak} \sim 2.7$ x 10^6 K, is strikingly similar to the XRT Be-thin image. One can ascertain that the dominant emission in the Be-thin images arise from $\sim$ 2.5 - 3 MK plasma which is located primarily in active regions and other sight of significant magnetic flux. The EIS 203.83 $\mathring{A}$ window containing the Fe XIII with $T_{peak} \sim 1.8$ x 10^6 K is very analogous to the XRT Al-poly image. Again we can connect the Al-poly detected emission to be dominated by plasma near 1.7 - 1.9 MK. The last comparison is more of a reach and not as similar, probably due to the fact the Al-mesh has such a wide spectral bandpass. The EIS 180.40 $\mathring{A}$ with Fe XI and $T_{peak} \sim 1.4$ x 10^6 K is most similar to XRT Al-mesh. The EIS 40" mosaics seem to be a good link to deriving the dominant range of temperatures that contribute to the XRT filters. Inherently the line emission from EIS data are centralized in temperature (see Figure 9.39), while the XRT filters are not directly traceable to a set of temperatures without other information.

The 40" slot data has spectral resolution on the order of 0.89 $\mathring{A}$, so there are blends included in the spectral windows listed above. These blends need to be fully accounted for for accurate em loci and implementing the full EIS 40" slot data set in DEM fitting. This is a process that will be undertaken in the future. Currently there are a few lines with minimal
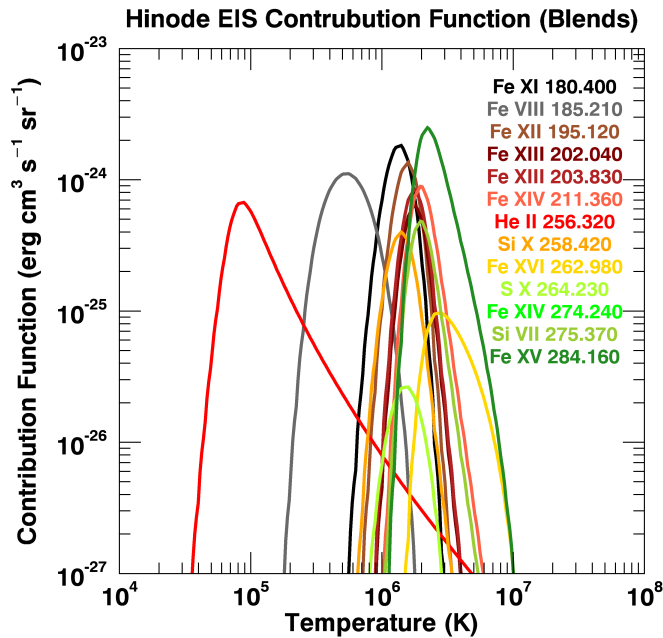
Figure 9.39: Example of the Hinode EIS line contribution functions $G(T, E_{ij}, n_e)$, (erg s^{-1} cm^3 sr^{-1}) using the nominal 'coronal' abundance and elecron number density of 10^9 cm^{-3}. A huge difference between EIS and the broadband spectrometers or filter images that have been discussed thus far is that the temperature response for the EIS lines are much more centralized in temperature. The 40" slot data has a lower spectral resolution nd thus there can be blends in each spectrally integrated EIS 40" slot image.

blending that can be included in the XIT DEM fitting procedure. These are 262.98 $\mathring{A}$ (Fe XVI), 275.37 $\mathring{A}$ (Si VII) and 284.16 $\mathring{A}$ (Fe XV). These EIS full Sun mosaics were summed for their positive count rate across the field of view, normalized by the total positive pixels and converted to units compatible with the line contribution function, $G(T, E_{ij}, n_e)$ to create em loci and be included in the DEM constraints. The results of including the small EIS subset with AIA, XRT and MinXSS-1 data is displayed in Figure 9.40. There is not much change in the DEM, demonstrating that the AIA, XRT and MinXSS-1 DEM is a solid realization of the full Sun DEM. Again, the incorporation of line blends will allow more EIS lines to be included and future SDO EVE data will bolster these full Sun DEM extractions.
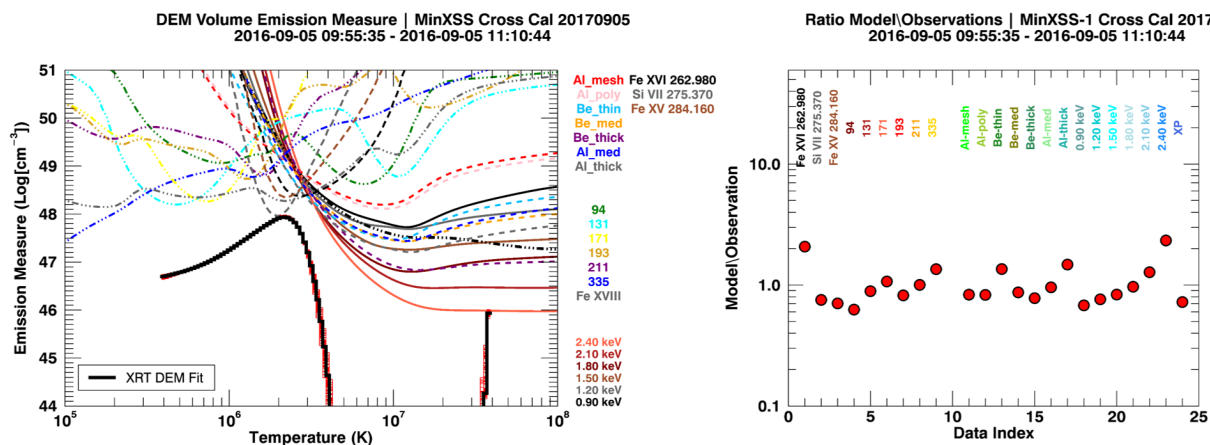
Figure 9.40: MinXSS-1 ⇔ XRT cross-calibration on 2016 September 5. Left plot: MinXSS-1, XRT, AIA and EIS DEM fit results. VEM vs. temperature using the XIT method (black thick histogram line). The thin red histogram lines are 100 Monte-Carlo realizations and give an indication of the fit uncertainty. The 40" slot full Sun mosaics have do not substantially improve the temperature discrimination. Right plot: MinXSS-1 X123 measured and DEM count rates.

9.10   Summary of MinXSS-1 Capabilities

The MinXSS CubeSats can provide the solar community with a new set of measurements that can augment current and future investigations of the solar corona. The SPS ancillary instrument, the X-ray detectors of XP and X123 have been characterized. The first version of MinXSS, MinXSS-1, has performed nominally over its mission at LEO. This dissertation describes the MinXSS instrument suite, the X123 FOV sensitivity, X123 spectral resolution vs. photon energy, XP and X123 effective area curves, X123 detector response matrix, XP and X123 temperature response, the X123 linearity of response, GOES flux levels vs. MinXSS-1 X123 measured integrated counts, and MinXSS-2 X123 estimated counts, inferred temperature and emission measures from MinXSS spectra, and emission measure loci for the discussed data. These realizations further the notion that CubeSats can conduct significant targeted science. A summary of the main attributes of MinXSS are listed below.

(1) MinXSS-1 X123 has an effective solar flux energy range of 0.8 - 12 keV (∼0.10 -

1.55 nm) with resolving power ∼40 at 5.9 keV, and with dead-time corrections applied accurate spectra up to low GOES X levels (but need to correct for pulse-pileup).

(2) The MinXSS CubeSats X123 have a relatively higher spectral resolution over a fairly broad bandpass that allow inference of elemental abundance values for the elements Fe, Ca, Si, Mg, S, Ar and Ni, when there are sufficient counts at X123 energies for their respective line groups. The observed elemental abundance variation in this work:

- clearly demonstrate a decrease in low FIP elements for flare-peak times vs. the pre-flare values for spectral fits with a single FIP-Bias multiplicative factor

- display variance in the fractionation pattern among the low FIP elements when all elements are allowed to vary for GOES levels > B1.

(3) MinXSS-1 X123 flare measurements in this dissertation indicate that the hotter components in the flaring plasma for the C2.7, M1.2 and M5.0 flares bare peak temperatures near 15, 13 and 20 MK, respectively.

(4) MinXSS-1 X123 and XP plasma temperatures inferences are self consistent and single X123 temperature fits (1TFree) are comparable with GOES XRS isothermal estimates between GOES ∼B1 - M5 levels (GOES XRS response becomes non-linear for lower flux levels). However, these single temperature fits can not account for high energy X123 spectral counts nor are suitable fits for an entire flare spectrum alone.

(5) MinXSS X123 can infer non-large-flaring Sun properties between 2.0 - 4 MK with high confidence, but limited capabilities for temperatures below 2.0 MK (due to limited sensitivity at lower energies, < 1 keV).

(6) MinXSS X123 can only set upper limits on the emission measure and cannot definitively constrain the temperature values for 'dimmer' plasma hotter than $\sim$5 MK during non-large-flaring times. This is due to the flattening nature of the temperature response above $\sim$4.5 MK for energy bins less than 3 keV and limited significant counts from energy bins greater than 3 keV. The latter is a consequence of the relatively small X123 aperture area (2.5×10^{-4} cm^2).

(7) MinXSS-1 X123 can set a lower limit on the hot-dimmer plasma (T $\geq$ 5 MK and VEM $\leq 10^{46}$ cm^{-3}) than the normal XRT full Sun observations.

(8) MinXSS-1 plus XRT plus SDO AIA data constrain the magnitude of the DEM from low temperatures to high temperatures ($0.4 \geq$ T ≥ 40 MK) of the full Sun. These are essentially broadband measurements. Emission line measurements, like from EIS, the Marshall Grazing Incidence X-ray Spectrometer (MaGIXS) [89], and EVE are needed to fully constrain the *shape* of the DEM.

9.11 Improvements of MinXSS-2

The MinXSS-2 X123 has a thinner Be window along with a lower noise preamplifier that will provide an improved low energy response, possibly extending the low energy limit to 0.6 keV. The newer preamplifier for the MinXSS-2 X123 Fast SDD detector allows for a better spectral resolution for the same nominal peaking time as the MinXSS-1 X123. MinXSS-2 X123 will be operated with a shorter peaking time for the that will allow for accurate spectra for a higher input flux. Preliminary estimates suggest GOES levels around X2 are the maximum that the MinXSS-1 X123 can handle before the spectra will need further processing to retain fidelity.

Chapter 10

MinXSS Quiescent Sun (QS) and Active Region (AR) Contribution Study

In Chapter 9 we learned about the MinXSS-1 plasma diagnostic capabilities and limitations. It is clear that to obtain a more complete description of the solar plasma temperature distribution ($0.4 \geq T \geq 40$ MK), MinXSS-1 data need to be combined with XRT and AIA full Sun images. We now apply this technique to:

(1) Obtain a quiet Sun (the Sun with no active regions on the Earth side of the disc) soft X-ray spectrum and DEM.

(2) Estimate an active region spectrum and DEM by using the QS measurements, before the active region rotates on the solar limb to remove the QS contributions to both the soft X-ray flux and QS DEM.

This case study is to verify that MinXSS-1 data can be used to temporally isolate the active region contribution to the MinXSS-1 count rate. We focus on the quiescent period from 2017 March 14 - March 18 and starting on March 18 an active region starts to rotate into the line-of-sight of Earth. Thus we take the 2017 March 14 - March 16 as the QS times (MinXSS-1 data is averaged over this time frame to improve the signal-to-noise) and March 21 between 11:46:19 - 12:57:05 UT for the AR measurements. Figure 10.1 displays the GOES XRS 0.1 - 0.8 nm flux stability from 2017 March 14 - 16 (except for the dropouts due to GOES eclipse season) and validating its candidacy for QS measurements. Also displayed are GOES fluxes for the AR timeframe. The MinXSS-1 inverted photon flux for both the QS

observations and the AR (full Sun) observations are in the right panel in Figure 10.1. The QS is about $\frac{1}{3}$ of the total X123 spectrally integrated count rate on 2017 March 21. This again exemplifies the dominance of active region emission in the MinXSS-1 signal.
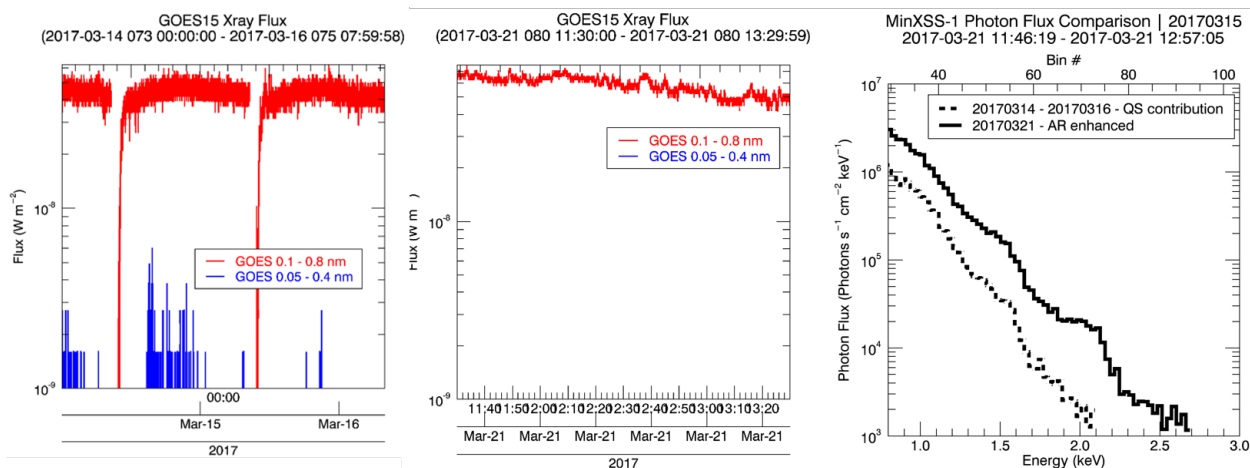
Figure 10.1: GOES 0.1 - 0.8 nm (red) and 0.05 - 0.4 nm (blue) energy fluxes vs. time for the QS extraction (2017 March 14 - 16, GOES ∼A4) and the AR contribution estimation (2017 March 21, GOES ∼A6). The Sun was very 'quiet'. Middle plot: Right plot: X123 directly derived ('inverted') photon flux incident on the X123 aperture.

The difference between the full Sun AR and QS spectra (in count space) are used to extract the AR portion of the signal and is plotted in Figure 10.2. This differenced signal will be referred to as the AR signal and the full Sun spectrum on 2017 March 21 as the 'full Sun' measurements for the rest of this dissertation. All three of these spectra were fit with OSPEX 1T and 2TFree fits and DEM estimations.
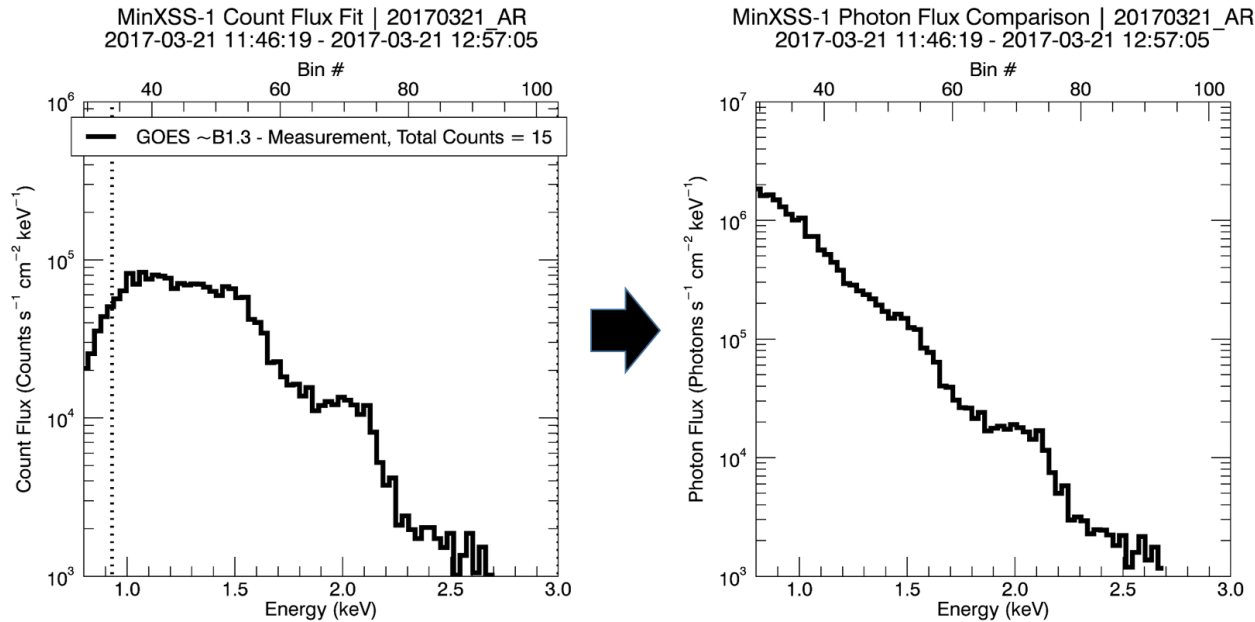
Figure 10.2: Left plot: The estimated active region contribution to the MinXSS-1 X123 count flux and is the difference between the count rate in the 2017 March 21 spectra and the averaged 2017 March 14 - 16 spectra. Right plot: Active region photon flux incident on the X123 aperture, derived from the count flux measurements.

10.1 Spectral Parameter Fits

The OSPEX 1T and 2TFree fits for the QS are very similar and thus the 1TFree fit is chosen to represent the QS for this study. The full Sun was fit two ways. The first is the traditional 2TFree fit and the second method is a 2T component on top of the 1T QS fit fixed to serve as the background. The first version resulted in 1.8 MK and a dimmer ~4.2 MK components. The second version, which is displayed in Figure 10.3 resulted in 2.1 MK component at 3.2×10^{48} cm^{-3} and an extremely dim (3 orders of magnitude lower) 10 MK component at 8.0×10^{45} cm^{-3}. This hotter component is likely not this large in emission measure, if present at all, and this will be demonstrated in the DEM fits. Similar to the results in Chapter 9, the 1T and 2TFree MinXSS-1 X123 fits always over-estimate the magnitude of the emission measure for the best fit temperature components. The AR component 2TFree fit has an abundance near 0.78, which is fairly close to the Feldman 1992

values.
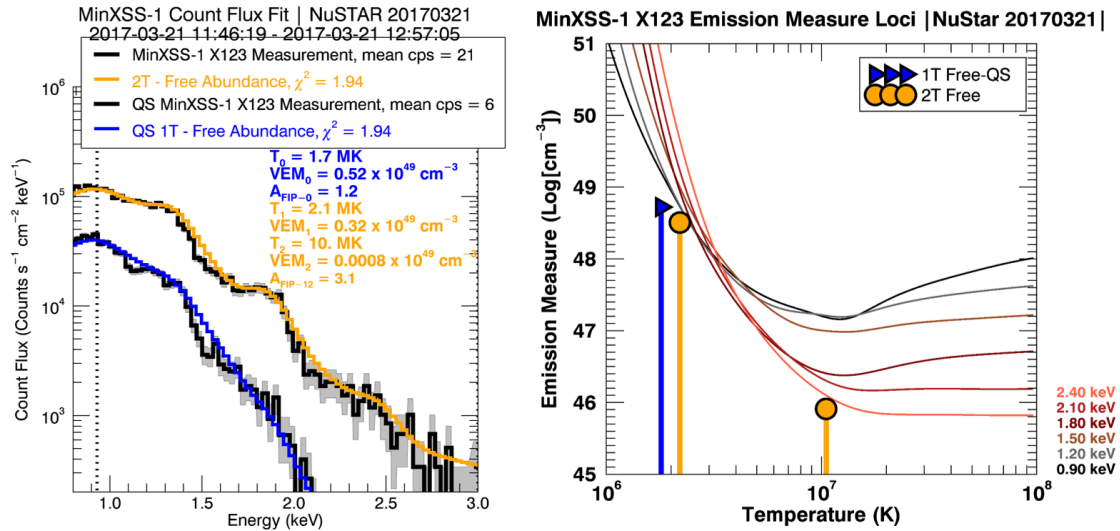
Figure 10.3: Left plot: MinXSS-1 X123 count flux and OSPEX spectral fits for the QS (2017 March 14 - 16; blue lines and symbols) and AR enhancement (2017 March 21; orange lines and symbols). Right plot: X123 and XP em loci with the 1T, 2T Free OSPEX fits and the GOES photospheric (pentagon) and coronal (square) values overplotted. The stated abundance values have been multiplied by 4 (Feldman 1992 * 4).

Table 10.1 lists the MinXSS-1 QS 1T fit result which yields a 1.7 MK and 5.2×10^{48} cm^{-3} component with an abundance value of 0.3 (where $A_{low-fip} = 1$ is the Feldman 1992 abundances, coronal). This abundance value is similar to the photospheric values (Caffau et al. 2011). The QS temperature fit value of 1.7 MK is very similar to the Sylwester et al. 2012 [146] results during the 2009 deep solar minimum. The SphinX spectrally resolved measurement fits yielded a range of QS temperatures between 1.7 - 1.9 MK and emission measure values between 0.4 - 1.1 $\times 10^{48}$ cm^{-3}. Given that the SphinX measurements were the lowest X-ray signals ever recorded and lower than the GOES XRS 0.1 - 0.8 nm detection threshold (3.7×10^{-9} W m^{-2}), the emission measure values are at least a factor of 5 lower than the measurements presented here. GOES is also very non-linear in the A level and thus the GOES level is not very indicative, as observed in Woods et al. 2017 [158]. So the SphinX measurements could be claimed to be during solar conditions equivalent to an

effective GOES low A level, while the MinXSS-1 QS measurements were near a measured GOES A4 level.

The 2016 June 29 - July 01 time frame 1TFree fits for the QS conditions are during GOES $\sim$A5 level. The emission measure is almost a factor of two larger (9.57×10^{48} cm^{-3}) than the 2017 March times. The temperature is a little hotter at 2.09 MK. The abundnace estimate is consistent with the previous QS fits at a value near 0.3.

Solar observations using an earlier version of the X123 on sounding rocket flights were conducted in 2012 June 23 (Rocket-1) and 2013 October 21 (Rocket-2) and were analyzed in Caspi et al. 2015 [28]. GOES measurements yield 2.34×10^{-7} W m^{-2} (B2 level) and 1.00×10^{-6} W m^{-2} (C1 level), with a micro flare occurring near the 2013 measurement. 2-temperature fits analogous to the 2TFree in this dissertation were conducted as well as power-law DEM fits. The full solar spectrum was fit, meaning no estimation of a background nor active region component was made in the analysis. So the best comparison to this study is the full Sun spectral fit of MinXSS-1 which are in Table 10.2. The low-fip factors are different among all three observations. The 2012 rocket flight had course binning and thus limited abundance sensitivity as compared to the 2013 rocket flight and MinXSS-1. MinXSS-1 has A$_{low-fip}$ = 0.71, Rocket-1 A$_{low-fip}$ = 0.9 and Rocket-2 A$_{low-fip}$ = 0.4. It is clear from these results that the inferred abundance can vary easily by a factor of two for differing solar conditions and GOES flux levels. There currently appears to be no clear trend between these three data sets, except that a micro flare occurred just before the 2013 measurement and could be the reason for the lower fip value. If chromospheric evaporation is a dominant process in micro flares, than this would bring photospheric plasma into the corona and lower the inferred low-fip factor. More targeted analysis of abundances is needed in the future.

Table 10.1: Comparison of quiet Sun 1T fits for the MinXSS-1 X123 data discussed in this dissertation on 2017 March 14 - 16, 2016 June 29 - July 01 and inferred from the CORONAS – PHOTON SphinX measurements during the deep solar minimum in 2009.

Instrument	GOES Level	Observation Times (UT)	EM_1 $(10^{48}$ cm$^{-3})$	T_1 (MK)	FIP-Bias$_1$ $(0.25 \approx$ photospheric) $(1 =$ coronal)
MinXSS-1 X123	$\sim$A4	2017-Mar-14 00:28:35 - 2017-Mar-16 07:02:21	5.2 (0.06)	1.79 (0.04)	0.30 (0.06)
MinXSS-1 X123	$\sim$A5	2016-Jun-29 10:29:32 - 2016-Jul-01 22:55:53	9.57 (0.66)	2.09 (0.03)	0.31 (0.03)
SphinX	< A1	2009-Feb-22 - 2009-Sep-16	0.71 $(^{+0.23}_{-0.19})$	1.78 (0.07)*	1.0 (fixed)

Table 10.2: Comparison of 2T fits for the MinXSS-1 X123 on 2017 March 21, 2016 September 05, 2016 July 23, 2016 July 20, 2016 July 7, and the sounding rocket X123 measurments from Caspi et al. 2015 [28] on 2012 June 23 and 2013 October 21. Both measurements are full Sun integrated and have not subtracted any background (quiet Sun) contributions to the count rate.

Observatory	GOES Level	Observation Times (UT) (UT)	EM$_1$ (10^{48} cm^{-3})	T$_1$ (MK)	EM$_2$ (10^{48} cm^{-3})	T$_2$ (MK)	FIP-Bias$_{12}$ (0.25 ≈ photospheric) (1 = coronal)
MinXSS-1	~A6	2017-Mar-21 11:46:19 - 12:57:05	16.86 (3.50)	1.67 (0.08)	0.14 (0.08)	4.21 (0.55)	0.71 (0.08)
MinXSS-1	~B1	2016-Sep-05 09:55:35 - 11:10:44	192.53 (83.14)	1.32 (0.09)	3.61 (0.90)	2.95 (0.13)	0.74 (0.08)
MinXSS-1	~B5	2016-Jul-23 01:15:05 - 01:39:45	76.80 (8.00)	1.86 (0.05)	1.80 (0.20)	4.80 (0.12)	0.55 (0.02)
MinXSS-1	~B3	2016-Jul-20 18:04:13 - 18:28:53	87.30 (8.10)	1.82 (0.04)	1.30 (0.20)	4.68 (0.14)	0.54 (0.02)
MinXSS-1	~B3	2016-Jul-07 23:41:03 - 2016-Jul-08 00:04:24	108.00 (7.50)	1.70 (0.02)	1.20 (0.10)	4.58 (0.08)	0.72 (0.03)
Rocket-1	~B2	2012-Jun-23 ~19:30:00 - ~19:36:00	4.9 (N/A)	2.9 (N/A)	0.01 (N/A)	11.00 (N/A)	0.9 (0.05)
Rocket-2	~C1	2013-Oct-21 ~18:00:00 - ~18:06:00	38.0 (N/A)	2.7 (N/A)	0.31 (N/A)	8.7 (N/A)	0.4 (0.05)

The Capsi et al. 2015 fits yield a persistent $\sim$3 MK component with hotter and dimmer components of 8.7 and 11 MK respectively, for the 2012 and 2013 observations. The MinXSS-1 full Sun 2TFree fit on 2017 March 21 estimate a bright $\sim$1.7 MK component, presumably having significant contribution from the QS, based on the QS fits. The secondary component is at 4.2 MK with emission measure near 10^{48} cm^{-3}. The rocket results infer hotter plasma with emission measure two orders of magnitude lower than the dominant component. This is not obtained in the full Sun MinXSS-1 2TFree fits, but a hotter component near 10 MK, is necessary to fit the excess in MinXSS-1 count rate above 2.3 keV in the spectral fit in Figure 10.3. Again, this fit had a fixed 1TFree QS component and the residual was fit with a 2TFree model and assumed to be entirely originating from the lone active region on the limb (or to any changes in the QS baseline flux over the 5 days). Nonetheless, this extremely dim (8×10^{45} cm^{-3}) 10 MK component is not likely to exist at this emission measure value. If it does exist, it must be lower than $\times 10^{45}$ cm^{-3} based on the DEM fits extracted in Section 10.2. The results in Section 10.2 demonstrate again the power of DEM fits to exclude over-estimated emission measure values from isothermal or bithermal spectral fits.

In comparison to the pre-flare values discussed earlier in this dissertation in the month of July in 2017. There is a bright cooler component between 1.3 - 1.86 MK with emission measures ranging from 76 - 192 $\times 10^{48}$ cm^{-3}. There is a persistent hotter dim component that is inferred at the edge of the MinXSS-1 X123 diagnostic capabilities. This component has temperatures between 4.58 - 4.80 MK and an emission measures between 1.2 - 1.8 $\times 10^{48}$ cm^{-3}. The MinXSS-1 and Hinode XRT cross-calibration observations on 2016 September 05 09:55:35 - 11:10:44 UT full Sun observations have a similar low temperature component but the hotter temperature component is near 2.95 MK. Low-fip abundance values range from 0.54 - 0.75 (factors of 2 - 3 times photospheric). A clearer picture will emerge as more data is analyzed.

10.2   Differential Emission Measure (DEM)

Differential emission measure (DEM) analysis using XIT was pursued to refine the temperature structure of the QS and AR. The XRT synoptic full Sun images were used to analyze the QS and AR times. A sample of the images are in Figure 10.4 and the white box displays the region of XRT and AIA images used to extract the AR signal. The boxed region in the images are not the exact location of the selected region actually analyzed, that region is $X_{\Theta 1}$ = -1050", $X_{\Theta 2}$ = -900", $Y_{\Theta 1}$ = 50" and $Y_{\Theta 2}$ = 250". The XRT Be-thin images for the QS times barely has any signal. This again demonstrates that the Be-thin images are basically AR flux and temperatures around ~2.5 to 3 MK. The Al-mesh and Al-poly are much lower count flux than the MinXSS-1 and XRT cross-calibration times in 2016 September 5.

The AIA images in Figure 10.5 show that the 193 $\mathring{A}$ signal does not diminish significantly (because of the lower temperature response), and that the 94 $\mathring{A}$ image is much dimmer like the XRT images. Fe XVIII signal is basically non-existent, furthering the notion that active regions contain the majority of plasma hotter than 2.5 MK. The HMI image does not show any strong surface line-of-sight magnetic field features that correlate well with the presence of high temperature plasma.

The QS and full Sun DEMs (2017 March 21) are computed by taking the full MinXSS signal and the full Sun positive pixels of the XRT and AIA image. The XRT and AIA data for the active region DEM is only the positive pixel contribution discussed above. The majority of the Be-thin, Al-med and Be-thick counts come from the active region. The DEM results are in Figure 10.7. Panel A confirms the lack of plasma with significant emission measure (VEM $\geq 10^{44}$ cm^{-3}) above 3 MK, and a precipitous drop in the presence in plasma emitting for temperatures near 2 MK. This explains the lack of signal in the XRT Be-thin images, the minimal detected X123 counts above 2 keV and the absence of any inferred AIA Fe XVIII component. The peak in the emission is between 1 - 2 MK, which is consistent with the
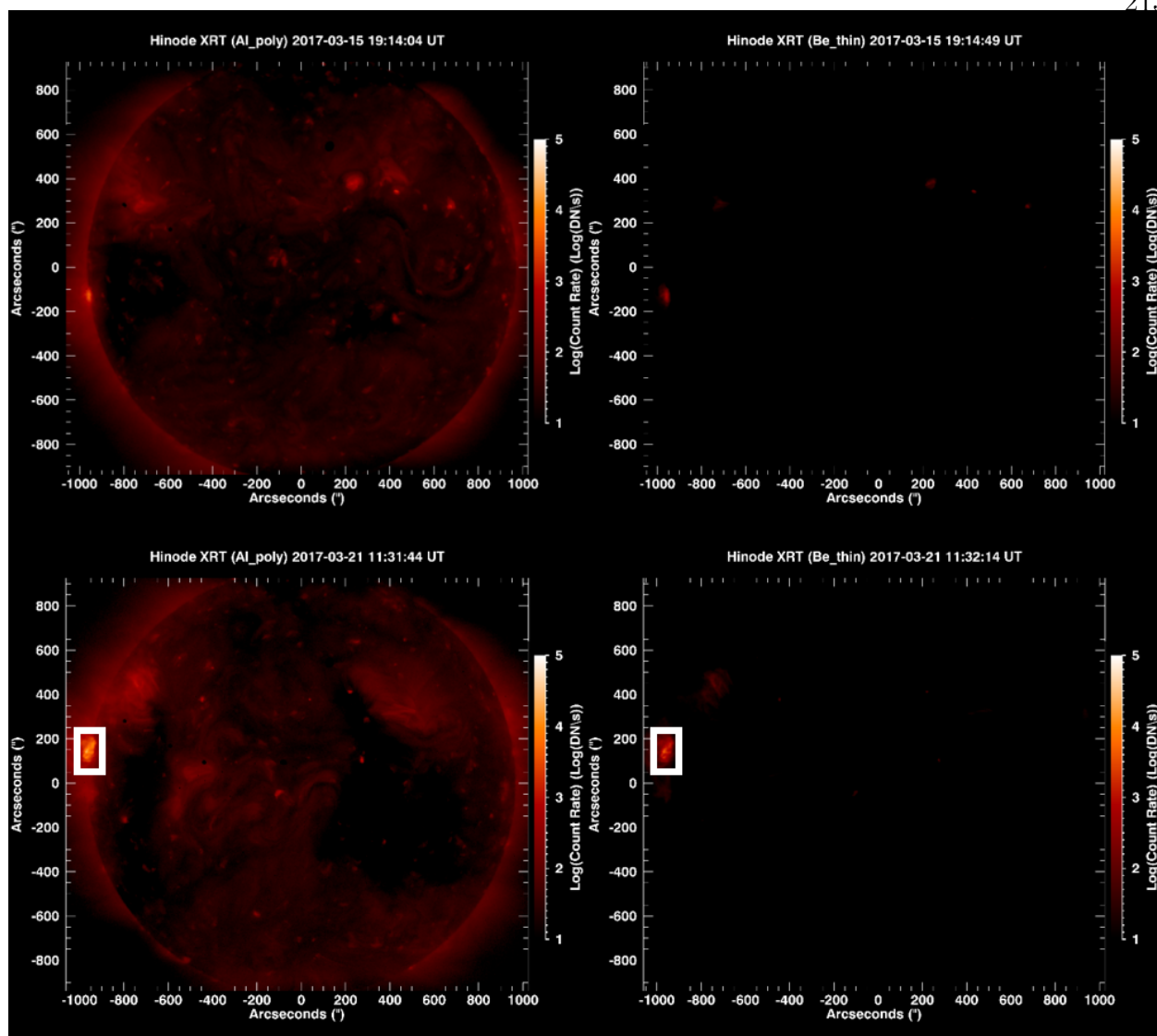
Figure 10.4: Top Row: QS Hinode XRT Al-poly (left) and Be-thin (right) Log-count rate images. Bottom Row: AR Hinode XRT observation with Al-poly (left) and Be-thin (right) images. The white box indicates the location of the AR that has rotated into the line of sight.

MinXSS-1 1TFree spectral fit (1.7 MK). This bolsters the reliability of the extremely low spectrally integrated X123 signal (6 counts s^{-1}) to still extract reasonable plasma inferences of the full Sun. Even though MinXSS-1 has limited sensitivity for plasma below 2 MK, a moderate estimation of the plasma temperature can still be made, but not necessarily the magnitude of this plasma's emission measure.
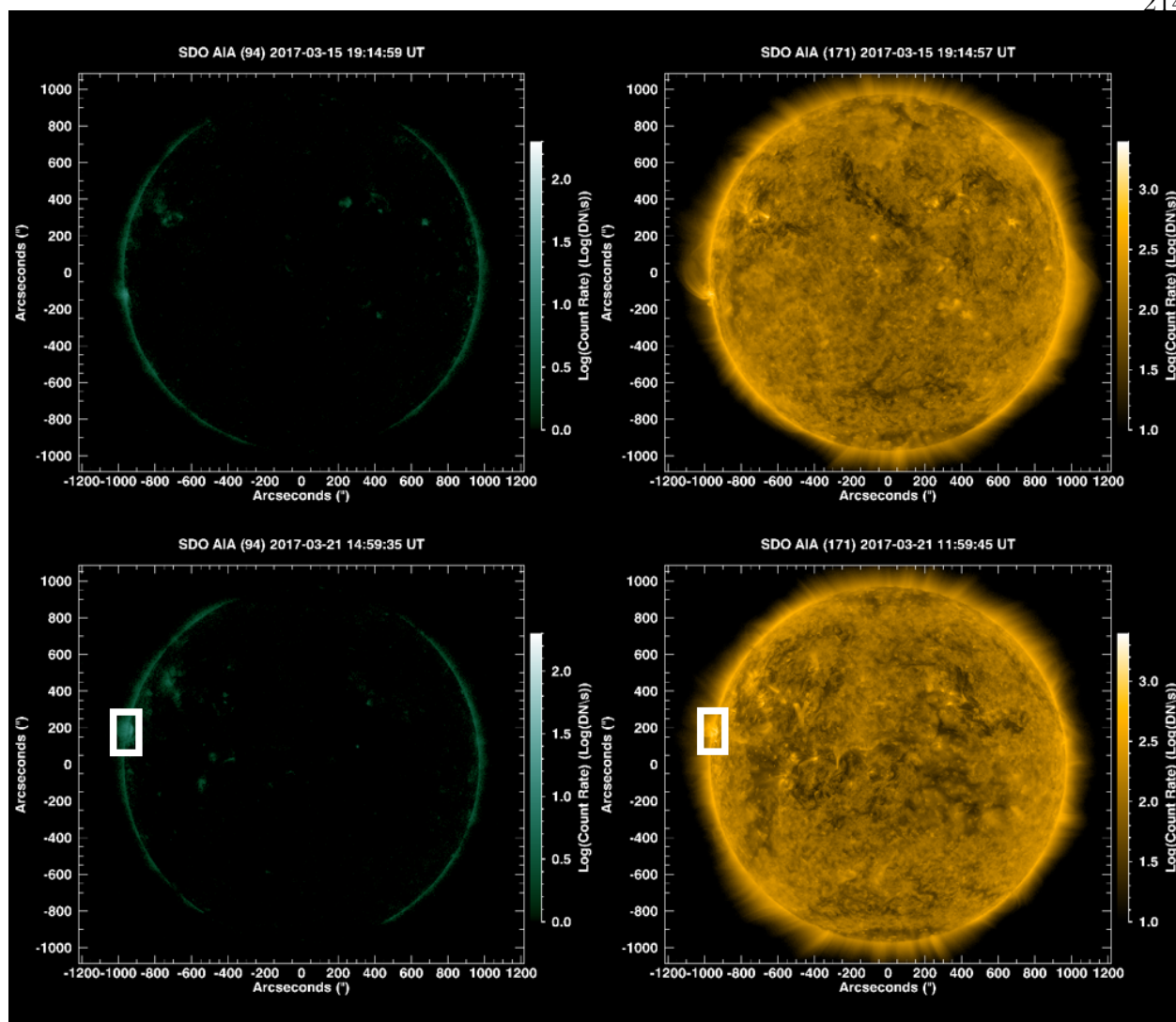
Figure 10.5: Top Row: QS SDO AIA 94 $\mathring{A}$ (left) and 193 $\mathring{A}$ (right) log-count rate images. Bottom Row: AR SDO AR observation with AIA 94 $\mathring{A}$ (left) and 193 $\mathring{A}$ (right) images. The white box indicates the location of the AR that has rotated into the line of sight.

The QS DEM signal predictions are within roughly a factor of 2 except for Al-mesh and Al-poly. These are the most sensitive XRT filters to the contamination layer and it will take a more thorough investigation to estimate how much of a role this is playing (if any) in this DEM analysis (the MinXSS-1 cross-calibration study was conducted fairly recently after an XRT bake-out). The full Sun observation including the active region has a very similar VEM vs. temperature distribution below 2 MK. These can be interpreted as the QS
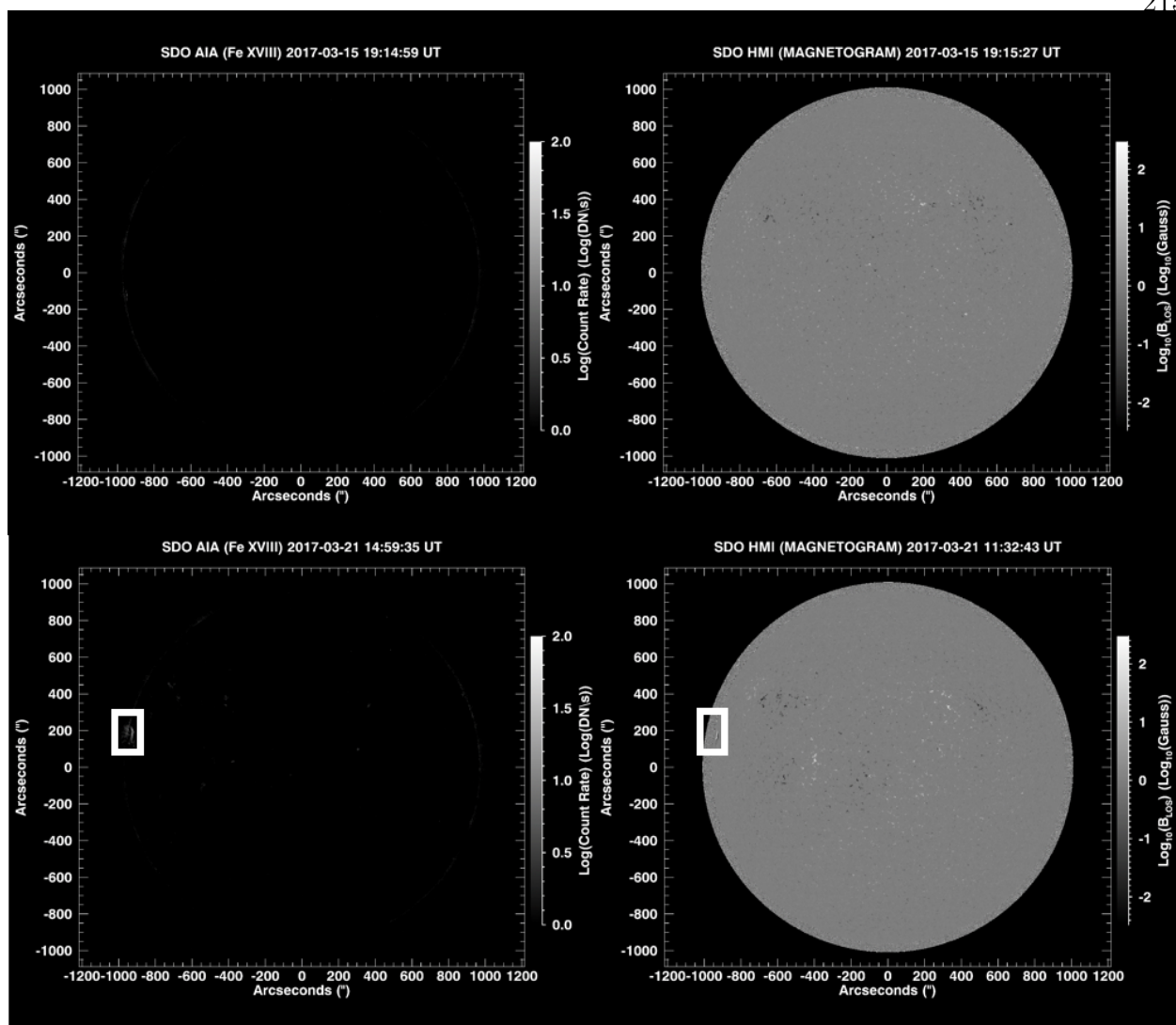
Figure 10.6: Top Row: QS SDO AIA FeXVIII (left) and HMI (right) log-count rate images or log of gauss. Bottom Row: AR SDO AR observation with AIA 94 $\mathring{A}$ (left) and 193 $\mathring{A}$ (right) images. The white box indicates the location of the AR that has rotated into the line of sight.

dominating this emission. A prominent 'hump' has appeared for plasma above 3 MK, that is many orders of magnitude larger than in the QS DEM. This should be almost entirely due to the active region that recently rotated into the Earth line-of-sight field of view (see Figure 10.8). This secondary feature has a maximum between 5 - 6 MK and extends to 7 - 8 MK as it steeply falls off. This hotter plasma content was not inferred for the MinXSS-1 XRT cross-calibration study on 2016 September 5. The 2016 September 5 DEM had VEM

$\leq 10^{44}$ cm^{-3}) above 4 MK. During that observation set there was only one very old, diffuse active region, but the Sun had a much higher total soft X-ray flux. The GOES levels was near B1 (10^{-8} W m^{-2}), the MinXSS-1 X123 total integrated counts near 83 count s^{-1}, the XRT filter image count rates were higher and so were the AIA 94 $\mathring{A}$ count rates.

The levels for this full Sun 2017 March 21 observation are at least a factor of 2 for the GOES fluxes ($\sim$A4, 4×10^{-9} W m^{-2}), factor of 4 for the X123 spectrum (21 counts s^{-1}) and much lower for the XRT and AIA images. Thus the total spatially integrated signals in GOES, MinXSS-1, XRT, nor AIA alone is not indicative of hotter (T $\geq$ 5 MK) plasma presence. DEM fit must be conducted, unless there is an instrument that is sensitive to photon fluxes greater than 5 keV (in the absence of non-thermally generated photons). Again, using the MinXSS-1 observations and the full Sun DEMs as a guide for translating solar inferences to full star integrated measurements in the future, this points out important caveats to any stellar investigation where very high resolution spectra is not available.

The ratio of the DEM predicted counts to measured counts is similar to the QS result, meaning that there is agreement to within a factor of 2 (common for DEM studies) except for Al-mesh and Al-poly. Panel C in Figure 10.7 is the DEM result estimating the AR only contribution using the time differenced MinXSS-1 observation and the boxed region from XRT and AIA images. The dominant feature for plasma below 3 MK has diminished. This is the combination of the peripheral QS plasma in the box and the outer regions of the AR. The high temperature 'hump' from 5 - 8 MK persists and at basically the same magnitude in VEM vs. temperature. This result confirms that the hot plasma content resides in the AR and reaffirms the notions of hot plasma in active regions.

The ratio of the signals agree to within a factor of 1.5 for all data sets except the X123 0.9, 1.2 and 1.5 keV sets. This can be due to changes in the QS emission from the QS time frames from the background subtraction. Other reasons are being investigated. This study has proven the capability of MinXSS-1 data combined with XRT and AIA data to extract the active region emission on the Sun. This technique is only successful if there is a QS

time to conduct baseline MinXSS-1 measurements for and if there is only one or two active regions on the disc. The amount of hot plasma relative to cool plasma, the shape of the DEM at the high temperature roll-over (the slope) and the temporal variation of the DEM are important guides in constraining coronal heating models.

The corroborating measured spectra with numerical modeling of QS and AR plasma conditions is important fir constraining the viable coronal heating processes, both through the temperature distribution and the elemental abundance variations. As discussed earlier in Section 6.2.2 most heating models that invoke Alfvén waves [3, 149] generated by the jostling of kilogauss magnetic flux tubes (magnetic bright points) and eventually dissipation by some mechanism (possibly turbulence) as a viable process for heating the corona. Observations show the transverse footpoint RMS motion to be on the order of 1 - 2 km s^{-1}. When incorporated into full Sun 3D models this results in coronal active region plasma temperatures that peak near 3 MK [151]. This would be consistent with our 2016 September 5 cross-calibration DEM investigation, which had an older, diffuse and brighter active region.

On the contrary, heating models that include an ensemble of impulsive heating events (possibly driven by magnetic reconnection from the same photospheric footpoint motions) that generate a fainter and hotter (T $\geq$ 5 MK) plasma contribution, is consistent with the AR DEM that we have extracted here in this study [86, 87]. The impulsive heating models generally use spatially averaged calculation on single loops and predict this temperature presence in the cores of active regions on very small spatial scales. A further complication is that the ensemble of events could interact with each other and hence modify the expected DEM realized. Moreover, there has not been a full Sun 3D simulation to predict the global properties of an impulsive dominated heating process.

With all of these caveats in mind the DEM shape, especially the high temperature fall off could yield information on the timescales of the heating events, the magnitude of the events and if non-equilibrium heating of ions or electrons is occurring [13]. The 2017 March 21 limb viewed active region is more consistent with the impulsive heating (nanoflare) mech-

anism. For completeness, in the study by Asgari-Targhi et al. 2015 [8], it was demonstrated from simplified simulation study (not full Sun 3D) that faster transverse footpoint motions on the order of 5 - 6 km s^{-1} could generate plasma near 5 MK. These faster motions have not been observed with current observatories and thus would have to be on very small spatial scales, likely within magnetic flux tubes on the order of 100 km.

Conclusion from analysis conducted thus far, active regions appear to be variable with age, magnetic complexity and elemental abundance. Further studies should be done to track and map observables to active region age, complexity, abundance and other features. Our DEM results are consistent with the highly referenced results from Brosius et al. 1996 [20] using the Solar EUV Rocket Telescope and Spectrograph (SERTS) observations in 1991 and 1993. We both obtain a dominant QS contribution between 1 - 2 MK and AR induced peaks by 3 MK and then 4 - 5 MK. These are promising results which encourage more complex studies in the future.
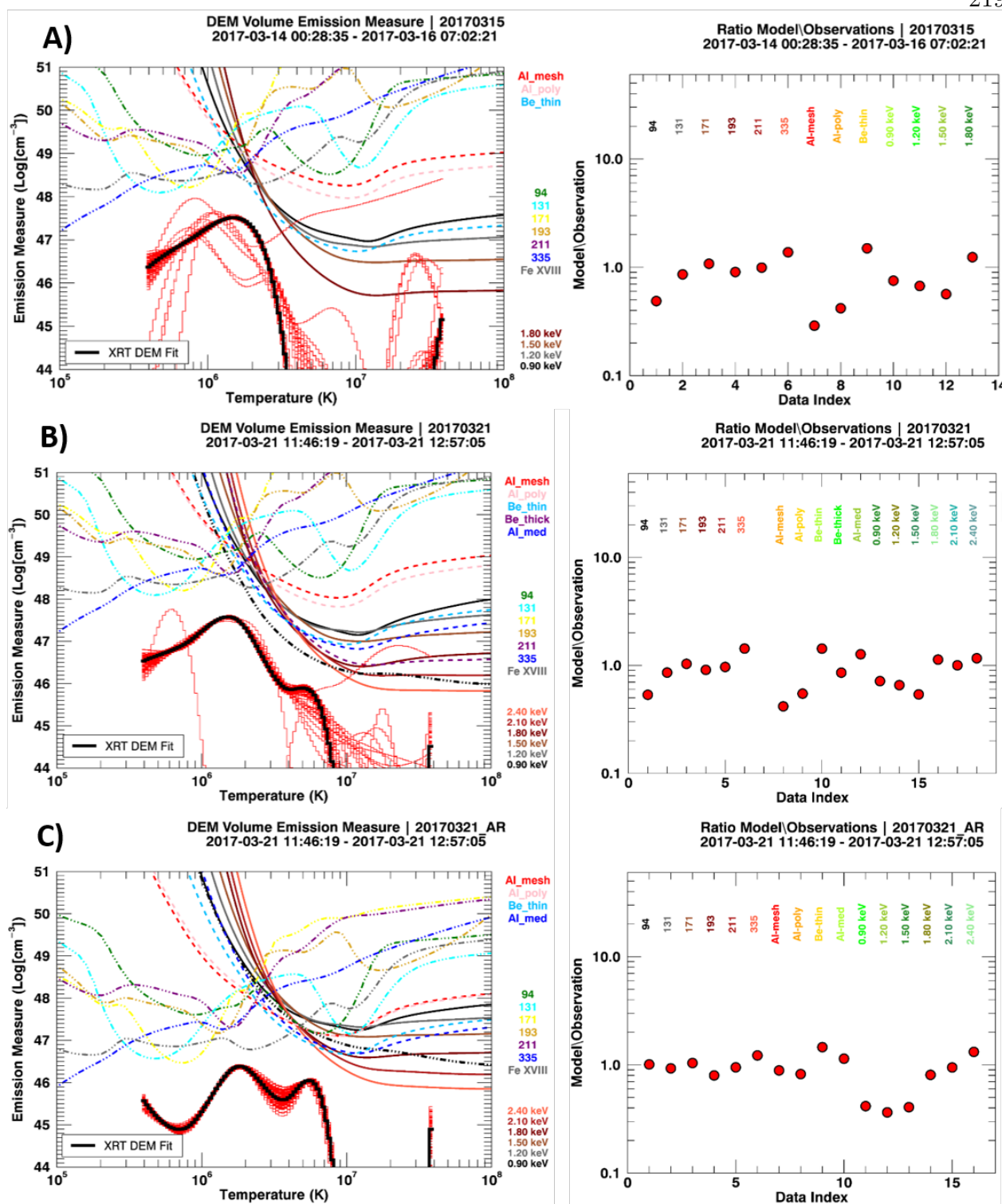
Figure 10.7: MinXSS-1, XRT and AIA combined DEM during 'quiescent' times (A) centered on 2017 March 15, time with an active region (B) on 2017 March 21, and the contribution from that same active region extracted (C). DEM predicted count rates are within roughly a factor of two for all data sets except Al-mesh and Al-poly in (A) and (b). The QS DEM peaks between 1 - 2 MK, which is common for the quiet Sun in the absence of active regions or large flares. The amount of plasma radiating for T ≥ 2 MK drops precipitously. The AR DEM has significant contributions up to T ≈ 7 MK
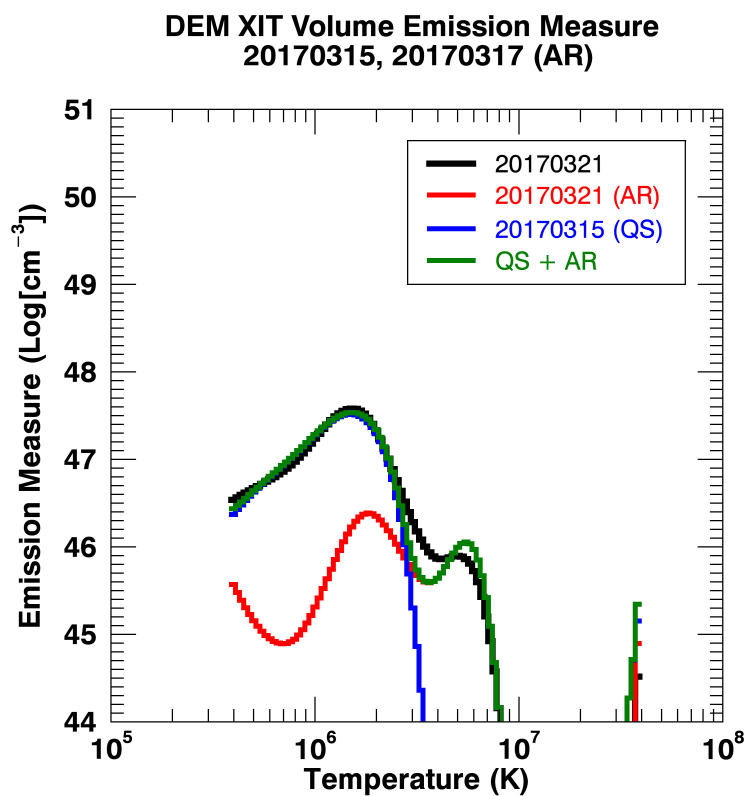
Figure 10.8: Comparison of the quiet Sun (blue), Sun with an active region (black), active region contribution (red), and the sum of the quiet Sun and active region contribution (green). The consistency between the green and the black line indicate the validity of the estimated active region contribution, which is particularly important for the MinXSS methodology.

10.3   Elemental Abundance Variations

It was noted in Section 6.2.3 that there is a variation in the low-fip elements in quiet Sun regions vs. active regions. AIA spectra contribution in all of the EUV filters are dominated by Fe lines. Thus, AIA is not a feasible instrument to infer low-fip enhancements. Changing the low-fip abundance in the spectral models used to compute the AIA temperature responses simply scales the response up and down, almost uniformly. XRT is extremely sensitive to abundance changes but cannot independently infer the low-fip enhancement. A similar sensitivity to abundance and lack of abundance determination is inherent with GOES XRS method White et al. 2005 [155].

MinXSS-1 is the only instrument in this study that can assess the elemental abundance due to its spectral resolution. The resolving power is just enough to discern differences in the count rate at particular elemental spectral features. Albeit this procedure is emission model dependent because MinXSS X123 cannot resolve spectral lines. The DEM fit in essence are sensitive to elemental abundances, particularly XRT and X123. The best fit MinXSS-1 X123 abundance was used for each respective DEM fit. The real variation is in the 1T and 2TFree fits. The QS best fit value of 0.3 is between the 'Hybrid' value (0.5) and photospheric (0.25) value. The accuracy in the abundance determination is limited for the lower count rates (6 counts s-1). Hence this abundance determination needs to be followed up with a statistical study on many QS observations.

The AR spectral fits yield expected abundance values near the common factor of 3 - 4 times the photospheric values (0.78) so there is no mystery here. Another ideal future investigation is the tracking of AR elemental abundance (along with temperature) vs. AR age (time after photospheric flux emergence). Overall MinXSS X123 provides the important ability to determine elemental abundances, an additional diagnostic tool not readily available with the current X-ray and UV instrumentation. Solar flares are known to have variable abundance Dennis et al. 2015 [38], the next study exemplifies the MinXSS-1 X123 capability

to infer not only the low-fip multiplicative factor, but also the elemental abundances of multiple elements individually.

Chapter 11

MinXSS Flare Study on 2016 July 24

There were a series of flares that erupted from a single active region group on 2016 July 24 from roughly 11:30 - 15:00 UT. Series of sequential flare eruptions over spans of a few hours is not very frequent, but it is not uncommon for an active region group to have a few flares occur in a day. Many times the first couple of flares trigger the later eruptions. Most of the flares were mostly GOES C class (C1, C1.6, C5.1, C6.0, C7.0 and C7.0). Due to eclipse times and sparsity of downlinked data at the time of analysis, MinXSS-1 did not measure every flare. Figure 11.1 shows the GOES flux transients due to the flare series and the corresponding 5 minute averaged MinXSS-1 X123 total counts. In this Chapter the X123 OSPEX spectral fits and implications of MinXSS-1 measurement of six of the flares are discussed.
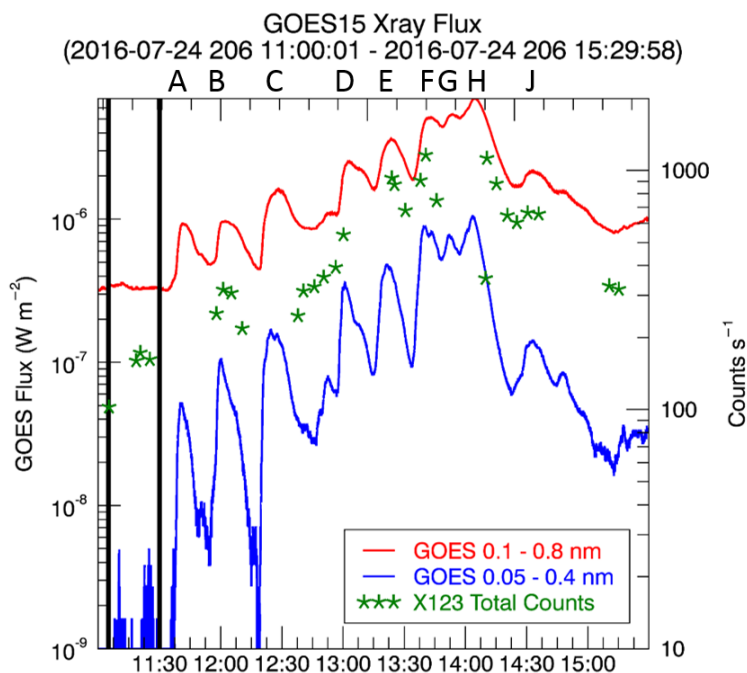
Figure 11.1: GOES XRS 0.1 - 0.8 nm (red line) and 0.05 - 0.4 (blue line) nm flux time series with the X123 total counts overplotted (green asterisks). The 5 minute averages X123 total counts follows the general trend of the GOES XRS measurements.

11.1 Spectral Parameter Fits

The X123 flare series of 2016 July 24 were fit by the OSPEX suite in SSW. The model class of fits that will be discussed in this Chapter are 1TFree, 2TFree, 1TAllFree and 2TAllFree. The details on these classifications were discussed in Section 9.3 and the reader is refered there for a reminder. Figure 11.2 displays four of the flares fit with the four spectral models. The pre-flare is taken as the 5 minute average of any MinXSS-1 X123 measurements between roughly 11:00:00 - 11:30:00 UT. This signal measurement is then subtracted from the remaining dataset. The residual is considered the flare contribution and are fit.

The 1TFree model consistently has the poorest fit to both the pre-flare and the flare spectrum. A single temperature is a limited model for the complex nature of a solar flare and while in some instances there can be a peak temperature that can dominate the radiative output, flares are not iso-thermal. Furthermore the single multiplicative factor for all the

low-fip elements has been observed to not adequately describe solar flare spectra, when the measurements have high enough spectral resolution to discern abundance variations. Pioneering studies performed by Dennis et al. 2015 using MESSENGER SAX data [38], have proven that the solar flare abundance is in general, much more complex than a single low-fip multiplier for Fe, Ni, Si, Ca, S (mid-fip) and Mg.

The 1TAllFree model improves upon the abundance inference limitation by allowing the elements Fe, Ni, Mg, Si, S, Ca and Ar to vary in abundance. This provides a much better fit than the 1TFree model (lower $\chi^2_{reduced}$), but still suffers from the limitation of describing the flare plasma being at a single temperature. The 2TFree has moderate improvement on the 1TAllFree, in terms of the statistical metric of $\chi^2_{reduced}$ for some flares but is worst for others. The secondary temperature and emission measure gives more freedom in fitting the flare spectrum. This secondary temperature freedom also affects the elemental abundance impact on the spectra due to the temperature dependence of a certain element's ionic spectral line groups.

The 2TAllFree are the best fits (lowest $\chi^2_{reduced}$) of all the models and thus, the I will only discuss in the remainder of this Chapter. This model has the highest number of free parameters, so it is not surprising that it can obtain a lower $\chi^2_{reduced}$ as long as the model used to approximate the data is *reasonable*. It is important to note, as discussed in Section 9.3 that not every element is allowed to vary for every single fit arbitrarily. There is a minimum signal-to-noise (5 for this data set) that each elements 'dominate' spectral feature must attain before the fit will, autonomously, allow that element's abundance to vary for that specific time interval being fit. With this background knowledge, I proceed to discuss the flare series results in depth.

Consistent with the common flare description, observed is an increase in the GOES 0.05 - 0.4 nm flux, then a rise in the 0.1 - 0.8 nm flux, then the MinXSS-1 X123 count rate (due to the lower spectral coverage, and these lower energy photons dominating the spectral count rate) [6]. This follows the theory that flares accelerate particles both towards the less
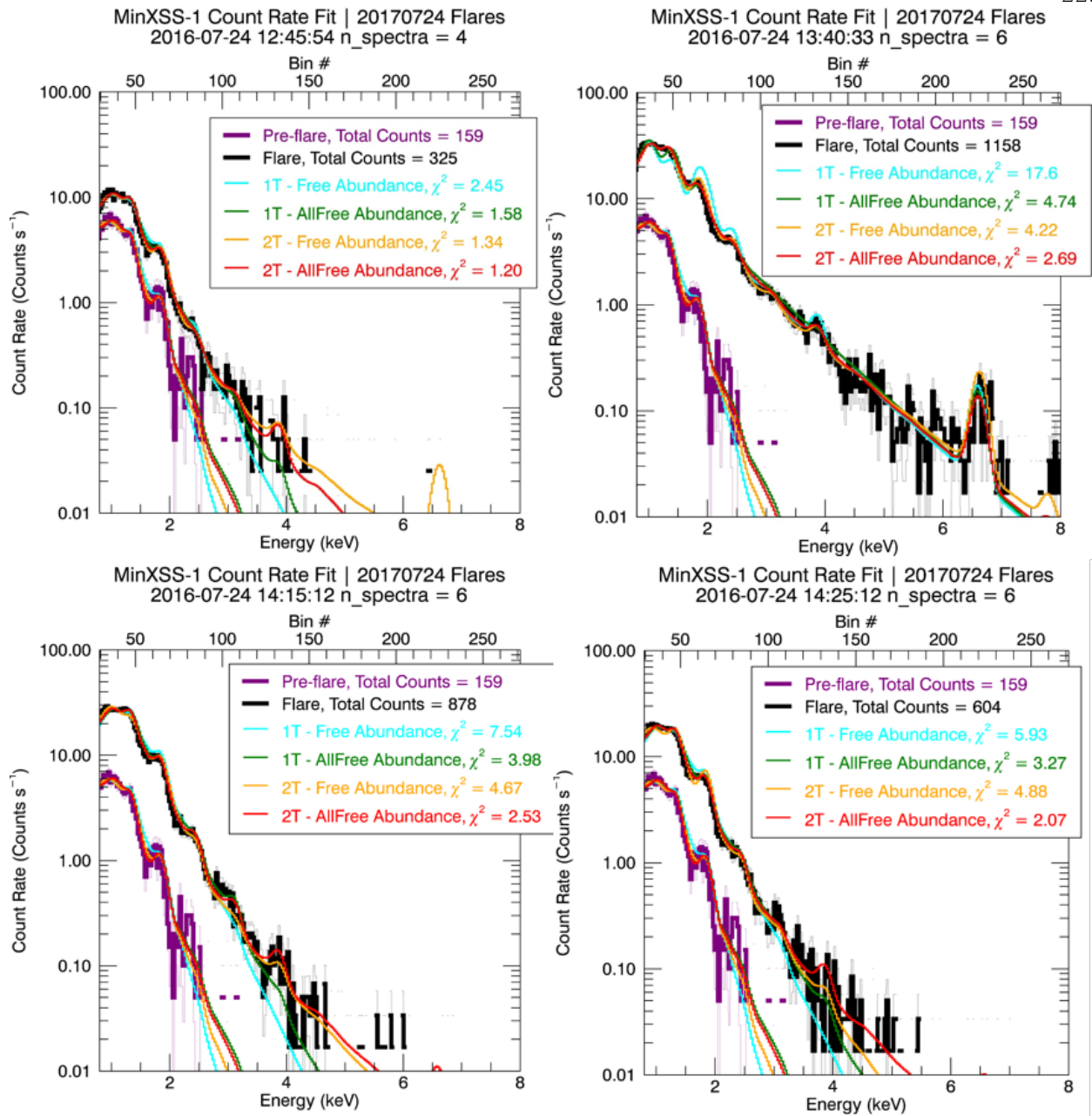
Figure 11.2: OSPEX Fits of the B and C class flares on 2016 July 24. The 1TFree fits are cyan, the 1TAllFree are green, the 2TFree are orange and the 2TAllFree are Red. The 2TAllFree are the best fits (lowest $\chi^2_{reduced}$) of all the models.

dense plasma towards interplanetary space (generating microwaves) and towards the more dense chromosphere (generating hard X-rays and soft X-rays). These particles interact with the lower atmosphere and generate a flux of heat and particles back up the flare loops, which
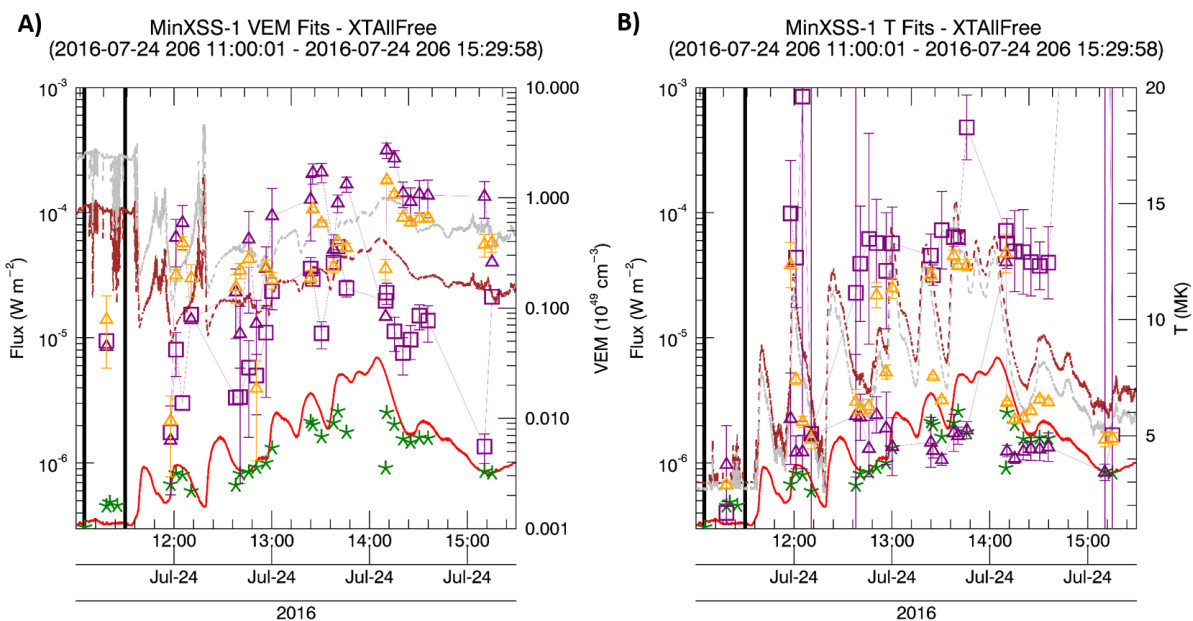
Figure 11.3: OSPEX XTAllFree (1TAllFree and 2TAllFree) Fits of the flares on 2016 July 24. The 1T components are orange, the 2T components are purple (traingle and squares). The top panel is the volume emission measure and the bottom panel is the temperature. The maroon line is the GOES coronal abundance estimation and the silver is the photospheric abundance value.

cool via radiation of soft X-rays and UV. The later phase is the majority of the radiation that MinXSS detects.

The emission measure for both the 1TAllFree (orange) and 2TAllFree (purple) increases during the flare times and the temperature increases. The temperature commonly can reach well over 5 MK for flares, and nominally between 10 - 20 MK during flare peaks. The MinXSS-1 5 minute averaged data is not directly comparable to the 2 second averaged GOES values, thus the changes in emission measure and temperature will not necessarily be in sync. There can be a few reasons for this at least with respect to the plotted data in Figure 11.3. The GOES data displayed is 2 second averages, while the MinXSS-1 data has been averaged over 5 minutes. MinXSS-1 will miss many of the temporal features. The 5 minute averages were chosen to minimize noise in the signals for spectral fitting. Also, the MinXSS-1 effective area is relatively small, so the flux in energy bins greater than 6 keV

rarely have enough counts to be included in the spectral fitting. GOES has a larger effective area at the higher energy X-rays and thus greater spectral sensitivity than MinXSS-1 X123 for the higher energy photons.

The evaporation of heated ions from the chromosphere up into the corona should have direct effects on the subsequent radiation in the soft X-rays and UV. In detail, if the chromospheric plasma has a different chemical composition relative to the plasma nominally radiating in the corona, then one expects to observe a change in the inferred elemental abundance from measurements sensitive to abundance changes. This leads to the importance of MinXSS-1 spectrally resolved measurements being able to determine changes in elemental abundances. Changes in abundance can be linked to various physical processes and mass flow in the solar atmosphere.

11.2   Elemental Abundance Variations

The 2TAllFree model fits of the MinXSS-1 X123 spectral measurements of the 2016 July 24 flare series yields results consistent with recent literature on the elemental abundance variations observed in solar flares. In general the thought is that the upwelling chromospheric plasma into the corona will have a low-fip abundance closer to photospheric values (similar to Caffau et al. 2011, $A_{low-fip} \sim 0.25$), rather than the traditional 'coronal' values (Feldman 1992 $A_{low-fip} \sim 1.0$). The abundance values derived here are **relative** abundance changes inferred with respect to a nominal basis set. The basis set is Feldman 1992. If the specific element's abundance is not allowed to vary during the fit, then it is fixed at the Feldman 1992 value.

Fe XXIV and Fe XXV have dominant emission lines that contribute to a large spectral feature near 6.7 keV and is commonly discussed in RHESSI flare observations. Additionally, there is the Fe-Ni complex near 8 keV. Both features are only significant in the X123 count rate for the C7.0 and C5.0 flare observed here. Thus, the Fe and coupled Ni abundance were determined from the features near 1.0 and 1.1 keV. The Fe and Ni abundance does, in general,
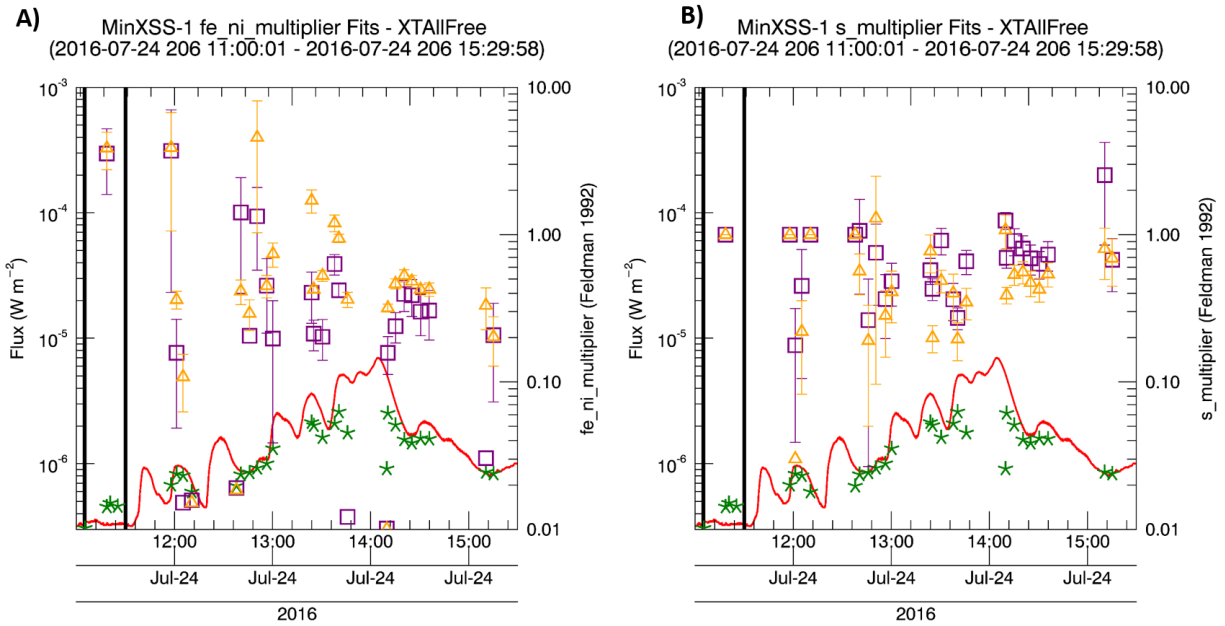
Figure 11.4: OSPEX XTAllFree abundance Fits for Fe, Ni (left) and S (right) of the flares on 2016 July 24. The 1T components are orange, the 2T components are purple (traingle and squares). Fe and Ni have enough signal to noise to be free for most times to allow the abundance to be free. In general, most of the values decrease during the flares. The same appears to be true for S.

decrease during the flares discussed here, relative to the pre-flare value (inside the vertical black lines in Figure 11.4). As the flares increase in magnitude (GOES Classification) the Fe and Ni abundance enhancement decreases further. This is a good indirect (more direct would be images of the plasma flow up into the atmosphere and simultaneous changes in the radiation details and in situ plasma composition measurements) indication of plasma flow from the chromosphere to the corona.

S has a spectral line group feature near 2.7 keV that is used to set the mid-fip element's abundance free or not. Once the flare magnitude is large enough, a S elemental abundance between 0.4 - 0.7 is inferred. The variation from pre-flare values is not obtainable because the pre-flare spectrum lacked enough signal-to-noise near the 2.7 keV feature for it to be set free. Figure 11.5 demonstrate a similar trend for Mg (spectral features near 1.35 keV) as Fe and Ni. The abundance is below coronal values (commonly between 0.3 - 0.8) and much
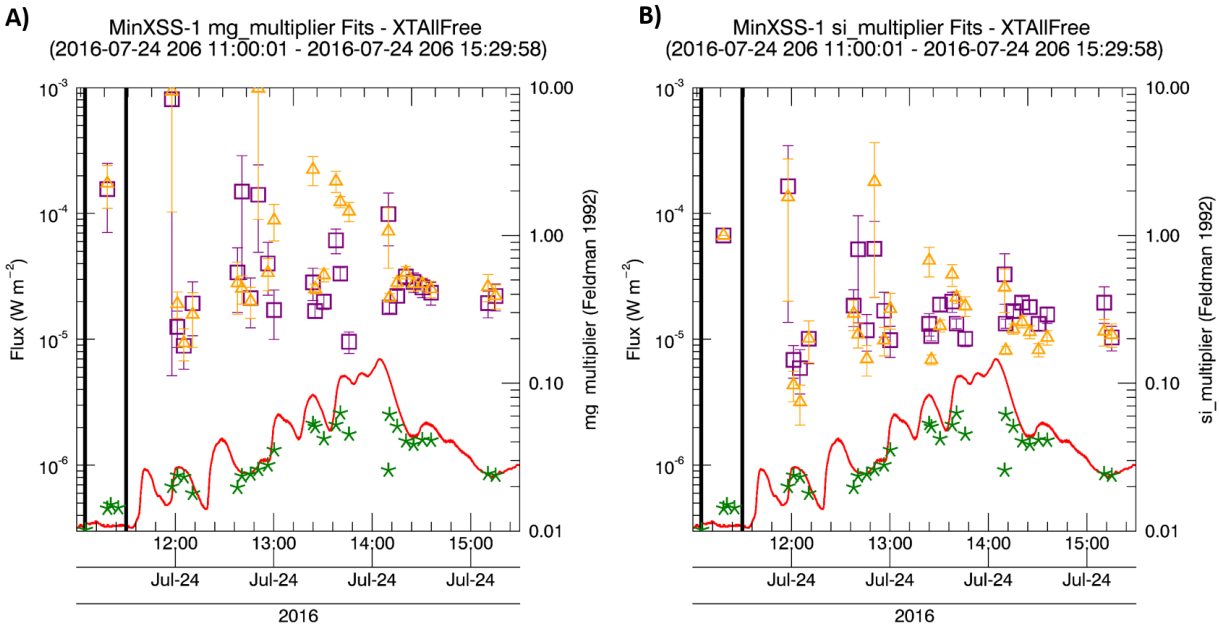
Figure 11.5: OSPEX XTAllFree abundance Fits for Mg (left) and Si (right) of the flares on 2016 July 24. The 1T components are orange, the 2T components are purple (traingle and squares). Mg abundance decreases during the flares and so does Si.

lower than the pre-flare fit value near 2.2. Even though the pre-flare value for Si was fixed, the flare values seem telling. The abundance hovers between 0.2 - 0.5 for the majority of the flare times and is consistent with the other low-fip elements of Mg, Fe and Ni, and the mid-fip S. These inferences greatly bolster the arguement for chromospheric evaporation.

The Ca feature near 4 keV did not attain a high enough signal-to-noise except for one time frame were it displayed a sub-coronal abundance. There is not much more that can be stated on this element. Ar is the one high-fip element in the MinXSS-1 X123 bandpass that could be allowed to vary. The fits show an enhancement for some instances and a depresion for others. Ar is known to have anomolous abundance effects durring flares [40, 39], and more studies with MinXSS (preferably coordinated with simultaneous Hinode EIS observations) is needed for definitive statements on the Ar abundance variations.

The elemental abundance of He, Ne, C, O, F, N, Na, Al and K were fixed at their Feldman 1992 values. Most of these elements are considered high-fip and thus are not
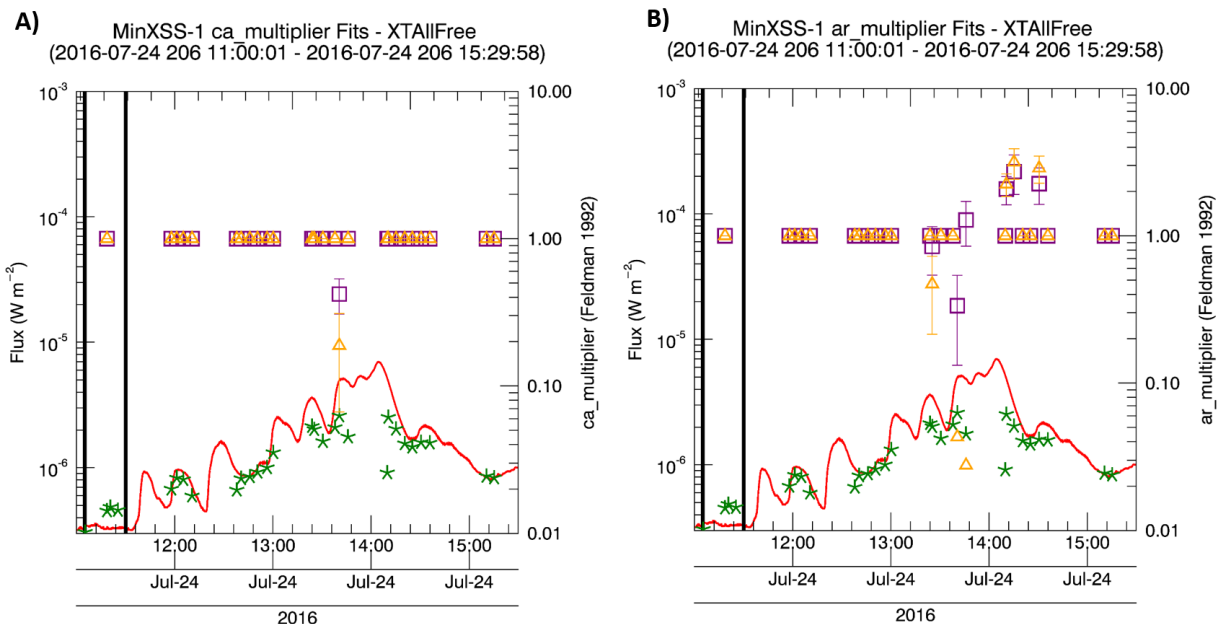
Figure 11.6: OSPEX XTAllFree abundance Fits for Ca (left) and Ar (right) of the flares on 2016 July 24. The 1T components are orange, the 2T components are purple (traingle and squares). Ca only has a few instances where the signal-to-noise ratio in the 4 keV spectral feature is large enough to allow the Ca abundance to be free. All that can be stated is that it is less than the Feldman 1992 values when allowed to be free. Ar is a high-fip element and shows an enhancement for some instances and a depresion for others. Ar is known to have anomolous abundance effects durring flares [40, 39].

expected to vary much during flares. Ironically Ar is also a high-fip element and has shown significant variations. The abundances of these elements were varied in unison to assess any sensitivity to changes in the MinXSS-1 X123 spectra. Best fit values almost were always 1 and there are not any noticible changes in the spectrum due to changes in their abundance at least in the SSW Chianti data base for plasma temperatures greater than 2 MK. These elements are expected to contribute to the number of free electrons and could modify the free-free continuum in the MinXSS-1 bandpass. But as stated earlier, no noticable change has been observed in varing the abundances of these elements in the current modelling framework.

Overall the MinXSS-1 measurements and 2TAllFree spectral fits of the flare series on 2016 July 24 are consistent with expected flare emission measures and peak temperatures.

What is unique about this data set is the ability of MinXSS-1 X123 to estimate the abundances of Fe and Ni, S, Si, Ma, Ca and Ar seperately. Besides MESENGER SAX and Hinode EIS, there has not been solar coronal measurements with this capability for some time. The results indicate that chromospheric evaporation is very likely to occur in flares, based on the soft X-ray signatures. This highlights one of the main diagnostics of the MinXSS CubeSat instrument suite.

Chapter 12

MinXSS and Future Solar Investigations

12.1   Summary of MinXSS and the Solar Corona

The MinXSS CubeSats have reopened the door to investigate the solar corona through spectrally resolved measurements in the soft X-rays. The MinXSS-1 CubeSat has operated nominally (beside a few anomalies) for the majority of the $\sim$1-year mission. In summary, I have been fortunate to be part of a team that has enabled:

(1) New solar measurements from sparsely observed 0.8 - 12 keV energies.

(2) MinXSS-1 quality measurements from A4 - M5 levels (without special processing).

(3) Estimations of an active region spectrum and DEM.

(4) Estimations of a quiet Sun spectra and DEM.

(5) Cross-calibration with the GOES XRS.

(6) Cross-checked a two solar flares RHESSI.

(7) Cross-calibration with the Hinode XRT.

(8) Cross-calibration with the SDO AIA.

(9) New inferences of elemental abundances in the solar corona.

These new capabilities are now available for the entire solar physics science community. There are a wide array of scientific possibilities with the upcoming launch of MinXSS-2. I have desire to utilize the MinXSS-2 CubeSat measurements with other satellite data for the investigations discussed in Section 12.2.

12.2   Future Solar Investigations

Why the Solar corona is over 1 million degrees Kelvin while the solar surface is around 5,700 K is still in debate. The two leading theories involve impulsive processes (nanoflares) and wave dissipation (Alfvén waves). Both processes use magnetic fields as a medium to transfer convective kinetic energy to thermal energy. This proposal aims to investigate the presence of spectral signatures predicted by theories and models through soft X-ray (SXR) and Extreme Ultraviolet (EUV) observations. First, I will determine if there is a link between the presence of hot-dim plasma (which is predicted by a certain class of nanoflare models) and its elemental abundance vs. AR age. I propose to use simultaneous observations by the NuSTAR satellite, which has the SXR spectral coverage and photon flux sensitivity to detect hot-dim plasma in non-large flaring (quiescent) active regions (ARs); the MinXSS CubeSat, which has the SXR spectral resolution to deduce elemental abundances; and Hinode XRT and EIS, SDO AIA and eventually MaGIXS for additional information. Second, I will evaluate if the latest simulations of Alfvén wave dissipation can generate the Solar X-ray flux. I will compare synthetic observables from numerical simulations of Alfvén wave dissipation to the data sets previously mentioned for specific times. These complimentary investigations will provide insight on the viability of current coronal heating theories.

12.2.1   Where is the Hot Dim Plasma Content in Quiescent Solar Active Regions?

A current mystery in solar physics is why the upper solar atmosphere, the corona, has a temperature of over 1 MK while the solar surface, the photosphere, is at around 5,700 K.

While the primary heating source of the corona is still in debate, the notion that the origin is magnetic in nature is not in question. Additionally, the solar atmosphere has a complex magnetic spatial structure with temporal variations, thus leading to possible intricacies in the coronal heating processes. Two prevalent heating theories are (1) impulsive, small scale magnetic reconnection events (nanoflares) and (2) Alfvén wave dissipation [86]. As a postdoc, I propose to address two main questions: **(Q1) Is the presence of plasma with temperatures (T) greater than 6 MK and emission measures (EM) less than 10^{27} cm^{-5} (so-called hot-dim plasma) in quiescent active regions (ARs) dependent upon the AR age?** and **(Q2) Is the dissipation of Alfvén waves a suitable heating source to explain both the coronal X-ray and Extreme Ultraviolet (EUV) emissions from the corona?**
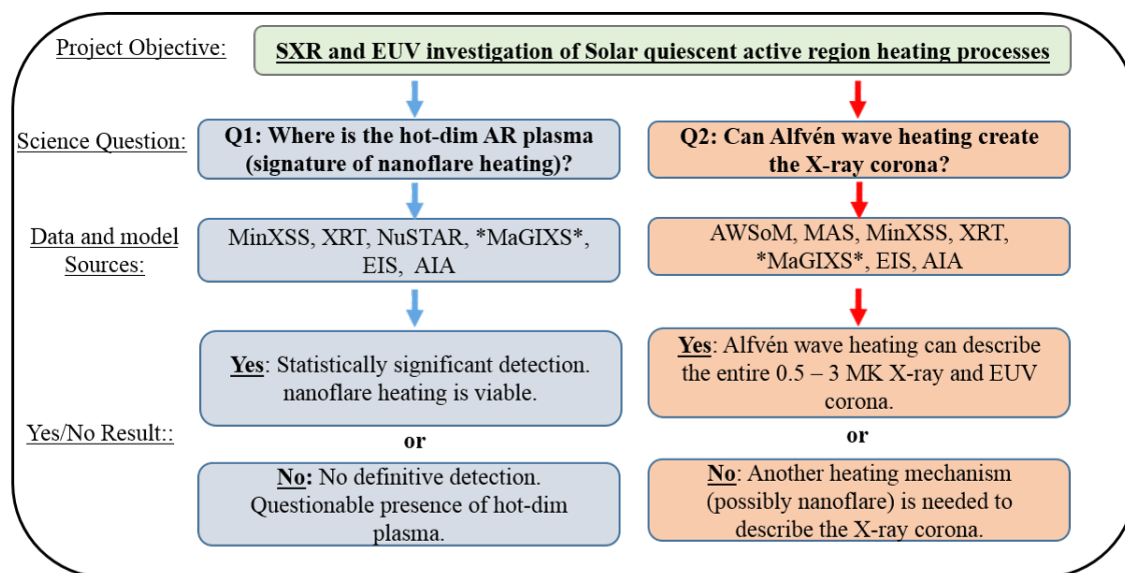
Figure 12.1: Proposed project outline.

Soft X-ray (SXR) spectral measurements provide an unambiguous diagnostic for estimating the temperature distribution ($T \geq 1$ MK) and chemical composition of coronal plasma. New SXR measurements will provide vital tools for understanding the fundamental processes that heat the corona. These measurements are being obtained near continuously

(except for eclipse times) from the Miniature X-ray Solar Spectrometer (MinXSS) CubeSat, intermittently (target of opportunity observations) from the Nuclear Spectroscopic Telescope Array (NuSTAR), and in the near future from the Marshall Grazing Incidence X-ray Spectrograph (MaGIXS) sounding rocket flight. This proposal aims to investigate the observational signatures of these two solar coronal heating theories as outlined below and summarized in Figure 12.2.1.

(1) <u>Investigate the presence and chemical composition (abundance)</u> of hot-dim plasma in quiescent (non-large flaring) ARs through SXR and EUV observations, which can reveal a signature of impulsive (nanoflare like) heating process.

(2) <u>Estimate the contribution</u> of Alfvén wave heating to the SXR flux, by using numerical simulations to create synthetic data and then comparing them to observations.

Both coronal heating theories revolve around kinetic energy generated by photospheric convective fluid motions that jostle magnetic field lines rooted in the photosphere. The kinetic energy is converted to magnetic energy, which is either dissipated by reconnecting magnetic field lines that create small-scale, quickly occurring impulsive events [124], or by the interaction of waves on the magnetic field lines causing small-scale turbulence that leads to heating of the plasma [3]. While both processes are likely to be occurring, this proposal aims to understand the presence and relative contributions of these two phenomena to the coronal conditions.

Q1: Is the presence of hot (T > 6 MK ⇔ log(T) > 6.78), dim (EM < 10^{27} cm^{-5}) plasma in quiescent active regions (ARs) dependent upon AR age?

The episodic heating theory of the solar corona envisions small-scale magnetic processes (called nanoflares) that dissipate magnetic energy that has been converted from the kinetic energy associated with photospheric convection [124]. Each bursty event is postulated to release small amounts of energy ($< 10^{24}$ ergs), that for low frequency events,

near-instantaneously heats the local plasma to above 5 MK ($\log(T) \sim 6.7$). This plasma is theorized to quickly cool and thus spend the majority of time below 5 MK [87].
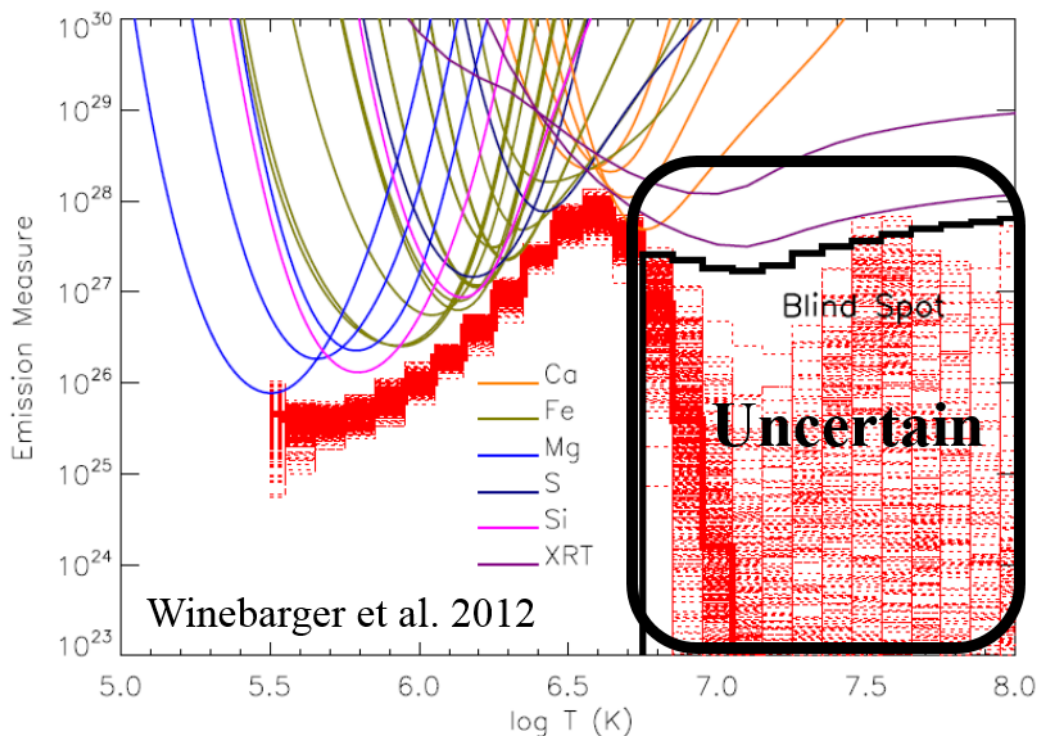
Figure 12.2: Active region emission measure distribution hot temperature component (5 MK $> \log_{10}(T) = 6.7$) is poorly constrained by current EUV and SXR observations. Emission measure units are in column (cm^{-5}). Adapted from [157].

But, the ensemble of randomly occurring impulsive events could continuously generate coronal plasma at temperatures above 5 MK, with only dim emission - perhaps 3 orders of magnitude fainter than the cooler component (< 5 MK; see Figure 12.2.1). Thus, the direct detection of the predicted hot-dim plasma has been elusive with current solar SXR instrumentation, which lack the necessary intensity sensitivity and extreme ultraviolet (EUV) instrumentation which can suffer from cooler plasma contributions in the passband.

There have been several attempts at measuring this hot-dim component. A few reported detections have been by SXR full sun spectrometers, such as SPHinX [111] and X123 [28] narrow FOV spectrometers like RESIK [?], full sun spatially resolved imagers of Yohkoh

SXT [**?**], Hinode X-ray Telescope (XRT), and RHESSI [137]. All these investigations suffer from instrumental limitations, hindering their ability to make an unambiguous inference of the hot-dim plasma. The spectrally resolved and spatially integrated measurements of SPHinX was averaged over ~17 days (losing temporal sensitivity), the published X123 data was only from a 5 minute rocket flight and RESIK data were averaged over a 1 month period. Combined analysis using SXR images from XRT and EUV spectra from the Hinode EUV Imaging Spectrograph (EIS), suffer from a hot-dim temperature blind-spot for T > 6 MK and EM < 10^{27} cm^{-5} [157] (see Figure 12.2.1). This blind spot is primarily due to spectral confusion for SXR > 1 keV in the XRT filters. Likewise, Yohkoh SXT has spectrally confused filter images with contributions from cooler plasma. The most solid inkling of a hot-dim plasma detection has come from the Extreme Ultraviolet Normal Incidence Spectrograph (EUNIS-13) rocket flight [21].

NuSTAR has conducted spectrally (~ 0.4 keV FWHM) and spatially resolved (~ 18") solar measurements over its ~11' (~1/3 the radius of the Sun) FOV, and the spectral coverage (3 - 10 keV) and sensitivity (effective area ~700 cm^2 at 3 keV, ~200 times larger than RHESSI, a dedicated solar X-ray observatory) to make unambiguous detections of hot-dim plasma in solar ARs. Previously published solar pointings with NuSTAR place upper limits on any hot-dim plasma component, but did not infer a plasma component greater than 5 MK (with detector livetime-limited data) [67]. *This contrasts with other studies that claim hot-dim plasma detection!!.* The previous NuSTAR observations were of older active regions (1 - 2 weeks old).

Perhaps the presence of the hot-dim plasma has a dependence on AR age? Previous studies such as [148] have provided evidence that early in AR evolution (a few days after photospheric magnetic flux emergence) emission from hotter (3 - 4 MK) EUV lines (like Ca XV) are enhanced relative to cooler (0.6 - 0.9 MK) lines (Si VII), (see Figure 12.3).

Additionally, a few studies similar to [156] of EUV lines yield strong evidence of elemental abundance variations in ARs (see Figure 12.4). Within a few days an emerging
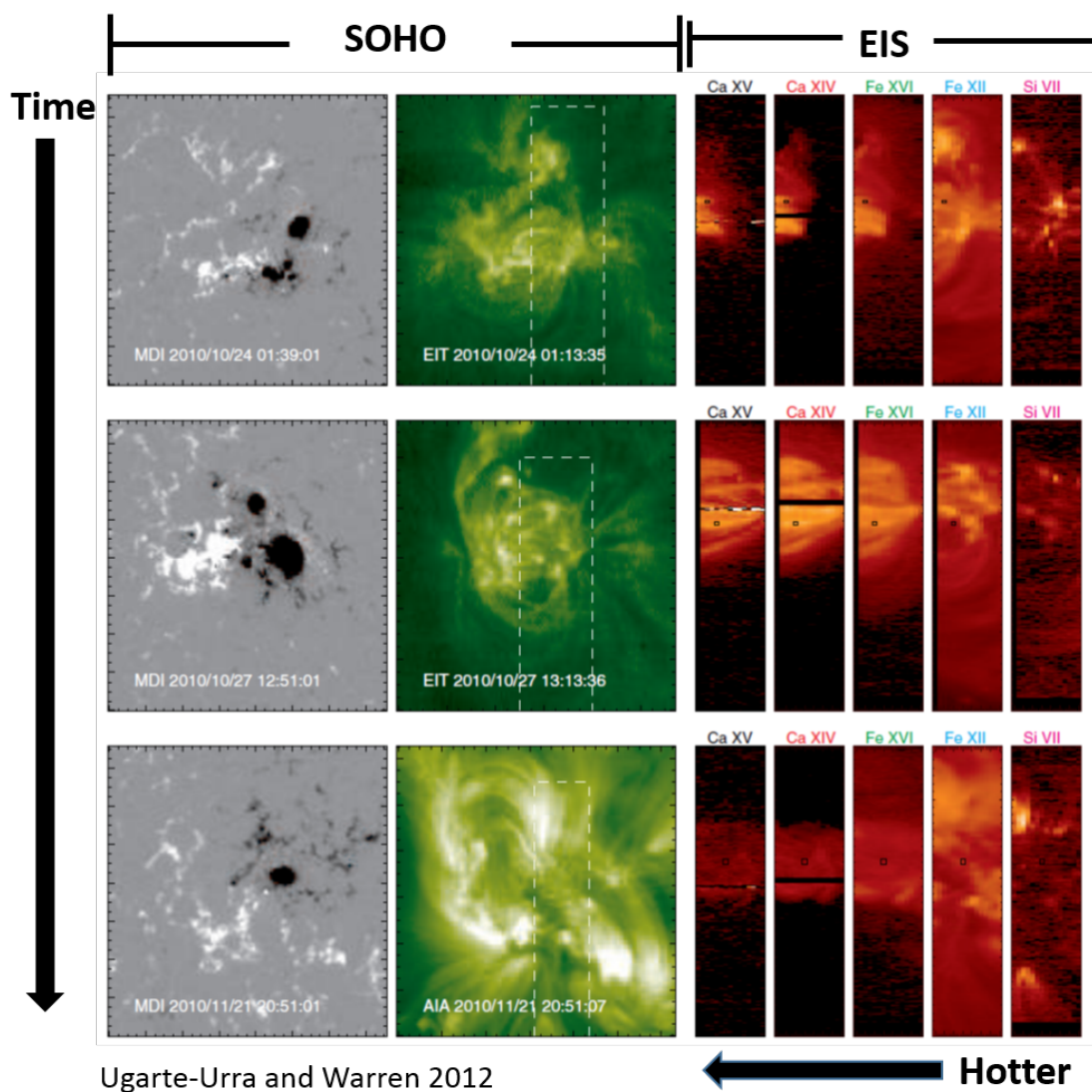
Figure 12.3: Adapted from [148]. During early phases of active region evolution, emission from hotter EUV lines (Ca XV; 3 - 4 MK) is enhanced with respect to cooler (Si VII; 0.6 - 0.9 MK) compared to later times in active region life spans.

AR can have an enrichment of low first ionization elements (FIP < 10 eV), such as Mg, Fe and Si, from photospheric abundance values ($A_{photospheric} = 1$), to the so called coronal abundance ($A_{coronal} \sim 4*A_{photospheric}$) or even greater. There is a lack of literature of similar studies in the SXR. If impulsive nanoflare processes are similar to their larger counterparts, then it is postulated that photospheric material would be driven up to the corona in ARs.

This change could possibly be inferred from SXR spectral measurements. Thus, there could be a connection between AR heating processes and the AR elemental composition.
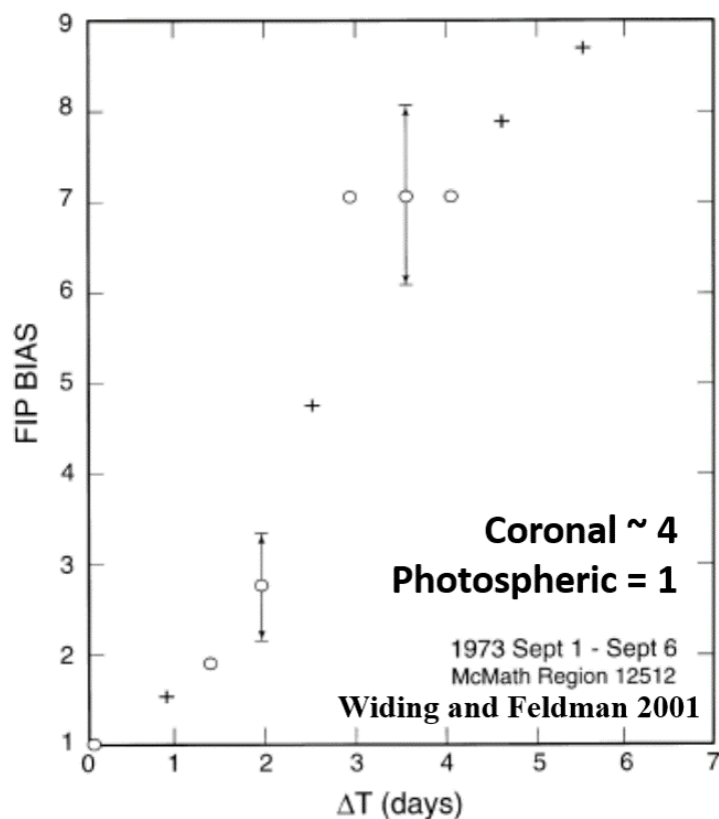
Figure 12.4: Adapted from [156]. Active region elemental abundance can transition rapidly in a few days after magnetic flux emergence. The data is from EUV Mg and Ne line ratios.

The Miniature X-ray Solar Spectrometer (MinXSS) CubeSat has the spectral resolution ($\sim$0.15 FWHM) from 1.0 - 10 keV to estimate elemental abundances [158]. Due to the smaller aperture and hence lower effective area ($\sim$10^{-4} cm^2) of the MinXSS spectrometer, significant counts can be expected from 1 - $\sim$2.5 keV for the solar flux levels I propose to observe, with near overlap with NuSTAR. A recent example of simultaneous NuSTAR and MinXSS measurements, when the GOES 0.1 - 0.8 nm flux was at $\sim$7 x 10^{-8} W m^{-2} levels is in Figure 12.5. The data are indicative of the expected count rate and photon flux estimation that are expected to be observed during this project. Single temperature (1T) spectral fits yield consistent plasma estimations and flux levels (keeping in mind the difference in the

instruments' FOVs).

I propose to observe as many separate sets of quiescent ARs that have recently emerged (within 2 - 4 days) as possible to assesss the presence of hot-dim plasma with NuSTAR and simultaneous elemental abundances with MinXSS. MinXSS continuously observes the Sun (expect for LEO eclipse periods). MinXSS-2 (identical to MinXSS-1) is scheduled to launch not earlier than June 2018 for up to a four year mission. I will target ARs that emerge on the solar east limb, monitor its SXR evolution with mutiple NuSTAR observations separated by at least 1 day and preferably no more than 3 days, before the region rotates out of the Earth line-of-sight on the west limb.

It is desired that the observed ARs emerge during solar conditions with no well-defined ARs already present to minimize ghost rays in the (photon contributions from sources not in the field of view) and ease the extraction of the target AR flux contribution to the MinXSS count rate. These conditions will occur more frequently over the next 2 - 3 years as solar cycle minimum nears. MinXSS integrates the SXR flux over the full Sun. Thus, coordinated Hinode XRT full Sun images will be taken to assist in extracting the NuSTAR observed AR contribution to the MinXSS spectrum (cross calibration between MinXSS and Hinode XRT is in progress). Additionally, the solar spectrum measured by MinXSS before the AR emerged will be used as a baseline for quiet Sun (QS) SXR. When available, Hinode EIS data will be used to assess the cooler plasma emission component. Solar Dynamics Observatory (SDO) AIA EUV filter images will be also analyzed for context. SDO HMI magnetograms will be used through the helioviewer.org tool to observe emerging flux. I am part of the NuSTAR Heliophysics group, which have been conducting solar measurements and have developed NuSTAR solar analysis tools in addition to existing software (XSPEC, OSPEX and SSW). Spectral fits and calculated differential emission measures will be used to estimate the plasma temperature distribution.

Additionally, I will collaborate with the MaGIXS sounding rocket team at the NASA Marshall Space Flight Center and Smithsonian Astrophysical Observatory (SAO) to use
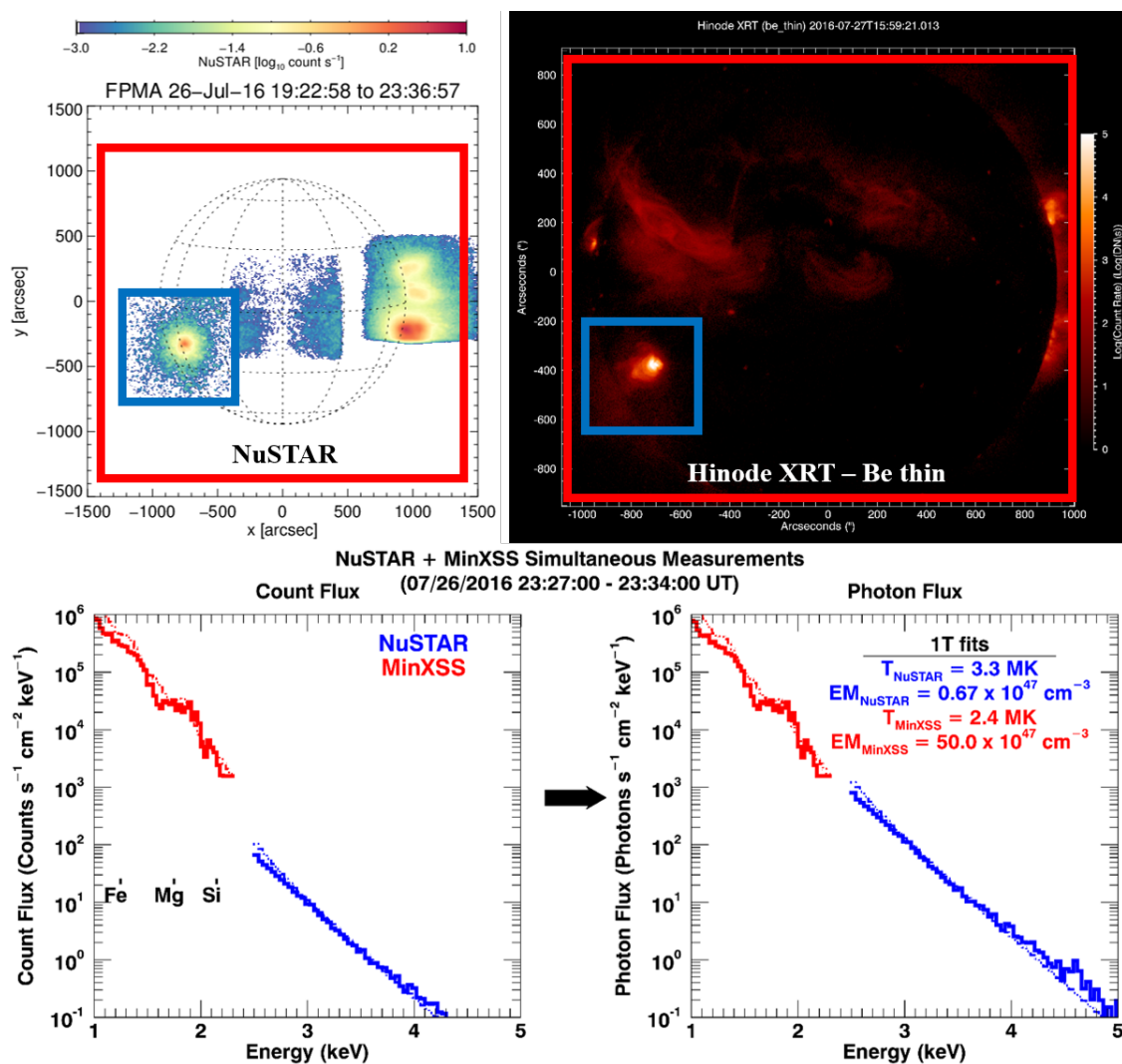
Figure 12.5: Top Left: Previous NuSTAR solar measurement. Top Right: Closest time Hinode XRT Be-thin image to the NuSTAR measurement. The blue (red) box indicates the spatial region that the NuSTAR (MinXSS) measurements (soilid lines), inferred photon flux and 1T fit results (dash-dot lines). The emission measure (EM) is listed in volume units (cm^3).

observational data from their spatially resolved slit spectra from ∼0.5 - 2 keV with 2.4 x 10^{-4} keV FWHM resolution at 1.24 keV (0.6 2.4 nm, with 2 x 10^{-4} nm FWHM resolution) during their rocket flight in the summer of 2019 to augment this study. MaGIXS will directly measure spectrally resolved lines of ionized Mg, Ne, Fe and O with formation temperatures between 2 - 7 MK. The ratios of the high and low temperature lines for the same element

yield temperature estimates. The ratios of the low and high FIP element lines of similar formation temperatures (e.g. Mg XI/O VIII, at T ∼ 2.5 MK and Fe XVII/Ne X at T ∼ 4 MK) yield direct estimates of FIP enhancements over photospheric abundances. If no hot-dim plasma is detected, the more likely scenario is heating primarily by Alfvén wave dissipation.

12.2.2 Numerical Simulation Investigation of Heating Mechanisms in Quiescent Solar Active Regions.

Q2: Is Alfvén wave dissipation a suitable heating source to explain the coronal X-ray emission, in addition to the EUV emission?

The interaction of outward propagating Alfvén waves from the jostling of photospheric magnetic flux tubes and reflected (from the radial density gradient in the solar atmosphere) inward propagating Alfvén waves results in a leakage of energy to lower density plasma (the corona) [150]. Only about 10% of the Alfvén wave energy is believed to reach the corona, but this appears to be enough to create 1 - 3 MK plasma [8], which can explain the QS and AR plasma, especially if there is no significant detection of a secondary hot-dim AR component from **Q1**. The 3D Magnetohydrodynamic (3DMHD) Alfvén Wave Solar Model (AWSoM) code, [151], has successfully implemented Alfvén wave heating to create many realistic aspects of the solar corona, such as electron-ion temperature anisotropies, the 1 - 3 MK coronal plasma, AR EUV emission enhancement (from comparison with AIA and STEREO images), see Figure 6 for example synthetic AIA images. These synthetic images yield some of the most realistic quantitative comparisons to the solar coronal conditions and the best qualitative comparison to AIA images. Also, the Predictive Sciences Magnetohydrodynamic Algorithm outside a Sphere (MAS) code [103] has an analytical form of Alfvén wave heating in its energy equation. This allows for turning 'on and off' the Alfvén wave contribution to the evolution of the plasma in the code so the influence on the radiative diagnostics can be directly analyzed.

I will work with both the AWSoM team and the MAS team which have agreed to collaborate on a project to determine if synthesized spectra from the AWSoM and MAS codes can create the observed solar SXR emission. I will use the temperatures, densities, and velocities output by the AWSoM and MAS codes as inputs to the Chianti atomic database [161] to generate synthetic data to compare to MinXSS SXR spectra, XRT images, and future MaGIXS SXR spectra. Comparison to EIS EUV full sun spectral maps will help constrain the capability to recreate the detailed atmospheric temperature structure. 3DMHD numerical simulations are great tools to aid in the interpretation of radiation diagnostics and to assess the accuracy of the physics believed to describe astronomical systems.

The AWSoM and MAS numerical simulations will be used to compare radiation inferred plasma properties (from DEMs, filter images from SXR and EUV observatories) to the 3D distributions predicted by the numerical codes. This will provide guidance on what biases, caveats, and issues are implicit in MinXSS full-sun spectra, XRT and AIA filter images, and MaGIXS and EIS slit spectral images. This will enhance knowledge on to improve designs of future instruments. The supercomputing resources available at my postdoc institution can be used to speed up and complete the investigations involving numerical simulations addressing **Q2**.
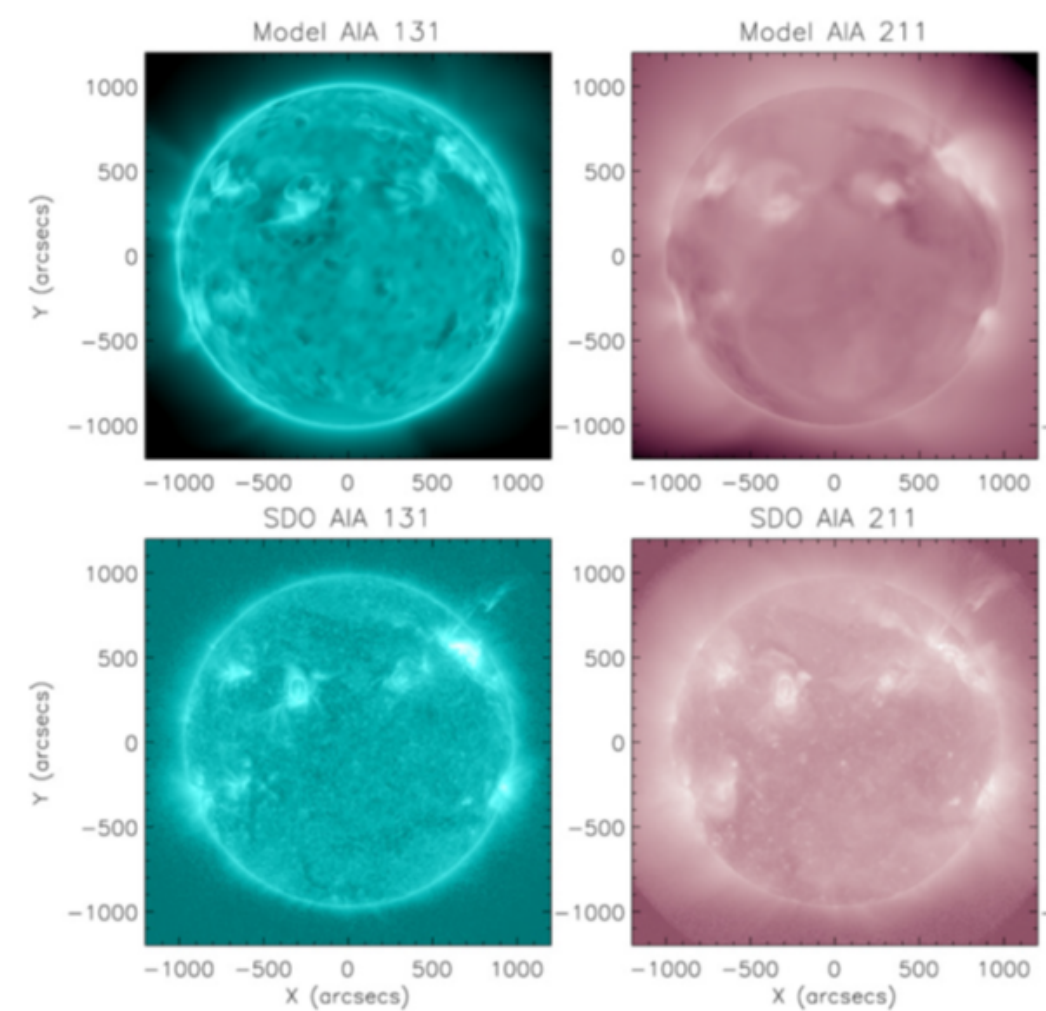
Figure 12.6: Comparison of AWSom synthesized EUV and AIA images. The figure is adapted from van der Holst et al. 2014 [151].

Bibliography

[1] B. P. Abbott, R. Abbott, T. D. Abbott, M. R. Abernathy, F. Acernese, K. Ackley, C. Adams, T. Adams, P. Addesso, R. X. Adhikari, and et al. Observation of Gravitational Waves from a Binary Black Hole Merger. <u>Physical Review Letters</u>, 116(6):061102, February 2016.

[2] S. Agostinelli, J. Allison, K. Amako, J. Apostolakis, H. Araujo, P. Arce, M. Asai, D. Axen, S. Banerjee, G. Barrand, F. Behner, L. Bellagamba, J. Boudreau, L. Broglia, A. Brunengo, H. Burkhardt, S. Chauvie, J. Chuma, R. Chytracek, G. Cooperman, G. Cosmo, P. Degtyarenko, A. Dell'Acqua, G. Depaola, D. Dietrich, R. Enami, A. Feliciello, C. Ferguson, H. Fesefeldt, G. Folger, F. Foppiano, A. Forti, S. Garelli, S. Giani, R. Giannitrapani, D. Gibin, J. J. Gómez Cadenas, I. González, G. Gracia Abril, G. Greeniaus, W. Greiner, V. Grichine, A. Grossheim, S. Guatelli, P. Gumplinger, R. Hamatsu, K. Hashimoto, H. Hasui, A. Heikkinen, A. Howard, V. Ivanchenko, A. Johnson, F. W. Jones, J. Kallenbach, N. Kanaya, M. Kawabata, Y. Kawabata, M. Kawaguti, S. Kelner, P. Kent, A. Kimura, T. Kodama, R. Kokoulin, M. Kossov, H. Kurashige, E. Lamanna, T. Lampén, V. Lara, V. Lefebure, F. Lei, M. Liendl, W. Lockman, F. Longo, S. Magni, M. Maire, E. Medernach, K. Minamimoto, P. Mora de Freitas, Y. Morita, K. Murakami, M. Nagamatu, R. Nartallo, P. Nieminen, T. Nishimura, K. Ohtsubo, M. Okamura, S. O'Neale, Y. Oohata, K. Paech, J. Perl, A. Pfeiffer, M. G. Pia, F. Ranjard, A. Rybin, S. Sadilov, E. Di Salvo, G. Santin, T. Sasaki, N. Savvas, Y. Sawada, S. Scherer, S. Sei, V. Sirotenko, D. Smith, N. Starkov, H. Stoecker, J. Sulkimo, M. Takahata, S. Tanaka, E. Tcherniaev, E. Safai Tehrani, M. Tropeano, P. Truscott, H. Uno, L. Urban, P. Urban, M. Verderi, A. Walkden, W. Wander, H. Weber, J. P. Wellisch, T. Wenaus, D. C. Williams, D. Wright, T. Yamada, H. Yoshida, D. Zschiesche, and G EANT4 Collaboration.

[3] H. Alfvén. Magneto hydrodynamic waves, and the heating of the solar corona. <u>Mon. Not. Roy. Astron. Soc.</u>, 107:211, 1947.

[4] C. Allende Prieto, D. L. Lambert, and M. Asplund. The Forbidden Abundance of Oxygen in the Sun. <u>Astrophys. J. Lett.</u>, 556:L63–L66, July 2001.

[5] U. Arp, C. Clark, L. Deng, N. Faradzhev, A. Farrell, M. Furst, S. Grantham, E. Hagley, S. Hill, T. Lucatorto, P.-S. Shaw, C. Tarrio, and R. Vest. SURF III: A flexible

synchrotron radiation source for radiometry and research. Nuclear Instruments and Methods in Physics Research A, 649:12–14, September 2011.

[6] M. J. Aschwanden. Physics of the Solar Corona. (2nd edition). December 2005.

[7] M. J. Aschwanden, P. Boerner, C. J. Schrijver, and A. Malanushenko. Automated Temperature and Emission Measure Analysis of Coronal Loops and Active Regions Observed with the Atmospheric Imaging Assembly on the Solar Dynamics Observatory (SDO/AIA). *Solar Phys.*, 283:5–30, March 2013.

[8] M. Asgari-Targhi, J. T. Schmelz, S. Imada, S. Pathak, and G. M. Christian. Modeling of Hot Plasma in the Solar Active Region Core. *Astrophys. J.*, 807:146, July 2015.

[9] M. Asplund, N. Grevesse, and A. J. Sauval. The Solar Chemical Composition. In T. G. Barnes, III and F. N. Bash, editors, Cosmic Abundances as Records of Stellar Evolution and Nucleosynthesis, volume 336 of Astronomical Society of the Pacific Conference Series, page 25, September 2005.

[10] M. Asplund, N. Grevesse, A. J. Sauval, C. Allende Prieto, and D. Kiselman. Line formation in solar granulation. IV. [O I], O I and OH lines and the photospheric O abundance. *Astron. Astrophys.*, 417:751–768, April 2004.

[11] M. Asplund, N. Grevesse, A. J. Sauval, and P. Scott. The Chemical Composition of the Sun. *Annual Review of Astron and Astrophys.*, 47:481–522, September 2009.

[12] David Attwood. Soft X-Rays and Extreme Ultraviolet Radiation: Principles and Applications. Cambridge University Press, New York, NY, USA, 1st edition, 2007.

[13] W. T. Barnes, P. J. Cargill, and S. J. Bradshaw. Inference of Heating Properties from "Hot" Non-flaring Plasmas in Active Region Cores. I. Single Nanoflares. *Astrophys. J.*, 829:31, September 2016.

[14] Burkhard Beckhoff, Birgit Kanngieber, Norbert Langhoff, Reiner Wedell, and Helmut Wolff. Handbook of Practical X-Ray Fluorescence Analysis. Springer-Verlag Berlin Heidelberg, New York, NY, USA, 1st edition, 2006.

[15] A. O. Benz. Flare Observations. Living Reviews in Solar Physics, 14:2, December 2017.

[16] W. P. Blair, K. S. Long, O. Vancura, C. W. Bowers, A. F. Davidsen, W. V. D. Dixon, S. T. Durrance, P. D. Feldman, H. C. Ferguson, R. C. Henry, R. A. Kimble, G. A. Kriss, J. W. Kruk, H. W. Moos, and T. R. Gull. Discovery of a fast radiative shock wave in the Cygnus Loop using the Hopkins Ultraviolet Telescope. *Astrophys. J. Lett.*, 379:L33–L36, September 1991.

[17] W. P. Blair, R. Sankrit, and S. Tulin. Far Ultraviolet Spectroscopic Explorer and Hopkins Ultraviolet Telescope Observations of Radiative Shocks in the Cygnus Loop. *Astrophys. J. Supp.*, 140:367–388, June 2002.

[18] S. Bosch, J. Ferré-Borrull, N. Leinfellner, and A. Canillas. Effective dielectric function of mixtures of three or more materials: a numerical procedure for computations. Surface Science, 453:9–17, May 2000.

[19] F. Bridou, M. Cuniot-Ponsard, J.-M. Desvignes, M. Richter, U. Kroth, and A. Gottwald. Experimental determination of optical constants of mgf2 and alf3 thin films in the vacuum ultra-violet wavelength region (60124nm), and its application to optical designs. Optics Communications, 283(7):1351 – 1358, 2010.

[20] J. W. Brosius, J. M. Davila, R. J. Thomas, and B. C. Monsignori-Fossi. Measuring Active and Quiet-Sun Coronal Plasma Properties with Extreme-Ultraviolet Spectra from SERTS. Astrophys. J. Supp., 106:143, September 1996.

[21] J. W. Brosius, A. N. Daw, and D. M. Rabin. Pervasive Faint Fe XIX Emission from a Solar Active Region Observed with EUNIS-13: Evidence for Nanoflare Heating. Astrophys. J., 790:112, August 2014.

[22] E. B. Burgh, S. R. McCandliss, and P. D. Feldman. Rocket Observations of Far-Ultraviolet Dust Scattering in NGC 2023. Astrophys. J., 575:240–249, August 2002.

[23] E. Caffau, H.-G. Ludwig, M. Steffen, B. Freytag, and P. Bonifacio. Solar Chemical Abundances Determined with a CO5BOLD 3D Model Atmosphere. Solar Phys., 268:255–269, February 2011.

[24] L. R. Canfield, G. Hass, and W. R. Hunter. The optical properties of evaporated gold in the vacuum ultraviolet from 300 to 2 000 angstroms. Journal de Physique, 1(1):124–129, Jan 1964.

[25] L. R. Canfield, G. Hass, and J. E. Waylonis. Further studies on mgf2-overcoated aluminum mirrors with highest reflectance in the vacuum ultraviolet. Appl. Opt., 5(1):45–50, Jan 1966.

[26] R. C. Carrington. Description of a Singular Appearance seen in the Sun on September 1, 1859. Mon. Not. Roy. Astron. Soc., 20:13–15, November 1859.

[27] B.W. Carroll and D.A. Ostlie. An Introduction to Modern Astrophysics. Pearson Addison-Wesley, 2007.

[28] A. Caspi, T. N. Woods, and H. P. Warren. New Observations of the Solar 0.5-5 keV Soft X-Ray Spectrum. Astrophys. J. Lett., 802:L2, March 2015.

[29] R. Cen, T. M. Tripp, J. P. Ostriker, and E. B. Jenkins. Revealing the Warm-Hot Intergalactic Medium with O VI Absorption. Astrophys. J. Lett., 559:L5–L8, September 2001.

[30] M. C. M. Cheung, P. Boerner, C. J. Schrijver, P. Testa, F. Chen, H. Peter, and A. Malanushenko. Thermal Diagnostics with the Atmospheric Imaging Assembly on board the Solar Dynamics Observatory: A Validated Method for Differential Emission Measure Inversions. Astrophys. J., 807:143, July 2015.

[31] John Hennessy April D. Jewell Shouleh Nikzad Kevin France Christian Carter, Christopher Samuel Moore. Characterizing environmental effects on visible and uv reflectance of ald-coated optics, 2016.

[32] I. J. D. Craig and J. C. Brown. Fundamental limitations of X-ray spectra as diagnostics of plasma temperature structure. *Astron. Astrophys.*, 49:239–250, June 1976.

[33] J. L. Culhane, L. K. Harra, A. M. James, K. Al-Janabi, L. J. Bradley, R. A. Chaudry, K. Rees, J. A. Tandy, P. Thomas, M. C. R. Whillock, B. Winter, G. A. Doschek, C. M. Korendyke, C. M. Brown, S. Myers, J. Mariska, J. Seely, J. Lang, B. J. Kent, B. M. Shaughnessy, P. R. Young, G. M. Simnett, C. M. Castelli, S. Mahmoud, H. Mapson-Menard, B. J. Probyn, R. J. Thomas, J. Davila, K. Dere, D. Windt, J. Shea, R. Hagood, R. Moye, H. Hara, T. Watanabe, K. Matsuzaki, T. Kosugi, V. Hansteen, and Ø. Wikstol. The EUV Imaging Spectrometer for Hinode. *Solar Phys.*, 243:19–61, June 2007.

[34] B. De Pontieu, A. M. Title, J. R. Lemen, G. D. Kushner, D. J. Akin, B. Allard, T. Berger, P. Boerner, M. Cheung, C. Chou, J. F. Drake, D. W. Duncan, S. Freeland, G. F. Heyman, C. Hoffman, N. E. Hurlburt, R. W. Lindgren, D. Mathur, R. Rehse, D. Sabolish, R. Seguin, C. J. Schrijver, T. D. Tarbell, J.-P. Wülser, C. J. Wolfson, C. Yanari, J. Mudge, N. Nguyen-Phuc, R. Timmons, R. van Bezooijen, I. Weingrod, R. Brookner, G. Butcher, B. Dougherty, J. Eder, V. Knagenhjelm, S. Larsen, D. Mansir, L. Phan, P. Boyle, P. N. Cheimets, E. E. DeLuca, L. Golub, R. Gates, E. Hertz, S. McKillop, S. Park, T. Perry, W. A. Podgorski, K. Reeves, S. Saar, P. Testa, H. Tian, M. Weber, C. Dunn, S. Eccles, S. A. Jaeggli, C. C. Kankelborg, K. Mashburn, N. Pust, L. Springer, R. Carvalho, L. Kleint, J. Marmie, E. Mazmanian, T. M. D. Pereira, S. Sawyer, J. Strong, S. P. Worden, M. Carlsson, V. H. Hansteen, J. Leenaarts, M. Wiesmann, J. Aloise, K.-C. Chu, R. I. Bush, P. H. Scherrer, P. Brekke, J. Martinez-Sykora, B. W. Lites, S. W. McIntosh, H. Uitenbroek, T. J. Okamoto, M. A. Gummin, G. Auker, P. Jerram, P. Pool, and N. Waltham. The Interface Region Imaging Spectrograph (IRIS). *Solar Phys.*, 289:2733–2779, July 2014.

[35] G. Del Zanna. The multi-thermal emission in solar active regions. *Astron. Astrophys.*, 558:A73, October 2013.

[36] G. Del Zanna, K. P. Dere, P. R. Young, E. Landi, and H. E. Mason. CHIANTI - An atomic database for emission lines. Version 8. *Astron. Astrophys.*, 582:A56, October 2015.

[37] G. Del Zanna, K. P. Dere, P. R. Young, E. Landi, and H. E. Mason. CHIANTI - An atomic database for emission lines. Version 8. *Astron. Astrophys.*, 582:A56, October 2015.

[38] B. R. Dennis, K. J. H. Phillips, R. A. Schwartz, A. K. Tolbert, R. D. Starr, and L. R. Nittler. Solar Flare Element Abundances from the Solar Assembly for X-Rays (SAX) on MESSENGER. *Astrophys. J.*, 803:67, April 2015.

[39] G. A. Doschek and H. P. Warren. The Mysterious Case of the Solar Argon Abundance near Sunspots in Flares. *Astrophys. J.*, 825:36, July 2016.

[40] G. A. Doschek, H. P. Warren, and U. Feldman. Anomalous Relative Ar/Ca Coronal Abundances Observed by the Hinode/EUV Imaging Spectrometer Near Sunspots. *Astrophys. J. Lett.*, 808:L7, July 2015.

[41] D. H. Dowell and J. F. Schmerge. Quantum efficiency and thermal emittance of metal photocathodes. Physical Review Special Topics Accelerators and Beams, 12(7):074201, July 2009.

[42] B.T. Draine. Physics of the Interstellar and Intergalactic Medium. Princeton Series in Astrophysics. Princeton University Press, 2010.

[43] H. Ehrenreich, H. R. Philipp, and B. Segall. Optical Properties of Aluminum. Physical Review, 132:1918–1928, December 1963.

[44] A. G. Emslie, B. R. Dennis, A. Y. Shih, P. C. Chamberlin, R. A. Mewaldt, C. S. Moore, G. H. Share, A. Vourlidas, and B. T. Welsch. Global Energetics of Thirty-eight Large Solar Eruptive Events. *Astrophys. J.*, 759:71, November 2012.

[45] D. Fabbian, M. Asplund, P. S. Barklem, M. Carlsson, and D. Kiselman. Neutral oxygen spectral line formation revisited with new collisional data: large departures from LTE at low metallicity. *Astron. Astrophys.*, 500:1221–1238, June 2009.

[46] D. Fabbian, E. Khomenko, F. Moreno-Insertis, and Å. Nordlund. Solar Abundance Corrections Derived Through Three-dimensional Magnetoconvection Simulations. *Astrophys. J.*, 724:1536–1541, December 2010.

[47] D. Fabbian, F. Moreno-Insertis, E. Khomenko, and Å. Nordlund. Solar Fe abundance and magnetic fields. Towards a consistent reference metallicity. *Astron. Astrophys.*, 548:A35, December 2012.

[48] U. Feldman. Elemental abundances in the upper solar atmosphere. *Physica Scripta*, 46:202–220, September 1992.

[49] K. France, S. R. McCandliss, E. B. Burgh, and P. D. Feldman. Rocket and Far Ultraviolet Spectroscopic Explorer Observations of IC 405: Differential Extinction and Fluorescent Molecular Hydrogen. *Astrophys. J.*, 616:257–265, November 2004.

[50] Kevin France, Keri Hoadley, Brian T. Fleming, Robert Kane, Nicholas Nell, Matthew Beasley, and James C. Green. The slice, chess, and sistine ultraviolet spectrographs: Rocket-borne instrumentation supporting future astrophysics missions. Journal of Astronomical Instrumentation, 05(01):1640001, 2016.

[51] H. A. Garcia. Temperature and emission measure from GOES soft X-ray measurements. *Solar Phys.*, 154:275–308, October 1994.

[52] G. A. Gary. Plasma Beta above a Solar Active Region: Rethinking the Paradigm. *Solar Phys.*, 203:71–86, October 2001.

[53] S. Gburek, J. Sylwester, M. Kowalinski, J. Bakala, Z. Kordylewski, P. Podgorski, S. Plocieniak, M. Siarkowski, B. Sylwester, W. Trzebinski, S. V. Kuzin, A. A. Pertsov, Y. D. Kotov, F. Farnik, F. Reale, and K. J. H. Phillips. SphinX: The Solar Photometer in X-Rays. *Solar Phys.*, 283:631–649, April 2013.

[54] Steven M. George. Atomic layer deposition: An overview. Chemical Reviews, 110(1):111–131, 2010. PMID: 19947596.

[55] Steven M. George and Younghee Lee. Prospects for thermal atomic layer etching using sequential, self-limiting fluorination and ligand-exchange reactions. ACS Nano, 10(5):4889–4894, 2016. PMID: 27216115.

[56] Dulal Chandra Ghosh, Tanmoy Chakraborty, and Bhabatosh Mandal. The electronegativity scale of allred and rochow: revisited. Theoretical Chemistry Accounts, 124(3):295–301, Oct 2009.

[57] L. Golub, E. Deluca, G. Austin, J. Bookbinder, D. Caldwell, P. Cheimets, J. Cirtain, M. Cosmo, P. Reid, A. Sette, M. Weber, T. Sakao, R. Kano, K. Shibasaki, H. Hara, S. Tsuneta, K. Kumagai, T. Tamura, M. Shimojo, J. McCracken, J. Carpenter, H. Haight, R. Siler, E. Wright, J. Tucker, H. Rutledge, M. Barbera, G. Peres, and S. Varisco. The X-Ray Telescope (XRT) for the Hinode Mission. *Solar Phys.*, 243:63–86, June 2007.

[58] L. Golub and J.M. Pasachoff. The Solar Corona. The Solar Corona. Cambridge University Press, 2010.

[59] D.F. Gray. The Observation and Analysis of Stellar Photospheres. Cambridge University Press, 2005.

[60] J. C. Green. Little mirror, big science. In Space Telescopes and Instrumentation 2012: Ultraviolet to Gamma Ray, volume 8443 of *Proceedings of SPIE*, page 844302, September 2012.

[61] J. C. Green, C. S. Froning, S. Osterman, D. Ebbets, S. H. Heap, C. Leitherer, J. L. Linsky, B. D. Savage, K. Sembach, J. M. Shull, O. H. W. Siegmund, T. P. Snow, J. Spencer, S. A. Stern, J. Stocke, B. Welsh, S. Béland, E. B. Burgh, C. Danforth, K. France, B. Keeney, J. McPhate, S. V. Penton, J. Andrews, K. Brownsberger, J. Morse, and E. Wilkinson. The Cosmic Origins Spectrograph. *Astrophys. J.*, 744:60, January 2012.

[62] B. W. Grefenstette, L. Glesener, S. Krucker, H. Hudson, I. G. Hannah, D. M. Smith, J. K. Vogel, S. M. White, K. K. Madsen, A. J. Marsh, A. Caspi, B. Chen, A. Shih, M. Kuhar, S. E. Boggs, F. E. Christensen, W. W. Craig, K. Forster, C. J. Hailey, F. A. Harrison, H. Miyasaka, D. Stern, and W. W. Zhang. The First Focused Hard X-ray Images of the Sun with NuSTAR. *Astrophys. J.*, 826:20, July 2016.

[63] N. Grevesse, M. Asplund, and A. J. Sauval. The Solar Chemical Composition. *Space Sci. Rev.*, 130:105–114, June 2007.

[64] N. Grevesse and A. J. Sauval. Standard Solar Composition. *Space Sci. Rev.*, 85:161–174, May 1998.

[65] D.J. Griffiths. Introduction to Electrodynamics. Prentice Hall, 1999.

[66] Jeffrey W. Kruk H. Warren Moos, Stephan R. McCandliss. Fuse: lessons learned for future fuv missions, 2004.

[67] I. G. Hannah, B. W. Grefenstette, D. M. Smith, L. Glesener, S. Krucker, H. S. Hudson, K. K. Madsen, A. Marsh, S. M. White, A. Caspi, A. Y. Shih, F. A. Harrison, D. Stern, S. E. Boggs, F. E. Christensen, W. W. Craig, C. J. Hailey, and W. W. Zhang. The First X-Ray Imaging Spectroscopy of Quiescent Solar Active Regions with NuSTAR. *Astrophys. J. Lett.*, 820:L14, March 2016.

[68] I. G. Hannah and E. P. Kontar. Differential emission measures from the regularized inversion of Hinode and SDO data. *Astron. Astrophys.*, 539:A146, March 2012.

[69] C. J. Hansen and S. D. Kawaler. Stellar Interiors: Physical Principles, Structure, and Evolution, volume XIII. Springer-Verlag, Berlin Heidelberg New York, 1st edition, 00/1994 1994. JILA Pub. 5220.

[70] F. A. Harrison, W. W. Craig, F. E. Christensen, C. J. Hailey, W. W. Zhang, S. E. Boggs, D. Stern, W. R. Cook, K. Forster, P. Giommi, B. W. Grefenstette, Y. Kim, T. Kitaguchi, J. E. Koglin, K. K. Madsen, P. H. Mao, H. Miyasaka, K. Mori, M. Perri, M. J. Pivovaroff, S. Puccetti, V. R. Rana, N. J. Westergaard, J. Willis, A. Zoglauer, H. An, M. Bachetti, N. M. Barrière, E. C. Bellm, V. Bhalerao, N. F. Brejnholt, F. Fuerst, C. C. Liebe, C. B. Markwardt, M. Nynka, J. K. Vogel, D. J. Walton, D. R. Wik, D. M. Alexander, L. R. Cominsky, A. E. Hornschemeier, A. Hornstrup, V. M. Kaspi, G. M. Madejski, G. Matt, S. Molendi, D. M. Smith, J. A. Tomsick, M. Ajello, D. R. Ballantyne, M. Baloković, D. Barret, F. E. Bauer, R. D. Blandford, W. N. Brandt, L. W. Brenneman, J. Chiang, D. Chakrabarty, J. Chenevez, A. Comastri, F. Dufour, M. Elvis, A. C. Fabian, D. Farrah, C. L. Fryer, E. V. Gotthelf, J. E. Grindlay, D. J. Helfand, R. Krivonos, D. L. Meier, J. M. Miller, L. Natalucci, P. Ogle, E. O. Ofek, A. Ptak, S. P. Reynolds, J. R. Rigby, G. Tagliaferri, S. E. Thorsett, E. Treister, and C. M. Urry. The Nuclear Spectroscopic Telescope Array (NuSTAR) High-energy X-Ray Mission. *Astrophys. J.*, 770:103, June 2013.

[71] G. Hass and J. E. Waylonis. Optical Constants and Reflectance and Transmittance of Evaporated Aluminum in the Visible and Ultraviolet. Journal of the Optical Society of America (1917-1983), 51:719, July 1961.

[72] Georg Hass. Reflectance and preparation of front-surface mirrors for use at various angles of incidence from the ultraviolet to the far infrared. J. Opt. Soc. Am., 72(1):27–39, Jan 1982.

[73] E. Hecht. Optics. Pearson education. Addison-Wesley, 2002.

[74] B. L. Henke, E. M. Gullikson, and J. C. Davis. X-Ray Interactions: Photoabsorption, Scattering, Transmission, and Reflection at E = 50-30,000 eV, Z = 1-92. Atomic Data and Nuclear Data Tables, 54:181–342, July 1993.

[75] John Hennessy, April D. Jewell, Kunjithapatham Balasubramanian, and Shouleh Nikzad. Ultraviolet optical properties of aluminum fluoride thin films deposited by atomic layer deposition. Journal of Vacuum Science & Technology A: Vacuum, Surfaces, and Films, 34(1):01A120, 2016.

[76] John Hennessy, Christopher S. Moore, Kunjithapatham Balasubramanian, April D. Jewell, Kevin France, and Shouleh Nikzad. Enhanced atomic layer etching of native aluminum oxide for ultraviolet optical applications. Journal of Vacuum Science & Technology A: Vacuum, Surfaces, and Films, 35(4):041512, 2017.

[77] S. M. Hill, V. J. Pizzo, C. C. Balch, D. A. Biesecker, P. Bornmann, E. Hildner, L. D. Lewis, R. N. Grubb, M. P. Husler, K. Prendergast, J. Vickroy, S. Greer, T. Defoor, D. C. Wilkinson, R. Hooker, P. Mulligan, E. Chipman, H. Bysal, J. P. Douglas, R. Reynolds, J. M. Davis, K. S. Wallace, K. Russell, K. Freestone, D. Bagdigian, T. Page, S. Kerns, R. Hoffman, S. A. Cauffman, M. A. Davis, R. Studer, F. E. Berthiaume, T. T. Saha, G. D. Berthiume, H. Farthing, and F. Zimmermann. The NOAA Goes-12 Solar X-Ray Imager (SXI) 1. Instrument, Operations, and Data. Solar Phys., 226:255–281, February 2005.

[78] S.-n. Ishikawa, L. Glesener, S. Christe, K. Ishibashi, D. H. Brooks, D. R. Williams, M. Shimojo, N. Sako, and S. Krucker. Constraining hot plasma in a non-flaring solar active region with FOXSI hard X-ray observations. Pub. Astron. Soc. Japan, 66:S15, December 2014.

[79] J.D. Jackson. Classical electrodynamics. Wiley, 1975.

[80] Christopher S. Moore April D. Jewell Shouleh Nikzad Kevin C. France Manuel A. Quijada John J. Hennessy, Kunjithapatham Balasubramanian. Performance and prospects of far ultraviolet aluminum mirrors protected by atomic layer deposition. Journal of Astronomical Telescopes, Instruments, and Systems, 2:2 – 2 – 9, 2016.

[81] R. Kano, T. Sakao, H. Hara, S. Tsuneta, K. Matsuzaki, K. Kumagai, M. Shimojo, K. Minesugi, K. Shibasaki, E. E. Deluca, L. Golub, J. Bookbinder, D. Caldwell, P. Cheimets, J. Cirtain, E. Dennis, T. Kent, and M. Weber. The Hinode X-Ray Telescope (XRT): Camera Design, Performance and Operations. Solar Phys., 249:263–279, June 2008.

[82] R. A. M. Keski-Kuha, J. I. Larruquert, J. S. Gum, and C. M. Fleetwood. Optical Coatings and Materials for Ultraviolet Space Applications. In J. A. Morse, J. M. Shull, and A. L. Kinney, editors, Ultraviolet-Optical Space Astronomy Beyond HST, volume 164 of Astronomical Society of the Pacific Conference Series, page 406, 1999.

[83] H. Kim, H.-B.-R. Lee, and W.-J. Maeng. Applications of atomic layer deposition to nanofabrication and emerging nanodevices. Thin Solid Films, 517:2563–2580, February 2009.

[84] K.-J. Kim. Characteristics of synchrotron radiation. In American Institute of Physics Conference Series, volume 184 of American Institute of Physics Conference Series, pages 565–632, April 1989.

[85] E. Marsh Udo H. Schuehle Philippe Lemaire Alan H. Gabriel Jean-Claude Vial Michael Grewing Martin H.C. Huber S. D. Jordan Arthur I. Poland Roger J. Thomas Mikhael Kuehne J. Gethyn Timothy Donald M. Hassler Oswald H. W. Siegmund Klaus Wilhelm, W. Curdt. Some design and performance features of sumer: solar ultraviolet measurements of emitted radiation, 1995.

[86] J. A. Klimchuk. On Solving the Coronal Heating Problem. Solar Phys., 234:41–77, March 2006.

[87] J. A. Klimchuk. Key aspects of coronal heating. Philosophical Transactions of the Royal Society of London Series A, 373:20140256–20140256, April 2015.

[88] G.F. Knoll. Radiation Detection and Measurement. John Wiley & Sons, 2010.

[89] K. Kobayashi, J. Cirtain, L. Golub, A. Winebarger, E. Hertz, P. Cheimets, D. Caldwell, K. Korreck, B. Robinson, P. Reardon, T. Kester, C. Griffith, and M. Young. The Marshall Grazing Incidence X-ray Spectrograph (MaGIXS). In Society of Photo-Optical Instrumentation Engineers (SPIE) Conference Series, volume 8147 of Proceedings of SPIE, page 81471M, September 2011.

[90] T. Kosugi, K. Matsuzaki, T. Sakao, T. Shimizu, Y. Sone, S. Tachikawa, T. Hashimoto, K. Minesugi, A. Ohnishi, T. Yamada, S. Tsuneta, H. Hara, K. Ichimoto, Y. Suematsu, M. Shimojo, T. Watanabe, S. Shimada, J. M. Davis, L. D. Hill, J. K. Owens, A. M. Title, J. L. Culhane, L. K. Harra, G. A. Doschek, and L. Golub. The Hinode (Solar-B) Mission: An Overview. Solar Phys., 243:3–17, June 2007.

[91] W. F. Krolikowski and W. E. Spicer. Photoemission Studies of the Noble Metals. I. Copper. Physical Review, 185:882–900, September 1969.

[92] Nasrat Raouf Shouleh Nikzad Michael Ayala Stuart Shaklan Paul Scowen Javier Del Hoyo Manuel Quijada Kunjithapatham Balasubramanian, John Hennessy. Coatings for uvoir telescope mirrors, 2015.

[93] J. M. Laming. The FIP and Inverse FIP Effects in Solar and Stellar Coronae. Living Reviews in Solar Physics, 12:2, September 2015.

[94] E. Landi and J. A. Klimchuk. On the Isothermality of Solar Plasmas. Astrophys. J., 723:320–328, November 2010.

[95] E. Langereis, S. B. S. Heil, H. C. M. Knoops, W. Keuning, M. C. M. van de Sanden, and W. M. M. Kessels. TOPICAL REVIEW: In situ spectroscopic ellipsometry as a versatile tool for studying atomic layer deposition. Journal of Physics D Applied Physics, 42(7):073001, April 2009.

[96] Juan I Larruquert and Ritva A.M Keski-Kuha. Far ultraviolet optical properties of mgf2 films deposited by ion-beam sputtering and their application as protective coatings for al. Optics Communications, 215(1):93 – 99, 2003.

[97] Younghee Lee, Jaime W. DuMont, Andrew S. Cavanagh, and Steven M. George. Atomic layer deposition of alf3 using trimethylaluminum and hydrogen fluoride. The Journal of Physical Chemistry C, 119(25):14185–14194, 2015.

[98] Younghee Lee, Jaime W. DuMont, and Steven M. George. Trimethylaluminum as the metal precursor for the atomic layer etching of al2o3 using sequential, self-limiting thermal reactions. Chemistry of Materials, 28(9):2994–3003, 2016.

[99] Younghee Lee and Steven M. George. Atomic layer etching of al2o3 using sequential, self-limiting thermal reactions with sn(acac)2 and hydrogen fluoride. ACS Nano, 9(2):2061–2070, 2015. PMID: 25604976.

[100] J. R. Lemen, A. M. Title, D. J. Akin, P. F. Boerner, C. Chou, J. F. Drake, D. W. Duncan, C. G. Edwards, F. M. Friedlaender, G. F. Heyman, N. E. Hurlburt, N. L. Katz, G. D. Kushner, M. Levay, R. W. Lindgren, D. P. Mathur, E. L. McFeaters, S. Mitchell, R. A. Rehse, C. J. Schrijver, L. A. Springer, R. A. Stern, T. D. Tarbell, J.-P. Wuelser, C. J. Wolfson, C. Yanari, J. A. Bookbinder, P. N. Cheimets, D. Caldwell, E. E. Deluca, R. Gates, L. Golub, S. Park, W. A. Podgorski, R. I. Bush, P. H. Scherrer, M. A. Gummin, P. Smith, G. Auker, P. Jerram, P. Pool, R. Soufli, D. L. Windt, S. Beardsley, M. Clapp, J. Lang, and N. Waltham. The Atmospheric Imaging Assembly (AIA) on the Solar Dynamics Observatory (SDO). Solar Phys., 275:17–40, January 2012.

[101] R. P. Lin, B. R. Dennis, G. J. Hurford, D. M. Smith, A. Zehnder, P. R. Harvey, D. W. Curtis, D. Pankow, P. Turin, M. Bester, A. Csillaghy, M. Lewis, N. Madden, H. F. van Beek, M. Appleby, T. Raudorf, J. McTiernan, R. Ramaty, E. Schmahl, R. Schwartz, S. Krucker, R. Abiad, T. Quinn, P. Berg, M. Hashii, R. Sterling, R. Jackson, R. Pratt, R. D. Campbell, D. Malone, D. Landis, C. P. Barrington-Leigh, S. Slassi-Sennou, C. Cork, D. Clark, D. Amato, L. Orwig, R. Boyle, I. S. Banks, K. Shirey, A. K. Tolbert, D. Zarro, F. Snow, K. Thomsen, R. Henneck, A. McHedlishvili, P. Ming, M. Fivian, J. Jordan, R. Wanner, J. Crubb, J. Preble, M. Matranga, A. Benz, H. Hudson, R. C. Canfield, G. D. Holman, C. Crannell, T. Kosugi, A. G. Emslie, N. Vilmer, J. C. Brown, C. Johns-Krull, M. Aschwanden, T. Metcalf, and A. Conway. The Reuven Ramaty High-Energy Solar Spectroscopic Imager (RHESSI). Solar Phys., 210:3–32, November 2002.

[102] L. J. Lingg. Lanthanide Trifluoride Thin Films. PhD thesis, THE UNIVERSITY OF ARIZONA., 1990.

[103] R. Lionello, M. Velli, C. Downs, J. A. Linker, and Z. Mikić. Application of a Solar Wind Model Driven by Turbulence Dissipation to a 2D Magnetic Field Configuration. *Astrophys. J.*, 796:111, December 2014.

[104] W. Liu, V. Petrosian, B. R. Dennis, and Y. W. Jiang. Double Coronal Hard and Soft X-Ray Source Observed by RHESSI: Evidence for Magnetic Reconnection and Particle Acceleration in Solar Flares. *Astrophys. J.*, 676:704–716, March 2008.

[105] R. P. Madden, L. R. Canfield, and G. Hass. On the vacuum-ultraviolet reflectance of evaporated aluminum before and during oxidation∗. J. Opt. Soc. Am., 53(5):620–625, May 1963.

[106] D. C. Martin, J. Fanson, D. Schiminovich, P. Morrissey, P. G. Friedman, T. A. Barlow, T. Conrow, R. Grange, P. N. Jelinsky, B. Milliard, O. H. W. Siegmund, L. Bianchi, Y.-I. Byun, J. Donas, K. Forster, T. M. Heckman, Y.-W. Lee, B. F. Madore, R. F. Malina, S. G. Neff, R. M. Rich, T. Small, F. Surber, A. S. Szalay, B. Welsh, and T. K. Wyder. The Galaxy Evolution Explorer: A Space Ultraviolet Survey Mission.

[107] J. P. Mason, T. N. Woods, A. Caspi, P. C. Chamberlin, C. Moore, A. Jones, R. Kohnert, X. Li, S. Palo, and S. C. Solomon. Miniature X-Ray Solar Spectrometer: A Science-Oriented, University 3U CubeSat. Journal of Spacecraft and Rockets, 53:328–339, March 2016.

[108] John J. Bacinski Daniela Calzetti John E. Krist John W. MacKenty J. Piquero Massimo Stiavelli Massimo Robberto, Anand Sivaramakrishnan. Performance of hst as an infrared telescope, 2000.

[109] Shouleh Nikzad Matthew Beasley, Frank Greer. Progress in new ultraviolet reflective coating techniques, 2011.

[110] D. M. Meyer, M. Jura, and J. A. Cardelli. The Definitive Abundance of Interstellar Oxygen. *Astrophys. J.*, 493:222, January 1998.

[111] M. Miceli, F. Reale, S. Gburek, S. Terzo, M. Barbera, A. Collura, J. Sylwester, M. Kowalinski, P. Podgorski, and M. Gryciuk. X-ray emitting hot plasma in solar active regions observed by the SphinX spectrometer. *Astron. Astrophys.*, 544:A139, August 2012.

[112] C. S. Moore, J. Hennessy, A. D. Jewell, S. Nikzad, and K. France. Recent developments and results of new ultraviolet reflective mirror coatings. In Space Telescopes and Instrumentation 2014: Ultraviolet to Gamma Ray, volume 9144 of *Proceedings of SPIE*, page 91444H, July 2014.

[113] C. S. Moore, J. Hennessy, A. D. Jewell, S. Nikzad, and K. France. Atomic Layer Deposited (ALD) coatings for future astronomical telescopes: recent developments. In Advances in Optical and Mechanical Technologies for Telescopes and Instrumentation II, volume 9912 of *Proceedings of SPIE*, page 99122U, July 2016.

[114] C. S. Moore, J. Hennessy, E. Kersgaard, A. D. Jewell, S. Nikzad, and K. France. Current progress in the characterization of atomic layer deposited AlF$_3$ for future astronomical ultraviolet mirror coatings. In UV, X-Ray, and Gamma-Ray Space Instrumentation for Astronomy XIX, volume 9601 of *Proceedings of SPIE*, page 96010X, August 2015.

[115] C. S. Moore, T. N. Woods, A. Caspi, and J. P. Mason. The Miniature X-ray Solar Spectrometer (MinXSS) CubeSats: spectrometer characterization techniques, spectrometer capabilities, and solar science objectives. In Space Telescopes and Instrumentation 2016: Ultraviolet to Gamma Ray, volume 9905 of *Proceedings of SPIE*, page 990509, July 2016.

[116] H. W. Moos, W. C. Cash, L. L. Cowie, A. F. Davidsen, A. K. Dupree, P. D. Feldman, S. D. Friedman, J. C. Green, R. F. Green, C. Gry, J. B. Hutchings, E. B. Jenkins, J. L. Linsky, R. F. Malina, A. G. Michalitsianos, B. D. Savage, J. M. Shull, O. H. W. Siegmund, T. P. Snow, G. Sonneborn, A. Vidal-Madjar, A. J. Willis, B. E. Woodgate, D. G. York, T. B. Ake, B.-G. Andersson, J. P. Andrews, R. H. Barkhouser, L. Bianchi, W. P. Blair, K. R. Brownsberger, A. N. Cha, P. Chayer, S. J. Conard, A. W. Fullerton, G. A. Gaines, R. Grange, M. A. Gummin, G. Hebrard, G. A. Kriss, J. W. Kruk, D. Mark, D. K. McCarthy, C. L. Morbey, R. Murowinski, E. M. Murphy, W. R. Oegerle, R. G. Ohl, C. Oliveira, S. N. Osterman, D. J. Sahnow, M. Saisse, K. R. Sembach, H. A. Weaver, B. Y. Welsh, E. Wilkinson, and W. Zheng. Overview of the Far Ultraviolet Spectroscopic Explorer Mission. *Astrophys. J. Lett.*, 538:L1–L6, July 2000.

[117] N. Narukage, T. Sakao, R. Kano, H. Hara, M. Shimojo, T. Bando, F. Urayama, E. Deluca, L. Golub, M. Weber, P. Grigis, J. Cirtain, and S. Tsuneta. Coronal-Temperature-Diagnostic Capability of the Hinode/ X-Ray Telescope Based on Self-Consistent Calibration. *Solar Phys.*, 269:169–236, March 2011.

[118] N. Narukage, T. Sakao, R. Kano, M. Shimojo, A. Winebarger, M. Weber, and K. K. Reeves. Coronal-Temperature-Diagnostic Capability of the Hinode/ X-Ray Telescope Based on Self-consistent Calibration. II. Calibration with On-Orbit Data. *Solar Phys.*, 289:1029–1042, March 2014.

[119] Å. Nordlund, R. F. Stein, and M. Asplund. Solar Surface Convection. Living Reviews in Solar Physics, 6:2, April 2009.

[120] Cosmic Origins Program Office. Cosmic origins program annual technology report, https://ntrs.nasa.gov/search.jsp?r=20160011973. Technical report, NASA, 2016.

[121] R. G. Ohl, R. H. Barkhouser, S. J. Conard, S. D. Friedman, J. Hampton, H. W. Moos, P. Nikulla, C. M. Oliveira, and T. T. Saha. Performance of the Far Ultraviolet Spectroscopic Explorer mirror assemblies. In S. Fineschi, C. M. Korendyke, O. H. Siegmund, and B. E. Woodgate, editors, Instrumentation for UV/EUV Astronomy and Solar Missions, volume 4139 of Proc.SPIE, pages 137–148, December 2000.

[122] B. D. Oppenheimer, R. Davé, N. Katz, J. A. Kollmeier, and D. H. Weinberg. The intergalactic medium over the last 10 billion years - II. Metal-line absorption and physical conditions. *Mon. Not. Roy. Astron. Soc.*, 420:829–859, February 2012.

[123] E. D. Palik. Handbook of optical constants of solids III. Academic Press, 1998.

[124] E. N. Parker. Nanoflares and the solar X-ray corona. *Astrophys. J.*, 330:474–479, July 1988.

[125] M. D. Perrin, J. R. Graham, J. E. Larkin, S. Wiktorowicz, J. Maire, S. Thibault, M. P. Fitzgerald, R. Doyon, B. A. Macintosh, D. T. Gavel, B. R. Oppenheimer, D. W. Palmer, L. Saddlemyer, and J. K. Wallace. Imaging polarimetry with the Gemini Planet Imager. In Adaptive Optics Systems II, volume 7736 of *Proceedings of SPIE*, page 77365R, July 2010.

[126] W. D. Pesnell, B. J. Thompson, and P. C. Chamberlin. The Solar Dynamics Observatory (SDO). *Solar Phys.*, 275:3–15, January 2012.

[127] N. Pinna and M. Knez. Atomic Layer Deposition of Nanostructured Materials. Wiley, 2012.

[128] M. A. Quijada, J. Del Hoyo, and S. Rice. Enhanced far-ultraviolet reflectance of MgF_2 and LiF over-coated Al mirrors. In Space Telescopes and Instrumentation 2014: Ultraviolet to Gamma Ray, volume 9144 of *Proceedings of SPIE*, page 91444G, July 2014.

[129] G. A. P. Rayet. . Compt. Rend. 67, 757, 67, 1868.

[130] F. Reale, P. Testa, J. A. Klimchuk, and S. Parenti. Evidence of Widespread Hot Plasma in a Nonflaring Coronal Active Region from Hinode/X-Ray Telescope. *Astrophys. J.*, 698:756–765, June 2009.

[131] R. H. Redus, A. C. Huber, and D. J. Sperry. Dead time correction in the dp5 digital pulse processor. In 2008 IEEE Nuclear Science Symposium Conference Record, pages 3416–3420, Oct 2008.

[132] D. Ristau, S. Gunster, S. Bosch, A. Duparre, E. Masetti, J. Ferre-Borrull, G. Kiriakidis, F. Peiro, E. Quesnel, and A. Tikhonravov. Ultraviolet optical and microstructural properties of MgF2 and LaF3 coatings deposited by ion-beam sputtering and boat and electron-beam evaporation. *Applied Optics*, 41:3196–3204, June 2002.

[133] D. J. Sahnow, H. W. Moos, T. B. Ake, J. Andersen, B.-G. Andersson, M. Andre, D. Artis, A. F. Berman, W. P. Blair, K. R. Brownsberger, H. M. Calvani, P. Chayer, S. J. Conard, P. D. Feldman, S. D. Friedman, A. W. Fullerton, G. A. Gaines, W. C. Gawne, J. C. Green, M. A. Gummin, T. B. Jennings, J. B. Joyce, M. E. Kaiser, J. W. Kruk, D. J. Lindler, D. Massa, E. M. Murphy, W. R. Oegerle, R. G. Ohl, B. A. Roberts, M. L. Romelfanger, K. C. Roth, R. Sankrit, K. R. Sembach, R. L. Shelton, O. H. W. Siegmund, C. J. Silva, G. Sonneborn, S. R. Vaclavik, H. A. Weaver, and

E. Wilkinson. On-Orbit Performance of the Far Ultraviolet Spectroscopic Explorer Satellite. *Astrophys. J. Lett.*, 538:L7–L11, July 2000.

[134] J. Sánchez Almeida and M. Martínez González. The Magnetic Fields of the Quiet Sun. In J. R. Kuhn, D. M. Harrington, H. Lin, S. V. Berdyugina, J. Trujillo-Bueno, S. L. Keil, and T. Rimmele, editors, Solar Polarization 6, volume 437 of Astronomical Society of the Pacific Conference Series, page 451, April 2011.

[135] C. E. Schlemm, R. D. Starr, G. C. Ho, K. E. Bechtold, S. A. Hamilton, J. D. Boldt, W. V. Boynton, W. Bradley, M. E. Fraeman, R. E. Gold, J. O. Goldsten, J. R. Hayes, S. E. Jaskulek, E. Rossano, R. A. Rumpf, E. D. Schaefer, K. Strohbehn, R. G. Shelton, R. E. Thompson, J. I. Trombka, and B. D. Williams. The X-Ray Spectrometer on the MESSENGER Spacecraft. *Space Sci. Rev.*, 131:393–415, August 2007.

[136] J. T. Schmelz, M. Asgari-Targhi, G. M. Christian, R. S. Dhaliwal, and S. Pathak. Hot Plasma from Solar Active Region Cores: a Test of AC and DC Coronal Heating Models? *Astrophys. J.*, 806:232, June 2015.

[137] J. T. Schmelz, V. L. Kashyap, S. H. Saar, B. R. Dennis, P. C. Grigis, L. Lin, E. E. De Luca, G. D. Holman, L. Golub, and M. A. Weber. Some Like It Hot: Coronal Heating Observations from Hinode X-ray Telescope and RHESSI. *Astrophys. J.*, 704:863–869, October 2009.

[138] J. T. Schmelz, D. V. Reames, R. von Steiger, and S. Basu. Composition of the Solar Corona, Solar Wind, and Solar Energetic Particles. *Astrophys. J.*, 755:33, August 2012.

[139] J. T. Schmelz, S. H. Saar, E. E. DeLuca, L. Golub, V. L. Kashyap, M. A. Weber, and J. A. Klimchuk. Hinode X-Ray Telescope Detection of Hot Emission from Quiescent Active Regions: A Nanoflare Signature? *Astrophys. J. Lett.*, 693:L131–L135, March 2009.

[140] J. Schou, P. H. Scherrer, R. I. Bush, R. Wachter, S. Couvidat, M. C. Rabello-Soares, R. S. Bogart, J. T. Hoeksema, Y. Liu, T. L. Duvall, D. J. Akin, B. A. Allard, J. W. Miles, R. Rairden, R. A. Shine, T. D. Tarbell, A. M. Title, C. J. Wolfson, D. F. Elmore, A. A. Norton, and S. Tomczyk. Design and Ground Calibration of the Helioseismic and Magnetic Imager (HMI) Instrument on the Solar Dynamics Observatory (SDO). *Solar Phys.*, 275:229–259, January 2012.

[141] P. A. Scowen, T. Tripp, M. Beasley, D. Ardila, B.-G. Andersson, J. Maíz Apellániz, M. Barstow, L. Bianchi, D. Calzetti, M. Clampin, C. J. Evans, K. France, M. García García, A. Gomez de Castro, W. Harris, P. Hartigan, J. C. Howk, J. Hutchings, J. Larruquert, C. F. Lillie, G. Matthews, S. McCandliss, R. Polidan, M. R. Perez, M. Rafelski, I. U. Roederer, H. Sana, W. T. Sanders, D. Schiminovich, H. Thronson, J. Tumlinson, J. Vallerga, and A. Wofford. Finding the UV-Visible Path Forward: Proceedings of the Community Workshop to Plan the Future of UV/Visible Space Astrophysics. *Pub. Astron. Soc. Pac.*, 129(7):076001, July 2017.

[142] J. D. Scudder. Why all stars should possess circumstellar temperature inversions. *Astrophys. J.*, 398:319–349, October 1992.

[143] A. Seechi. . Le Soleil, 2nd edn., Gauthier-Villars, Paris, 1875.

[144] K. Sembach, D. Calzetti, D. Ebbets, J. Green, M. Greenhouse, S. Heap, L. Hillenbrand, M. Kaiser, J. Lazio, and P. Marcum. Cosmic origins program analysis group (copag) report to paul hertz regarding large mission concepts to study for the 2020 decadal survey. Technical report, NASA, 2015.

[145] P.-S. Shaw, U. Arp, R. D. Saunders, D.-J. Shin, H. W. Yoon, C. E. Gibson, Z. Li, A. C. Parr, and K. R. Lykke. Synchrotron radiation-based irradiance calibration from 200 to 400 nm at the Synchrotron Ultraviolet Radiation Facility III. *Applied Optics*, 46:25–35, January 2007.

[146] J. Sylwester, M. Kowalinski, S. Gburek, M. Siarkowski, S. Kuzin, F. Farnik, F. Reale, K. J. H. Phillips, J. Bakała, M. Gryciuk, P. Podgorski, and B. Sylwester. SphinX Measurements of the 2009 Solar Minimum X-Ray Emission. *Astrophys. J.*, 751:111, June 2012.

[147] S. Tsuneta, K. Ichimoto, Y. Katsukawa, S. Nagata, M. Otsubo, T. Shimizu, Y. Suematsu, M. Nakagiri, M. Noguchi, T. Tarbell, A. Title, R. Shine, W. Rosenberg, C. Hoffmann, B. Jurcevich, G. Kushner, M. Levay, B. Lites, D. Elmore, T. Matsushita, N. Kawaguchi, H. Saito, I. Mikami, L. D. Hill, and J. K. Owens. The Solar Optical Telescope for the Hinode Mission: An Overview. *Solar Phys.*, 249:167–196, June 2008.

[148] I. Ugarte-Urra and H. P. Warren. Is Active Region Core Variability Age Dependent? *Astrophys. J.*, 761:21, December 2012.

[149] A. A. van Ballegooijen, M. Asgari-Targhi, and M. A. Berger. On the Relationship Between Photospheric Footpoint Motions and Coronal Heating in Solar Active Regions. *Astrophys. J.*, 787:87, May 2014.

[150] A. A. van Ballegooijen, M. Asgari-Targhi, S. R. Cranmer, and E. E. DeLuca. Heating of the Solar Chromosphere and Corona by Alfvén Wave Turbulence. *Astrophys. J.*, 736:3, July 2011.

[151] B. van der Holst, I. V. Sokolov, X. Meng, M. Jin, W. B. Manchester, IV, G. Tóth, and T. I. Gombosi. Alfvén Wave Solar Model (AWSoM): Coronal Heating. *Astrophys. J.*, 782:81, February 2014.

[152] A. Vidal-Madjar and R. Ferlet. Ultraviolet Studies of Extra-Solar Planets. In M. E. van Steenberg, G. Sonneborn, H. W. Moos, and W. P. Blair, editors, American Institute of Physics Conference Series, volume 1135 of American Institute of Physics Conference Series, pages 268–277, May 2009.

[153] H. P. Warren and D. H. Brooks. The Temperature and Density Structure of the Solar Corona. I. Observations of the Quiet Sun with the EUV Imaging Spectrometer on Hinode. _Astrophys. J._, 700:762–773, July 2009.

[154] M. A. Weber, E. E. Deluca, L. Golub, and A. L. Sette. Temperature diagnostics with multichannel imaging telescopes. In A. V. Stepanov, E. E. Benevolenskaya, and A. G. Kosovichev, editors, Multi-Wavelength Investigations of Solar Activity, volume 223 of IAU Symposium, pages 321–328, 2004.

[155] S. M. White, R. J. Thomas, and R. A. Schwartz. Updated Expressions for Determining Temperatures and Emission Measures from Goes Soft X-Ray Measurements. _Solar Phys._, 227:231–248, April 2005.

[156] K. G. Widing and U. Feldman. On the Rate of Abundance Modifications versus Time in Active Region Plasmas. _Astrophys. J._, 555:426–434, July 2001.

[157] A. R. Winebarger, H. P. Warren, J. T. Schmelz, J. Cirtain, F. Mulu-Moore, L. Golub, and K. Kobayashi. Defining the "Blind Spot" of Hinode EIS and XRT Temperature Measurements. _Astrophys. J. Lett._, 746:L17, February 2012.

[158] T. N. Woods, A. Caspi, P. C. Chamberlin, A. Jones, R. Kohnert, J. P. Mason, C. S. Moore, S. Palo, C. Rouleau, S. C. Solomon, J. Machol, and R. Viereck. New Solar Irradiance Measurements from the Miniature X-Ray Solar Spectrometer CubeSat. _Astrophys. J._, 835:122, February 2017.

[159] T. N. Woods, F. G. Eparvier, R. Hock, A. R. Jones, D. Woodraska, D. Judge, L. Didkovsky, J. Lean, J. Mariska, H. Warren, D. McMullin, P. Chamberlin, G. Berthiaume, S. Bailey, T. Fuller-Rowell, J. Sojka, W. K. Tobiska, and R. Viereck. Extreme Ultraviolet Variability Experiment (EVE) on the Solar Dynamics Observatory (SDO): Overview of Science Objectives, Instrument Design, Data Products, and Model Developments. _Solar Phys._, 275:115–143, January 2012.

[160] J. J. Yeh and I. Lindau. Atomic Subshell Photoionization Cross Sections and Asymmetry Parameters: 1 <= Z <= 103. Atomic Data and Nuclear Data Tables, 32:1, 1985.

[161] P. R. Young, K. P. Dere, E. Landi, G. Del Zanna, and H. E. Mason. The CHIANTI atomic database. Journal of Physics B Atomic Molecular Physics, 49(7):074009, April 2016.

[162] S. Zeighami, A. R. Ahangarzadeh Maralani, E. Tavabi, and A. Ajabshirizadeh. Evidence of Energy Supply by Active-Region Spicules to the Solar Atmosphere. _Solar Phys._, 291:847–858, March 2016.

[163] B. Ziaja, R. A. London, and J. Hajdu. Ionization by impact electrons in solids: Electron mean free path fitted over a wide energy range. Journal of Applied Physics, 99(3):033514–033514–9, February 2006.

Appendix   A

Reflectance Calculations

The reflectance calculations displayed throughout this entire dissertation is described in this Appendix. The matrix calculations are extremely useful for multiple film systems. We will start with discussing the power of thin films in modifying the optical properties of materials.

A.1   Matrix Formulation for Optical Calculations

Thin films modify the surface admittance of a substrate, which is the ratio of the tangential components of the magnetic to electric fields *at* the interface between two media, $Y = \frac{H}{E}$. Thin films can modify the optical properties via optical interference effects (vs. thermal, mechanical, an applied voltage, applied magnetic field, etc.). The phase shift induced upon light transversing a thin film of thickness, d_j, is calculated by Equation A.1.

$$
\begin{aligned}
\delta_j &= \frac{2\pi d_j \sqrt{n_j^2 - k_j^2 - n_0^2 \sin^2 \theta_0 - 2i n_j k_j}}{\lambda} \\
&= \frac{2\pi n_j d_j \cos \theta_j}{\lambda}, \quad for \quad k_j = 0
\end{aligned}
\tag{A.1}
$$

Thin film effects are important for this dissertation, but we will describe a process to calculate the transmittance and reflectance of any combination of films on top of a substrate in the following sections. First, we must set up a basis set for our calculations. We can choose an orthogonal basis set defined by the plane of incidence for the incident, transmitted and

reflected light propagation directions. This theory, interprets the majority of the light energy propagating as rays. The wave nature of light is used for the computation of interference effects. Here we follow the derivations in Hecht 2002 [73] and Angus Macleod Optics Notes https://www.thinfilmcenter.com/ocdm.php with slight modifications.

First, we must define the plane of incidence, which is the plane containing the incident, reflected and transmitted rays. The plane of incidence is perpendicular to the defined interface between two media (see Figure A.1). The normal of the interface between the two media is used to define the angles of incidence, θ_i, reflection, θ_r, and transmission θ_t. These angles are related to one another (for adjacent media) by the angle modified optical constants, η via Snell's law (see Equation A.4).

$$\eta_s = (n - ik)\cos\theta \tag{A.2}$$

$$\eta_p = \frac{(n - ik)}{\cos\theta} \tag{A.3}$$

$$\eta_0 \sin\theta_0 = \eta_1 \sin\theta_1 = ... = \eta \sin\theta \tag{A.4}$$

Next, we can compute the photon induced tangential electric and magnetic field amplitudes *at* the interface between two media, which we will label a and b. We shall focus on the amplitudes on the forward side, + and the back side, - of the interface. The amplitudes on each side of the interface can be combined and used to calculate the the reflectance, R, transmitance, T and absorptance, A in a thin film system.

$$\mathbf{E} = E^+ + E^- \tag{A.5}$$

$$\mathbf{H} = H^+ - H^- = \eta(E^+ - E^-) \tag{A.6}$$
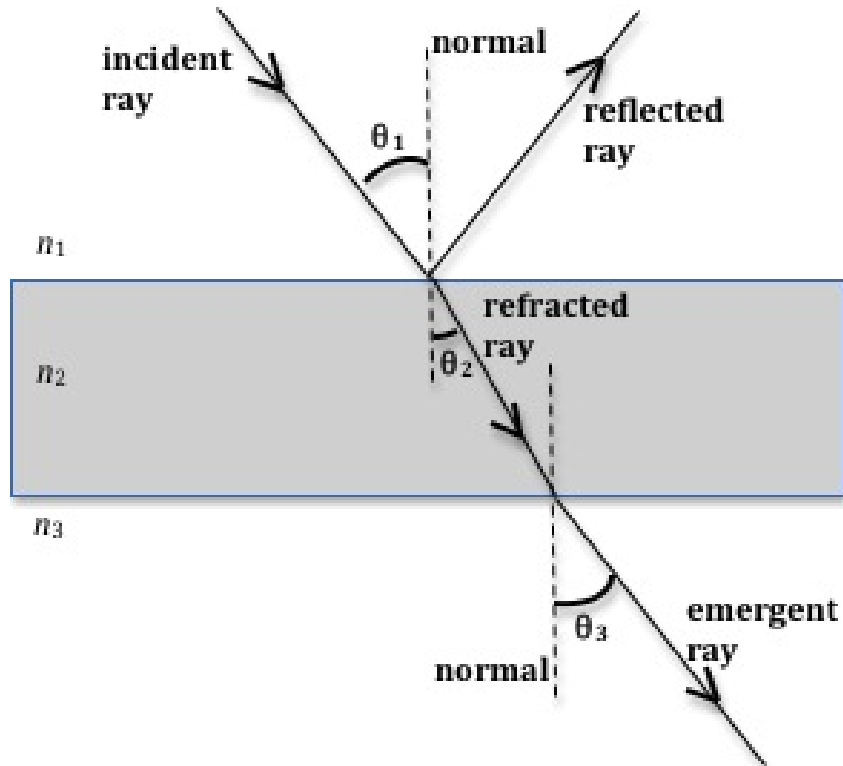
Figure A.1: Diagram describing the ray approximation of light propagation from medium with with index of refraction, n_1 and angle of incidence, θ_1, the reflected angle from the normal, θ_1, in the secondary medium with, n_2, and angle of propagation, θ_2, and a third medium with n_3, and angle of propagation, θ_3. The plane in which the incident and reflected ray propagate is called the plane of incidence. Image credit: http://www.webassign.net/ labsgraceperiod/ncsulcpem2/lab_6/manual.html.

We can solve for the positive and negative labeled waves (forward and backward side of the interface *at* the interface from the previous expressions, in

$$E_b^+ = 0.5\left(\mathbf{E}_b + \frac{\mathbf{H}_b}{\eta} \right) \tag{A.7}$$

$$E_b^- = 0.5\left(\mathbf{E}_b - \frac{\mathbf{H}_b}{\eta} \right) \tag{A.8}$$

$$E_a^+ = E_b^+ e^{i\delta} \tag{A.9}$$

$$E_a^- = E_b^- e^{-i\delta} \tag{A.10}$$

then plug the expressions in Equation A.7, Equation A.8, Equation A.9, and Equation A.10 into Equation A.5 and Equation A.6. After rearranging terms and applying Euler's equation, $e^{i\phi} = \cos\phi + i\sin\phi$ we rewrite the exponentials with the phase differences, δ, to arrive at the expressions below for the electric and magnetic field amplitudes between the interface of medium a and medium b.

$$\mathbf{E}_a = \cos\delta \cdot \mathbf{E}_b + i\frac{\sin\delta}{\eta} \cdot \mathbf{H}_b \tag{A.11}$$

$$\mathbf{H}_a = i\eta\sin\delta \cdot \mathbf{E}_b + i\cos\delta \cdot \mathbf{H}_b \tag{A.12}$$

The left sides of Equation A.11 and Equation A.12 only is dependent upon the medium a and the expressions on the right sides of the same equations only are variables of the medium b. Thus, the linear relationship allows a matrix formulation to be implemented.

$$\begin{bmatrix} \mathbf{E}_a \\ \mathbf{H}_a \end{bmatrix} = \begin{bmatrix} \cos\delta_j & \frac{i\sin\delta_j}{\eta_j} \\ i\eta_j\sin\delta_j & \cos\delta_j \end{bmatrix} \begin{bmatrix} \mathbf{E}_b \\ \mathbf{H}_b \end{bmatrix}$$

The equation above is the matrix expression relation the tangential wave amplitudes of medium a and medium b at their respective interface. The matrix relating the media wave amplitudes is only dependent upon the thin film material properties, namely the optical constants, η and the phase shift induced, δ. The matrix dependent only on η and δ is called the characteristic matrix. The separability of the film properties (characteristic matrix) from the wave amplitudes allows the separate computation of the influence induced by *any number of films* between a medium a and medium b. Thus, we can calculate an 'effective' characteristic matrix of a thin film system (composed of many thin films, by the product of all the characteristic matrices). THis simplicity promotes efficient and expedient calculation

of optical properties (reflectance, transmittance and absorptance of a series thin film on a substrate.

$$\begin{bmatrix} B \\ C \end{bmatrix} = \left\{ \prod_{j=1}^{N} \begin{bmatrix} \cos\delta_j & \frac{i\sin\delta_j}{\eta_j} \\ i\eta_j\sin\delta_j & \cos\delta_j \end{bmatrix} \right\} \begin{bmatrix} 1 \\ \eta_{sub} \end{bmatrix}$$

where

$$B = \frac{\mathbf{E}_a}{\mathbf{E}_b} \tag{A.13}$$

plus,

$$C = \frac{\mathbf{H}_a}{\mathbf{E}_b} \tag{A.14}$$

and,

$$\eta_{sub} = \frac{\mathbf{H}_b}{\mathbf{E}_b} \tag{A.15}$$

The matrix equation above is for q number of films on top of a substrate with optical constants η_{sub}. This is the matrix calculation process used in this dissertation. The new variables B and C are the normalized tangential electric and magnetic field amplitudes respectively.

$$\rho = \frac{\eta_0 B - C}{\eta_0 B + C} \tag{A.16}$$

ρ is essential the Fresnel Coefficient for the entire thin film system and substrate. η_0 is the optical constants from the incident medium (first medium) used in the calculation. In general, because η and δ can be complex (have a real and imaginary component), ρ can be complex. We can multiply ρ by its complex conjugate, ρ^* to compute the reflectance, R.

$$R = \frac{I_r\cos\theta_r}{I_i\cos\theta_i} = \rho\rho^* = \left(\frac{\eta_0 B - C}{\eta_0 B + C}\right)\left(\frac{\eta_0 B - C}{\eta_0 B + C}\right)^* \tag{A.17}$$

Equation A.17 yields the reflected light intensity in the tangential component with respect to the interface. This incorporates the projected illuminated area, which is equal for the incident and reflected light beams because the medium is the same, $\theta_r = \theta_i$. Thus, the area conceals out and the calculation is simplified. For the transmittance calculation, the media have different optical constants, thus different projected areas for oblique angles of incidence, $\theta_t \neq \theta_i$. Thus the transmittance calculation is a little different.

$$T = \frac{I_t \cos \theta_t}{I_i \cos \theta_i} = \frac{4\eta_0 Real(\eta_{sub})}{(\eta_0 B + C)(\eta_0 B + C)^*} \tag{A.18}$$

In lossy media ($k \neq 0$), absorption will occur during the light passage through the thin films. Following conservation of energy, an approximate expression for the absorptance of a 'perfect' (homogeneous, low surface roughness, minimal diffuse scattering, etc.) thin film can be calculated from A = 1 - R - T. Where R is from Equation A.17 and T is from Equation A.18. Setting the film thickness equal to 0 to understand the general effects changing n or k have on reflectance. Figure A.2 demonstrates that n being equal between the two media load to 100% transmittance, and any deviations from this equality results in a mismatch and light reflection. k equal to zero has no light loss in the media, but increases in k leads directly to light absorption. Some metals, have n < 1 and k > 1, which leads to large quantities of light being reflected, but a shallow skin depth (light penetration depth into the media). Thus metals, are great reflectors of light, but will always result in light loss, due to the photon induced surface currents from free electrons being dissipated by collisions and converted to heat.
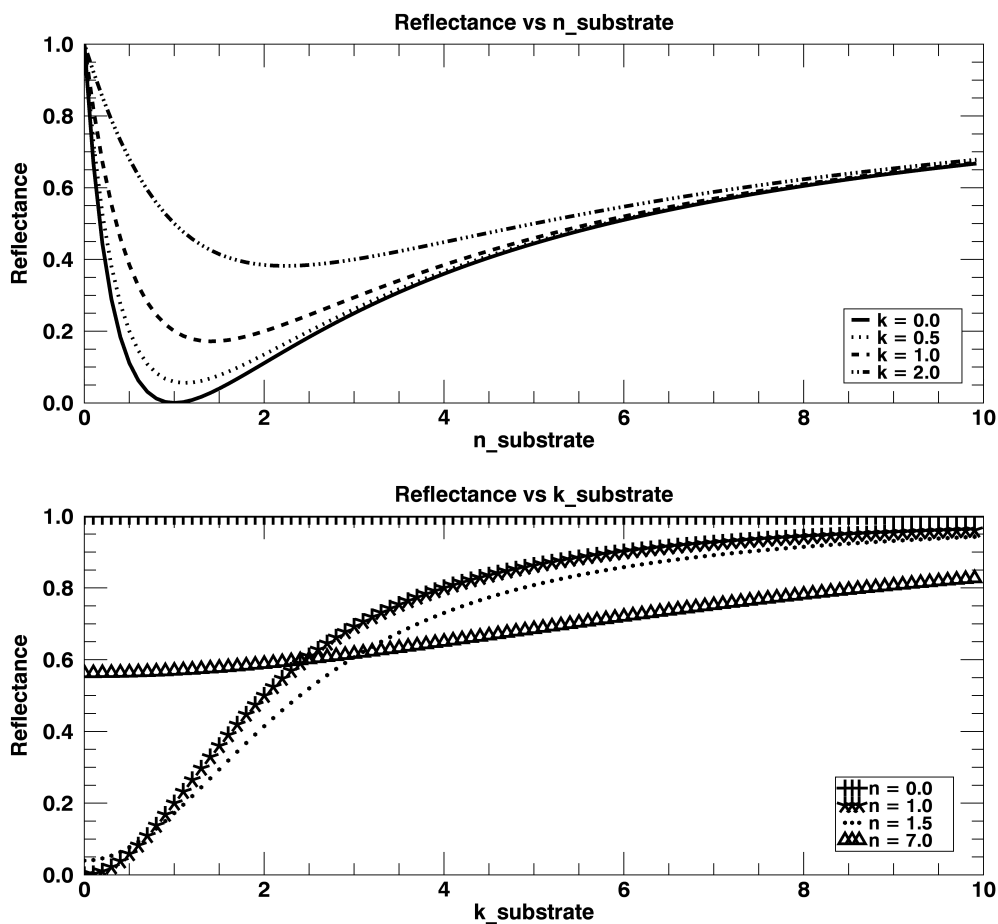
Figure A.2: Top Plot: Theoretical reflectance as a function of n vs. fixed k in air. For k = 0 and n = 1.0, the reflectance vanishes because n = n_{air}. Bottom Plot: Theoretical reflectance as a function of k vs. fixed n in air. For n = 0 the reflectance is 100% for all k, because the numerator and the denominator are the same and cancel out when n = 0.

Appendix B

Spectroscopic Ellipsometry

The JPL MDL HORIBA UVISEL2 Polarization/Phase Modulation (PM) Spectroscopic Ellipsometer can determine the ellipsometric angles of psi (Ψ) and delta (Δ) from measurements of I_S and I_C. Ψ is related to the ratio of the modulus of the Fresnel coefficients for p and s states ($\tan \Psi = |r_p|/|r_s|$) and is indicative of the polarized reflection amplitudes. Figure B.1 displays the SE layout used to conduct ex-situ measurements of ALD AlF$_3$ film optical properties. The light source is a Xenon arc lamp, which emits light towards a polarizer. This polarized light reflects off the sample, undergoes a change in polarization state (which is the measured output by the SE), passes through a Photoelastic Modulator (PEM; the Modulator) and passes through another polarizer (the Analyzer) undergoing two more possible polarization state changes. The resultant intensity is dispersed by a monochromator and subsequently measured by photomultipliers in the UV-Vis and an InGaAs detector in the IR.
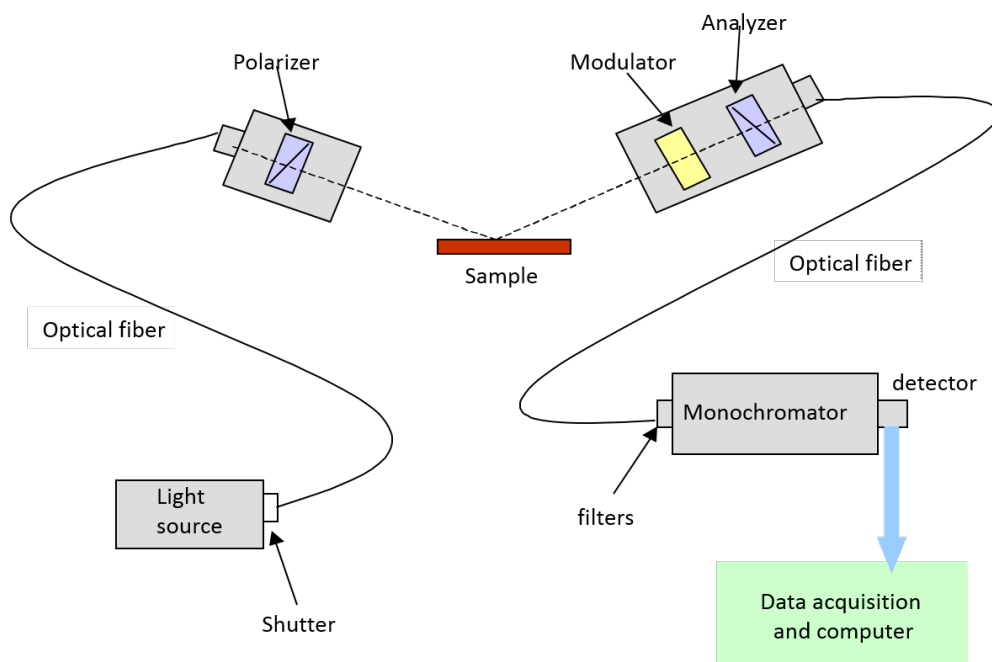
Figure B.1: Reprinted with permission from HORIBA and from Moore et al. 2015 [114]: HORIBA UVISEL2 Spectroscopic Ellipsometer (SE) Layout. This SE uses Polarization/Phase Modulation (PM) to conduct ambient measurements with a Xenon arc lamp light source and a polarizer to set the initial polarization state. Light reflected off the sample may undergo a polarization state change, which can be a function of wavelength. A Photoelastic Modulator (PEM; the Modulator) modifies the polarization state of the reflected light which is then 'analyzed' by a second polarizer (the Analyzer). The resultant intensity is dispersed by a monochromator and detected by photomultipliers in the UV-Vis and an InGaAs detector in the IR. Ellipsometric angles Δ and Ψ as a function of wavelength can be extracted from measurements of $I_S = \sin 2\Psi \sin \Delta$ and $I_C = \sin 2\Psi \cos \Delta$. The SE was also used to measure unpolarized reflectance for $\Theta = 45°$ from $200 - 800$ nm.

Appendix C

Object Spectral Executive (OSPEX) Fitting Details

The Objectix Spectral Executive (OSPEX) fitting suite (https://hesperia.gsfc.nasa.gov/ ssw/packages/spex/doc/ospex_explanation.htm) is the process used to fit the soft X-ray spectral measurements of MinXSS-1 and RHESSI in this dissertation. OSPEX is a package available in Solarsoftware (SSW) and is written in the Interactive Data Language (IDL). The data is supplied in count rate (counts s^{-1}), the instrument detector response matrix (DRM) converts the model input photon spectrum to model count rate units. The model count rate is compared quantitatively to the measured count rate via the chi-squared metric ($\chi^2_{reduced}$). The input parameters, are varied until the minimal chi-square is achieved. This is generally taken as the best fit paramaters. Monte Carlo runs are performed around the best fit values to provide an estimate of the uncertainties. THe returned uncertatinies are 1σ assuming that the curature matrix is gaussian near the minimum of the $\chi^2_{reduced}$ surface.

OSPEX provides many photon spectral models for fitting. The only model discussed in this dissertation is the v_th (variable thermal), which contains, thermal bremsstrahlung, free-bound, and bound-bound transitions. The energy offsett for MinXSS-1 X123 is allowed to vary in OSPEX to better constrain its variance during the MinXSS-1 mission.